A 3D microrobotic actuator for micro and nano manipulation

Steven Banerjee

A thesis

presented for the Degree

of

Master of Engineering

in

Mechanical Engineering

at the

University of Canterbury

Christchurch, New Zealand

University of Canterbury

2015

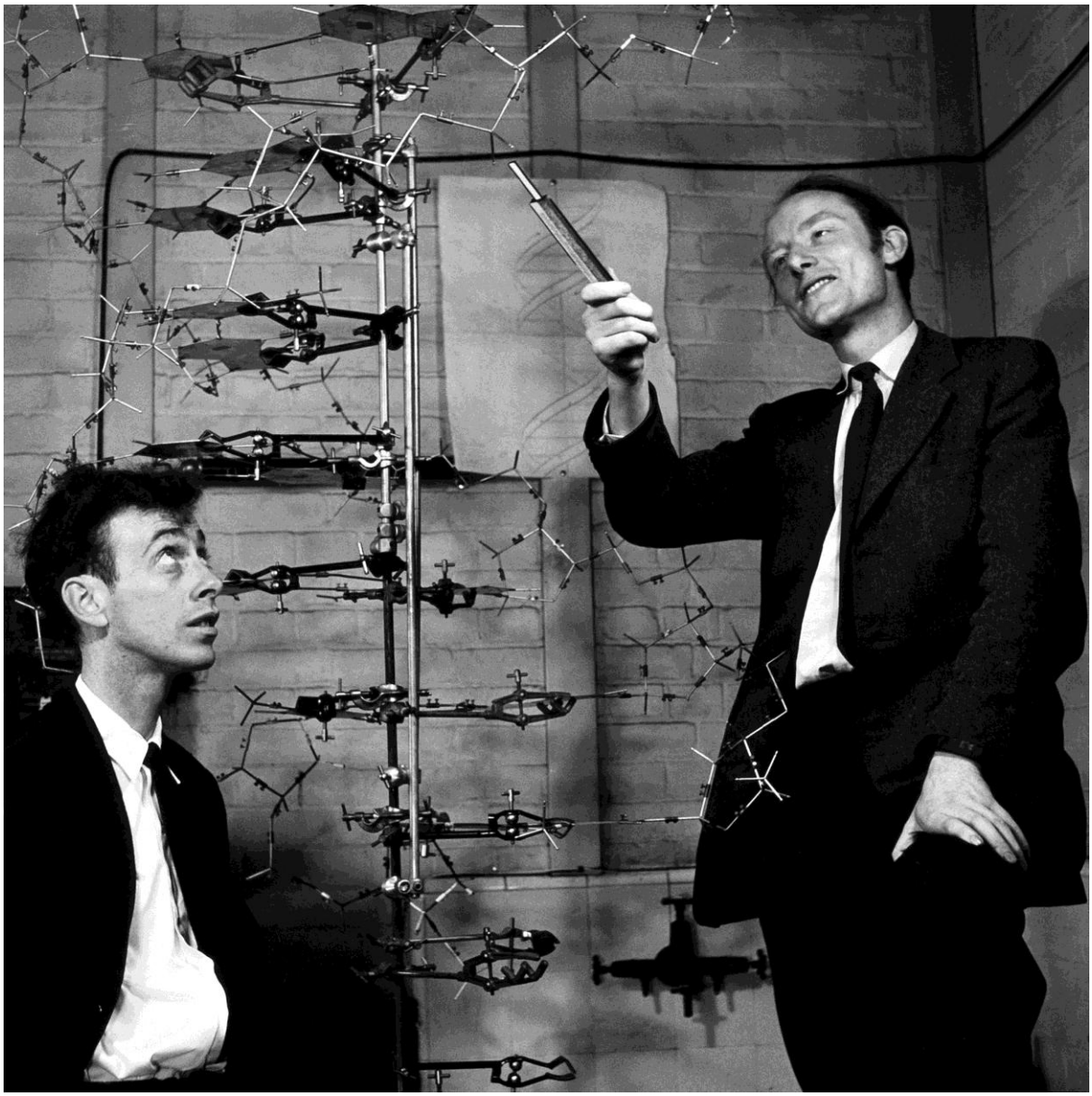

James Watson (left) and Francis Crick (right) with their model of part of a DNA molecule in 1953 at the Cavendish Laboratory in Cambridge University. Their work on the structure of DNA was performed with knowledge of Chargaff's ratios of the bases in DNA and some access to the X-ray crystallography of Maurice Wilkins and Rosalind Franklin at King's College, London. Combining all of this work led to the deduction that DNA exists as a double helix, thus to its structure. Crick, Watson and Wilkins shared the 1962 Nobel Prize for Physiology or Medicine, Franklin having died of cancer in 1958. (Science Source, Photo Researchers Inc., New York)

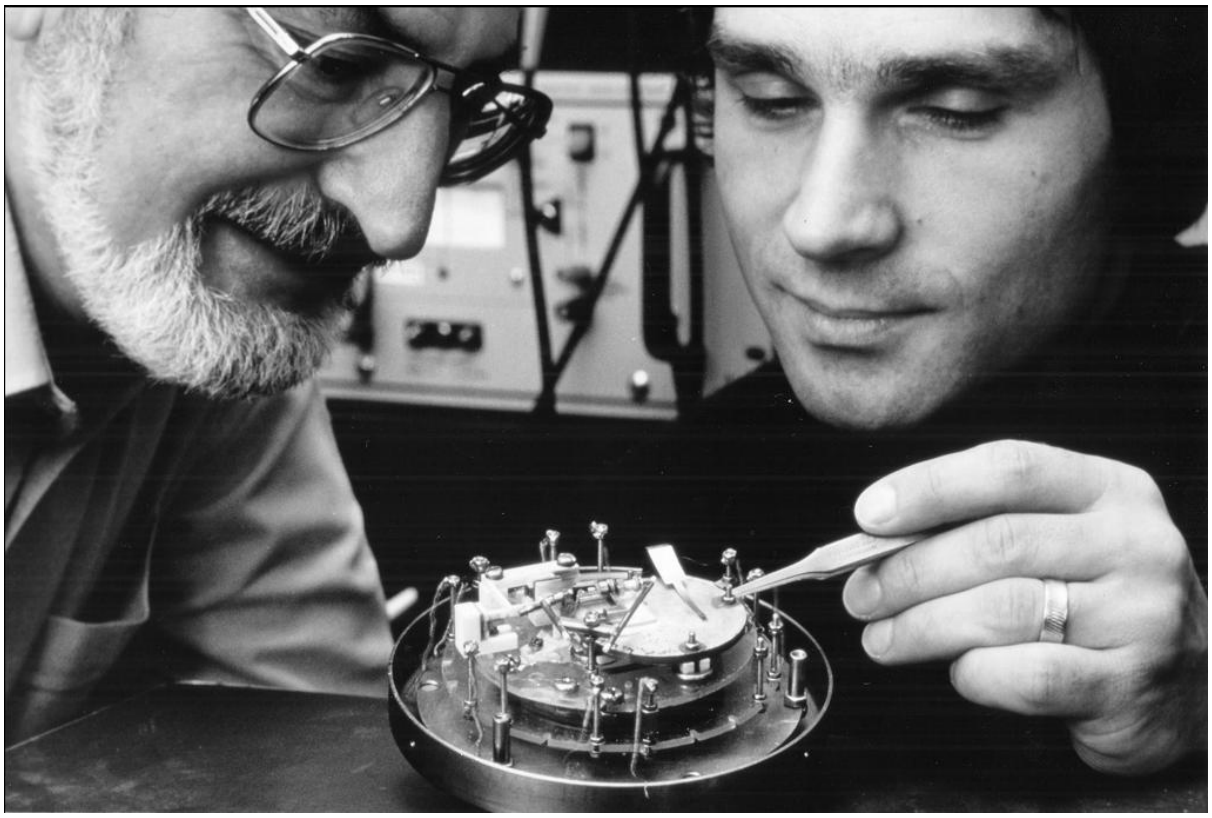

Heinrich Rohrer (left) and Gerd Binnig (right) from IBM Zurich Research Laboratory were awarded the Nobel Prize in Physics for their invention of the Scanning Tunneling Microscope. This was the beginning of the Nanotechnology age (IBM Corporation Photo Archive)

Dedicated to my mother, father, brother, Dr. William David Troughton and Rev Russell James!

ACKNOWLEDGEMENTS

I am greatly indebted to a large number of people for assistance of one sort and another in producing this thesis. In particular, I wish to express my gratitude to Professors Wenhui Wang, Maan Alkaisi and Stefanie Gutschmidt for suggesting this work and for all their guidance and encouragement. I am also grateful to Professor Richard Blaikie for many helpful discussions regarding brilliant fabrication ideas. I should like to thank Professor Xinyu Liu from McGill University for much help with the fabrication of the 4SA microrobot.

I would not be writing this if it weren't for the technicians, engineers and interns who helped me along the way with their brilliant hands-on-experience. Thank you Julian Murphy, Bruce Sparks, Gary Turner and Helen Devereux, because of whom I could run all my experiments.

This research is a consequence of funding from - the Mechanical Engineering Department for awarding me the Premier PhD scholarship; the MacDiarmid Institute for allowing me to use its sophisticated machines; Research & Innovation Office and The Maurice & Phyllis Paykel Trust for their research grants. Thank you very much.

ABSTRACT

Following the invention of the atomic force microscopy, AFM has revolutionised not only surface sciences but also biological sciences more recently. From being used as a microscope with atomic resolution generating 3D topography of surfaces to being used as a micro and nanomanipulation tool to manipulate single atoms; from studying the dynamics and mechanical properties of different cell types and molecules to being used in force spectroscopy and studying cell stiffness to detect cancer. Nonetheless, a majority of such work has occurred for single-scale manipulation with one probe. There have been some work in the past two decades to achieve parallel manipulation but none of them have been able to achieve independent 3D actuation of the probes critical for targeted biomanipulation.

We propose a new type of parallel architecture based microrobotic actuator that integrates arrays of microneedles with independent 3D mobility. We focus on the design of the parallel architecture and more specifically on a single-unit actuator (4SA and 3SA microrobot). The parallel architecture is designed as a hexagonal shaped structure to enable accommodation of multiple 3SA microrobots in a small space with efficiently laid electrical interconnects. It is found that the 3SA microrobot performs better in terms of motion performance and integration in the parallel architecture. The range of design dimensions are conceptualised and the design is analysed using extensive analytical and finite element analyses models. The 3SA microrobot can achieve a displacement of up to *72* μm in-plane at *160* V and *7* μm in out-of-plane at *35* V. We have also successfully demonstrated the vertical motion using a parallel-plate actuator arrangement of a long standing silicon tower underneath a microstage. Our first fabricated 4SA microrobot achieves an in-plane motion of up to *10* μm at *120* V and more than *0.5* μm at *600* V. We also propose two new fabrication process sequences designed to fabricate the microrobot and introduce a new blind feedback mechanism for achieving

vertical biomanipulation by detecting the change in voltage-displacement plot as signature for manipulation. Our PID control mechanism utilises visual feedback for in-plane alignment and blind feedback for out-of-plane alignment of the microneedles. We have successfully demonstrated the feasibility of our blind feedback system by designing a macro-manipulation experiment.

PREFACE

This thesis describes work undertaken at the Department of Mechanical Engineering and was supported by a generous funding from the Premier PhD Scholarship and travel grants from The MacDiarmid Institute for Advanced Materials and Nanotechnology, Maurice & Phyllis Paykel Trust, College of Engineering and the Research & Innovation Office.

Aspects of this thesis have been/will be patented and published in the following journals and conference proceedings:

[P1] S. Banerjee and S. Gutschmidt (2015) *Routing arrangement of control wires for platforms in the array and Voltage feedback for controlling platform displacement along the Z-axis* US and NZ Provisional Patent application pending

[J1] S. Banerjee and S. Gutschmidt (2014) *A 3D microrobotic actuator for micro and nano manipulation* Sensors and Actuators A: Physical (*in preparation*)

[J2] S. Banerjee, D. Muss and S. Gutschmidt (2014) *A Blind feedback mechanism for single cell manipulation* Biomedical Microdevices (*in preparation*)

[J3] A.S. Banerjee, R. Blaikie, and W. Wang (2011) *Microfabricated XYZ stage-needle structure for cellular delivery and surgery* Materials Science Forum, 700 pp.195-198

And have been presented at the following international conferences:

[C1] S. Banerjee, WH. Wang and S. Gutschmidt (2014) *Design and analysis of a 3D actuator for robotic manipulation* Proceedings of ASME International Mechanical Engineering Congress & Exposition, Montreal, Paper#39308 (*oral*)

[C2] S. Banerjee, S., M.A. Alkaisi, and S. Gutschmidt (2014) *Fabrication of a 3D microrobotic parallel actuator architecture* Proceedings of 11th Annual International

Wafer-Level Packaging Conference and Tabletop Exhibition, San Jose, California (*oral*)

[C3] S. Banerjee, WH. Wang and S. Gutschmidt (2013) *Silicon Centipede 1.0 - Design and performance of a micro-chip for cellular delivery* Proceedings of MicroNanoConference'13, Netherlands (*oral*)

[C4] A.S. Banerjee (2012) *A Microfabrication based 3-axis MEMS probe array architecture* Japan Advanced Institute of Science and Technology (*invited poster*)

[C5] A.S. Banerjee, R. Blaikie, X. Liu and W. Wang (2011) *Design and analysis of single crystal silicon 3-axis MEMS probe array architectures for cellular delivery* 37th International Conference on Micro and Nano Engineering (MNE), Berlin (*poster*)

[C6] A.S. Banerjee, R. Blaikie, and W. Wang (2011) *Microfabricated XYZ stage-needle structure for cellular delivery and surgery* 5th International Conference on Advanced Materials and Nanotechnology (AMN-5), Wellington (*poster*)

CONTENTS

LIST OF FIGURES

LIST OF TABLES

NOMENCLATURE

F_e:	Electrostatic force generated by the comb drive actuator
ρ:	Poisson's ratio, 0.28 for silicon
i:	Number of actuation comb finger pairs
ε:	$=8.85\times10^{-12}C^2N^{-1}m^{-2}$ is the permittivity of air
t_f:	Thickness of comb finger
gs_f:	The gap spacing between the adjacent comb fingers
V:	Actuation DC voltage
F_{el}:	Lateral electrostatic force
m_o:	Initial comb finger overlap
δ_x:	Comb finger displacement in the *x* axis
y:	Comb finger displacement in the *y* axis
$K_{x,y}$:	In-plane axial spring constant
k_n:	Negative spring constant
k_l:	Lateral spring constant
k_s:	In-plane axial stiffness of the spring flexure beam
k_t:	In-plane axial stiffness of the tethering beam
E:	Young's modulus of silicon, *129.5* GPa
h_s, h_t:	Height or thickness of the spring flexure or tethering beams
w_s, w_t:	Width of the spring flexure or tethering beams
l_s, l_t:	Length of the spring flexure or tethering beams
$U_{x,y}$:	In-plane static displacement
$[K]$	Global stiffness matrix
$[k]_m$	Element stiffness matrix for element
m	Number of the grid element
δ:	Vertical displacement of the microstage in the 3SA microrobot for analytical modeling
Δ:	Sideway displacement of the microstage in the 3SA microrobot for analytical modeling
α:	Angular displacement of the tethering beam used in the in-plane slope deflection model of the 3SA microrobot
M_n:	Beam end moment
V_n:	Shear force acting on the beam
F_z:	Out-of-plane electrostatic force
N:	Restoring force
d_{iz}:	Vertical displacement about the *z*-axis in a grid stiffness matrix model
ϕ_{ix}:	Torsional rotation about the *x*-axis in a grid stiffness matrix model
ϕ_{iy}	Bending rotation about the *y*-axis in a grid stiffness matrix model

f_{iz}:	Transverse force about the *z*-axis in a grid stiffness matrix model
m_{ix}:	Torsional moment about the x-axis in a grid stiffness matrix model
m_{iy}	Bending moment about the *y*-axis in a grid stiffness matrix model
i, j:	Node representation in grid stiffness matrix model
G:	Shear modulus of rigidity
I:	Moment of inertia
J:	Torsional constant
$[T_G]$:	Transformation matrix relating local to global degrees of freedom for a grid
$\left[T_G^T\right]$:	Transpose of the transformation matrix
K_z	Out-of-plane stiffness
l_{sh}, w_{sh}	Length or width of shin in crab leg flexure beam
l_{th}, w_{th}	Length or width of thigh in crab leg flexure beam
I_{th}, I_{sh}	Moment of inertia of thigh and shin in crab leg flexure beam
l_{tr}	Length of the truss in folded flexure spring beam
I_{tr}	Moment of inertia of the truss in folded flexure spring beam
$\vec{e}_r$	Direction vector of the magnetic field
μ_0	Vacuum permeability, $4\pi \times 10^{-7}$ V.s/A.m
ψ	Magnetic flux of the electromagnet or permanent magnet
I	Current
l_{em}	Length of the electromagnet
r	Average winding radius of the copper coil over the iron core
B	Magnetic field
$H(s)$	Heaviside step function
s	Laplace transform from time
F_h	Magnetic force due to hysteresis
K_d	Derivative gain
K_p	Proportional gain
K_i	Integral gain

This page has been left blank intentionally

Executive Summary

Three main research objectives have been thoroughly discussed and explored in this thesis. Are we able to design a built-in-system with 3D motion capability on a parallel scale? Can we design fabrication processes to develop such a system? And can we design feedback systems for high-throughput parallel manipulation? In this pursuit, we introduce two designs of a MEMS based microrobot consisting of a microneedle with 3D mobility and present in-depth analyses of the design, new ways of fabricating the microrobots and experimental test results of their motion performance. Our primary goal is to integrate multiple microrobots into a parallel architecture for independent actuation of multiple microneedles for targeted micro- and nano-robotic manipulation tasks, such as single-cell analyses. The first generation design is named 4SA microrobot because of its four-sided orthogonal structure. The second generation design is named 3SA microrobot because of its three-sided *120°* structure. The transition from 4SA to 3SA design results in an increase by more than *40%* in the number of microrobots that can be integrated into the parallel architecture with two less electrical interconnects for every actuator side. The microrobots can be densely packed into a hexagonal structure with efficiently laid out electrical connections.

There have been several attempts in the past *15* years to automate such cell manipulation; these have been reviewed in Chapter 1. None of them have been able to achieve a throughput rate of performing parallel cell manipulation, critical for disease research and drug discovery. Moreover, much work has been done trying to parallelise the microprobe/microneedle architecture in order to achieve high-throughput results for micro and nano-robotic manipulation. Nonetheless as we report in Chapter 1, all such designs and systems are limited in terms of independent motion of microneedles across multiple axes. One of the main reasons for this restricted mobility is the complexity associated with achieving an out-of-

plane motion. Moreover, the control of multiple microneedles independently poses further challenges to automation. Limitations in fabrication of such a parallel architecture with mobility across multiple axes present additional difficulties as well.

There are several key engineering requirements and constraints including design of the microrobot in terms of vertical stiffness, achievement of vertical motion, integration of the microneedle into the microrobot and development of a scaled up model for the feedback mechanism. These have been addressed in detail in different chapters. After exploring the designs of the two microrobots in Chapter 2, we conceptualise the dimensions and analyse the system for these values. Due to the fact that there are two separate designs of the microrobot, their design analyses, fabrication and testing have been discussed separately. In Chapters 3-5, we focus solely on the 4SA microrobot. We discuss the analytical and FEA models developed to study its motion performance which includes grid stiffness matrix model, slope-deflection equation model, electrostatic, displacement, stress and modal analyses models. We present two distinct fabrication processes developed to fabricate the microrobot with integrated microneedle and bottom tower electrode, and successful demonstration of the 3D motion of the 4SA microrobot. The microrobot is able to achieve a reasonable displacement of up to *10* μm at an applied DC voltage of *120* V in-plane which can successfully cover almost *60%* of the surface area of a typical human cell, *15* μm in diameter. The vertical displacement achieved is slightly above *0.5* μm at *600* V showing a close conformity with the values as predicted in the analyses. In Chapters 6 and 7, we focus on 3SA microrobot for analyses and fabrication. It is predicted that the 3SA microrobot design could achieve a superior in-plane actuation (x, y) of *72* μm (±*36* μm) at *160* V and an out-of-plane actuation (z) of *7* μm at *35* V. Compared to this, a 4SA microrobot can achieve similar in-plane actuation and an out-of-plane actuation of *5.8* μm at *35* V. In Chapter 8, we report the successful implementation of a blind feedback mechanism for parallel vertical

manipulation using a macro-scale experiment and discuss a control scheme for the 3D motion of the microrobot incorporating our feedback mechanism. The controller has been designed such that the in-plane motion of the microneedles will be achieved via an open-loop control and the out-of-plane motion via a closed-loop control. In the final chapter, the empirical findings of this thesis are briefly summarised, original contributions are noted and a future research blueprint is outlined.

In brief, the original research contributions from this work are as follows:

- Design, analysis, fabrication and testing of 4SA microrobot.
- Design and analysis of 3SA microrobot.
- Successful implementation of the parallel-plate actuator for vertical manipulation and of the sensor for blind feedback.
- Design of two fabrication sequences to integrate microneedle and tower electrode to the microrobot.

Chapter 1: Introduction and Background

The two major components of the microrobot are the microneedle and the actuation mechanism that provide the 3D mobility. Therefore in this chapter, we discuss our motivation toward developing such a robotic system for manipulating single cells, discuss the prior art in terms of the developments in microneedles and nanoneedles and state-of-the-art in actuation systems. Based upon the critical findings from this review, we frame critical research questions and list a number of primary constraints that our system needs to satisfy.

1.1 Motivation

The Human Genome Project [1] was an international publicly funded $3 billion, 13-year research project. The first draft published in 2001, followed by a final draft in 2004, reports the identification and mapping of all the genes of the human genome and the sequence of chemical base pairs that build up the human DNA [1, 2]. Such genomic sequencing is gradually transforming medicine and life-sciences leading to an era of personalised medicine. This leads to a better molecular analysis depending upon specific genetic traits during the very early drug discovery stage can help avoid individual differences in response to drugs. One such case is of Rofecoxib (brand name Vioxx), a nonsteriodal anti-inflammatory drug for treating osteoarthritis which had to be withdrawn from the market after it was found to increase the risk of myocardial infarction and stroke [3]. An increasing amount of biological and medical research is focusing on such personalised drug discovery and development.

Moreover, the model of biology and medicine is changing from studying population based cells and concluding from the average values to single cells. Recent increased spending of more than $90 million by the American National Institutes of Health to accelerate the development of this model establishes the growing importance of biomanipulation at the singular cell level [4]. At the level of individual cells, all diseases show heterogeneity in their

pathology such as why some cells degenerate while other cells in their proximity are normal, or why some cells respond to drugs better than others. Thus, our primary goal is to develop a system that can address such single cells on a parallel scale in a targeted fashion. Understanding genetic behaviours at the single cellular level, yet having a high throughput system to manipulate multiple single cells simultaneously, will provide a significant leverage to drug discovery and research [5]. Thus single-cell manipulation and analysis has the potential of fundamentally changing how multicellular organisms work and generating new research questions [6].

Some of the widely used techniques for achieving cell manipulation have several limiting factors. For example, introducing deoxyribonucleic acid (DNA) or transgene into the nucleus of a cell where it is randomly inserted into the host genome for creating knockout mice is technically challenging. The transfection and survival rate are approximately *20%* [7]. There are various techniques for gene delivery including viral vectors, electroporation and liposomal carriers which are critical for investigating specific cellular responses [8]. For instance, viral vectors involve the viral particles that encapsulate a modified genome carrying a therapeutic gene cassette coupled with large DNA or RNA molecules in place of the viral genome that they introduce into the cells [9]. Thus even if the stable transgenic organism is created, it would have some of the viral genome integrated as well. The vector also limits the maximum size of the delivered transgene, thus limiting the amount of flanking DNA and regulatory elements introduced into the cell. The lack of these regions may reduce nuclear localisation, chromosomal integration and expression [10]. Electroporation is another physical technique of importing small molecules and macromolecules into cells via increased cell membrane permeability [11].

In general, there are several technologies for biomanipulation - more specifically, for introducing foreign materials into a cell - that can be broadly classified into optical, electrical,

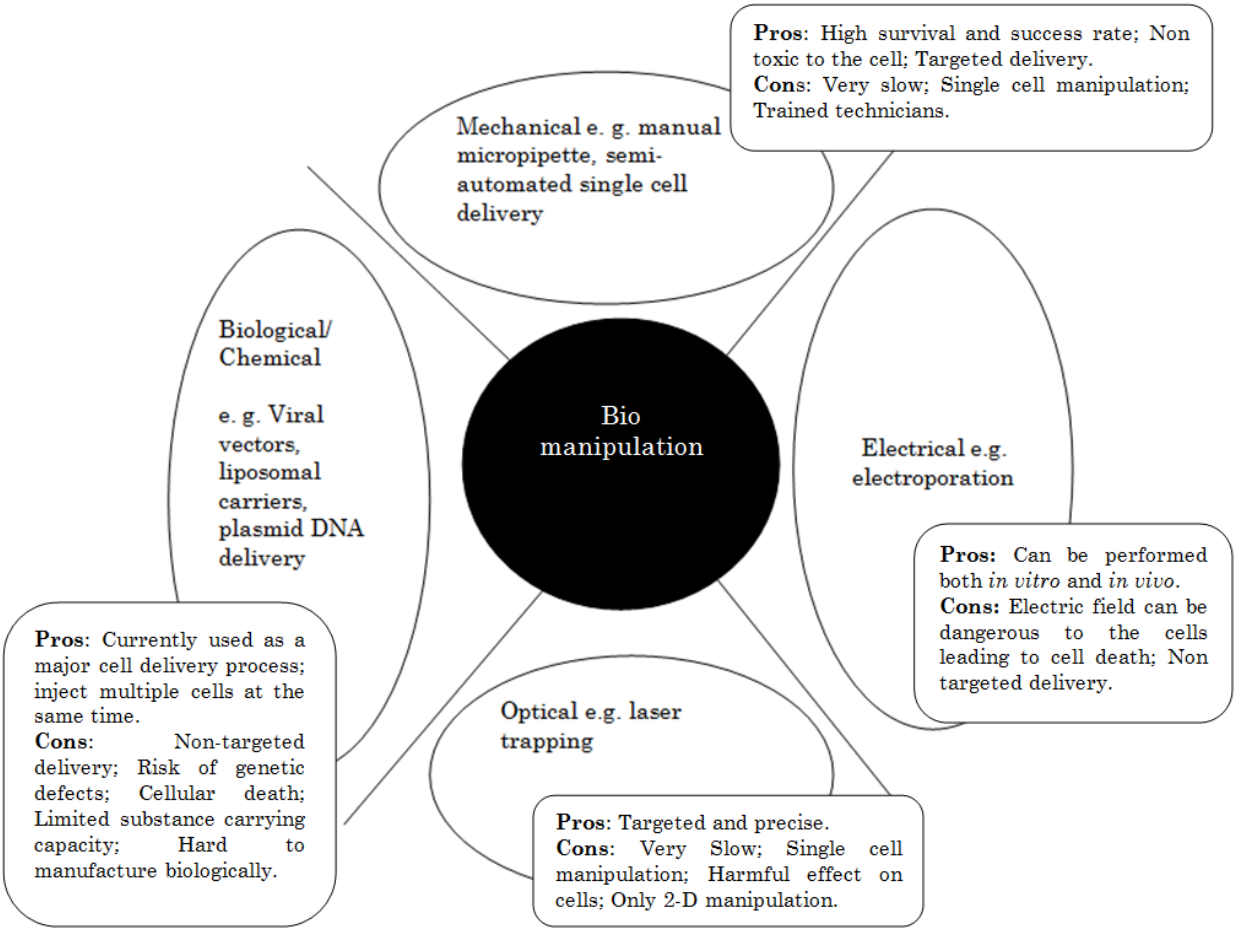

Figure 1.1 Different biomanipulation techniques.

biological and mechanical delivery as demonstrated in Figure 1. The advantages of these techniques are illustrated in Figure 1. Nonetheless, all of these methods share common disadvantages. They are harmful to cells to a major extent and methods like laser trapping [12] may induce abnormalities in the cells' genetic material. Moreover, methods like electric-field-induced rotation of cells [13] are not feasible due to the lack of means of holding the cell in place for manipulation, as the magnitude of electric fields has to be kept low to avoid damaging any cell. Most important, all of these techniques are only applicable to population-based cell manipulation and not for single cells.

In spite of the availability of several non-contact biomanipulation techniques, the contact delivery using microinjection remains one of the most prominent biomanipulation methods for manipulating cells that can inject large numbers and different types of macromolecules to

a wide variety of cell types coupled with high cell viability. Microinjection is the direct pressure injection of a solution into a cell through a glass capillary which is an effective and reproducible method for introducing exogenous material into cells in culture [14]. The molecules of interest include peptides, proteins, oligonucleotides, DNA and a variety of other substances that alter or assay cell function. Nonetheless, single-cell manipulation involves injecting one cell at a time with individual glass micropipettes observed under an optical microscope, which makes the task not only laborious causing human fatigue, but also limits its viability to only a small number of cells, for example *100* to *200* cells [15, 16].

There have been various efforts in automating cell manipulation by developing visually-guided systems, semi-automated and teleoperated systems. In automatic manipulation of biological cells or microassembling of micro-nano components, actuators with high-precision such as piezoelectric driven manipulators are used [17]. Most of the current actuators, based on electrostatic, thermal, magnetic or pneumatic principles are not suitable for operating in liquid surroundings. Sun and Nelson [18] have developed a microrobotic system capable of performing automatic embryo pronuclei DNA injection autonomously through a hybrid visual servoing control scheme that achieves a success rate of *100%*. Advancing this work, Wang et al [19] have developed a microrobotic system for fully automated zebrafish embryo injection integrating computer vision and motion control as shown in Figures 1.2 and 1.3. It achieves a high throughput rate of injecting *15* zebrafish embryos per minute with a *98%* survival rate, a *99%* success rate and a *98.5%* phenotypic rate. Nonetheless, the cell manipulation tests with our parallel architecture are yet to be achieved. Multiple bioactive foreign compounds such as plasmids, RNAs, antibodies, peptides, diffusion markers, elicitors etc. can be introduced into the same target single-cells [20].

A high throughput biomanipulation system developed by Matsuoka et al [20] is a single-cell manipulation supporting robot (SMSR). SMSR is applied for microinjection into rice

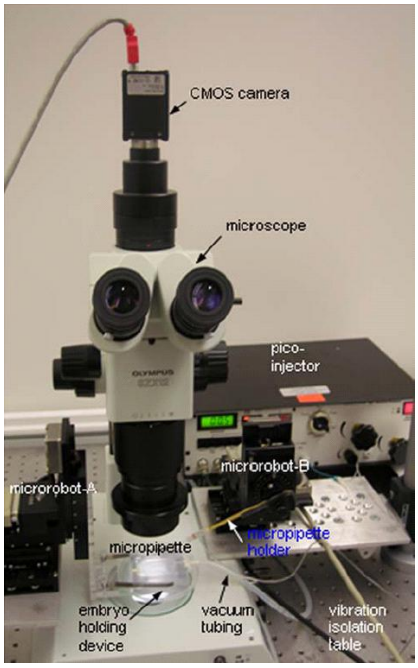

Figure 1.2 An automatic cell manipulation system having two 3D micromanipulators (microrobots A and B), camera and microscope for visual feedback and a computer controlled picoinjector provides positive pressure for material deposition [19].

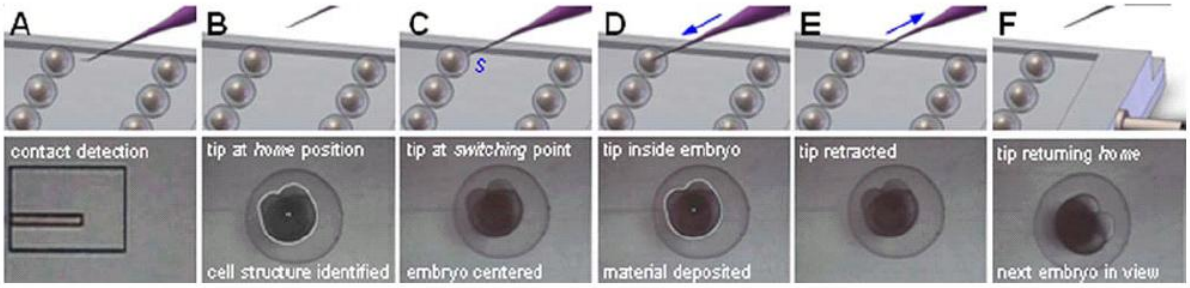

Figure 1.3 Illustration of the automated manipulation flow. Top row: 3-D view. Bottom row: microscopic (image) 2-D view. (A) Vertical height of the tip being determined by a computer vision approach. (B) Micropipette at home position (C) Micropipette positioned at the switching point (D) Micropipette tip penetrates the embryo and delivers materials (E) Micropipette retracts out of the embryo (F) Micropipette returns to the home position, and the next embryo is brought into the field of view [19].

protoplasts and mouse embryonic stem (ES) cells. Albeit this is one of the first published reports about successful microinjection into ES cells which is *17* times faster than that of the robot-less work, the success rate is very low: in case of rice protoplasts, it is *5-10%* (for non-adhesive cells) and *7-8%* (for adhesive cells) and in case of mouse ES cells, it is just *0.2-*

2.2%. Some other prominent automated biomanipulation systems reported in the literature include a computer controlled piezo-manipulator system for biomedical applications such as intracytoplasmic sperm injection (ICSI) [21]. In a relatively recent work, Anis et al [22] presents the preliminary results of the development of a fully automated workstation for single cell manipulation. It is capable of automated selection and transfer of individual living cells of interest to analysis locations.

Nevertheless there are several challenges in the automatic manipulation of single adherent cells [23]. In terms of biological delivery into cells, the volume delivered can be influenced by parameters such as applied injection pressure, the application time of the injection pressure and the level of the balance pressure. Either there is an undesired efflux from or influx into the micro-capillary. Some of the parameters that affect the hardware include:- size of the tip opening, tip length, surface treatment and possible tip breakage for micro-capillary tip, stability of the pressure source, accuracy of the pressure regulator, the speed of the check valve for the micro-injector, positioning accuracy and preciseness of the axial movement for the positioning and penetrating microrobots.

Although these robotic biomanipulation systems overcome the limitations experienced by manual manipulation, nonetheless they can only achieve a very slow throughput rate of up to *1500* cells per hour, significantly inefficient when it comes to disease research and drug discovery. Because of the limitations of the existing manipulation systems in terms of targeting single cells in a parallel form, we have been motivated to design a system that can achieve such a task. Therefore, it is first critical to understand the relevance of our microrobot in terms of how we plan to manipulate single cells using our proposed parallel architecture.

1.2 Proposed overall design concept

In order to appreciate the function of the microrobot better, it is critical to understand its

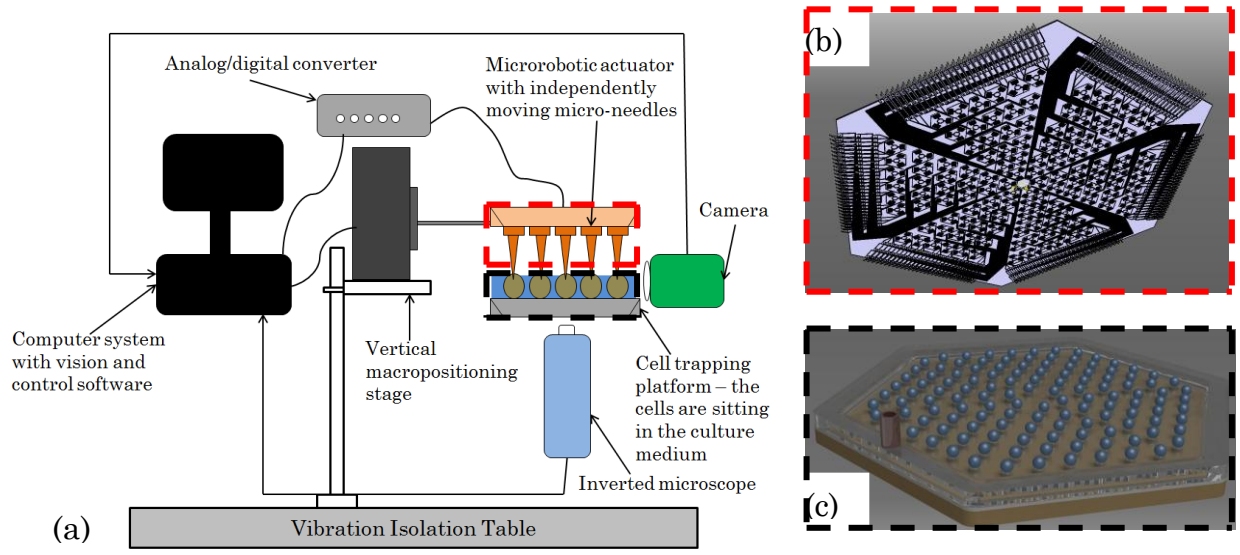

Figure 1.4 (a) Schematic of the proposed experimental setup for single-cell manipulation. Graphical illustration of **(b)** a parallel architecture chip (Section 2.2.2), and **(c)** a cell trapping platform (Section 2.2.2).

associated hardware and software and how the parallel architecture would target manipulate the cells. Our proposed experimental solution, schematically shown in Figure 1.4 consists of an inverted microscope with a CMOS camera, a separate CMOS camera placed sideways, a vertical macropositioning stage, the parallel architecture based microrobotic actuator (Figure 1.4b) placed directly on top of the cell trapping platform (Figure 1.1c), the host computer with a data acquisition card, vision and control software and the analog/digital converter that connects the computer with the actuator. The system setup is mounted on a vibration isolation table. The control mechanism for a *10×1* parallel architecture system has been explained in details in Section 8.3.4. To enable the readers appreciate the functionality of the parallel architecture better, this section gives a high-level overview of the single-cell manipulation operation.

The single cells are trapped into a cell trapping platform as explained in Section 8.3.1. The actuator is mounted using a vertical macropositioning stage and placed directly on top of the trapping platform. The inverted microscope captures the images of the single-cells and the vision software processes these multiple images to find the targeted zone inside the cell that

is to be manipulated. Once the target zone and its corresponding *xy* coordinates are identified, this information is fed into the control software that drives the in-plane motion of the microneedles on the actuator accordingly. Once the microneedles have been aligned as per the in-plane coordinates of the target zone, DC voltage is applied to the parallel plates of the actuator which pulls the microneedle backward, toward the silicon tower plate. This retracted position of the actuator is maintained until the next step. The vertical macropositioning stage is then driven to bring the actuator in this retracted state to the proximity of the single cells. The CMOS camera placed sideways records the vertical motion and verifies whether the microneedles are in the proximity of the cell. Once this information is verified, the control software drives the microneedle out-of-plane (opposite to the previous retracted position) by decreasing the DC voltage. The voltage-displacement feedback mechanism in the controller determines the single cell manipulation at this stage until the microneedle tip is at the target zone. Once the manipulation is complete, the vertical macropositioning stage pulls the actuator back and the next set of manipulation occurs.

One of the major challenges of this research is individual control of the microneedles and feedback during vertical manipulation mode. Our blind feedback, discussed in Chapter 8 is a solution to this problem. Nonetheless, there have been some research done to address this challenge and can be explored as befitting our system. For example, our design of experiment can take into consideration using interferometry for parallel readout of the vertical motion of the microneedle array as has been demonstrated by Sulchek et al [24]. This would require integrating the microstage with phase sensitive diffraction grating during fabrication. While the microstage in the actuator is in motion, the intensity of the diffracted orders is altered. This order intensity from each actuator microstage in the parallel architecture is measured with a custom array of silicon photodiodes with integrated complementary metal–oxide–semiconductor amplifiers. Reed et al [25] have also used a parallel readout scheme using the

strobed interferometric microscopy to probe the behavior of the individual cantilever in an eight cantilever array.

A major concern while bringing the actuator microneedles in proximity with the cells is the inevitable effect of electrolysis, anodisation and polarisation of the actuators if they are in contact with the polar cell culture medium that keeps the cells alive. It has been shown that in high dielectric constant fluids like a cell culture medium, water etc., the electrostatic actuation gains two orders of magnitude at the same potential compared to a normal air medium [26]. This can be exploited in future designs to gain significant motion at a much lesser driving voltage. Nonetheless, at equilibrium, ionic solutes in conducting fluids screen the electrode potential leading to its polarization and thus disable the actuator. This can be avoided through several ways:

- Removing the cell culture medium from the cell trapping platform momentarily during the manipulation process and then transferring the medium back into the platform once the manipulation is complete. Doing so would require the manipulation to occur in a short timeframe so that the cells remain alive during this transitional process.
- Isolating the actuator from the polar medium can solve the problem. But for that to happen would require the microneedle to be of significant height (e.g. at least *100* μm) so that the isolation is possible.
- Using frequency dependent electrostatic actuation by operating the comb-drive and parallel-plate actuators at a frequency modulated higher than the relaxation rate of the ions in solution [26-28]. But again this would be requiring ac signal for the actuator which would lead to Joule heating of the medium which might lead to cell damage. It must be taken into consideration that the heating does not damage the health of the cells.

The electrodes can also be protected with a conformal layer of parylene-C as a passivation scheme for the electrodes in corrosive media.

Over the course of this research, efforts have been made to establish communication with multiple biologists, material scientists and clinical researchers to identify a set of biomanipulation applications for the proposed parallel architecture based microrobotic chip technology [29]. To reiterate, some of these applications are noted here:

- Delivery of biomolecules to multiple singular cells using our proposed microrobotic chip technology and measuring the expression patterns of proteins and genes will be of critical importance in proteomics and genomics [30, 31].
- Tissues have a highly heterogeneous cell population [32]. For example, a cardiac tissue has diverse cell populations including cardiomyocytes, fibroblasts, endothelial cells, smooth muscle cells, leukocytes and a range of multipotent progenitor cells. Using our chip technology, it would become possible to perform massive single cell examination of different singular cardiac cell types [33].
- New breakthrough in stem-cell research has made possible for the generation of pluripotent stem cells from adult stem cells [34]. This has made opportunities for studying diseases in cells in a petri-dish rather than using animal models. Our actuator technology can be used to manipulate parallel arrays of these types of cells critical for drug discovery and development.

1.3 Background, problems and prior art

Our microrobotic actuator has two major components, the microneedle and the actuation system that gives the 3D mobility to it. In the forthcoming section, we review the prior art and development in terms of these two components. We'll review the major works in the past *15* years, the challenges and our proposed solutions to overcome these limitations. Our initial interest is in solid microneedles rather than hollow, owing to fabrication complexities

associated with the later. We envision the scope of our microrobotic actuator transcending the field of medicine, chemistry and material science, and acting as a substitute for Atomic Force Microscopy (AFM). The applications of such a microrobotic technology would be ranging from local functionalisation of nanoscale sensors, single molecule force spectroscopy, cell mechanical measurements, and development of micro/nano-arrays of DNA/protein for disease diagnostics. Some of these applications using current AFM technology have been addressed in these references [35, 36]. Nonetheless, we focus on the primary application of single cell manipulation for which the microrobot is being currently developed. There is a paradigm shift in biomanipulation from population-based analysis to single-cell analysis [4]. As technologies are improving in sensitivity and throughput sufficient to begin measuring and understanding heterogeneity in complex biological systems, single cell analysis is gaining prominence.

1.3.1 Prior art in microneedles and nanoneedles

Micro-/nano-needles have become a major research focus for almost two decades because of its use in biomedical applications including μTAS (micro Total Analysis Systems) [37]. Nevertheless their integration into self-governing microsystems has not been achieved yet due to complicated fabrication and process compatibility problems. Since microneedles form an integral part of our microrobot, a repository of works in this field in the past two decades has been reviewed in this section. There is one common disadvantage with all these microneedles though, that they are all stationary and have no individual mobility. We are interested in a mobile microneedle design that can effectively penetrate through a cell membrane (thickness ranging up to tens of nanometres) and thus lead to successful manipulation. This would require the tip of the microneedle to be ranging from submicron scale to a few tens of nanometres.

Microneedles fabricated using MEMS technology can be divided into two major categories: in-plane needles where the needle shaft is fabricated in a plane parallel to the substrate as shown in Figure 1.5, and out-of-plane needles which have their shafts perpendicular to the wafer plane as shown in Figure 1.6. While some of these in-plane needles allow for integration of electronics, nonetheless they can only be arranged in single rows and problems associated with interconnects make them very challenging to integrate with self-governing microsystems. On the contrary, the out-of-plane needles can be arranged in arrays so that fluid can be delivered or sampled over a wider area making the system more stable and robust [38].

The other major basis of classification of microneedles include: the method of delivery, whether fluid or material; and solid and hollow microneedles. In terms of transdermal drug delivery studies, much attention has been paid to solid microneedles. They have been used either to pierce holes in the skin as a pre-treatment before application of a transdermal patch or coated with drug that dissolves off the needles upon insertion into the skin [39]. On the contrary, hollow microneedles have received less focus because they are more challenging to use, for example in transdermal drug delivery. Due to their weak structures compared to solid

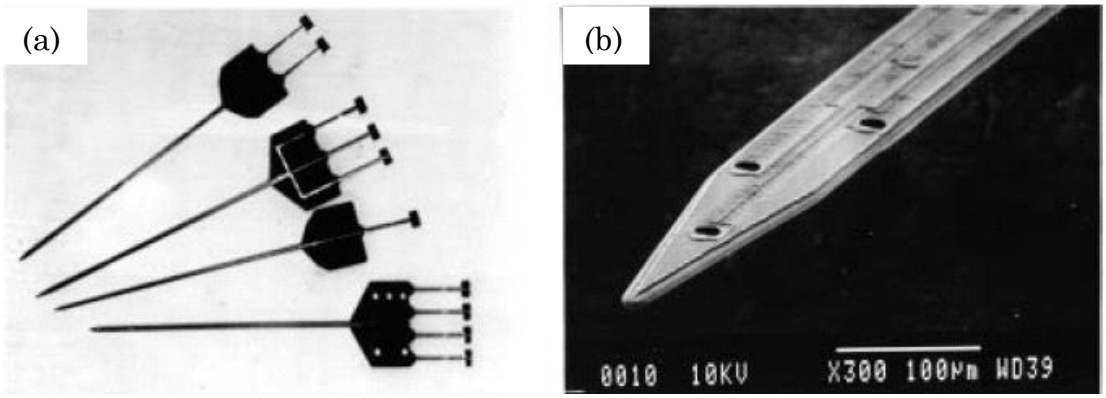

Figure 1.5 (a) Neural probe designs having one, two, three, and four micro channels for drug delivery. **(b)** Overall SEM view of a probe containing three drug delivery channels. Each outlet orifice has a recording site beside it. The site at the tip of the probe has a large area and can serve both for recording and stimulation [40].

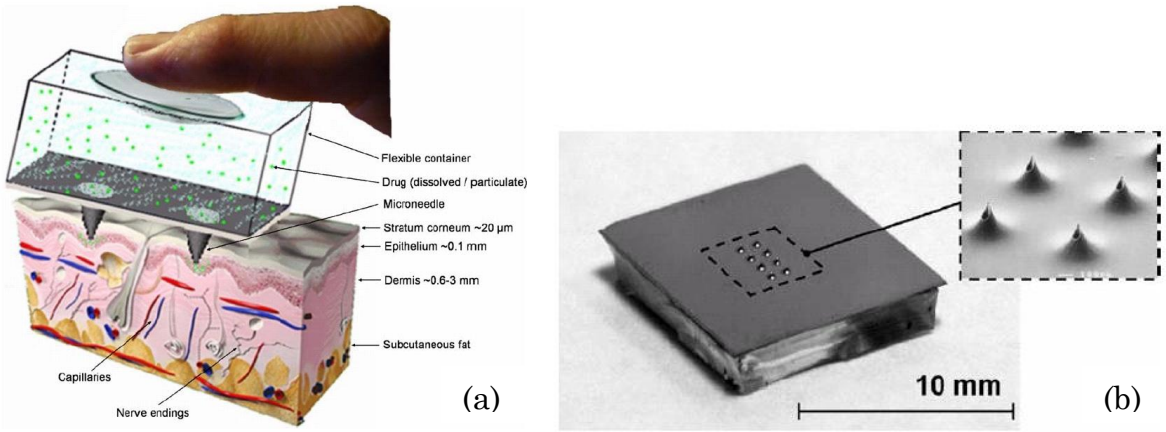

Figure 1.6 (a) Concept of a miniature syringe (*not to scale*). Pressing a finger on the deformable drug reservoir drives the needles into the skin and injects the drug suspension or solution into the epidermal skin layer. **(b)** A MEMS syringe with 8 silicon microneedles and a PDMS drug container [41].

microneedles, they have additional constraints on needle design and insertion methods [42, 43]. A majority of the microneedles developed have been used for transdermal drug delivery. Micro-/nano-needles for biomanipulation are usually used in conjunction with existing AFM infrastructure which has been discussed later in this section.

Following the pioneering work by Wise et al [44], there have been numerous studies that exploited integrated circuit technology to build neurological microneedles. One such hollow in-plane multichannel bulk-micro-machined microneedle is shown in Figure 1.5 [40]. It incorporates one to four flow channels and is capable of selectively delivering chemicals at the cellular level and electrically recording from and stimulating neurons *in vivo*. The needles bury micro-channels in the needle substrate and are compatible with the formation of electrode arrays for electrical recording and stimulation on the same chip, allowing multiple chemical delivery ports and multiple recording/stimulating sites on a single shank. One of the early works of manipulating biological cells in an arrayed fashion is a MEMS based chip consisting of an array of hollow micro-capillaries used for injection and a separate micro-chamber for cell trapping. This chip is capable of controlled DNA injection into the cells [45]. Nonetheless, these microneedles are static and thus highly targeted manipulation is

almost impossible. Stoeber and Liepmann [46] have developed a disposable hollow out-of-plane silicon needle bonded with a deformable poly dimethyl- siloxane (PDMS) reservoir for a suspension of lyophilised drug. The design avoids clog formation in the needle channels and permits a density of *600* needles/cm² for shaft length of *200* µm. Continuing on this previous work, Hafeli et al [41] presents a microfabrication process for silicon microneedle based out-of-plane miniature syringes. The fluid-filled reservoir consisting of the drug solution or microparticle suspension and made out of PDMS is bonded to the silicon substrate consisting of the hollow needles as shown in Figure 1.6. Teo et al [47] have fabricated both solid and hollow microneedles with straight-side walls for transdermal drug delivery. The solid microneedles are *130* µm high, *80* µm in diameter and an interneedle distance of *200* µm. The hollow microneedles are *150* µm high, have an interneedle distance of *200* µm and an inner and outer diameter of *25* µm/*60* µm and *80* µm/*100* µm respectively. Both types of needles are arranged in a *10* by *10* arrayed architecture and the hollow needles are coupled to a conventional *1* ml syringe.

Trimmer et al [48] have developed microneedles for injecting DNA into cells, having heights ranging from *10* µm to several hundred microns. They are pyramidal in shape with a

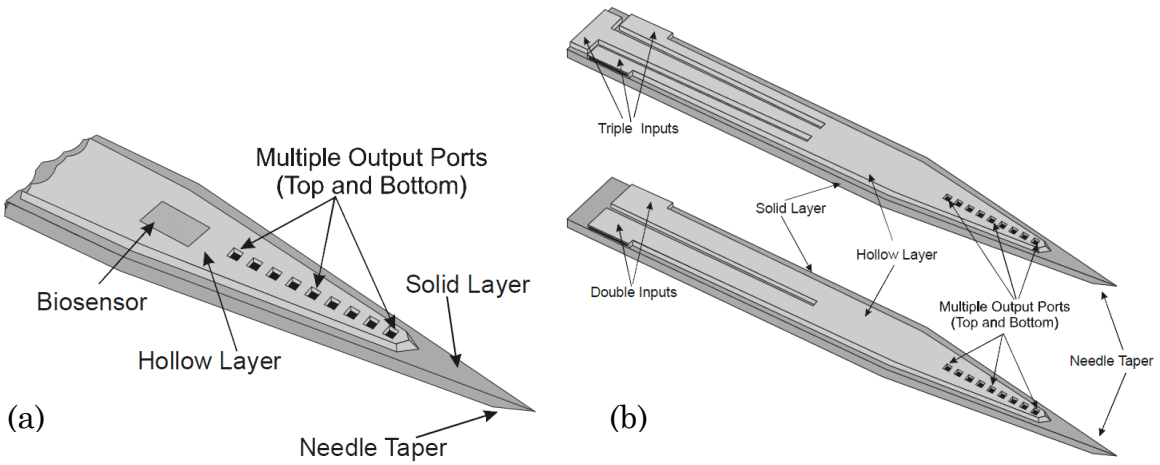

Figure 1.7 Schematic of tapered in-plane Microneedle (a) multiple output port needle with an integrated biosensor (b) multi-lumen design [49].

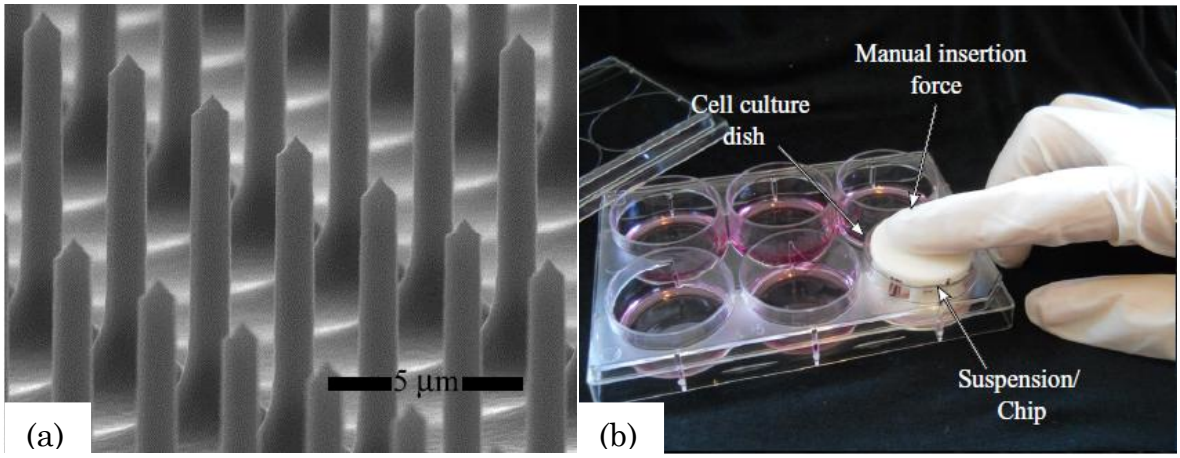

Figure 1.8 (a) SEM image of the silicon needles (b) The suspension and chip are placed in a culture dish with HeLa cells. Manual force is used to insert the needle array into the layer of HeLa cells, allowing the desired particles to enter the cells by diffusion [50].

half angle of about *13*° and the tip is ultra-sharp. It allows parallel cell injection in an orderly square pattern. The fabrication is done using bulk micromachining including anisotropic wet etching. These microneedles are used to inject DNA into tobacco leaves and nematode cells. A more recent work of parallel injection into HeLa *229* cells (*15* µm in diameter) is a MEMS chip having an array of static microneedles (*4* million in a single chip) with an average diameter of *1* µm, length of *8* µm and an interneedle spacing of *10* µm [50]. It is demonstrated in Figure 1.8. They are fabricated using a series of DRIE steps. HeLa cells usually stretch when they adhere to the culture dish, often reaching over *50* µm in lengths with a *10* µm width. The chip is connected to an ABS plastic based suspension using a compliant orthoplanar spring to allow vertical displacements and minimize other deflections.

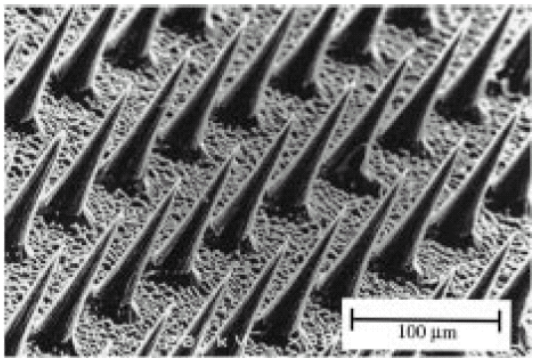

Figure 1.9 SEM image (*20* by *20* array) of microneedles [51].

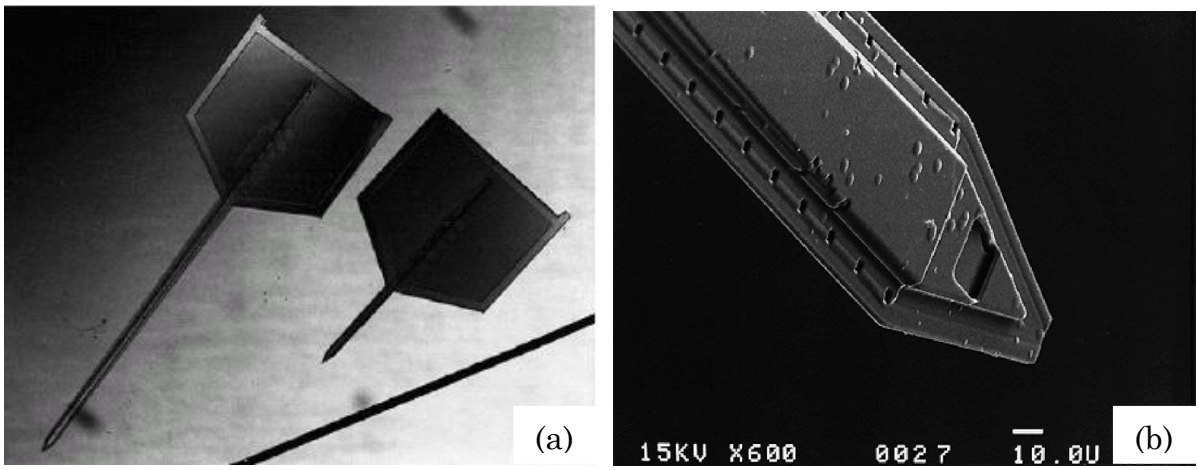

Figure 1.10 (a) Two silicon microneedles placed alongside a human hair. (b) Top view showing the tip end of a microneedle [52].

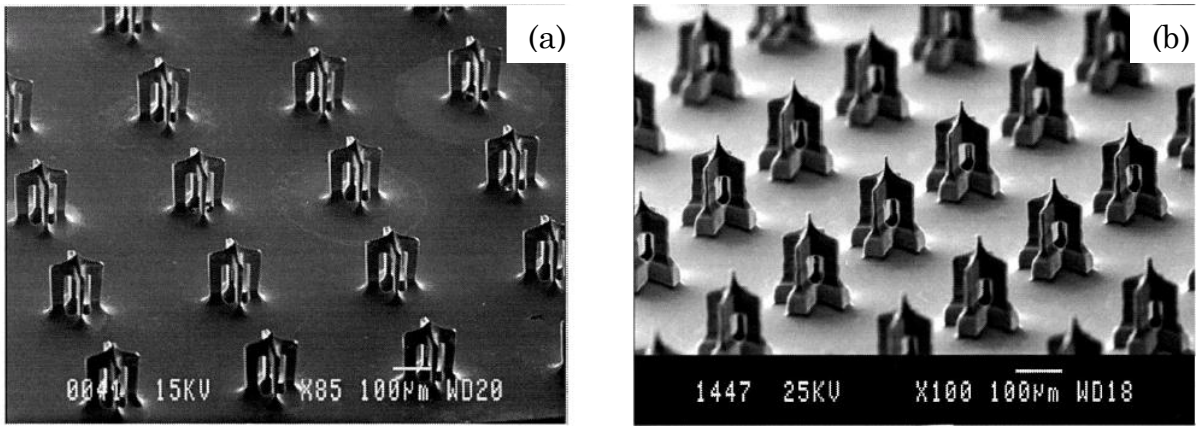

Figure 1.11 SEM image (a) of side-opened microneedles, the hole beginning at the base of the needle (b) of side-opened microneedles, the hole beginning approximately *50* µm above the base of the needle. The length of the structure is *210* µm [53].

The average cell survivability is *97.7%* after being penetrated with propodium iodide, a membrane impermeable dye.

Brazzle et al [54] have designed, fabricated and characterised a new type of fluid coupled hollow in-plane metallic micromachined needle arrays. Individual needle channels are *2* mm long and have center-to-center spacing of *200* µm. The inner dimensions of each needle are approximately *30* µm wide and *20* µm high. The total needle array width is *5.2* mm and the needle coupling channels centered along the length of each needle are *100* µm wide. Continuing on their previous designs, they have designed and fabricated a new type of hollow

metallic active microneedle as shown in Figure 1.7 [49]. The design includes tapered needle tips, multiple output ports on the back and front of each needle, multiple lumens and multiple input ports and bioluminescence based biosensors for monitoring metabolic levels.

Henry et al [51] have developed one of the first solid out-of-plane micro-machined needles for transdermal drug delivery which enhances transport of molecules across skin by more than four orders of magnitude as shown in Figure 1.11. The microneedles are fabricated as a *20* × *20* array with extremely sharp tips (radius of curvature < *1* μm) and *150* μm long. They are also used on human cadaver epidermis to test their transport-enhancing and mechanical properties. Lin and Pisano [52] have designed and fabricated hollow in-plane silicon-processed microneedles which are integrated with bubble-powered micro-pumps in the form of a series of polycrystalline silicon heater strips running across the floor of the channels at the shank end as shown in Figure 1.10.

Griss and Stemme [53] have developed a hollow out-of-plane silicon microneedle array (*21* needles) that has openings in the shaft rather than having an orifice at the tip, as shown in Figure 1.10. The microneedle array is assembled on a brass carrier that is connected to fluid silicone tube. The needle is *210* μm long. Nordquist et al [55] have showed that microneedles

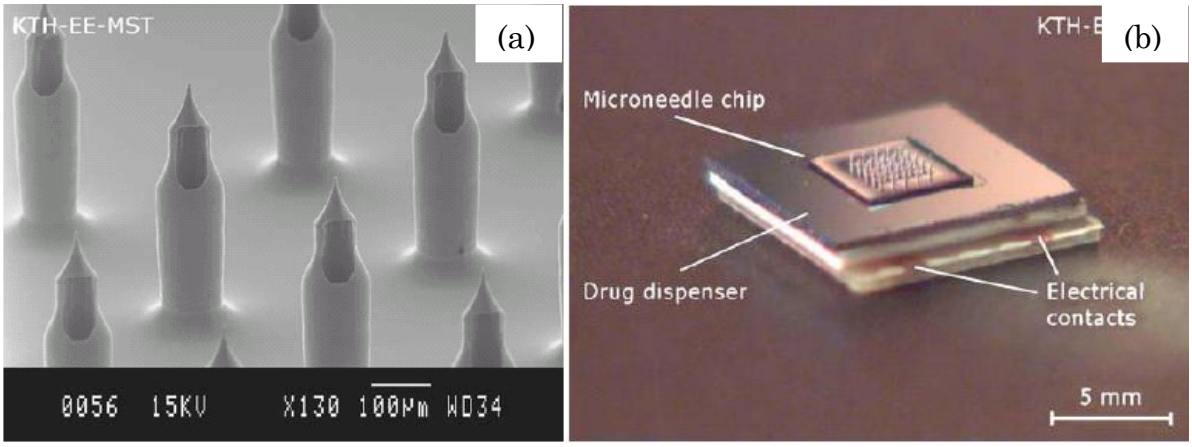

Figure 1.12 (a) SEM picture showing a close-up on several microneedles. (b) Assembled drug delivery patch. The unit can store and dispense *12* ml of liquid [55].

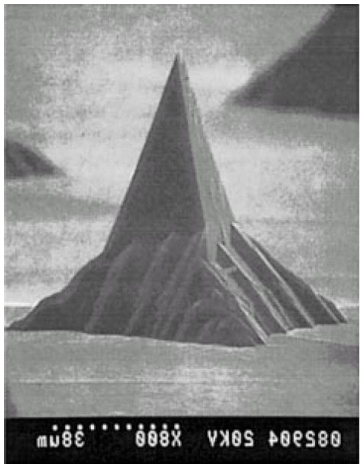

Figure 1.13 Silicon microprobe fabricated by anisotropic silicon etching [56].

are a possible treatment strategy for a common fast-acting insulin *Lispro*, which requires minimal training and attention as shown in Figure 1.12. The needles are organized on *4* × *4* mm^2 chips with *21* hollow needles. The needle array attached to a drug dispenser, fabricated using similar micro-fabrication techniques, is designed to store and dispense a drug volume at a certain flow rate. Its working principle is based on a thermally expandable silicone material which expands into a liquid reservoir and thereby causing the liquid to move. The expansion rate and thus the flow of the liquid, is controlled by the voltage supplied to the dispenser. Reed el al [56] have fabricated arrays of microneedles using anisotropic silicon etching for piercing compressed plaque and delivering anti-restenosis therapies into coronary arteries as shown in Figure 1.13.

In recent times, there has been an increasing interest in using existing AFM infrastructure for biomanipulation, although very little advancement has actually been made. Some examples of these include hollow AFM tips with diameter as small as *35* nm to dispense nanoscale quantity of glycerol based liquids [57]. The tips and substrate surface are functionalised with self-assembled monolayers to control their wetting properties. For example, functionalising the tip with dodecanethiol would make its outer surface hydrophobic thus confining the liquid meniscus in the vicinity of the aperture at the tip apex

and limit the spreading of the liquid at the tip. Such tips are fabricated using FIB technology. Regular arrays of nanodroplets of diameter down to *70* nm have been deposited on amine-functionalised silica substrates. The droplet volumes can be controlled down to tens of zeptoliters (10^{-21} L).

Similar technology, called the FluidFM [58], shown in Figure 1.14 uses such hollow AFM cantilever tips for liquid dispensing (such as dyes) and stimulation of single living cells (such as neuroblastoma cells) under physiological conditions. The AFM tips are embedded onto a channelled cantilever which in turn is connected to a reservoir located in the handling chip of the probe. The setup is connected to fluidic pressure source to control the pressure of delivery. Some examples include streptavidin dots being spotted on a biotin-functionalised surface in buffer and single vaccinia virions being deposited into single HeLa cells.

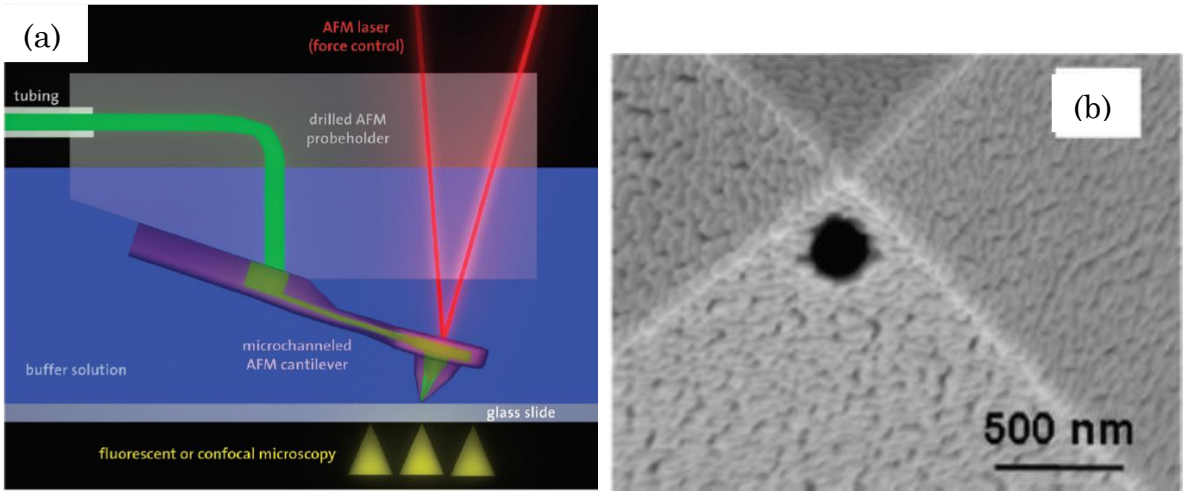

Figure 1.14 FluidFM technology (a) A microchanneled cantilever chip fixed to a drilled AFM probe holder. (b) SEM image of the aperture beside the apex of the pyramidal AFM tip for the intracellular injection experiments [58].

Thus, the critical findings from the review of the prior art in micro/nano-needles are:

- Integrating a hollow microneedle structure with the microrobotic actuator would involve complicated fabrication issues. In addition it would require having an embedded microfluidic channel through the microrobotic structure.
- None of the microneedles have any motion capability which is critical in our case for targeted manipulation.
- Majority of the developments have been made for transdermal drug delivery. Only a few works exist for biomanipulation.
- For transdermal drug delivery, there are different kinds of delivery mechanisms from fluid-filled reservoir consisting of a solution to bubble-powered micropumps. The FluidFM technology also uses a fluid-filled reservoir and a hollow AFM tip for printing DNA. Such delivery mechanisms however, if applied to our microrobot can make the design and fabrication very complicated.

1.3.2 Prior art in micro/nano-positioning stages

Microfabricated stages have been extensively studied in micro-optic and data storage systems. In the previous section, the prior art in the development of microneedles has been discussed. For our microrobotic actuation, we achieve mobility of these microneedles by integrating them with micro/nano-positioning stages. In this section, we will review a repository of works related to the development of such positioning stages that has occurred over the past decade and a half.

At IBM Almaden, Mamin and Rugar [59] pioneered the possibility of using an AFM tip for read-back and writing of topographical features for the purposes of data storage. Later in early *2002*, at IBM Zürich [60] the *Millipede technology* as shown in Figure 1.15 is invented which is a completely new approach for storing data at high speed and with an ultrahigh density. It is based on a mechanical parallel *xy* scanning of the entire cantilever array stage of

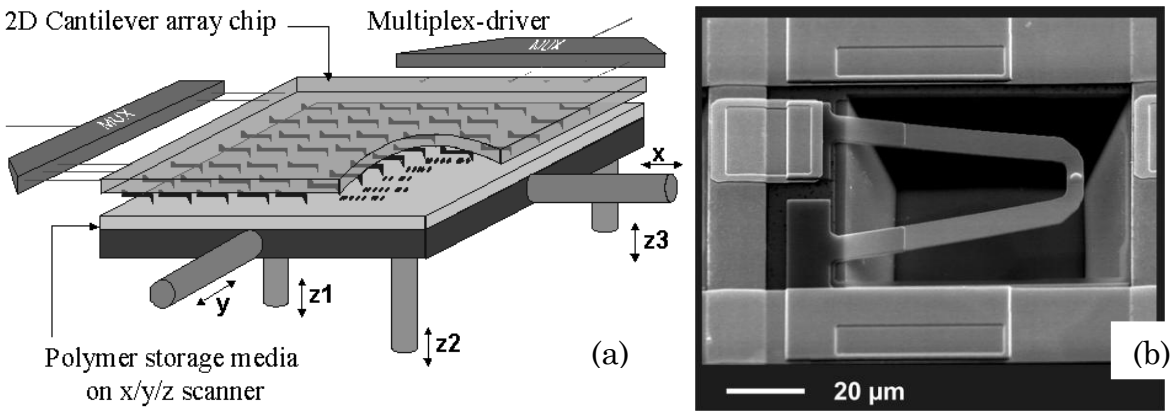

Figure 1.15 (a) IBM's *Millipede* concept (b) SEM image of thermomechanical cantilever with tip [60].

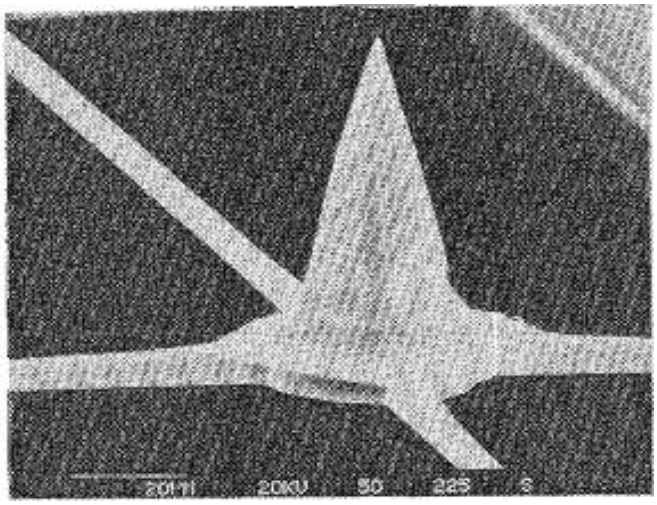

Figure 1.16 SEM image of a large tip integrated on the central stage of an *xy* micro stage [61].

the storage medium coupled with a feedback controlled *z* approaching and leveling scheme. This brings the entire cantilever array stage in contact with the magnetic storage medium. This tip medium is maintained and controlled while *xy* scanning is performed for write/read operation. Albeit this system can achieve individual motion of the cantilever tips in out-of-plane, but in-plane motion is non-independent.

One of the early works of fabricating and operating a silicon based *xy* microstage from 1995 has been shown in Figure 1.16. In-plane scanning and profiling is achieved via integrated comb actuators and a sharp AFM tip and optical detection is achieved through a via hole [61, 62]. The fabrication is a combination of RIE and silicon fusion bonding. The

maximum displacement observed is *12* μm for an applied voltage of *300* V and the microstage could be moved over an area of about *3* μm × *3* μm by actuating two combs with voltages of *150* V. Tips as high as *55* μm with an aspect ratio of about *1.7:1* and tip radius of curvature as small as *10* nm is fabricated for this system. Four sets of comb-actuators drive the stage each aligned at 90^0 with respect to the adjacent actuator. Researchers have also developed AFM platform to drive arrays (*2×1* and *4×4*) of piezoresistive probes in 2D for parallel imaging for life science applications [63]. The design, fabrication, modelling and control of a 2D electrostatic microactuator as shown in Figure 1.17 for precision manipulation tasks is demonstrated by Sun et al [64]. The fabrication involves DRIE on SOI wafer to form high aspect ratio suspending interdigitated comb-drive actuators. They are suspended by completely removing the substrate beneath the comb-drive structure. A PID controller is developed for actuating the stage and a capacitive position sensing mechanism. It is capable of measuring in-plane motions of up to *4.5* μm with a resolution of *0.01* μm in both *x* and *y* direction and is integrated to provide position feedback.

Further examples of 2D electrostatic stages include a two-depth *xy* micropositioning stage that is fabricated by deep silicon etching and infrared front-to-back alignment that can achieve a large in-plane displacement of *160* μm by *160* μm [65]. Kim and Kim [66] have developed a single crystal silicon (SCS) micro *xy* stage as shown in Figure 1.18a. The fabrication involves DRIE and chemical mechanical polishing (CMP). The fabricated actuator has a 2D active driving region of *50* μm × *50* μm and the sticking problem is eliminated by deep etching of the sacrificial glass substrate. A maximum travel range of *24* μm is obtained at about *20* V. Advancing on their previously developed model, they fabricated a micro *xy* stage with a *5* × *5* mm^2 stage area for application in nanometre scale data storage as shown in Figure 1.18b [67]. The square stage is successfully released from the substrate using micro-channel assisted release process (μCARP). The in-plane displacement

obtained is *36* µm (±*18* µm) at *0.1* Hz and *96* µm *(±48* µm) at *140* Hz for *12* V_{p-p}-quasi-static triangular wave with *7.5* V DC bias. The dynamic positioning range is *36* µm × *36* µm and the first resonance frequency is *164* Hz with very little mechanical interference.

Examples of thermally actuated 2D stages include a nanopositioner developed by Hubbard and Howell as shown in Figure 1.19 [68]. The device is surface micromachined in a two-layer polysilicon process using multi-user MEMS processes (MUMPs) and consists of two stages for independent coarse and fine position control. The first stage travels *52* µm between two discrete positions, and the second stage mounted on the first stage, moves continuously through an additional *8* µm in the same direction as the first stage, extending the total range to *60* µm at a driving current of *141-159* mA and power of *6.6-7.6* V or *0.93-1.21* W. An open loop control is used for the control scheme. MEMS nanopositioners that combine parallel bi-lever flexure mechanism with a bent beam thermal actuator has been developed by Bergna et al [69] as shown in Figure 1.20. The flexure mechanism amplifies and guides the motion of the actuator with high precision and the thermal actuator provides the necessary force and displacement. The authors apply an open-loop controller. The motion repeatability is found to be less than ±*7* nm, step sizes below *50* nm, the position resolution below *12* nm

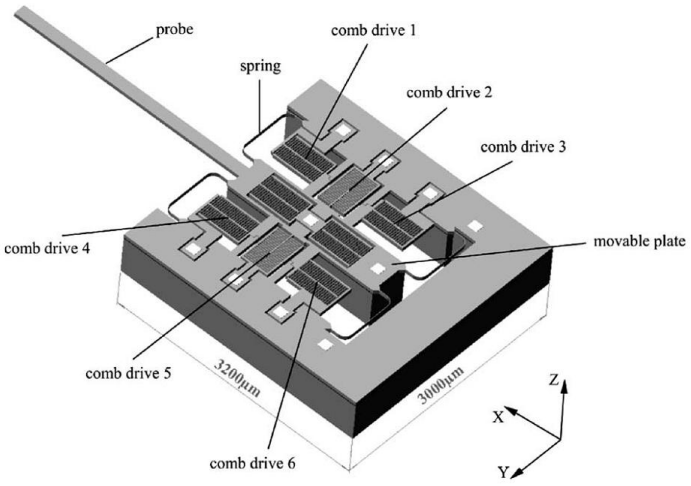

Figure 1.17 Solid model of the 2D electrostatic microactuator [64].

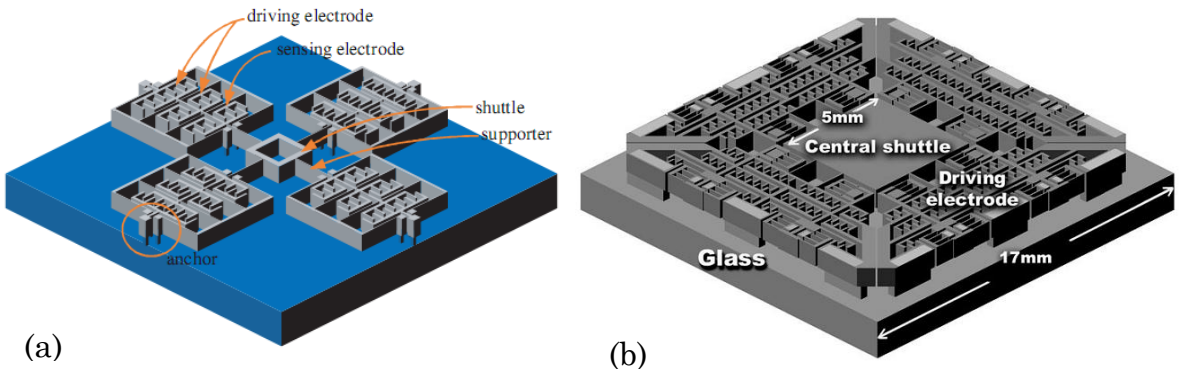

Figure 1.18 Schematic diagram of the electrostatic micro *xy* stage [66, 67].

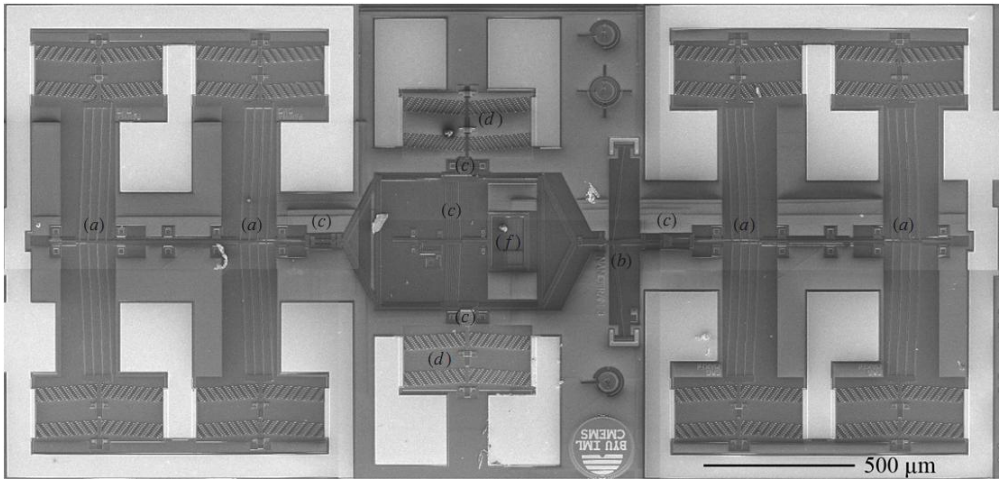

Figure 1.19 Components of the thermal nanopositioner: (a) ATIMs, (b) bistable mechanism, (c) sliding couplers, (d) TIMs, (e) amplifier mechanism and (f) gratings [68].

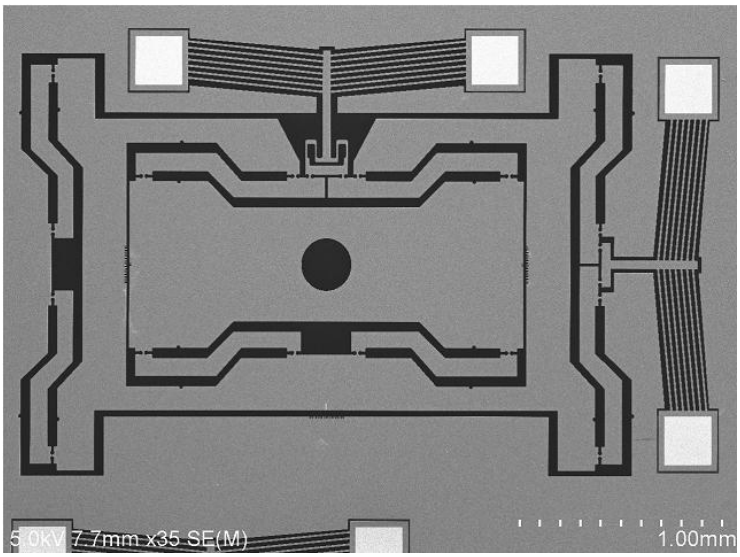

Figure 1.20 SEM image of 2D thermal nanopositioner [69]

and the maximum displacement is approximately *12* µm. Extending their previous work, Gorman et al [70] at the American National Institute of Standards and Technology (NIST) in Maryland uses three classical control approaches for controlling the 2D MEMS nanopositioner including: a quasi-static nonlinear open-loop controller, a nonlinear forward compensator, and a nonlinear PI controller. They use laser reflectance microscopy instead of SEM for achieving position measurements with nanometre resolution. All of the above 2D microstages would require further developments to apply them for vertical motion.

They have used this nanopositioner to propose a parallel architecture with multiple independently moving microstages [71]. Albeit this architecture can gain decent in-plane motion of up to *5* µm at around *10* V, there is significant crosstalk between the *x* and *y* axes of up to a quarter of a micron. An open-loop control approach is used to achieve motion resolution of the order of nanometres. This nanopositioner has been used as a capacitive based displacement sensor with sensitivity of *0.001* pF/um and permitting a displacement resolution of the order of *100* nm [72]. Further this nanopositioner has been used in conjunction with moving platform and struts to fabricated MEMS based Stewart platforms with 6D kinematic capability and sub-nano-scale resolution as shown in Figure 1.21 [73]. The nanopositioner and the moving platform have been fabricated using a series of DRIE on an SOI wafer. The struts are developed by etching straight tungsten rods until their thickness reaches *20%* of the original diameter. The measured maximum motion of the platform in the *x*, *y* and *z* directions are *60.45* µm, *62.36* µm and *41.28* µm respectively. The measured maximum rotation angles in *xz*, *yz* and *xy* plane are 1.4^0, 1.5^0 and 2.4^0 respectively. An actuator of this kind is not only bulky with a size of up to 10 mm, but involves complex fabrication including 3D assembly. Scaling this up to a parallel architecture design can exponentially complicate the design and fabrication.

One of the early works of 3D stage with vertical positioning capability is a self-assembled, surface micromachined micro *xyz* stage with lateral scanning of up to *120* µm, vertical scanning of up to *250* µm and fine positioning accuracy with step resolutions of *27* nm, using scratch drive actuators (SDA) [74]. The stage is shown in Figure 1.22. A group of nine SDAs have been integrated with each actuator plate and the micro-stage is fabricated using the three-layer polysilicon surface micromachining technology called (PolyMUMPS). It can be easily integrated with surface-micromechanical optical elements, such as micro-gratings,

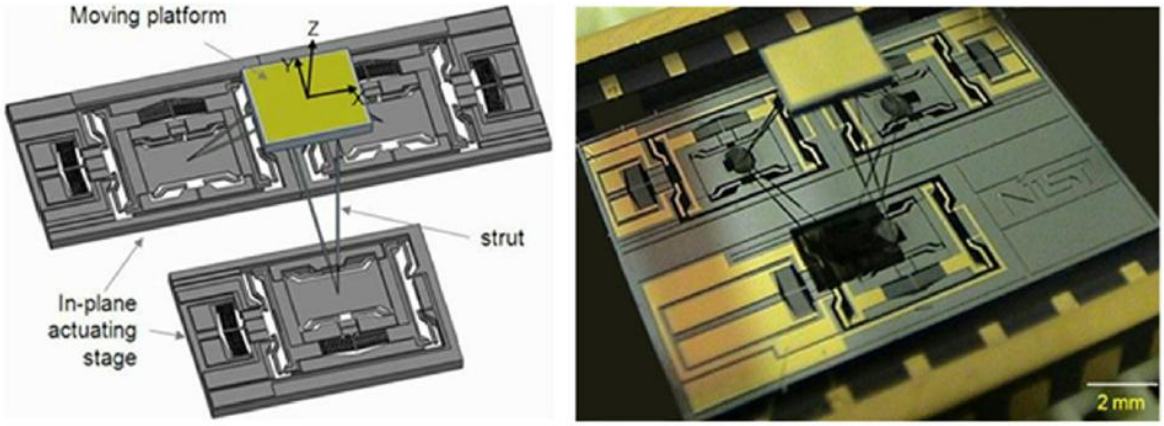

Figure 1.21 6D MEMS Stewart platform [73].

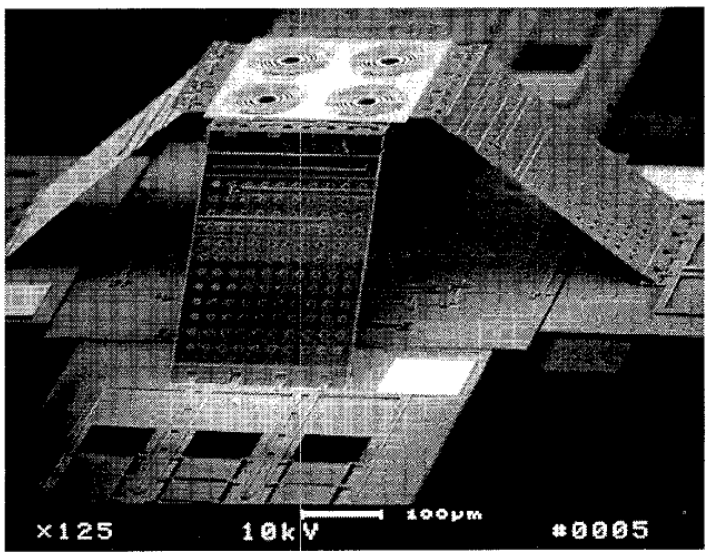

Figure 1.22 SEM image of 3D microstage [74]. Four micro fresnel lenses have been integrated with the *xyz* stage.

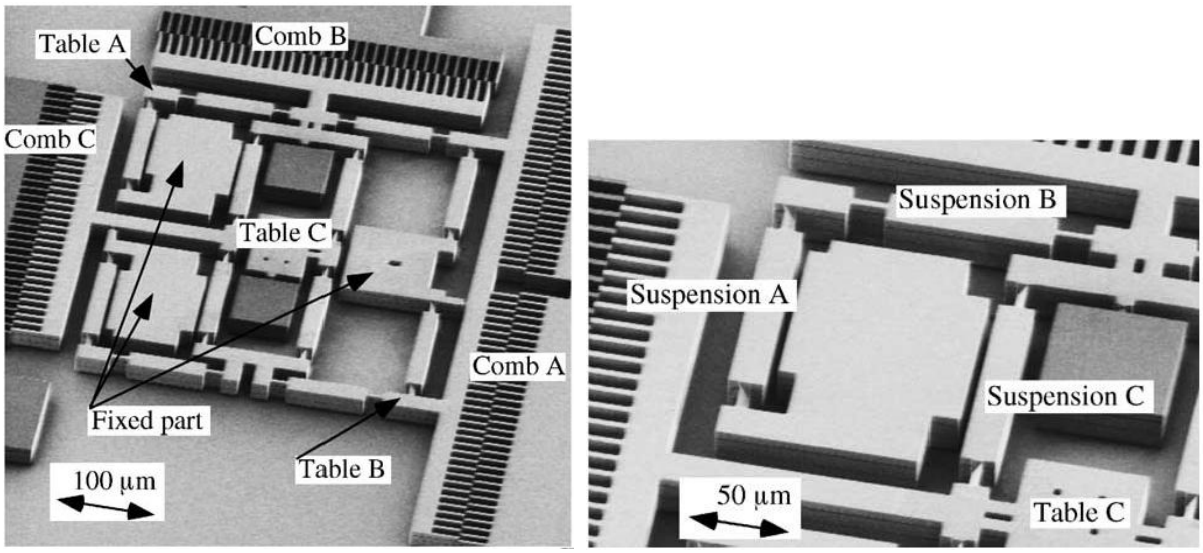

Figure 1.23 SEM images of 3D microactuator. Thickness of the stage is *25* μm. The angle of the inclined leaf spring in suspensions A and S is 30^0 [75].

micro-mirrors and refractive microlens. Although this stage can achieve significant vertical actuation, the in-plane actuation is not decoupled. Moreover integrating such a design which is quite macroscale similar to the 6D Stewart platform discussed above, in a parallel architecture with individually actuated microneedles would result in complex fabrication processes. Other examples of 3D stage driven by electrostatic comb actuators have been designed and fabricated by Ando and his team [75, 76]. In one version of the actuator, they design and develop three types of stages with varying vertical actuation. For example, in Type A stage, the maximum lift-up is *1* μm at a driving voltage of *170* V. In their advanced designs as shown in Figure 1.23, the stage consists of travelling tables, suspensions and comb actuators and fabricated using inductively coupled plasma etching (ICP), FIB and wet etching. The maximum in-plane displacement obtained is *1* μm at *97* V in the *x* direction and *0.13* μm at *105* V in the *y* direction. The maximum vertical displacement is *0.4* μm at a driving voltage *90* V. The major disadvantage with this design is in the significantly larger driving voltage needed to achieve minor displacements.

Further examples of 3D stages include a 3D micromirror device developed using a single wafer process with a unique integration of bulk and surface micromachining process steps. These steps include KOH bulk micromachining, high aspect ratio DRIE and electrochemical etching (ECE) [77]. Bottom electrode, flexure springs and micromirror plate are fabricated in single crystal silicon substrate layer, while the top electrode plate and bending springs are

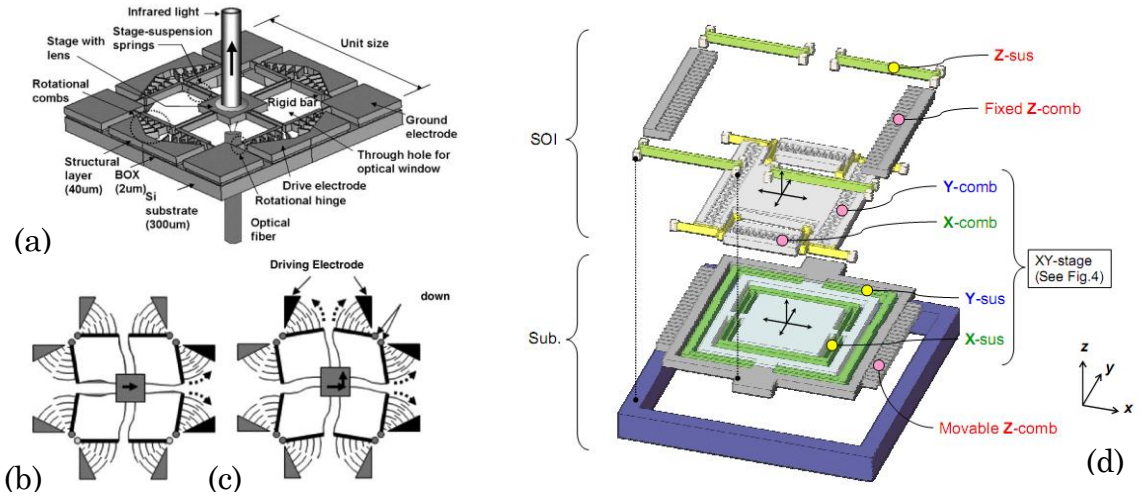

Figure 1.24 (a) Schematics of the *xy* stage, (b) simplified model showing the stage motion to the right by using a pair of rotational comb actuators on the right-hand side, and (c) diagonal motion by using the actuators on the top and right sides [78] (d) Schematic view of the electrostatic comb-driven *xyz* stage with topological layer switch architecture [79].

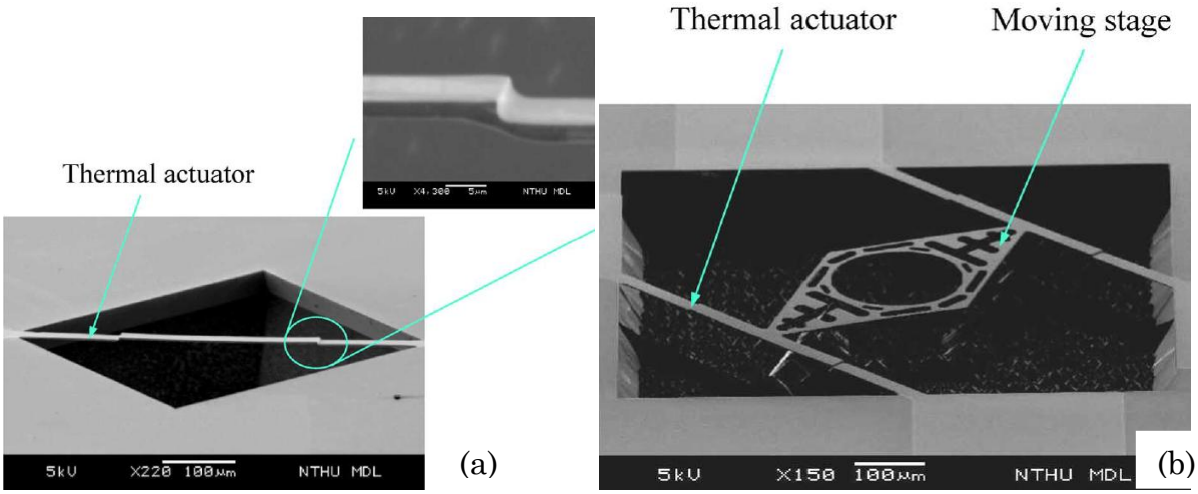

Figure 1.25 SEM images of (a) a step-bridge actuator, where the inset shows the zoom-in photo of the step structure, and (b) a moving stage that is integrated with two step-bridge actuators [80].

realised in polycrystalline silicon layers. A maximum angular deflection of *2°* is achieved. A micromachined *xy* stage as shown in Figure 1.24a consisting of eight *L* shaped spider-leg stage-suspension springs and rotational comb-drive actuators for 2D microlens scanner is developed by Kwon et al [78]. The fabrication is a combination of RIE and photolithography on an SOI wafer. The pitch of the microstage matrix is *2* mm. The stages which consist of five lenses have a diameter of *260* µm and sag of about *3* µm. An in-plane decoupled motion of *55* µm can be achieved with a drive voltage *40* V. 3D monolithic stage as shown in Figure 1.24d has been developed with electrostatic comb drive mechanism integrated in only two silicon layers and by three photolithography steps that topologically switches the allocation of layer for electrical and elastic components [79]. The stage can achieve a decoupled in-plane actuation and also in the diagonal direction of *19* µm at around *150* V, and a vertical actuation of maximum *2.12* µm with an applied voltage of *200* V.

Several out-of-plane thermally actuated microstages have been developed by incorporating beams with step or trench features. In one such work [80], the step-bridge structure design clamped at both ends to the substrate enables bending and subsequent buckling of the actuator in the vertical direction by Joule heating when applying with current. It is shown in Figure 1.25. It can achieve out-of-plane amplitude of *13* µm at a driving current of *54* mW. Actuator based on similar principle using flexural hinges and fabricated using the Memscap PolyMUMPs commercial process has been developed [81]. The vertical motion achieved is around *1* µm at an applied power of *1.92* mW. A vertical thermal chevron-type actuator similar in design to the one discussed above [69] has been developed using the PolyMUMPs process [81]. It can provide a vertical actuation of around *3.25-4.25* µm at *12* V. This commonly used chevron-type electrothermal actuators use an array of silicon beams arranged in parallel V-shape pairs to generate a 1D motion. These beams are designed with a pre-bend angle. When current is applied, the beam-pairs heat up via Joule heating which cause them to

expand and ultimately buckle. In a more recent work, using same principle but using a parallel arrangement of bent-beam structures, an out-of-plane motion of *85* μm could be achieved at *220* mA [82]. All of these electrothermal actuators have only a 1D vertical motion and most of them have a significant requirement of DC/AC current to achieve motion. Specifically for biomanipulation tasks, heating of the actuator and thus the microneedle, as in our design, can cause significant damage to the fragile biological structures and molecules.

Several interesting works based on electromagnetic out-of-plane actuation have been reported in the past decade and a half. Integrated permanent magnetic microactuators have been fabricated using micromachined polymer magnets [83]. The permanent magnets used are composed of magnetically hard ceramic strontium ferrite powder imbedded in epoxy resin. This polymer magnet on the free end of a copper cantilever beam and on the other side of the substrate, a planar square coil produces the magnetic field gradient necessary for the actuation of the magnet. The magnet is fabricated using a combination of sacrificial layer techniques and electroplating, screen printing and lamination. At the fundamental resonance frequency, large deflections in excess of *0.3* mm have been observed for driving currents of *20* mA. It is to be noted however, the dimensions of the structures range in several millimeters, quite gigantic for operating in a microworld. Cho and Ahn [84] have designed and fabricated bidirectional magnetic microactuator using electroplated CoNiMnP-based permanent magnet arrays. These arrays are placed at the tip of the silicon cantilever beam along the axis of the electromagnet. It can achieve a bidirectional actuation of up to ±*80* μm approximately at a DC current of *100* mA.

Another bi-directional electrothermal actuator made of polymide (PI) with different geometries has been developed [85]. The fabrication of the PI wafer involves Ni/Fe (*80/20*) perma-alloy deposition on the PI diaphragm by electroplating, high aspect ratio electroplating of copper planar coil, bulk micromachining and excimer laser selective ablation. Hard magnet

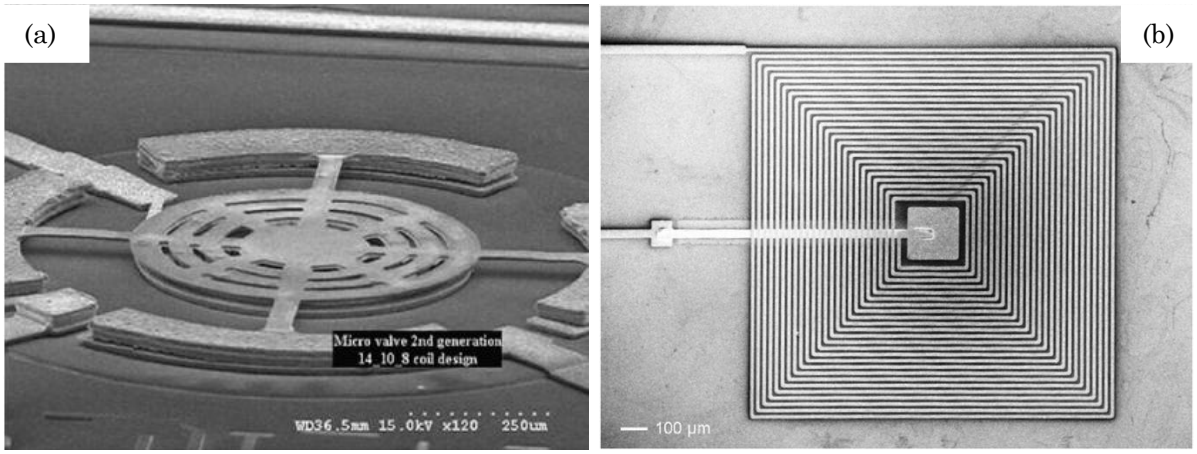

Figure 1.26 SEM image of (a) a four-legged microvalve [86] (b) microcoil and flexure supported platform housing the permanent magnet [87].

Fe/Pt is deposited at a low temperature of 300^0C which is sputtered onto the PI diaphragm to produce a perpendicular magnetic anisotropic field. The planar microcoil is fabricated on a separate silicon wafer. These two wafers are bonded to produce the final microactuator. It can achieve a vertical deflection angle of 78^0 and 74^0 at *4840* A/m. Based on similar principle, another design of electromagnetic actuator with three parylene diaphragms, spiral copper coils and permanent magnets has been developed [88]. Two types of electromagnetic actuators, one with flat diaphragm and another with corrugated one have been fabricated and tested. The static deflections of the flat diaphragm and the corrugated one are *15* µm and *30* µm at *1* Hz, respectively, when the input current amplitude is *100* mA.

Electromagnetically actuated microvalves, one of which is shown in Figure 1.25a have been developed and their dynamic response operating in open-air conditions have been measured experimentally for microfluidic applications [86]. The behaviour has been simulated using a 3D fluid-structural finite element model. The microvalve held in the open position by multiple support beams consists of a membrane suspended at *12* µm above the valve seat. The membrane produces small displacement dynamics under the influence of a magnetic force generated by the coil. The valve closing time at *1.02* A is *133* µs. In a more

recent work, electromagnetic motion stage, shown in Figure 1.26b and like the ones discussed before [84, 85, 88] has been used for scanning applications [87]. A bidirectional motion is achieved through an arrangement of copper-based planar coil and a permanent magnet. The microcoil is electroplated on a silicon substrate and the platform is fabricated through silicon bulk micromachining of an SOI wafer. Within a range of ±*2.7* μm, the motion is linear with no hysteresis. A scanning range of up to *200* Hz is achieved with open-loop control.

Thus, the critical findings from the review of the prior art in micro/nano-positioning stages are:

- None of the actuation stages have microneedles integrated onto them, except the 1D systems such as IBM's Millipede [89], Indermuhle and Rooij [90], or NIST's 1D/2D nanopositioners [72-74] among others.
- There are very few works on 3D or more than 3D actuation systems. The few that exists such as NIST's 6D Stewart platform [73], Fan et al's [74] integrated scratch-drive-actuators (SDA) and Ando's [75] electrostatic actuator are either bulky in size, or too complicated to fabricate with low motion performance or a combination of these factors.

1.4 Comparison of our microrobotic motion performance with prior art

Before we proceed further into the design and analyses of the microrobot in the subsequent chapters, it is critical to have a comparison of the motion performance of our microrobotic actuation with some of the well known previous works as illustrated in Figure 1.26. By motion performance, we refer to the motion range of the microrobot for different actuation voltages. A direct comparison of the maximum motion with previous works is complicated because of the multiple variables involved. For example, different works report their values for different parameters such as voltage, current and power against amplitude, stroke, tilt and displacement. The above graph plots maximum motion achieved by earlier works against

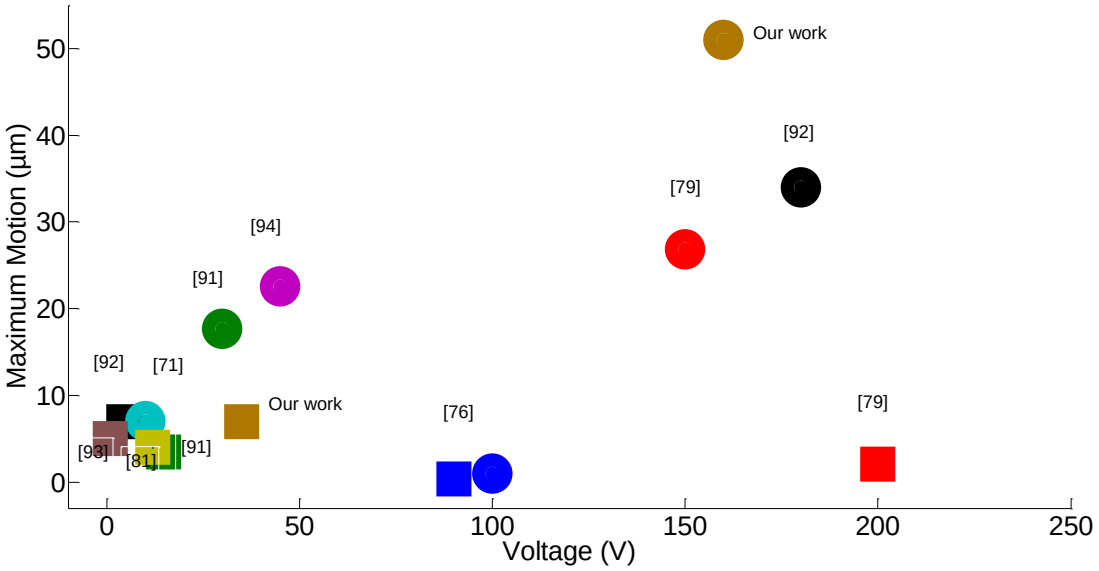

Figure 1.27 Comparison of our work with previously reported 1D, 2D and 3D actuators mentioned in [71, 76, 79, 81, 91-94]. The circles represent the absolute maximum in-plane motion and the squares represent the maximum out-of-plane motion.

voltage. The maximum in-plane motion considers the vector sum of *x* and *y* displacement (absolute in-plane actuation) while the out-of-plane motion is for *z* displacement.

To highlight some of these major works and how it performs in comparison with our microrobot: Gorman et al [71] have developed a *2×2* array of thermal *xy* nanopositioners that has a significantly coupled motion with very low motion performance of *5* μm (*x*) and *3.4* μm (*y*) at *10* V. Another thermally driven actuator of Sarov et al [93] can achieve a 1D *z* motion of *6* μm at *8* V. The electrostatically actuated stage using tilted leaf-springs of Ando et al [76] has a 1D *z* motion varying between *0.33* μm at *250* V, *1* μm at *170* V to *1.9* μm at *133* V. Takahashi et al's [79] electrostatically actuated stage can move by *19* μm (*xy*) at *120* V and *2.12* μm (*z*) at *200* V and Fowler et al's [94] 2D electrostatic stages can achieve an *xy* motion of *15* μm at *45* V. In comparison to the low motion performance of most of these actuators, our microrobot's motion performance is superior. An in-plane displacement of *72* μm (±*36*

μm) is achievable at around *160* V and out-of-plane displacement of around *7* μm at around *35* V.

1.5 Critical research questions

Based on the critical findings from the review of the prior art in Section 1.3, this dissertation strives to answer several critical research questions as listed below, thereby making original research contributions to the existing art:

[1] Can we have a built-in-system with *x,y,z* motion capability on a parallel scale?

[2] Are there fabrication processes available to develop such a system?

[3] Are blind feedback systems available for massively parallel vertical manipulation?

1.6 System constraints

The following list sums up the key engineering requirements and constraints placed on our system by either design of the actuator or fabrication or design of experiment. Each of these points will be addressed in more detail in the following chapters.

- **Design of the microrobot:** The vertical or *z* spring stiffness of the tethering and spring flexure beams must be greater than the elastic stiffness of the cell membranes (*0.001-0.1 mN/m*). Since electrostatic force is usually attractive, this effect needs to be reversed to achieve a targeted vertical manipulation.
- **Incorporating vertical motion:** The vertical motion achieved by the parallel-actuator arrangement of microstage and upstanding silicon tower is difficult to achieve due to the challenges in terms of positioning, alignment and bonding of the tower underneath the microstage.

- **Integrating microneedle:** Since our goal is to develop a microrobot with a microneedle integrated atop it, the fabrication process has to be designed for ease of integration and batch fabrication capability.
- **Designing scaled up model for blind feedback:** In order to test the feasibility of our blind feedback hypothesis, designing an equivalent scaled-up macroscopic experiment that can simulate the behavior of the microrobot for vertical manipulation is challenging. Electrostatic force that is significant in the micro/nano-scale becomes irrelevant in a macro-scale.

1.7 The organisation of this thesis

Rather than including an independent literature review chapter, every individual chapter except Chapters 2 and 5 start with a review of the prior art in relation to the topics discussed in that particular chapter. Chapter 2 introduces the structural design and working principle of the single-unit microrobot and the corresponding parallel architecture consisting of such multiple single-unit microrobots. We highlight two different designs of the microrobot – a four-sided single unit actuator (4SA) and a three-sided single unit actuator (3SA) and explain the science behind such a transition from 4SA to 3SA microrobot design. The dimensions of the actuator have been investigated by studying the physics of the component beam behaviour for a superior design. Chapter 2 demonstrates such analysis of the design in detail which sets the foundation for the following chapter. Chapter 3 extends on these investigated design parameters and sets final design dimensions of the 4SA microrobot before it is fabricated. These parameters are analysed through our analytical models and numerical simulations. The design is analysed analytically using stiffness matrix and slope-deflection equations and numerically using finite element analyses.

Chapter 4 extends on the design dimensions of Chapter 3 and introduces the fabrication sequence designed to manufacture the 4SA microrobot. This microrobot has been

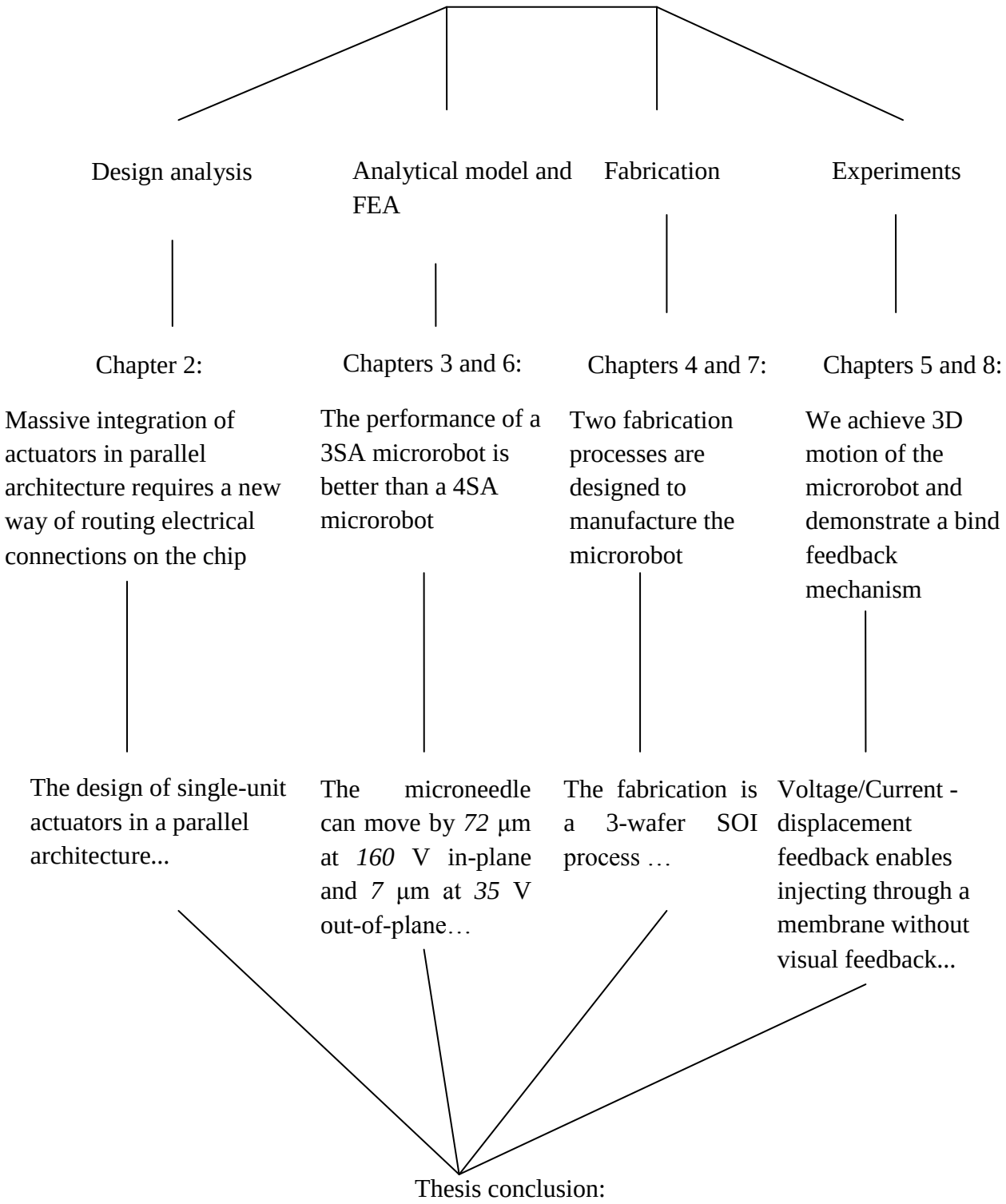

Figure 1.28 Structural flow of the dissertation where each chapter is internally supported by a different quantitative or qualitative argument or both.

manufactured at the Nanofabrication Center of the University of Canterbury and the Canadian Microelectronics Corporation (CMC) in Quebec, Canada. Two different fabrication processes, a single Si-wafer process (*with four masks*) and a 3-wafer SOI process (with six masks) have been designed and described. Certain interesting observations regarding the growth of nanopillars during reactive ion etch characterization of SiO_2 have also been reported.

Chapter 5 demonstrates the experimental results from the electrical characterisation tests of the 4SA microrobot. The vertical motion of the actuator using a parallel-actuator arrangement of an upstanding silicon tower underneath the microstage has been successfully demonstrated. Once, we discuss the design, analysis, fabrication and testing of the 4SA microrobot, the focus now shifts on to the design of the 3SA microrobot, superior in performance to its predecessor. Chapter 6 analyses this new design of the microrobot using a combination of analytical models and numerical simulations similar to Chapter 3. Based on these analyses, the dissertation claims that the performance of a 3SA microrobot is superior to a 4SA microrobot which allows more efficient integration into a parallel architecture. Chapter 7 then extends on these design dimensions and discusses the fabrication sequence and mask design rules to manufacture the first parallel architecture prototype of the 3SA microrobot (*2×1* array). This microrobot is being manufactured by the Canadian Microelectronics Corporation (CMC) in conjunction with Micralyne Inc. in Quebec, Canada, at the time the thesis has been written.

Chapter 8 introduces a new form of feedback mechanism for achieving biomanipulation through a macroscale manipulation experiment along with its corresponding PID control mechanism. The feedback uses both visual and non-visual blind feedback based on a voltage/current-displacement signature to detect the manipulation in a 3D workspace. Finally Chapter 9 discusses the outcomes and the original contributions of Chapters 2-8, evaluations

based on the thesis statement, specifications and constraints set in this chapter; addresses potential criticisms and outlines the future research areas that follow from the thesis. This is followed by appendices that describe the slope-deflection equations developed to analyse the in-plane motion performance of the actuator, and associated programs and circuit diagram used in simulations and experiments.

BIBLIOGRAPHY

[1] International Human Genome Sequencing Consortium, "Initial sequencing and analysis of the human genome," *Nature*, vol. 409, pp. 860-921, 2001.

[2] International Human Genome Sequencing Consortium, "Finishing the euchromatic sequence of the human genome," *Nature*, vol. 431, pp. 931-945, 2004.

[3] J. Karha and E.J. Topol, "The sad story of Vioxx, and what we should learn from it," *Cleveland Clinic Journal of Medicine,* vol. 71, pp. 933-939, 2004.

[4] National Institutes of Health (USA), "NIH Common Fund announces awards for Single Cell Analysis," 2012.

[5] M. Gerlinger et al., "Intratumor heterogeneity and branched evolution revealed by multiregion sequencing," *The New England Journal of Medicine,* vol. 366, pp. 883-892, 2012.

[6] J. Eberwine, JY. Sul, T. Bartfai and J. Kim, "The promise of single-cell sequencing," *Nature Methods,* vol. 11, pp. 25-27, 2014.

[7] R. J. Wall, "Pronuclear microinjection," *Cloning Stem Cells*, vol. 3, pp. 209-220, 2001.

[8] M. Belting, S. Sandgren and A. Wittrup, "Nuclear delivery of macromolecules: barriers and carriers," *Adv. Drug. Deliv. Rev.*, vol. 57, pp. 505-527, 2005.

[9] M.A. Kay, J.C. Gloriosco and L. Naldini, "Viral vectors for gene therapy: the art of turning infectious agents into vehicles of therapeutics," *Nature Medicine,* vol. 7, pp. 33-40, 2001.

[10] P. N. Moreira, "Efficient generation of transgenic mice with intact yeast artificial chromosomes by intracytoplasmic sperm injection," *Biol. Reprod.*, vol. 71, p. 1943, 2004.

[11] M. Cemazar, I. Wilson, G.U. Dachs, G.M. Tozier and G. Sersa, "Direct visualization of electroporation-assisted in vivo gene delivery to tumors using intravital microscopy – spatial and time dependent distribution.," *BMC Cancer,* vol. 4, pp. 81-88, 2004.

[12] A. Ashkin, "Acceleration and trapping of particles by radiation pressure," *Phys. Rev. Lett.,* vol. 4, pp. 156-159, 1970.

[13] M. Washizu, Y. Kurahashi, H. Iochi, O. Kurosawa, S. Aizawa, S. Kudo. Y. Magariyama and H. Hotani, "Dielectrophoretic measurement of bacterial motor characteristics," *IEEE Transactions on Industry Applications,* vol. 29, pp. 286-294, 1993.

[14] R. King, "Gene delivery to mammalian cells by microinjection," *Methods Mol. Biol.,* vol. 245, pp. 167-174, 2004.

[15] J. Kim, H. Ladjal, D. Folio and A. Ferreira, "Evaluation of telerobotic shared control strategy for efficient single-cell manipulation " *IEEE Transactions on Automation Science and Engineering,* vol. 9, pp. 402-406, 2012.

[16] D.J. Stephens and R. Pepperkok, "The many ways to cross the plasma membrane," *PNAS (USA),* vol. 98, pp. 4295-4298, 2001.

[17] K. Santa, M. Mews, and M. Riedmiller, "A neural approach for the control of piezoelectric micromanipulation robots," *Journal of Intelligent and Robotic Systems,* vol. 22, pp. 351-374, 1998.

[18] Y. Sun and B.J. Nelson, "Microrobotic cell injection," in *IEEE International Conference on Robotics and Automation*, Seoul, S. Korea, 2001, pp. 620-625.

[19] W.H. Wang, X. Liu, D. Gelinas, B. Ciruna and Y. Sun, "A fully automated robotic system for microinjection of zebrafish embryos," *PloS ONE,* vol. 2, pp. 1-7, 2007.

[20] H. Matsuoka, T. Komazaki, Y. Mukai, M. Shibusawa, H. Akane, A. Chaki, N. Uetake and M. Saito, "High throughput easy microinjection with a single-cell manipulation supporting robot," *Journal of Biotechnology*, vol. 116, pp. 185-194, 2005.

[21] K.K. Tan, S.C. Ng and Y. Xie, "Optimal intra-cytoplasmic sperm injection with a piezo micromanipulator," in *4th World Congress on Intelligent Control and Automation*, Shanghai, China, 2002, pp. 1120-1123.

[22] Y.H. Anis, M.R. Holl and D.R. Meldrum, "Automated vision-based selection and placement of single cells in micro well array formats," in *4th IEEE CASE*, Washington DC, USA, 2008, pp. 315-320.

[23] J. Kuncova and P. Kallio, "Challenges in capillary pressure microinjection," in *26th International Conference of the IEEE EMBS*, San Francisco, USA, 2004, pp. 4998-5001.

[24] T. Sulchek et al., "Parallel atomic force microscopy with optical interferometric detection," *Applied Physics Letters*, vol. 78, pp. 1787-1789, 2001.

[25] J. Reed, P. Wilkinson, J. Schmit, W. Klug and J.K. Gimzewski, "Observation of nanoscale dynamics in cantilever sensor arrays," *Nanotechnology*, vol. 17, pp. 3873-3879, 2006.

[26] T.L. Sounart, T.A. Michalske and K.R. Zavadil, "Frequency-dependent electrostatic actuation in microfluidic MEMS," *Journal of Microelectromechanical Systems*, vol. 14, pp. 125-133, 2005.

[27] V. Mukundan and B.L. Pruitt, "MEMS electrostatic actuation in conducting biological media," *Journal of Microelectromechanical Systems*, vol. 18, pp. 405-413, 2009.

[28] V. Mukundan, P. Ponce, H.E. Butterfield and B.L. Pruitt, "Modeling and characterization of electrostatic comb-drive actuators in conducting liquid media,"

Journal of Micromechanics and Microengineering, vol. 19, pp. 065008-065016, 2009.

[29] S. Banerjee, "The Silicon Centipede - Commercial opportunity assessment under the MacDiarmid commercialization fellowship program," University of Canterbury, Christchurch2013.

[30] L. Flatz et al., "Single-cell gene-expression profiling reveals qualitatively distinct CD8 T cells elicited by different gene-based vaccines," *Proceedings of the National Academy of Science (USA)*, vol. 108, pp. 5724-5729, 2011.

[31] M. Wu and A.K. Singh, "Single-cell protein analysis," *Current Opinion in Biotechnology*, vol. 23, pp. 1-6, 2011.

[32] D. Lovatt et al., "Transcriptome in vivo analysis (TIVA) of spatially defined single cells in live tissue," *Nature Methods*, vol. 11, pp. 190-196, 2014.

[33] A. R. Pinto, A. Chandran, N.A. Rosenthal and J.W. Godwin, "Isolation and analysis of single cells from the mouse heart," *Journal of Immunological Methods*, vol. 393, pp. 74-80, 2013.

[34] N. Sun, "Feeder-free derivation of induced pluripotent stem cells from adult human adipose stem cells," *PNAS (USA)*, vol. 106, pp. 15720-15725, 2009.

[35] I. Casuco, F. Rico and S. Scheuring, "Biological AFM: where we come from - where we are - where we may go," *Journal of Molecular Recognition*, vol. 24, pp. 406-413, 2011.

[36] F. Bano et al., "Toward multiprotein nanoarrays using nanografting and DNA directed immobilization of proteins," *Nano Letters*, vol. 9, pp. 2614-2618, 2009.

[37] P. Lisowski and P.W. Zarzycki, "Microfluidic paper-based analytical devices (μPADs) and micro total analysis systems (μTAS): development, applications and future trends," *Chromatographia*, vol. 76, pp. 1201-1214, 2013.

[38] B. Stoeber, and D. Liepmann, "Design, fabrication and testing of a MEMS syringe," in *Solid-State Sensor and Actuator Workshop*, Hilton Head Island, South Carolina, USA, 2002.

[39] P.M. Wang, M. Cornwell, J. Hill and M.R. Prausnitz, "Precise Microinjection into Skin Using Hollow Microneedles," *J Invest Dermatol* vol. 126, pp. 1080-1087, 2006.

[40] C. Jingkuang, K. D. Wise, et al, "A multichannel neural needle for selective chemical delivery at the cellular level," *IEEE Transactions on Biomedical Engineering,* vol. 44, pp. 760-769, 1997.

[41] U. Häfeli, A. Mokhtari, et al, "In vivo evaluation of a microneedle-based miniature syringe for intradermal drug delivery," *Biomedical Microdevices,* vol. 11, pp. 943-950, 2009.

[42] S.P. Davis, B. J. Landis et al., "Insertion of microneedles into skin: measurement and prediction of insertion force and needle fracture force," *Journal of Biomechanics* vol. 37, pp. 1155-1163, 2004.

[43] W. Martanto, *et al.*, "Microinfusion Using Hollow Microneedles," *Pharmaceutical Research*, vol. 23, pp. 104-113, 2006.

[44] K. D. Wise, J. B. Angell and A. Starr, "An Integrated Circuit Approach to Extracellular Microelectrodes,"*." IEEE Trans. Biomed. Engr.*, vol. 17, p. 238, 1970.

[45] K. Chun, G. Hashiguchi, H. Toshiyoshi and H. Fujita, "An array of hollow micro-capillaries for the controlled injection of genetic materials into animal/plant cells," in *IEEE MEMS*, Florida, USA, 1999, pp. 406-411.

[46] B. Stoeber and D. Liepmann, "Design, fabrication and testing of a MEMS syringe," in *Proceedings of Solid-State Sensor and Actuator Workshop*, Hilton Head Island, SC, 2002, pp. 2–7.

[47] M.A.L. Teo, C. Shearwood, KC Ng, J. Lu and S. Moochhala, "In Vitro and In Vivo Characterization of MEMS Microneedles," *Biomedical Microdevices,* vol. 7, pp. 47-52, 2005.

[48] W. Trimmer, *et al.*, "Injection of DNA into plant and animal tissues with micromechanical piercing structures," in *Micro Electro Mechanical Systems, 1995, MEMS '95, Proceedings. IEEE,* 1995, pp. 111-115.

[49] J. Brazzle, *et al.*, "Active microneedles with integrated functionality," in *Technical Digest of the 2000 Solid-StateSensor and Actuator Workshop,* , Hilton Head Isl., SC, 2000, pp. 199-202.

[50] G.H. Teichert, S. Burnett and B.D. Jensen, "A microneedle array able to inject tens of thousands of cells simultaneously," *Journal of Micromechanics and Microengineering,* vol. 23, 2013.

[51] S. Henry, D. V. McAllister et al., "Microfabricated microneedles: A novel approach to transdermal drug delivery," *Journal of Pharmaceutical Sciences,* vol. 87, pp. 922-925, 1998.

[52] L. Liwei and A. P. Pisano, "Silicon-processed microneedles," *Journal of Microelectromechanical Systems,* vol. 8, pp. 78-84, 1999.

[53] P. Griss and G. Stemme, "Side-opened out-of-plane microneedles for microfluidic transdermal liquid transfer," *Journal of microelectromechanical systems,* vol. 12, pp. 296-301, 2003.

[54] J.D. Brazzle, I. Papautsky and A.B. Frazier, "Hollow metallic micromachines needle arrays," *Biomedical Microdevices,* vol. 2, pp. 197-205, 2000.

[55] L. Nordquist, N. Roxhead, P. Griss and G. Stemme, "Novel microneedle patches for active insulin delivery are efficient in maintaining glycaemic control: an initial

comparison with subcutaneous administration," *Pharmaceutical Research,* vol. 24, pp. 1381-1388, 2007.

[56] M.L. Reed et al., "Micromechanical devices for intravascular drug delivery," *Journal of Pharmaceutical Sciences,* vol. 87, pp. 1387-1394, 1998.

[57] A. Fang, E. Dujardin and T. Ondarcuhu, "Control of droplet size in liquid nanodispensing" *Nano Letters,* vol. 6, pp. 2368-2374, 2006.

[58] A. Meister et al., "FluidFM combining atomic force microscopy and nanofluidics in a universal liquid delivery system," *Nano Letters,* vol. 9, pp. 2501-2507, 2009.

[59] H. Mamin and D. Rugar, "Thermomechanical writing with an atomic force microscope tip," *Applied Physics Letters,* vol. 61, p. 1003, 1992.

[60] P. Vettiger, G. Cross, M. Despont, U. Drechsler, U. Durig, B. Gotsmann, W. Haberle, M.A. Lantz, H.E. Rothuizen and R. Stutz,, "The" millipede"-nanotechnology entering data storage," *IEEE Transactions on nanotechnology,* vol. 1, pp. 39-55, 2002.

[61] P. Indermuhle and N. De Rooij, " Integration of a large tip with high aspect ratio on an xy-micro stage for AFM imaging," *The 8th International Conference on Solid-State Sensors and Actuators, and Eurosensors IX, Stockholm, Sweden,* pp. 652-655, June 25-29, 1995 Transducers 1995.

[62] P.F. Indermühle, V.P. Jaecklin, J. Brugger, C. Linder, N.F. De Rooij and M. Binggeli, "AFM imaging with an xy-micropositioner with integrated tip," *Sensors and Actuators A: Physical,* vol. 47, pp. 562-565, 1995.

[63] J. Polesel-Maris et al, "Piezoresistive cantilever array for life sciences applications," *Journal of Physics: Conference Series,* vol. 61, pp. 955-959, 2007.

[64] Y. Sun, *et al.*, "A high-aspect-ratio two-axis electrostatic microactuator with extended travel range," *Sensors and Actuators A: Physical,* vol. 102, pp. 49-60, 2002.

[65] C. Lee et al., "Single crystal silicon (scs) xy-stage fabricated by drie and ir alignment," in *The Thirteenth Annual International Conference on Micro Electro Mechanical Systems (MEMS) 2000.*, Miyazaki 2000, pp. 28–33.

[66] C. Kim and Y. Kim, "Micro XY-stage using silicon on a glass substrate," *Journal of Micromechanics and Microengineering*, vol. 12, pp. 103-107, 2002.

[67] C. Kim et al., "Silicon micro XY-stage with a large area shuttle and no-etching holes for SPM-based data storage," *Journal of microelectromechanical systems*, vol. 12, pp. 470-478, 2003.

[68] N. Hubbard and L. Howell, "Design and characterization of a dual-stage, thermally actuated nanopositioner," *Journal of Micromechanics and Microengineering*, vol. 15, p. 1482, 2005.

[69] S. Bergna et al., "Design and modeling of thermally actuated MEMS nanopositioners," in *IMECE2005, ASME International Mechanical Engineering Congress and Exposition*, Orlando, Florida, 2005.

[70] J. Gorman et al., "Control of MEMS nanopositioners with nano-scale resolution," in *IMECE2006 ASME International Mechanical Engineering Congress and Exposition*, Chicago, Illinois, 2006.

[71] J.J. Gorman, YS. Kim, A.E. Vladar and N.G. Dagalakis, "Design of an on-chip micro-scale nanoassembly system," in *4th International Symposium on Nanomanufacturing*, Cambridge, Massachusetts, 2006, pp. 160-165.

[72] S. Avramov-Zamurovic et al., "Embedded capacitive displacement sensor for nanopositioning applications," *IEEE Transactions on Instrumentation and Measurement*, vol. 60, pp. 2730-2737, 2011.

[73] S.H. Yang, YS. Kim, JM. Yoo and N.G. Dagalakis, "Microelectromechanical systems based Stewart platform with sub-nano resolution," *Applied Physics Letters,* vol. 101, pp. 101-105, 2012.

[74] L. Fan et al., "Self-assembled microactuated XYZ stages for optical scanning and alignment," *Transducers 1997 International Conference on Solid-State Sensors and Actuators,* pp. 319-322, June 16-19, 1997 1997.

[75] Y. Ando, "Development of three-dimensional electrostatic stages for scanning probe microscope," *Sensors and Actuators A: Physical,* vol. 114, pp. 285-291, 2004.

[76] Y. Ando, T. Ikehara and S. Matsumoto, "Design, fabrication and testing of new comb actuators realizing three-dimensional continuous motions," *Sensors and Actuators A: Physical,* vol. 97, pp. 579-586, 2002.

[77] J. Singh et al., "A novel electrostatic microactuator for large deflections in MEMS applications," *Thin Solid Films,* vol. 504, pp. 64-68, 2006.

[78] H. N. Kwon et al., "MicroXY stages with spider-leg actuators for two-dimensional optical scanning," *Sensors and Actuators A: Physical,* vol. 130-131, pp. 468-477, 2006.

[79] K. Takahashi et al., "Topological layer switch technique for monolithically integrated electrostatic XYZ-stage," in *IEEE MEMS,* Kobe, Japan, 2007, pp. 651-654.

[80] WC. Chen, PI. Yeh, CF. Hu and W. Fang, "Design and Characterization of Single-Layer Step-Bridge Structure for Out-of-Plane Thermal Actuator," *Journal of Microelectromechanical Systems,* vol. 17, pp. 70-77, 2008.

[81] K. Ogando, N.La. Forgia, J.J. Zárate and H. Pastoriza, "Design and characterization of a fully compliant out-of-plane thermal actuator," *Sensors and Actuators A: Physical,* vol. 183, pp. 95-100, 2012.

[82] YY. Kim, N.G. Dagalakis and S.K. Gupta, "Creating large out-of-plane displacement electrothermal motion stage by incorporating beams with step features. ," *Journal of Micromechanics and Microengineering,* vol. 23, pp. 1-10, 2013.

[83] L.K. Lagorce, O. Brand and M.G. Allen, "Magnetic microactuators based on polymer magnets," *IEEE Journal of Micromechanical Systems,* vol. 8, pp. 2-9, 1999.

[84] H. Cho and C.H. Ahn, "A bidirectional magnetic microactuator using electroplated permanent magnet arrays," *Journal of Microelectromechanical Systems,* vol. 11, pp. 78-84, 2002.

[85] C.T. Pan and S.C. Shen, "Magnetically actuated bi-directional microactuators with permalloy and Fe/Pt hard magnet," *Journal of Magnetism and Magnetic Materials,* vol. 285, pp. 422-432, 2005.

[86] R. Luharuka, S. LeBlanc, J.S. Bintoro, Y.H. Berthelot and P.J. Hesketh, "Simulated and experimental dynamic response characterization of an electromagnetic microvalve," *Sensors and Actuators A: Physical,* vol. 143, pp. 399-408, 2008.

[87] YM. Choi et al., "A high-bandwidth electromagnetic MEMS motion stage for scanning applications," *Journal of Micromechanics and Microengineering,* vol. 22, pp. 105012-105020, 2012.

[88] K.H. Kim, H.J. Yoon, O.C. Jeong and S.S. Yang, "Fabrication and test of a micro electromagnetic actuator," *Sensors and Actuators A: Physical,* vol. 117, pp. 8-16, 2005.

[89] P. Vettiger et al., "The" millipede"-nanotechnology entering data storage," *IEEE Transactions on nanotechnology,* vol. 1, pp. 39-55, 2002.

[90] P. F. Indermühle et al., "AFM imaging with an xy-micropositioner with integrated tip," *Sensors and Actuators A: Physical,* vol. 47, pp. 562-565.

[91] X. Liu, K. Kim and Y. Sun,, "A MEMS stage for 3-axis nanopositioning," *Journal of Micromechanics and Microengineering*, vol. 17, p. 1796, 2007.

[92] J. Dong and P. M. Ferreira, "Electrostatically actuated cantilever with SOI-MEMS parallel kinematic XY stage," *Journal of microelectromechanical systems*, vol. 18, p. 641, 2009.

[93] Y. Sarov, T. Ivanov, A. Frank and I.W. Rangelow, "Thermal driven multi-layer actuator for 2D cantilever arrays," *Appl Phys A*, vol. 102, pp. 61-68, 2011.

[94] A.G. Fowler, A.N. Laskovski, A.C. Hammond and S.O.R. Moheimani, "A 2-DOF electrostatically actuated MEMS nanopositioner for on-chip AFM," *Journal of Microeletromechanical Systems*, vol. 21, pp. 771-773, 2012.

Chapter 2: Design and Working Principle

2.1 Introduction[1]

This chapter describes the design of both the parallel architecture and the single-unit actuator followed by the investigation of beam behaviours to conceptualise the design for further analysis. The analyses of 4SA microrobot design will be dealt with in Chapter 3 and of 3SA microrobot design in Chapter 6. Section 2.2 describes the design of both 4SA and 3SA microrobots as well as the parallel architecture. Section 2.3 investigates the maximum 3D deflections of the tethering and spring flexure beams with respect to the change in cross-section area, aspect ratio and length of the beams. It also discusses the investigation of the different spring flexure beam types that result in the best motion performance for the microrobot. The chapter is summarised in Section 2.4.

2.2 Structural design, specification and working principle

We have considered several versions of the design of the microrobot and have focused our analyses on two types, the 4SA and 3SA microrobots. The 4SA microrobot has a four-sided orthogonal structure while the 3SA microrobot has a three-sided *120°* structure, thus resulting in a more densely packed parallel architecture without compromising the motion performance. This transition in the design is dealt in more detail in Section 2.2.1. The motion performance of a single microrobot in our context refers to the displacement of the microstage and hence the microneedle integrated on top of it at particular actuation voltages. We define precision of movement of the microneedles as the smallest step that they can move when increased in steps to target specific sections within the cell. The primary requirement of

[1] Elements of this chapter have been published/ presented in conferences C1, C2, C3, C4 and C5 or in preparation for journal(s) J1 and J3 and is a part of US and NZ provisional patent application pending P1.

the system is to achieve a maximum range of displacement of *1* µm to *30* µm in-plane and of up to *7* µm out-of-plane at a minimum voltage, for a high motion performance.

Considering the specific application to cell manipulation, the microrobot needs to satisfy several specification criteria such as the different dimensions of cells that it can manipulate; total motion range of the microneedle so that it can target specific cell organelles including the nucleus; corresponding actuation voltages to achieve the motion range for manipulation; inter-needle distance in the array; routing of the electrical wires that power these individual microrobots, power electronics which will be used to operate the array and the corresponding controller software and hardware. These specifications have been illustrated in Table 2.1 and explained in detail in this section. The power electronics and control software are discussed in Chapter 8. For most of the mammalian cell types with sizes ranging from *1* µm to *50* µm [1] and illustrated in Table 2.2, the in-plane motion range of our microrobot needs to be between *1* µm to *30* µm, depending on the position of specific cell organelles, such as nucleus. For the out-of-plane motion range, a displacement of up to *7* µm would be sufficient for vertical manipulation. Depending on the cell type, the volume of nucleus relative to the cell volume can range between *10-60%* with a *4-10* nm thickness of the membrane [2]. As will be seen in Chapters 3 and 6, that we will achieve such motion within an applied DC voltage of less than *170* V, which is not harmful to ensure the viability of the cells.

The actuation components around the microneedles that drive it, occupy a significant area in the range between *3-5* mm^2. Thus the interneedle distance or the pitch of the microneedles becomes a constraining factor for the overall design. This governs the size of the cell trapping platform as the distance between cells trapped in individual microwells will be of the same value as the pitch of the microneedles to allow targeted positioning. Otherwise, given the motion range of the microneedles in tens of microns, they would not be able to successfully place themselves over specific cell organelles if the geometry and size of the parallel

architecture does not match to that of the cell trapping platform. Further constraint in terms of the size and geometry has been explained in the subsequent section by referring to Figure 2.2.

Electrostatic actuation has been selected as our preferred actuation mechanism because it consumes much less power, its devices are smaller in size, and can achieve fine resolution and repeatability in electromechanical positioning. Moreover electrostatic actuation has faster switching speed coupled with the possibility of easier selectivity of electrode materials and easier integration with control electronics. Nevertheless, there are several issues that need to be overcome which include sticking/charging as static pull-in occurs when the distance between plates is *2/3* of the initial gap, along with high voltages and low electrostatic force generated for motion. Integration of electromagnetic actuation for achieving vertical motion is a potential possibility compared to electrostatic actuation. Nonetheless, for the initial design, it was decided to have a uniform actuation system for the ease of operation and fabrication. In future designs, electrostatic actuation can be used for in-plane motion and electromagnetic actuation can be used for out-of-plane motion, as discussed in Chapter 8.

The primary design criteria for the micropositioning stage that houses a microneedle is that each individual stage in a parallel architecture should have independent 3D mobility for precise and targeted manipulation tasks. Other design parameters include maximum stroke, access speed and precision. For dynamic applications, it should be noted however that it is not easy to realise a large displacement and a high speed simultaneously, because the large stroke requires a flexible suspension that reduces access speed due to the low natural frequency. Thus the actuation scheme, whether electrostatic or thermal or magnetic or piezoelectric among others have to be selected carefully that allows such a parallel integration. With the design being analysed in Chapters 3 and 6, it should be reiterated in here that there has to be a trade-off between superior actuation performance and the number of single-unit actuators that can be integrated in a parallel architecture.

Table 2.1 Specification of the proposed parallel actuator.

Desired operation ranges	*1* µm to *30* µm (in-plane); ~ *7* µm (out-of-plane)
Associated actuation voltages	*20* V to *160* V (in-plane); ~*35* V (out-of-plane)
Space limits of a single unit	*3-5* mm^2
Space limits of the parallel architecture	~*70* mm^2
Electrical wiring conditions	Minimum distance between the electrical interconnects before electrical coupling prevails is around *30* nm [3]
Power electronics	Refer to Sections 5.2 and 8.3.4
Controller software and hardware	Refer to Section 8.3.4

Table 2.2 Different types of cells and their corresponding sizes [4].

Cell type	**Diameter (µm)**
Human CD3+T	7.5
Chinese hamster ovary CHO-K1	15
Monkey kidney cell Cos-7	15
Human kidney HEK-293	14-16
Human cervical cancer HeLa	17-20
Hepatocytes HepG2	15
Human endothelial HUVEC	12-14
Hybridoma	13-14
T lymphocytes Jurkat E6-1	10
Human bone marrow K562	15
Mouse lymphoma L5178y	13
Human breast adenocarcinoma MCF7	15-17
Human bone marrow mesenchymal stem cells	15-16
Human monocyte	10
Mouse embryonic stem cells	13
Mouse fibroblasts NIH 3T3	15
Human-gradient centrifugation PBMC (isolated)	6-14
Human PBMC cultured	12.5
Rat adrenal gland PC12	10-13
Human red blood cells	5-6
Rat neural stem cells RNSC	11-13
Insect ovary (baculovirus expression) SF9	13
B lymphocytes U266	12
Human whole blood dilute & lyse counts	5-6

2.2.1 Single-unit actuator design and working principle

The single-unit actuator as shown in Figure 2.1 has a central microstage with a microneedle integrated on top of it (j). This central structure is driven via long slender tethering beams (b) which are fixed at the other end with support beam structures (d). These support beam structures are driven by an arrangement of comb-drives (c), having a fixed set of fingers anchored to the device silicon layer and the moving set of fingers connected to the support

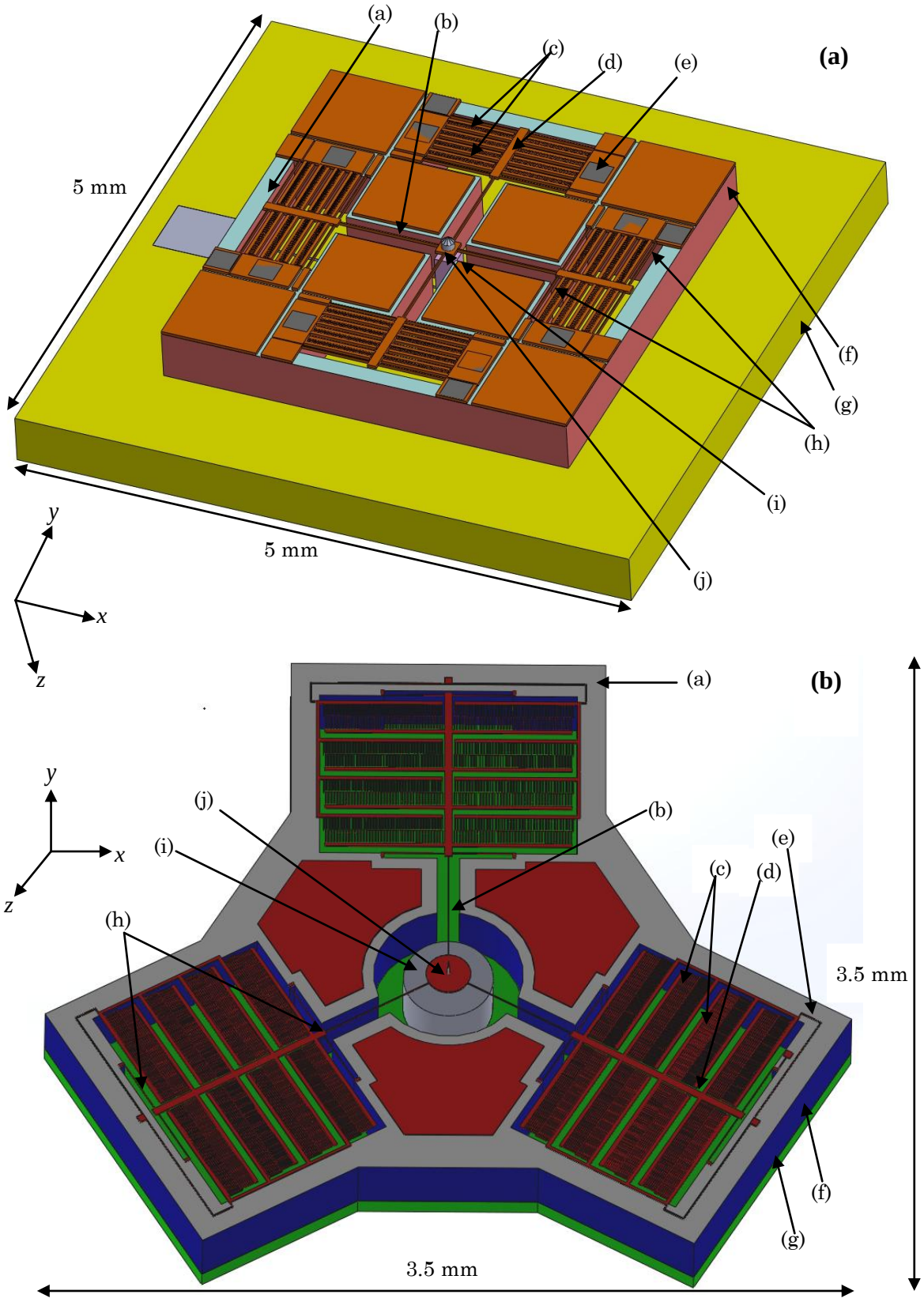

(a) Insulating oxide layer; (b) Tethering beam; (c) Comb-drive actuators; (d) Support beam; (e) Metal pad for electrical connection; (f) SOI wafer; (g) Bottom silicon wafer; (h) Spring flexure beam; (i) Bottom electrode/Silicon tower; (j) Microneedle integrated with microstage

Figure 2.1 Graphical illustrations of single-unit actuator designs (a) 4SA microrobot (b) 3SA microrobot.

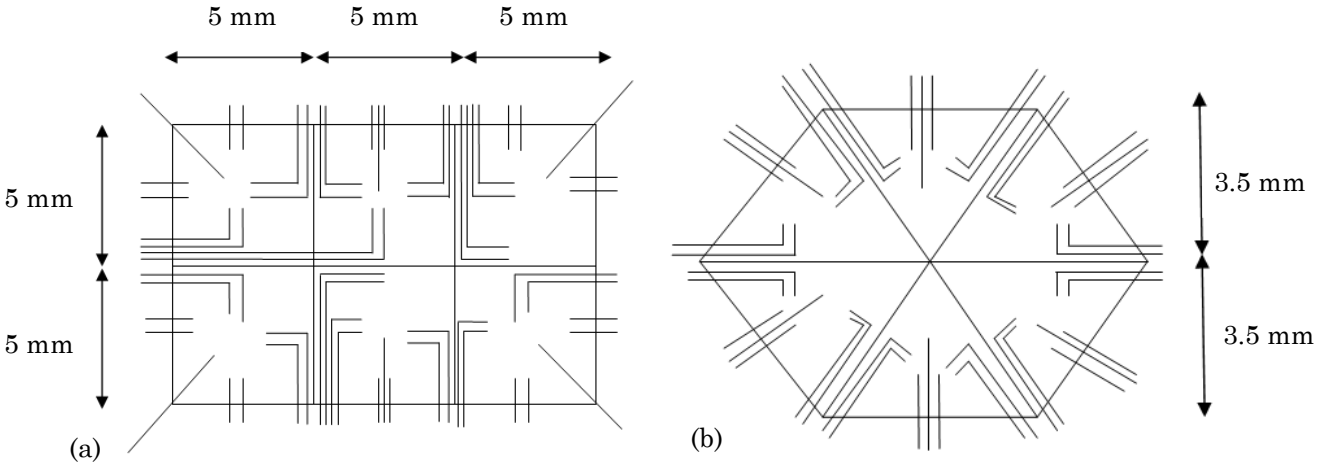

Figure 2.2 A simplified schematic of the packing density in a parallel architecture consisting of (a) 4SA microrobots and (b) 3SA microrobots.

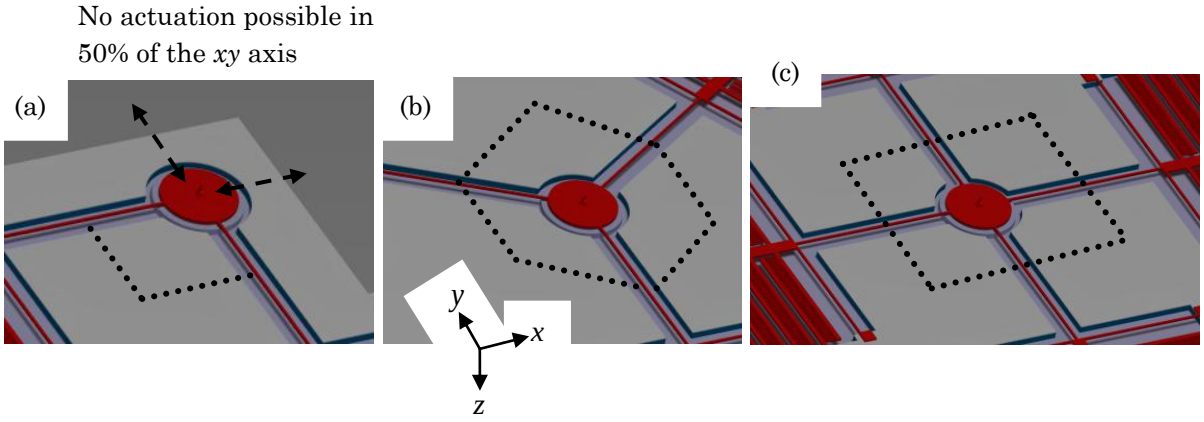

Figure 2.3 Graphical illustrations of different versions of single-unit actuators. The dashed black dot lines represent the in-plane zone of actuation (a) 2SA microrobot with sides orthogonal to each other and the ability to actuate in only one-half direction of the in-plane axis (b) 3SA microrobot with the sides inclined at 120^0 to each other (c) 4SA microrobot with the sides orthogonal to each other and both have the ability to actuate across the entire in-plane axes.

beam (d). This support beam is connected on both its ends by spring flexure beams (h) which gives structural stability during motion of the microstage (j). When potential difference is applied between the opposite set of comb-fingers (c) [5-9], the axial electrostatic electric field causes the fingers to move toward each other thus resulting in a pull motion. This can be converted into a pull-pull motion by operating the comb-drives (c) on the opposite side,

thereby increasing the motion range across a particular axis. A separate silicon substrate houses the long standing silicon tower structure (i). There is a gap between this tower and the microstage. A potential difference between these two structures results in a capacitive electrostatic force which leads to a vertical pull motion. All the structures in the microrobot are separated from each other by a thin insulating oxide layer. The electrical metal pads and the connections provide the interface to connect the microrobot with a printed circuit board for DC/AC power supply. For cell manipulation tasks, the in-plane motion of the microneedles will be achieved first followed by the out-of-plane motion.

The design of a single-unit actuator has transitioned from a four-sided actuator (4SA microrobot) to a three-sided actuator (3SA microrobot), as shown in Figure 2.1. As discussed later in Chapters 3 and 6, it is discovered that compromising a side of the microrobot does not affect the actuator motion performance; in fact the performance becomes better as higher motion range can be achieved at lesser actuation voltage along with the percentage reduction in the surface area in the parallel architecture. A simplified schematic of the difference in packing between 4SA and 3SA microrobots is illustrated in Figure 2.2. In order to densely pack the electrical interconnects corresponding to the microrobots efficiently, the effect of electrical coupling needs to be considered. The minimum distance between these electrical interconnects before electrical coupling prevails is around *30* nm [3]. Therefore considering an array with six microrobots, the 3SA microrobots have *42* electrical connections and occupy at least *43%* less surface area compared to the 4SA microrobots which have *54* electrical connections. Thus, in terms of the size, a transition from 4SA to 3SA not only reduces the number of electrical interconnects on every side by two, but also increases the density of microrobots that can be packed into a single parallel architecture.

In addition, we have also considered several variations in the design of a single-unit microrobotic actuator as shown in Figure 2.3. While design analyses have been performed for

4SA and 3SA microrobots, the design of a 2SA microrobot (Figure 2.3a) is not analysed. Having just two sides in a single-unit actuator, the zone of actuation of the microneedle almost reduces to *50%* in contrast to the achievable motion with the other two actuators. With the 2SA microrobot, because of the pull-mode, the microneedle can move in only one-half direction of *x* and *y* axes which significantly limits its motion. With the 3SA and 4SA microrobots, because of pull-pull mode, the actuation zone covers the entire *x* and *y* axes. In other variations of the microrobot, adding extra sides will continue increasing the spring stiffness of the system and will result in decreasing motion range.

The tethering beams in the 3SA microrobot are inclined at an angle of 120^0 compared to the 4SA and 2SA microrobots where the beams are placed orthogonally to each other. As discussed later in Chapters 3 and 6, the orthogonal arrangement enables a decoupled motion across the axes. Nonetheless, an angle of 120^0 also leads to a significant decoupled motion. Increasing the lateral stiffness of the spring flexure beams can reduce the coupling of motion across the axes.

2.2.2 Parallel architecture design and working principle

In Section 2.2.1, we have illustrated how the transition from 4SA to 3SA microrobot changes the design of the parallel architecture by means of a simplified schematic in Figure 2.2. The actual scaled up models have been illustrated in Figure 2.4 for 4SA microrobot and Figure 2.5 for 3SA microrobot. For the 4SA design, the linearly placed square shaped arrangement of the microrobots leads to their highest density of packing. In comparison, the 3SA design, with its hexagonal shaped arrangement of the microrobots leads to an even higher density of packing. As we scale up the array design from six microrobots shown in Figure 2.2 to more than *125* microrobots shown in Figures 2.4 and 2.5, at least *40%* more microrobots can be densely packed with the 3SA design compared to the 4SA design. Moreover, there is a

significant saving in the number of electrical interconnections by almost *300*. Because the final array design consists of 3SA microrobots, we will further discuss the design of their corresponding parallel architecture.

The parallel architecture design consists of individual triangular islands with multiple 3SA microrobots extending from the center of the chip to the periphery, shown in Figure 2.5a. The array consists of *125* 3SA microrobots with a span of 5.5 cm from one end of the structure to the other. The geometry of the cell trapping platform, shown in Figure 2.6b, is governed by the geometry and size of the parallel architecture. The inter-microneedle distance dictates the inter-cellular distance on the cell trapping platform. For example, in a particular location on the array, the distance between two adjacent microneedles is *3* mm and their corresponding cells on the platform are also placed at *3* mm from each other. This is

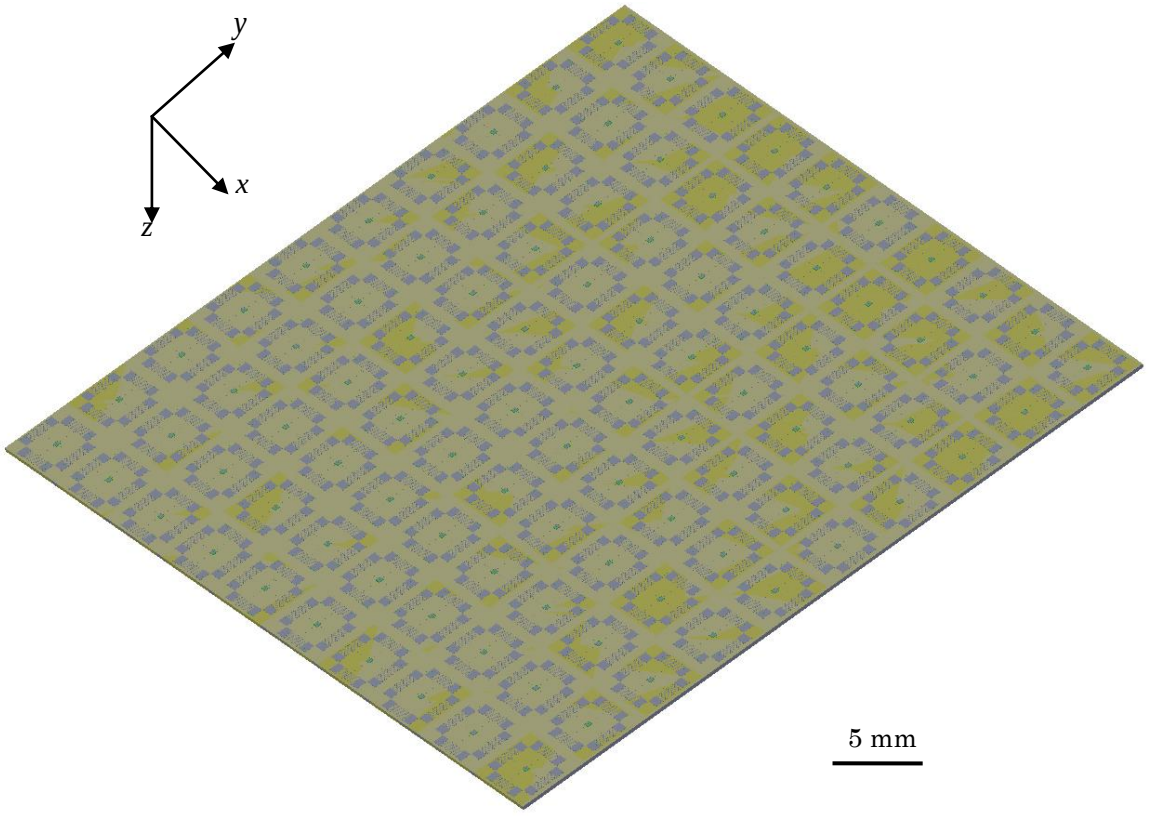

Figure 2.4 Graphical illustration of a parallel architecture consisting of 4SA microrobots.

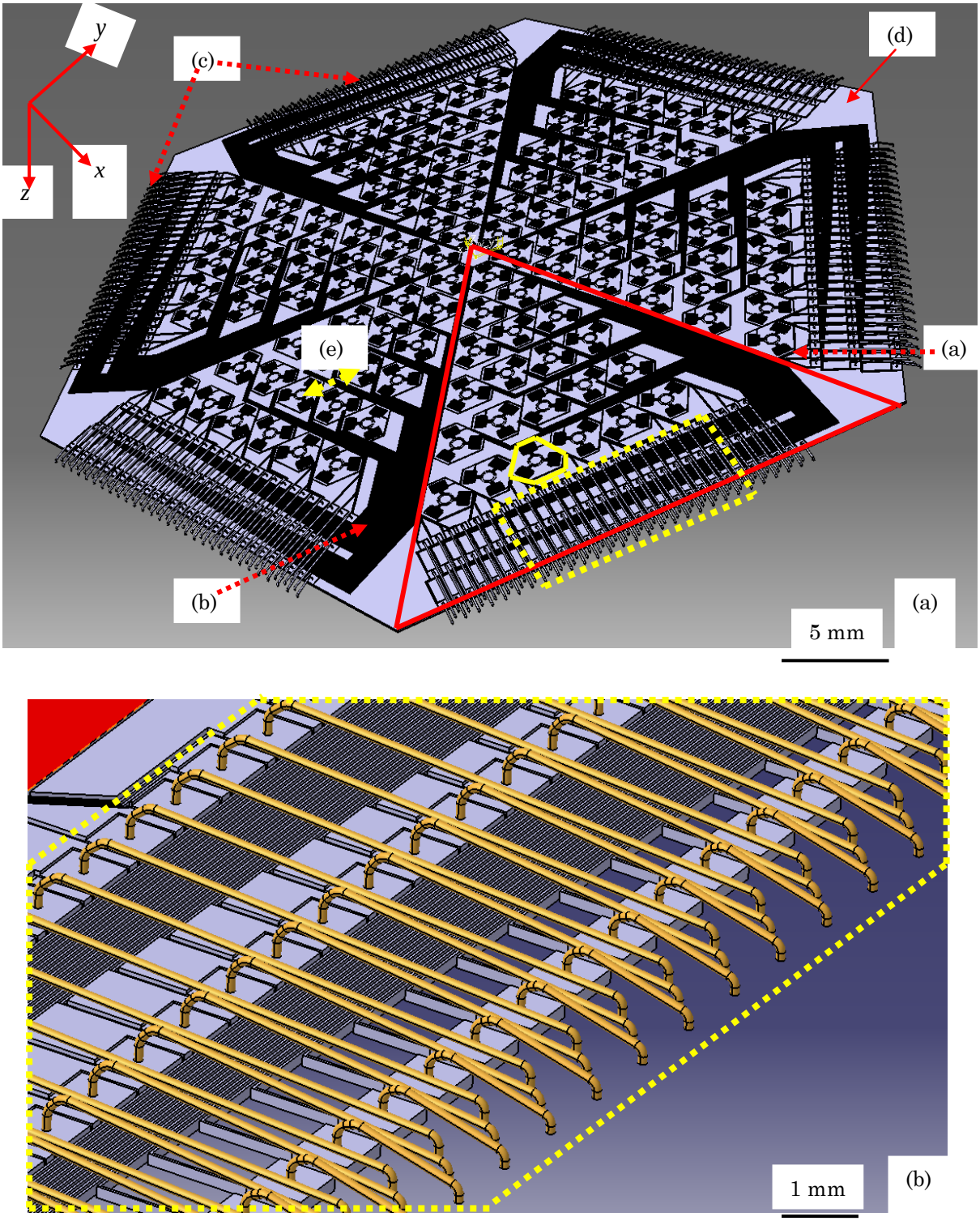

Figure 2.5 Graphical illustration of the parallel architecture consisting of 3SA microrobots (a) Full view with the triangular island (red), single-unit actuator (solid yellow) the electrical connections and wire bonding (dotted yellow). (b) Zoomed in view of the wire bonding; - (a) Single-unit actuator; (b) Electrical interconnects; (c) Wire bonding; (d) Silicon substrate with a thin film of insulating oxide on its top; (e) Inter-microneedle distance.

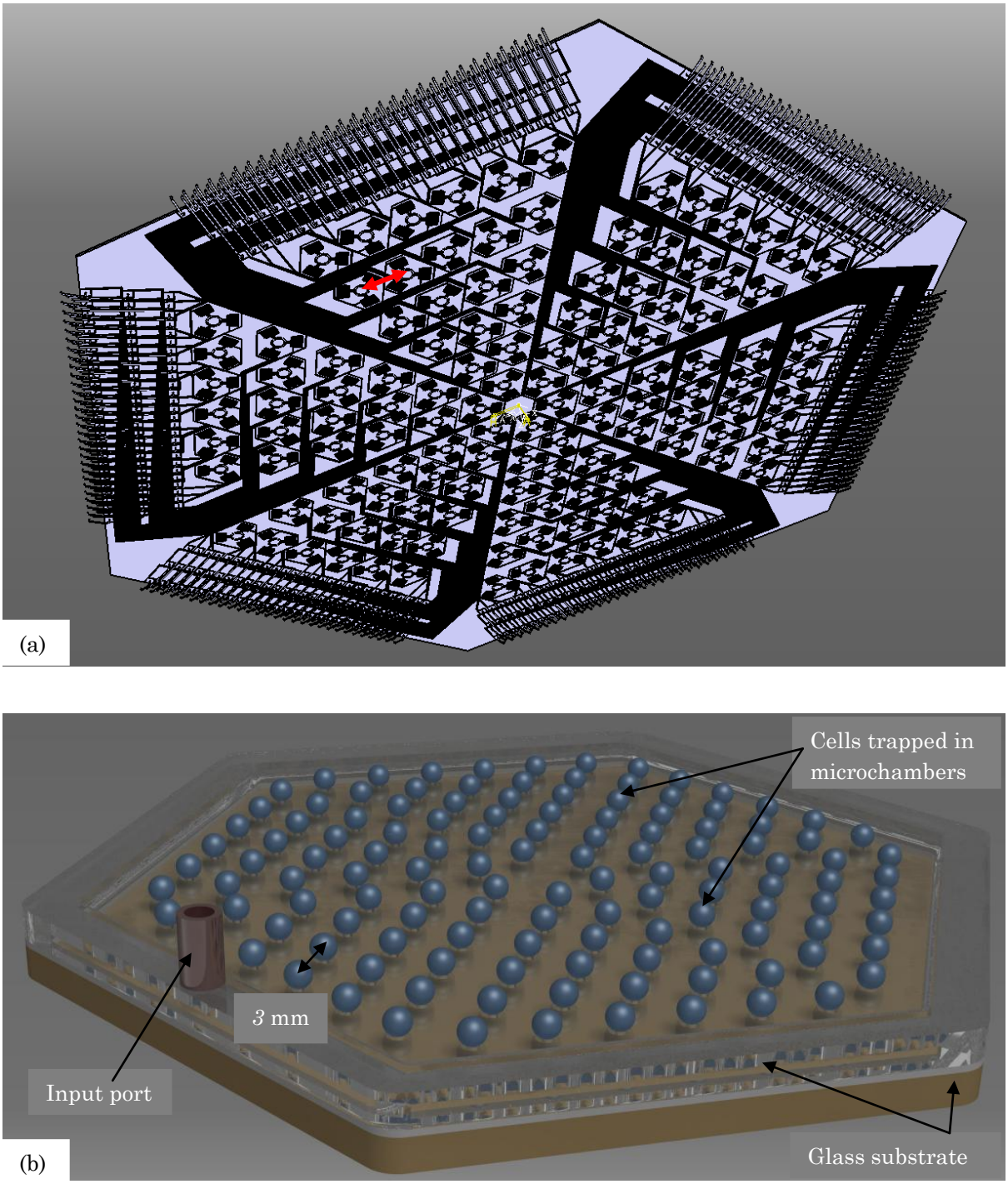

Figure 2.6 (a) A single parallel architecture chip (inverted) on top of a (b) cell trapping platform for immobilizing individual cells in individual microchambers. The intercellular distance is around *3* mm which is governed by the inter-microneedle distance of *3* mm.

done to ensure that the microneedles target specific cell organelles as their motion range is in tens of microns. The design of the microrobot needs to be such that the motion range of the

microneedle can accommodate a variety of biological cells for manipulation with sizes ranging from *1* µm to *50* µm [1] and as illustrated in Table 2.2. Traversing from the central vertex of the triangular island to the periphery of the chip, the pitch of the microneedles increases to accommodate more electrical interconnects. All of these closely spaced electrical interconnects are sitting on a thin film of oxide on top of the device silicon substrate, to insulate these interconnects from each other. Increasing the number of microrobots in a single parallel architecture will increase the density of electrical interconnects and thus the density of wire bonding increases significantly. This will, therefore, amplify the total span of the structure. This enhancement in size is however linear. In its current form, in Figure 2.5A, the electrical interconnects cannot be properly differentiated due to their large density. The zoomed in view with the differentiated wires has been illustrated in Figure 2.5b. Modern automatic wire-bonders simplify the task of wire-bonding individual actuators onto a ceramic pin package or printed circuit board. A major design concern is to insulate this whole system from getting in contact with a chemical cell culture medium which otherwise would short circuit the system. This issue has been discussed briefly in Section 1.2. This challenge is a future research area that needs to be addressed.

DC voltage is applied to the array with different values to every microrobot to enable individual control of the microneedles. Thus the voltage is first applied to comb-drive actuators in each of these microrobots to allow in-plane motion of the microneedles, so that they can be placed relative to specific cell organelles to be manipulated. Once the microneedles have been moved in *xy* workspace, voltage is applied to the parallel-plate actuator to allow out-of-plane motion of the microneedles, resulting in vertical manipulation in *z* workspace. The velocity of the microneedle will be around *0.5* - *2.5* mm sec^{-1}. Therefore the frequency associated with this movement is significantly less compared to the resonant frequencies of the actuator. The first resonant frequency of the actuator as predicted from

FEA is *12* kHz (in-plane mode for *xy*) and second resonant frequency is *27* kHz (*z* mode motion including flexure of comb-finger electrodes). Unless the cell manipulation occurs at a very high rate, closer to the resonant frequencies when dynamic response analysis becomes critical, otherwise the movement of the microneedles are static.

2.3 Design analysis for actuator components

The maximum bending and stretching of the tethering and spring flexure beams due to translational and axial deflections have been investigated. Based on this investigation, a range of dimensions are conceptualised and further analysed using analytical and numerical simulation models discussed in Chapters 3 and 6. The following criteria have been considered:

- Minimum longitudinal stretching of tethering beam, shown in Figure 2.7.
- Maximum bending of tethering beams for 3D motion range with decoupled motion across the axes. Motion coupling is a parasitic behavior that significantly affects the motion performance and structural integrity of the actuator. Under loading, bending of the tethering beams becomes the primary critical behavior that needs to occur with minimum coupling across the axes, as shown in Figure 2.8.
- Relationship between bending of spring flexure beams with bending of tethering beams, as shown in Figure 2.8.

The two important attributes that govern the behaviour of the actuator are bending and longitudinal stretching. Torsion during out-of-plane motion is another parameter that has been investigated using stiffness matrix model in Chapters 3 and 6. Knowledge of stretching of the tethering beams is critical to understanding the fatigue performance under repeated loading of the beams. Stretching can lead to increasing stiffness of the tethering beams which will affect the overall strength of the structure. Albeit the yield stress of silicon is quite high

i.e. *7000* MPa, the fatigue life of the beams under cyclic loading can be significantly affected if the stretching in the beams is substantial. Moreover with increasing bending in the beams, plastic behavior can be induced in them. This will result in a permanent elongation of the tethering beams and thus affecting the accuracy of motion performance.

Knowledge of bending of the tethering and spring flexure beams is critical to finding a trade-off between the desirable maximum bending of these beams and the permissible dimensions. For example, increasing the length or decreasing the thickness of the beams will apparently increase the motion performance, however at the cost of total size and spring stiffness of the actuator. The 3D behavior of the spring flexure beams which provides restoring force depend on the performance of the tethering beams. The stretching and bending phenomena are investigated for the following parameters, due to their significant contribution toward the motion of the actuator: cross-section area ($w \times h$), aspect ratio (w/h) and length (l) of the beam. Three thicknesses *10* μm, *20* μm and *25* μm are used to study the beam behaviours as limiting parameters. The interference in deflection of the tethering and spring flexure beams for both in-plane and out-of-plane actuation needs to be taken into account. Based on these criteria and parameters, six such scenarios are mapped out and analysed to conceptualise the beam dimensions for a superior design. The corresponding plots are shown in Figures 2.6 to 2.11:

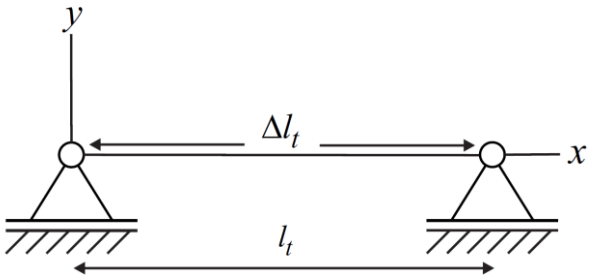

Figure 2.7 Tethering beam prone to longitudinal stretching.

(a) In-plane stretching of tethering beam compared with its bending. As discussed above, the goal is to minimise the beam stretching.

(b) In-plane bending of spring flexure beam compared with bending of tethering beam, as shown in Figure 2.8a.

(c) Out-of-plane bending of spring flexure beam compared with bending of tethering beam, as shown in Figure 2.8b.

(d) In-plane bending of tethering beam compared with its out-of-plane bending.

(e) In-plane bending of spring flexure beam compared with its out-of-plane bending.

(f) Stretching and bending of tethering and spring flexure beam compared with length.

The longitudinal stretching of the tethering beam is computed by [10],

$$\Delta l_t = \frac{F_e l_t}{EA} \tag{2.1}$$

where F_e is the electrostatic force, l_t is the lengths of tethering beam, A is the cross-section area of the beam and E is the Young's modulus.

The bending of the tethering beam is computed by,

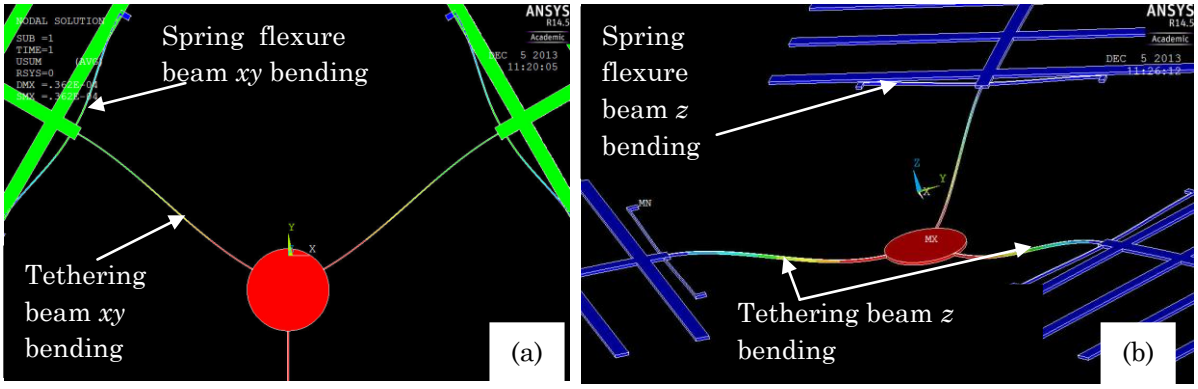

Figure 2.8 Structural simulation illustrations of the beams for (a) in-plane (b) out-of-plane bending. The colours represent the displacement.

$$w_{\max} = \frac{F_e l_t^3}{3EI} \tag{2.2}$$

where I is the second moment of inertia of the beam.

The bending of the spring flexure beam is computed by,

$$W_{\max} = \frac{F_e l_s^3}{192EI} \tag{2.3}$$

where l_s is the length of spring flexure beam.

Referring to Figure 2.9, the longitudinal stretching in tethering beam ranges from four to five orders of magnitude lower than the corresponding bending at a particular cross-section area and aspect ratio. The same is true with respect to length, as shown in Figure 2.14. For both in-plane and out-of-plane motions of tethering and spring flexure beams, the longitudinal stretching is negligible compared with bending, irrespective of the thickness of these beams.

Considering the effect of cross-sectional area, the in-plane bending of both tethering and spring flexure beams increases by more than *15* times with the increase in thickness from *10* μm to *25* μm, as seen in Figures 2.9a and 2.10a. This change is however not that dramatic during out-of-plane bending. For both types of beams with increase in thickness from *10* μm to *25* μm, the out-of-plane bending increases by only about *2.3-2.5* times, as seen in Figures 2.11a and 2.12a. Also for the same thickness, the in-plane and out-of-plane bending in tethering beams is almost *37.5* times higher than the bending in the spring flexure beams. For tethering and spring flexure beams of same thickness, the rate of decrease in in-plane bending is significantly faster than the out-of-plane bending. As the thicknesses increase, the points of intersection of the bending become farther apart, as shown in Figures 2.12a and 2.13a. For example, for the tethering beam thickness of *10* μm, the intersection point is at a cross-

section area of *100* μm^2. Comparatively, it is at *200* μm^2 for thickness of *20* µm and *250* μm^2 for thickness of *25* µm.

Considering the effect of aspect ratio, the behaviour is opposite to what it has been observed in case of cross-section area. In fact for design conceptualisation, the aspect ratio is a better metric compared to cross-sectional area since it represents the true dimensions of the beams. The in-plane bending of the tethering and spring flexure beams decreases by almost *15* times as the thickness increases from *10* µm to *25* µm, contrary to what has been observed in case of cross-section area (Figures 2.9b and 2.10b). Also, similar observations can be made for out-of-plane motion, where the bending decreases by *2.3-2.5* times, as the thickness increases from *10* µm to *25* µm (Figures 2.12b and 2.13b). However for the same thickness, the in-plane and out-of-plane bending in tethering beams is almost *37.5* times higher than the bending in the spring flexure beams which is similar to the pattern observed for cross-section area. Moreover similar trends in cross-section area can be observed in the rate of decrease in in-plane and out-of-plane bending for both tethering and spring flexure beams (Figures 2.12b and 2.13b).

Thus, while increasing the thickness can offer better in-plane bending, the out-of-plane bending is significantly compromised, weighing in the effect of cross-sectional area, aspect ratio and length on beam behaviours. Further it is necessary to define the *area of interest* for studying the range of dimensions for further analyses. It can be observed from Figures 2.9 to 2.14, that there is almost a common *95%* drop in in-plane and out-of-plane bending for the two types of beams up to cross-section area range of *50* μm^2 - *60* μm^2 and aspect ratio range of *0.5-0.6*. Beyond these points, the percentage drop in bending becomes comparatively lower as the cross-section area or the aspect ratio increases. For example between cross-section areas of *50* μm^2 to *100* μm^2, there is only *75%-78%* drop in bending. The trend is similar for aspect ratio ranging from *0.5* to *1.0*. Moreover while considering the effect of

length on beam behaviours, the in-plane and out-of-plane bending increases by almost *87%* for length ranging from *200* µm to *400* µm, *70%* for length ranging from *400* µm to *600* µm, *58%* for length ranging from *600* µm to *800* µm, *49%* for length ranging from *800* µm to *1000* µm and *42%* for length ranging from *1000* µm to *1200* µm. While having short beams can increase the stiffness significantly and reduce the 3D motion, too long beams with slender structure can make the actuator very fragile and increase its size.

Thus, for further analyses, the dimensions chosen are as follows:

- Cross-section area of *50* μm^2 for both tethering and spring flexure beams.
- Aspect ratio of 0.5 for both tethering and spring flexure beams.
- Length range of *800* µm to *1200* µm for tethering beams.
- Length range of *400* µm to *600* µm for spring flexure beams.

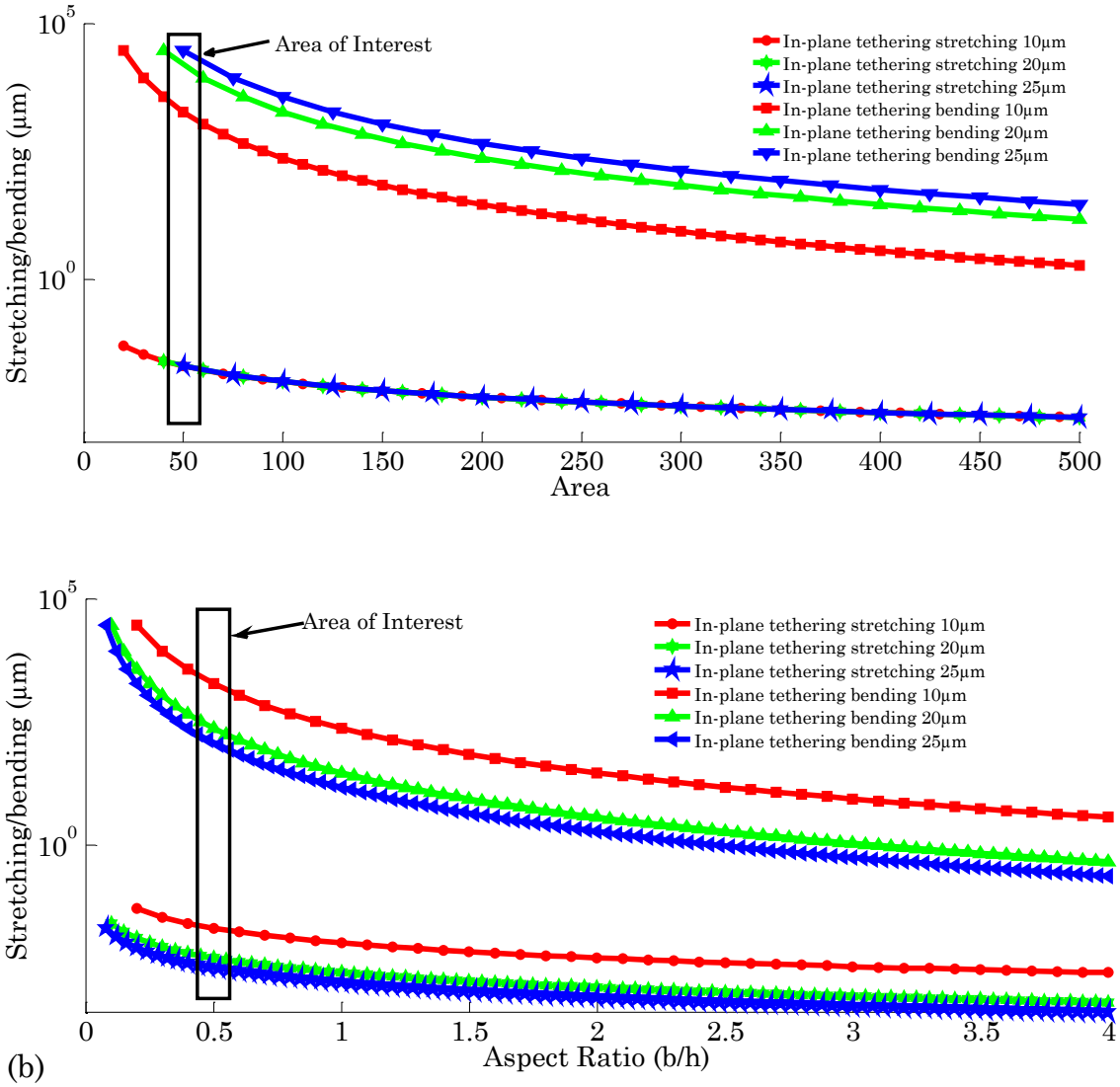

Figure 2.9 In-plane tethering beam stretching and bending with (a) Area (b) Aspect Ratio.

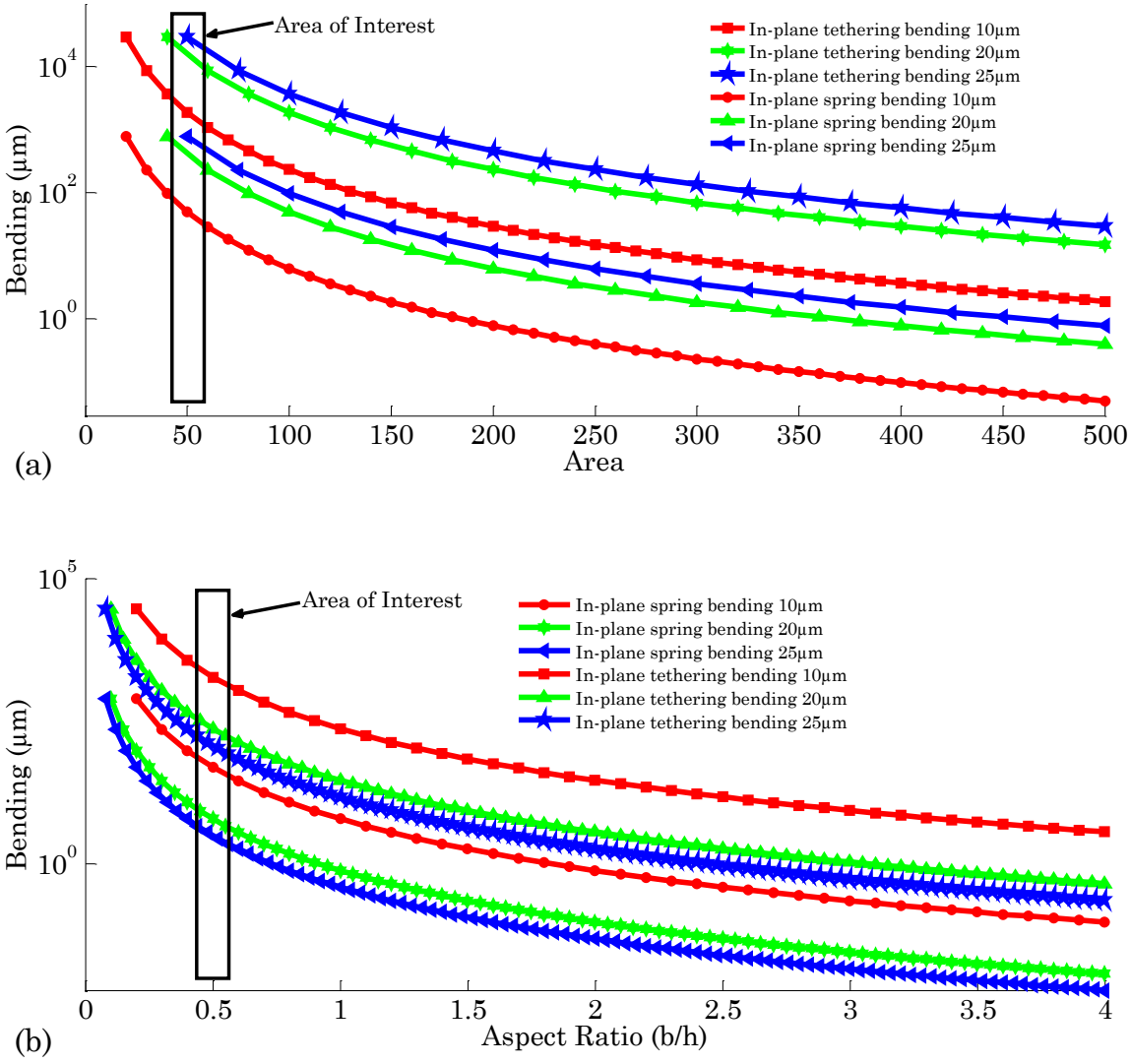

Figure 2.10 In-plane spring flexure beam bending and tethering beam bending with (a) Area (b) Aspect Ratio.

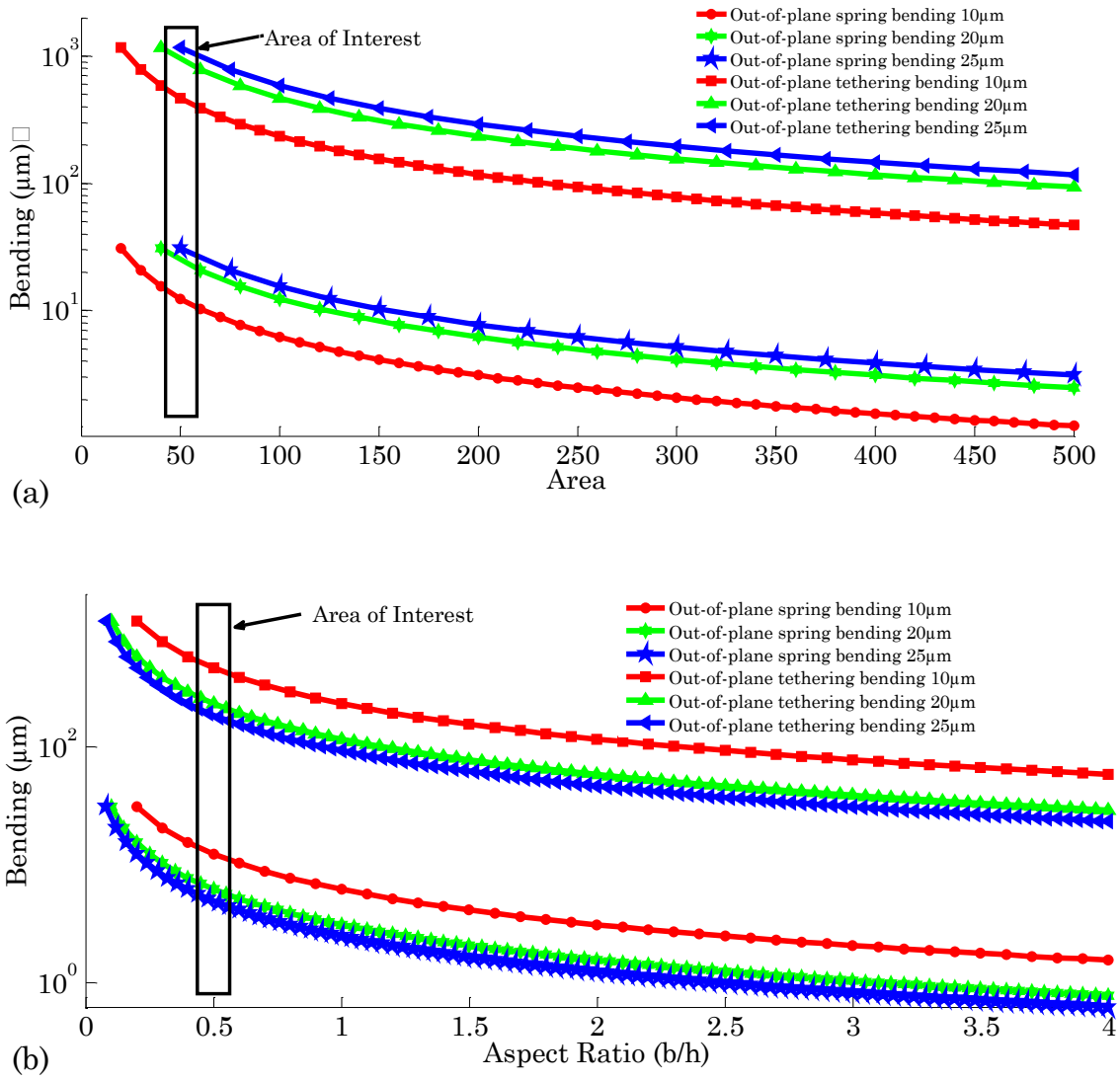

Figure 2.11 Out-of-plane spring flexure beam bending and tethering beam bending with (a) Area (b) Aspect Ratio.

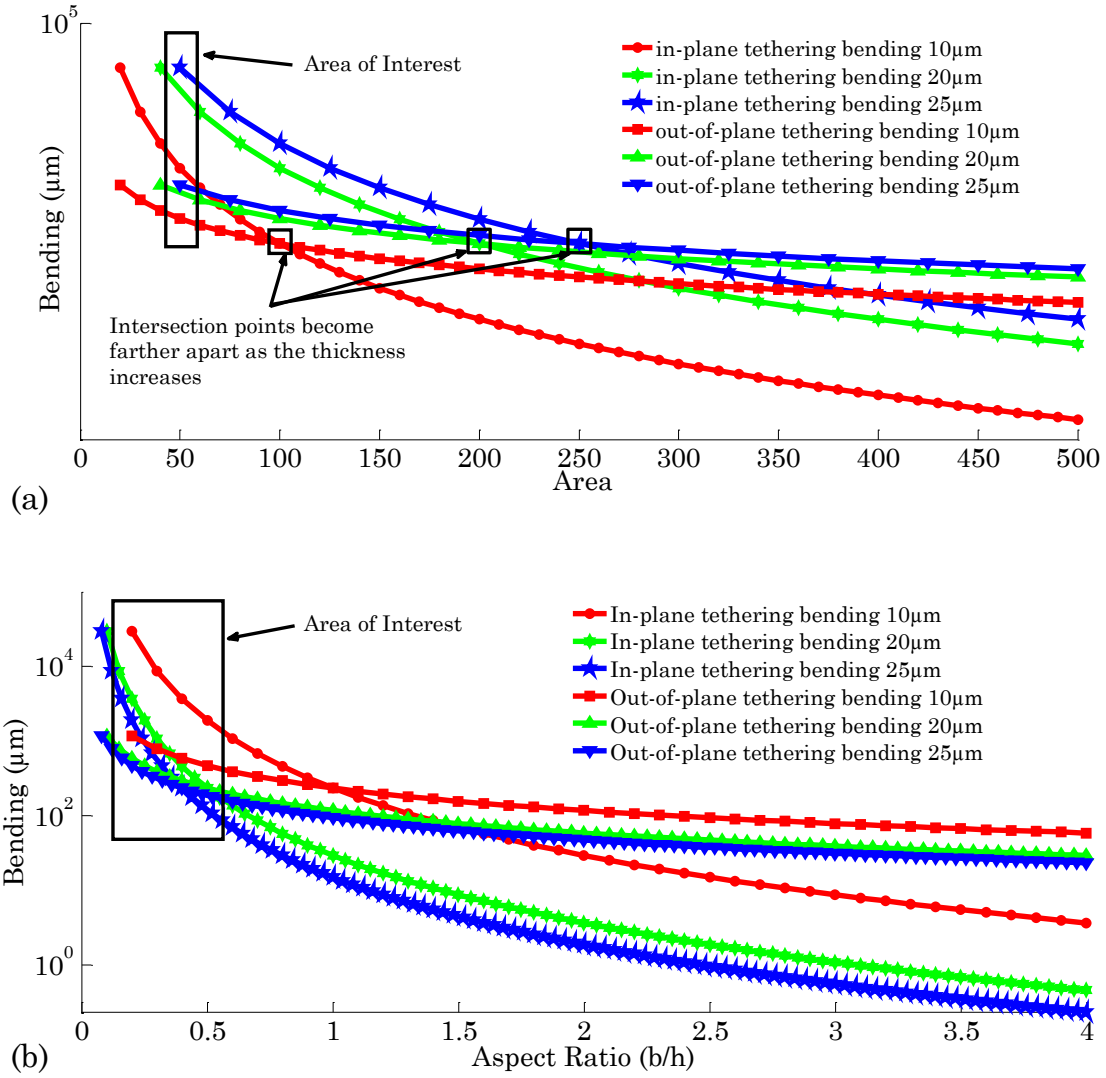

Figure 2.12 In-plane tethering beam bending and out-of-plane tethering beam bending with (a) Area (b) Aspect Ratio.

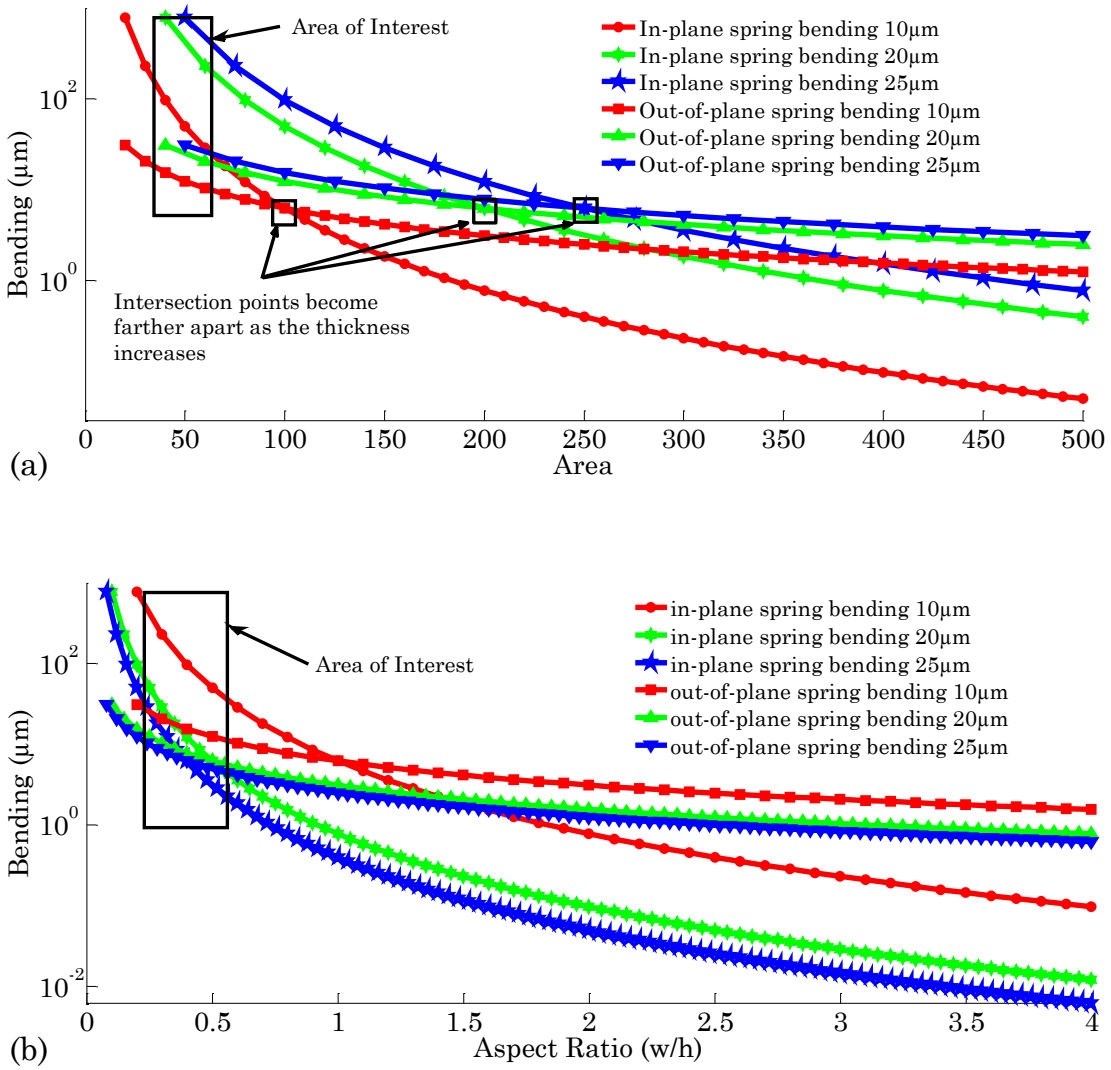

Figure 2.13 In-plane spring flexure beam bending and out-of-plane spring flexure beam bending with (a) Area (b) Aspect Ratio.

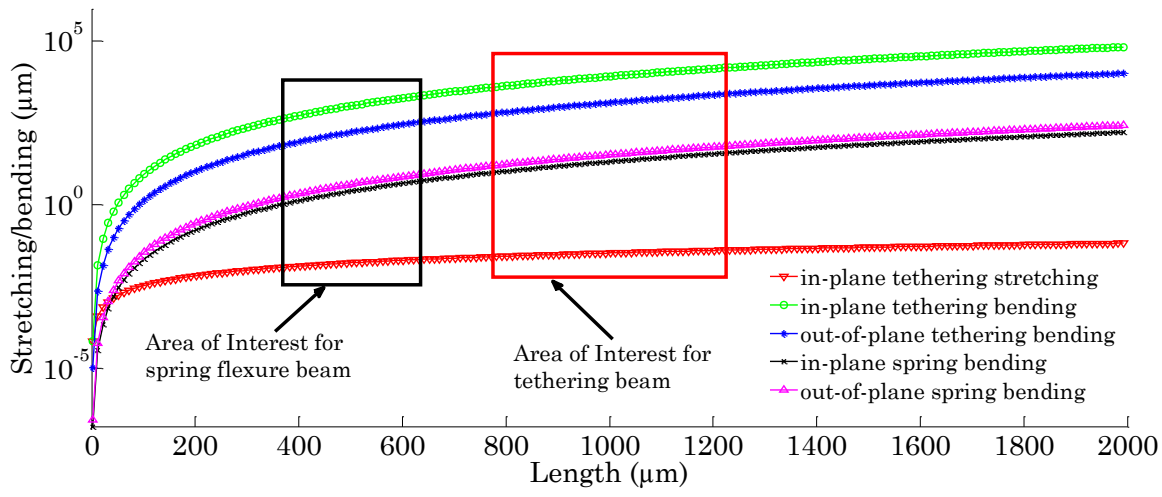

Figure 2.14 Stretching and bending of tethering and spring flexure beams with length.

The final dimensions of the microrobot have been further discussed in Chapters 3 and 6.

2.3.1 Design analysis of different types of spring flexure beams

We have investigated the motion performance of the microrobot design using finite element analysis (FEA) simulations for three different types of spring flexure beams - clamped-clamped, crab leg and single folded as shown in Figure 2.15. FEA simulations have been dealt in more depth in Chapters 3 and 6. The clamped-clamped spring flexure beam has a significant stiff nonlinear spring constant due to extensional axial stress in the rectangular beams. When the thigh section is added to the clamped flexure beam, it forms the crab leg spring flexure beam which reduces stiffness in the undesired direction and extensional axial stress in the flexure. The single folded flexure beam also reduces axial stress components in the beams by adding a truss to the parallel arrangement of beams and they are anchored near the center. This truss allows the end of the flexure to expand or contract in all directions [11].

For clamped-clamped spring flexure beam, the axial and lateral stiffness has been derived in Chapters 3 and 6. Thus we do not discuss them in this section. The out-of-plane stiffness K_z is,

$$K_z = \frac{2Ew_s h_s^3}{l_s^3} \tag{3.30}$$

For crab-leg spring flexure beam, the axial stiffness $K_{x,y}$ [11] is,

$$K_{x,y} = \frac{Eh_s w_{sh}^3 \left(4l_{sh} + \alpha l_{th}\right)}{l_{sh}^3 \left(l_{sh} + \alpha l_{th}\right)} \tag{3.31}$$

where h_s = thickness of the rectangular beam, l_{sh} and w_{sh} = length and width of the shin respectively, l_{th} and w_{th} = length and width of the thigh respectively and where

$\alpha = I_{sh}/I_{th} = \left(w_{sh}/w_{th}\right)^3$, I_{th} and I_{sh} are the moments of inertia of thigh and shin respectively.

And the lateral stiffness k_l is,

$$k_l = \frac{Eh_s w_{th}^3 \left(l_{sh} + 4\alpha l_{th}\right)}{l_{th}^3 \left(l_{sh} + \alpha l_{th}\right)} \tag{3.32}$$

Thus, the stiffness ratio is,

$$\frac{K_{x,y}}{k_l} = \frac{w_{th}^3 l_{sh}^3}{w_{sh}^3 l_{th}^3}\left(\frac{4l_{sh} + \alpha l_{th}}{l_{sh} + 4\alpha l_{th}}\right) \tag{3.33}$$

The out-of-plane stiffness K_z is,

$$K_z = \frac{48EI_{x,sh}}{l_{sh}^3} \tag{3.34}$$

where $I_{x,sh}$ = moment of inertia of shin about *x*-axis.

For single folded spring flexure beam, the axial stiffness $K_{x,y}$ is [11],

$$K_{x,y} = \frac{24EI_{z,s}}{l_s^3} \tag{3.35}$$

And the lateral stiffness k_l is,

$$k_l = \frac{4.8EI_{z,tr}}{l_{tr}^3} \tag{3.36}$$

The out-of-plane stiffness K_z is,

$$K_z = \frac{24EI_{x,s}}{l_s^3} \tag{3.37}$$

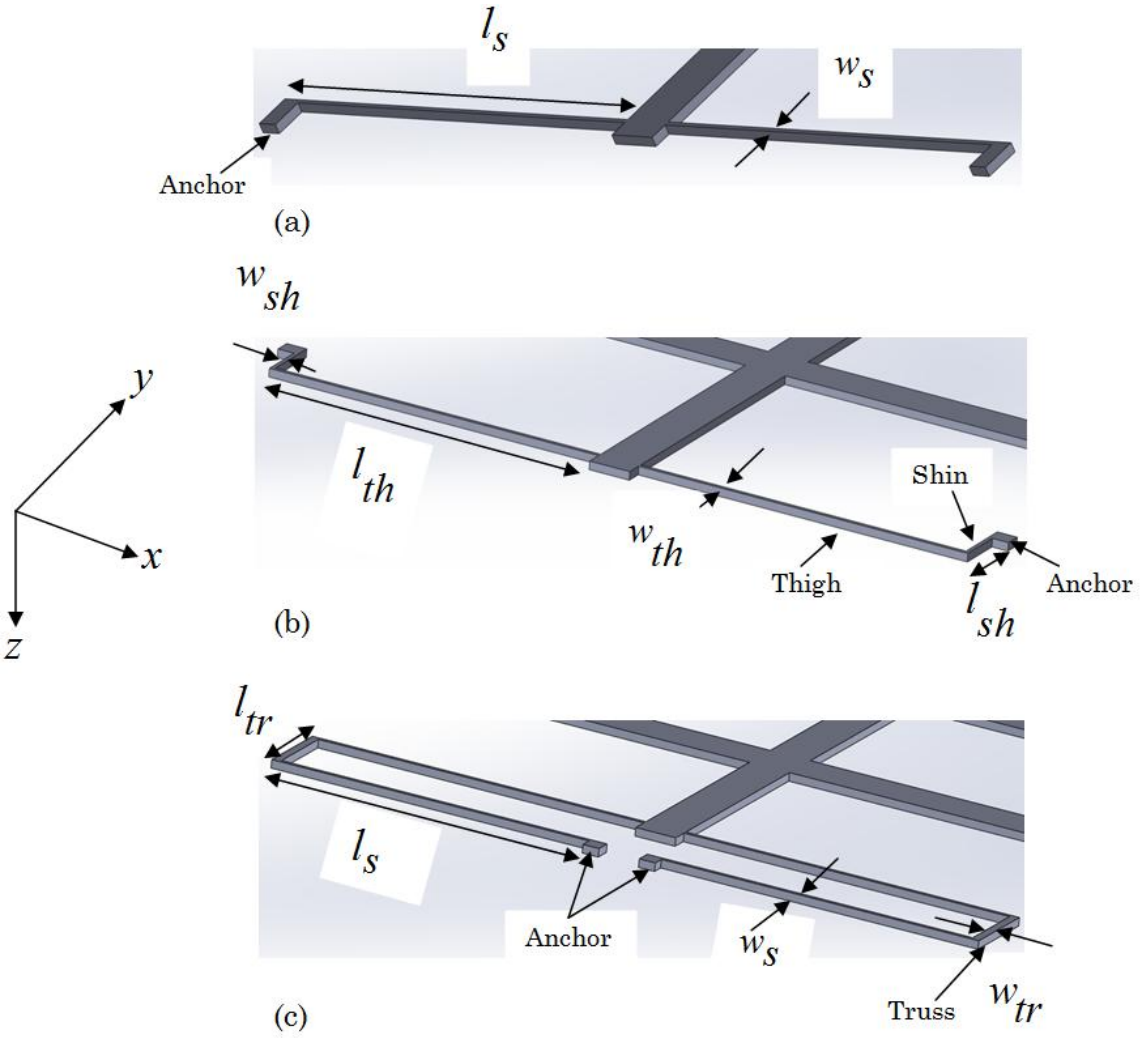

Figure 2.15 Different spring flexure beam types used for analysis (a) clamped-clamped (b) crab leg (c) single folded, thickness = h_s

where l_{tr} = length of the truss and it is assumed that the truss is significantly stiffer than the beams. For detailed analysis on the spring flexure beams, the reader is referred to Fedder [11].

For in-plane actuation, the performance of the actuator with single-folded flexure beam is *40%* better than clamped-clamped or crab leg flexure beams at higher voltages as shown in Figure 2.16. For example, at *160* V, the single folded flexure beam can achieve an in-plane motion of *60* μm compared to around *35* μm achievable by clamped-clamped or crab-leg flexure beams. This is better highlighted in Figure 2.17. The in-plane motion of the actuator

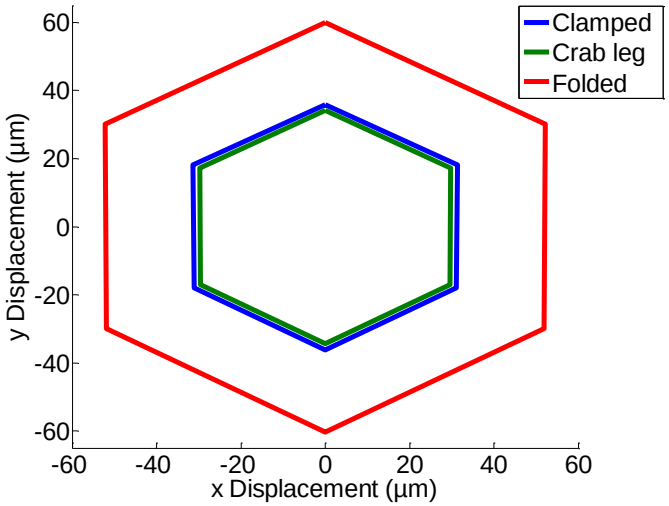

Figure 2.16 2D surface plots for in-plane displacements for different spring flexure beam types for applied DC voltages of 160 V. The tethering beam length is *800* µm and the suspended structure thickness = *10* µm.

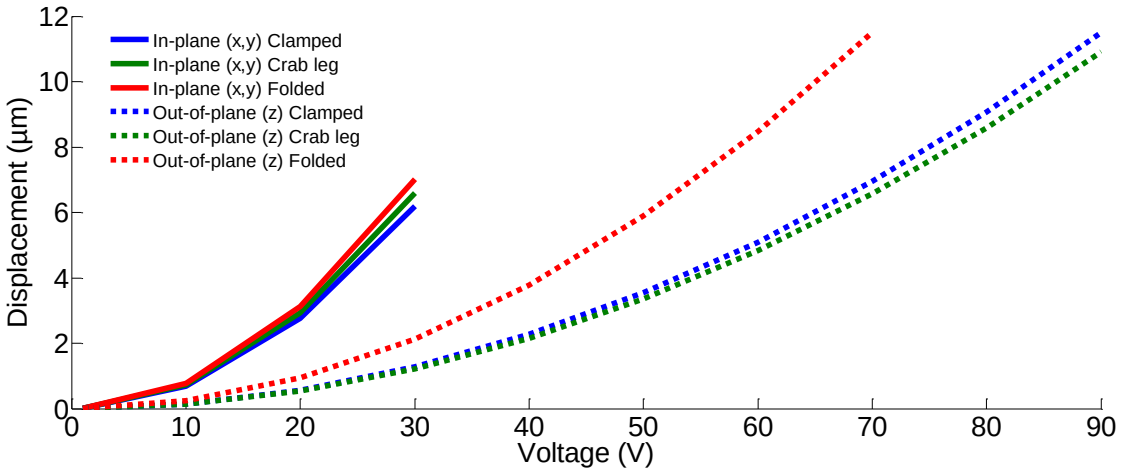

Figure 2.17 In-plane and out-of-plane displacements for three different spring flexure beam types for different applied DC voltages for 3SA microrobot for tethering beam length of *800* µm and for actuator plate gaps of *15* µm. Suspended structure thickness = *10* µm.

is in close proximity to each other at lower voltages, but drifts farther apart as the voltage increases. The out-of-plane motion of the single-folded flexure beam is almost *40%* higher than the other two spring flexure beam types. At *70* V, the folded beam type achieves a motion of almost *11.5* µm compared to almost *7* µm with clamped-clamped and *6.5* µm with crab-leg flexure beams. Nonetheless with a folded flexure beam, during out-of-plane motion,

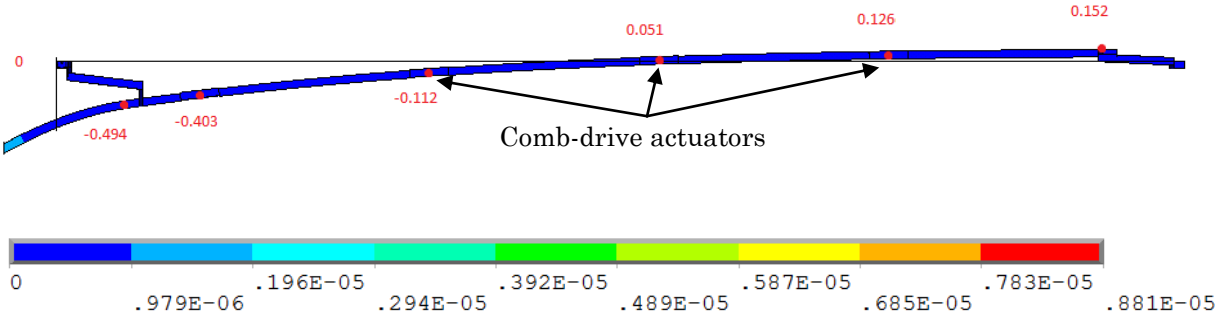

Figure 2.18 Cross-section view of the downward sagging of the comb-finger structures (represented by red dots) during out-of-plane actuation of the micro-needle with single-folded spring flexure beams is as much as between *0.5-1* µm at *20* V. The tethering beam length is *1200* µm and the suspended structure thickness is *10* µm.

the comb-drive actuators get disoriented out-of-plane by as much as *35-40%* of the total motion of the center microstage and thus the microneedle (Figure 2.18). This can have significant effect on the overall stability of the actuator during 3D motion. For this reason, the folded flexure beam is not a good option in the design of the 3SA microrobot. Therefore the clamped-clamped spring flexure beam is the best possible option for the design of the microrobot. Further from the 2D surface plot of the 3SA microrobot in Figure 2.19, it is clear

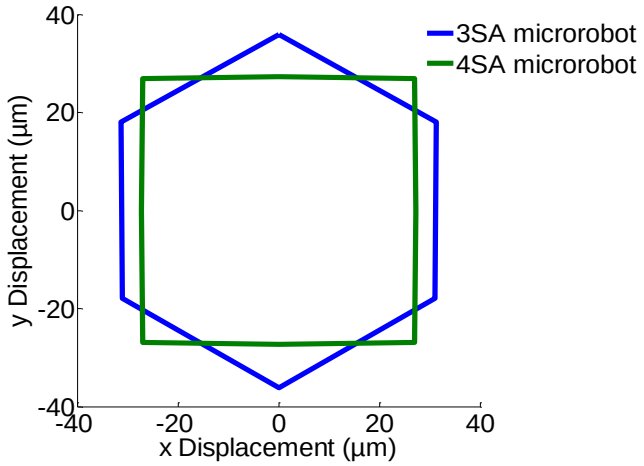

Figure 2.19 2D surface plots for comparing the performance of 3SA and 4SA microrobot. The in-plane motion is for clamped-clamped spring flexure beam for applied DC voltages of 160 V. The tethering beam length is *800* µm and the suspended structure thickness = *10* µm.

that the 3SA microrobot is more efficient than the 4SA microrobot using such a clamped-clamped flexure beam.

2.4 Closure and original contributions

This chapter explains in detail the scientific argument behind transitioning from a 4SA microrobot design to a 3SA microrobot. The corresponding parallel architecture can then integrate multiple such microrobots with higher density of packing. Electrostatics has been chosen as the actuation mechanism for the design that has evolved from a 4SA to a 3SA microrobotic actuator. The design of the microrobotic actuator is further conceptualised and supplemented with analyses regarding the flexibility of component beams including tethering and spring flexure beams. The analyses also involve investigating the motion performance of the microrobot *w.r.t.* three different spring flexure beam types. Longitudinal stretching is found to be negligible, several orders of magnitude lower than the 3D bending of the beams. The design conceptualisation gives us critical information in terms of cross-section area and aspect ration of the beams for optimal tradeoff between bending and integration of multiple actuators in a parallel architecture.

Chapter 2 makes the following original contributions to the study of micro-electro-mechanical-systems (MEMS) based single cell manipulation, sensors and actuators:

- A new type of actuator, namely 4SA microrobot is designed that can achieve 3D motion of the microneedle at the centre using an arrangement of comb-drive actuators for in-plane motion and parallel-plate actuator for out-of-plane motion. In reference to the critical findings from the study of the prior art in positioning stages in Section 1.3.2, our microrobot incorporates a microneedle onto a central microstage and achieves a 3D motion without having a complicated design or being bulky in size.

- A new type of actuator, namely 3SA microrobot is further designed that can also achieve 3D motion of the microneedle. Nonetheless, in this design, the actuator sides are arranged at an angle of 120^0 to each other in comparison to the orthogonal arrangement in the 4SA microrobot. A review of the prior art in Section 1.3.2 reveals that none of the positioning systems have been able to achieve a design such as ours.
- A new type of parallel architecture is proposed consisting of arrays of microrobots each capable of individual 3D motion of the microneedles. Such a parallel architecture that can achieve such independent control of the microneedles is non-existent as evident from the review in Section 1.3.2. There are a few parallel architecture systems with integrated microneedles such as in the cases of IBM Zurich's millipede technology [12], EPFL's parallel AFM imaging [13, 14], TU Ilmenau's scanning proximal probes [15, 16], University of Twente's cantilever arrays [17] and TU Delft's piezo-thermal probe array [18]. Nonetheless, all of these systems are primarily for scanning probe microscopy and have 1D independent actuation of the probes.
- We conceptualise the design to have an estimate of a range of dimensions for further analytical and finite element analyses. The design conceptualisation reveals that the cross-section area of the beams must not be greater than 50 μm^2 and the aspect ratio not greater than 0.5 for optimal tradeoff between bending and integration of multiple actuators in a parallel architecture.

BIBLIOGRAPHY

[1] D. S. Goodsell, *The Machinery of Life*, 1st ed.: Springer-Verlag, 1998.

[2] R. Milo, P. Jorgensen and M. Springer, "The database of useful biological numbers," *Nucleic Acids Research,* vol. 38, pp. 750-753, 2010.

[3] C.P. Wong, KS. Moon and Y. Li, *Nano-Bio- Electronic, Photonic and MEMS Packaging*: Springer, 2010.

[4] T. R. Gregory, *The evolution of the genome*, 1st ed.: Elsevier Academic Press, 2005.

[5] A.G. Fowler, A.N. Laskovski, A.C. Hammond and S.O.R. Moheimani, "A 2-DOF electrostatically actuated MEMS nanopositioner for on-chip AFM," *Journal of Microeletromechanical Systems,* vol. 21, pp. 771-773, 2012.

[6] Y. Sun et al., "A high-aspect-ratio two-axis electrostatic microactuator with extended travel range," *Sensors and Actuators A: Physical,* vol. 102, pp. 49-60, 2002.

[7] R Legtenberg, AW Groeneveld and M Elwenspoek, "Comb-drive actuators for large displacements " *Journal of Micromechanics and Microengineering,* vol. 6, pp. 320-329, 1996.

[8] J. Dong and P. M. Ferreira, "Electrostatically actuated cantilever with SOI-MEMS parallel kinematic XY stage," *Journal of microelectromechanical systems,* vol. 18, p. 641, 2009.

[9] S. Polit and J. Dong, "Development of a high-bandwidth xy nanopositioning stage for high-rate micro-/nanomanufacturing," *IEEE/ASME Transactions on Mechatronics,* vol. 16, pp. 724-733, 2011.

[10] R. C. Hibbeler, *Mechanics of Materials* 8ed.: Prentice Hall, 2010.

[11] G. Fedder, "Simulation of Microelectromechanical Systems," PhD, Electrical Engineering and Computer Sciences, Massachusetts Institute of Technology, Cambridge, 1994.

[12] P. Vettiger, G. Cross, M. Despont, U. Drechsler, U. Durig, B. Gotsmann, W. Haberle, M.A. Lantz, H.E. Rothuizen and R. Stutz, "The" millipede"-nanotechnology entering data storage," *IEEE Transactions on nanotechnology,* vol. 1, pp. 39-55, 2002.

[13] L. Sache, H. Kawakatsu, Y. Emery and H. Bleuler, "Massively parallel atomic force microscope with digital holographic readout," *Journal of Physics: Conference Series,* vol. 61, pp. 668-672, 2007.

[14] F. Loizeau, "Two-dimensional cantilever array with varying spring constants and tip radii for life-science applications," *Micro & Nano Letters,* vol. 7, pp. 301-305, 2012.

[15] K. Ivanova, Y. Sarov, Tzv. Ivanov, A. Frank, J. Zollner, Ch. Bitterlich, U. Wenzel, B.E. Volland, S. Klett, I.W. Rangelow, P. Zaweirucha, M. Zielony, T. Gotszalk, D. Dontov, W. Schott, N. Nikolov, M. Zier, B. Schmidt, W. Engl, T. Sulzbach and I. Kostic, "Scanning proximal probes for parallel imaging and lithography," *J. Vac. Sci. Technol. B,* vol. 26, pp. 2367-2373, 2008.

[16] Y. Sarov, T. Ivanov, A. Frank and I.W. Rangelow, "Thermal driven multi-layer actuator for 2D cantilever arrays," *Appl Phys A,* vol. 102, pp. 61-68, 2011.

[17] W.W. Koelmans et al., "Cantilever arrays with self-aligned nanotips of uniform height," *Nanotechnology,* vol. 23, p. 135301, 2012.

[18] A. Gaitas and P. French, "Piezo-thermal probe array for high throughput applications," *Sensors and Actuators A: Physical,* vol. 186, pp. 125-129, 2012.

Chapter 3: Performance Analysis of the Behaviour of 4SA Microrobot

3.1 Introduction and Background[1]

In the previous chapter, the design dimensions of the beam components of the microrobot have been investigated and conceptualised. This chapter discusses in detail the analytical model and FEA simulations developed to analyse the motion performance of the 4SA microrobot based on these dimensions. The analyses of the 3SA microrobot have been dealt separately in Chapter 6. The analytical model for the simplified geometry of the microrobot is based on elastic stiffness and grid-stiffness matrix approaches [1]. Detailed finite element analyses (FEA) using ANSYS *v13.0/14.5* have been performed for the complex geometry of the microrobot to analyse the behaviour of the beam components. The analytical and FEA models have been validated against each other and later with the experimental test results in Chapter 5 thus proving the accuracy of our model. The critical motion performance criterion is to achieve maximum 3D motion of the microneedle at the minimum voltage possible, within the yield stress of silicon, *7000* MPa.

While a number of major works in positioning stages have been reviewed in section 1.3.2, this section discusses further some more recent important works over the last decade specifically focused on the design and performance of these stages. A 2D *xy* MEMS stage has been reported that uses a parallel kinematics mechanism (PKM) for its design [2]. This stage (end-effector) actuated by electrostatic forces can provide an actuation motion range of around *16* μm at a driving voltage of *45* V. The design dimensions include comb actuator design with *150* pair fingers with a *3* μm finger gap and thickness of *50* μm, with folded

[1] Elements of the following chapter have been published/ presented in conferences C1, C3 and C5 or in preparation for journal(s) J1.

spring beam lengths extending as high as *1.8* mm. An advanced design of the stage, shown in Figure 3.1a is reported by the same group that can achieve an out-of-plane motion of *7* μm at a driving voltage of *4.5* V along with the in-plane actuation [3]. The same group has developed a 3D truss-like PKM nanopositioning stage structure, shown in Figure 3.1b that can produce in-plane *xy* actuation of *18* μm and angular θ actuation of 1.72^0 at a driving voltage of *85* V [4]. Unlike in their previous work [2, 3], where the end-effector is connected to a parallelogram four-bar linkage arranged in an orthogonal fashion, this new design consists of three in-parallel identical kinematic chains arranged in a triangular fashion forming an angle of 120^0 with each other. This design is however different to the design of our 3SA microrobot. The torsion bar connected to the end effector consists of the cantilever that provides the rotary compliance of the cantilever structure that enables its out-of-plane motion. Such analytical model has also been used to design another high-bandwidth piezo-driven parallel kinematic 2D nanopositioning stage [5]. Each of the two axes in the monolithic stage design is composed of a decoupling with compliant beams and circular flexure hinges. A *6* by *6* Jacobian matrix has also been used to kinematically model a flexure-based, 6D hexapod nanopositioner [6]. This macro-scale nanopositioner similar to the one discussed in Section 1.3.2, Figure 1.21 consist of base stages, six struts and a top platform.

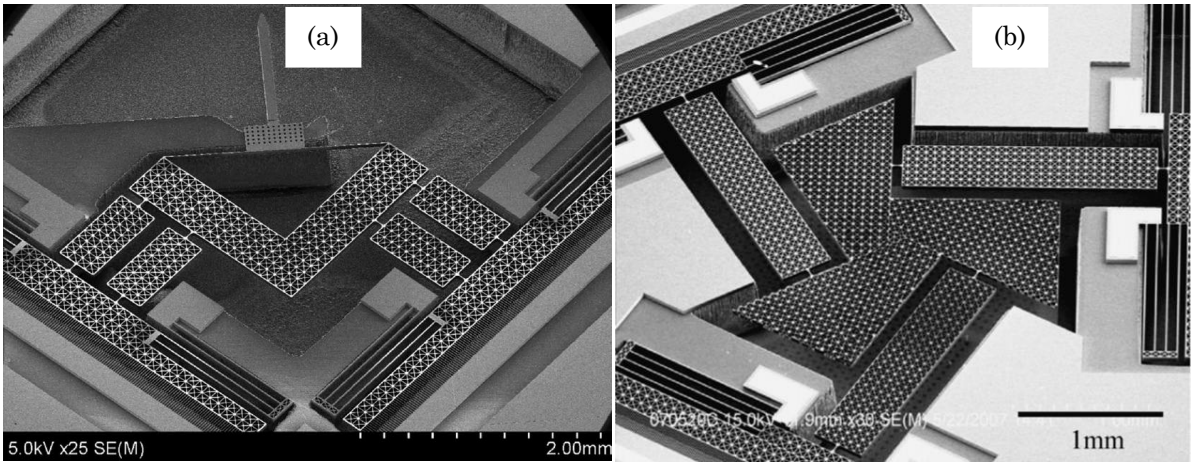

Figure 3.1 SEM image of the (a) 2D parallel kinematic *xy* stage [3]. (b) 3D planar nanopositioning stage [4].

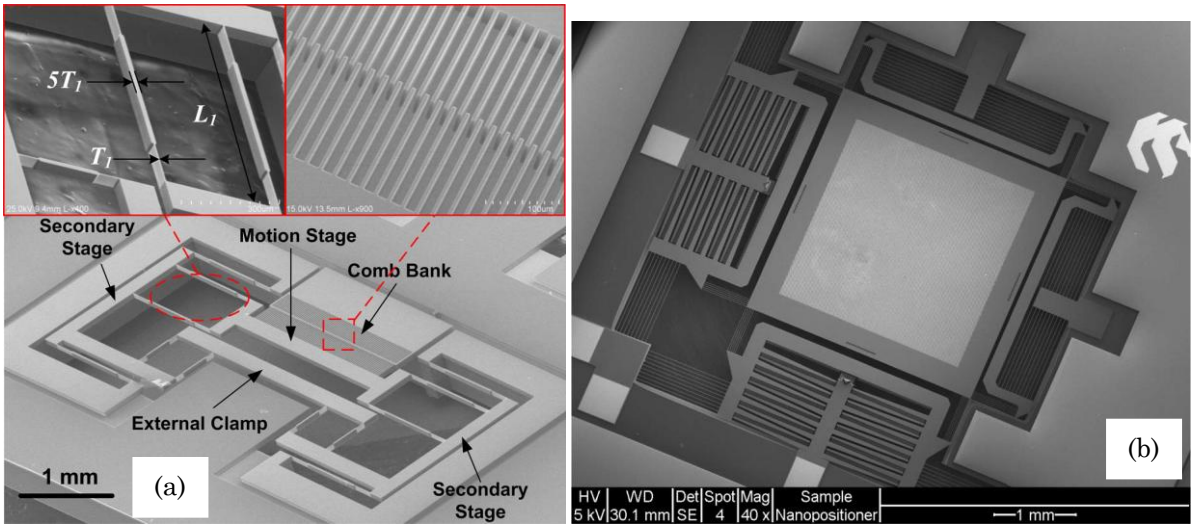

Figure 3.2 SEM image of the (a) comb-drive actuator employing the C-DP-DP flexure [7] (b) 2D nanopositioner [8].

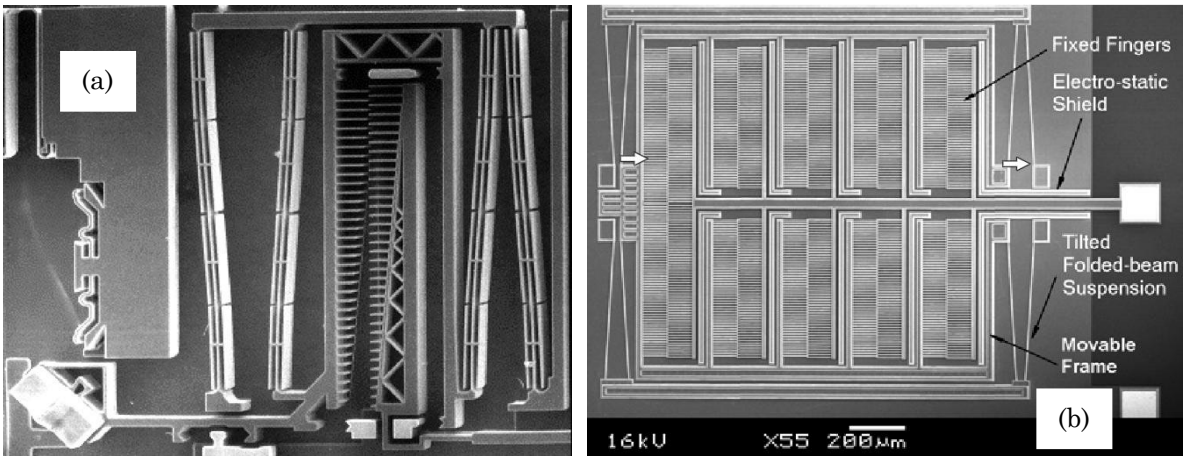

Figure 3.3 SEM image of the comb-drive actuator with (a) linearly engaging comb teeth and a prebent suspension [9]. (b) Tilted folded-beam suspension [10].

Some other more recent works on in-plane electrostatic actuated stages include the works of Olfatnia et al [7] and Fowler et al [8]. Using a clamped paired double parallelogram (C-DP-DP) flexure mechanism, shown in Figure 3.2a, Olfatnia et al [7] achieved a large actuation of *245* µm at *120* V. The design dimensions include flexure beam length of *1* mm and a comb-finger gap ranging from *4* µm to *6* µm. The advantage of this system is the arrangement of the kinematic linkages which results in a high stiffness ratio resulting in a

large displacement. Another interesting 2D stage, shown in Figure 3.2b is developed by Fowler et al [8], wherein the large central positioning stage *3* mm×*3* mm in size is connected to the electrostatic actuators using multiple parallel thin beam springs concentrated close to the corners of the stage. This reduces the moment of inertia of the stage which thereby prevents rotational oscillations of the stage. This nanopositioner, used as the scanning stage of a commercial AFM can achieve an actuation of *16* μm at *45* V.

Some other interesting designs of comb-actuators include work done by Jensen at al [11] and Harouche and Shafai [12]. In the former, instead of using fingers with rectangular profile, researchers have designed shaped comb-fingers with linear/cubic force profiles to be used as tunable resonators, thus allowing them to operate over a wide range of spring stiffness. In the later [12], researchers have used FEM to simulate different types of jagged shaped comb actuators operating under dc voltage. They have modelled the behavior analytically using Arbitrary Lagrangian-Euler (ALE) formulation.

Grade et al [9] designed various forms of comb-drive actuators by modifying the folded-flexure beams and comb-actuators, shown in Figure 3.3a. For example, one design consists of comb-drive actuators with a U-shaped shuttle and only two folded-suspension beams. In another design, they have achieved larger motion by using linearly engaging teeth and a pre-bent suspension as shown in Figure 3.3a. This improves the suspension stiffness ratio and reduces the side instability by a factor of *30*. They achieve an in-plane actuation of *110* μm at *150* V for comb-finger gaps varying from *6.5* μm to *8.5* μm and suspension lengths from *600* μm to *1100* μm. In another tilted folded-beam suspension study, shown in Figure 3.3b [10], the researchers improve the stability of the comb-drive actuator and travel range without compromising the performance. Another clever design modification [13] has allowed researchers to overcome the *pull-in instability* travel range. Electrostatic comb micro-actuators can allow the actuation to approximately one-third of the total gap between comb-

fingers before pull-in of the fingers occur and short-circuit the system, irrespective of stiffness and mass. Nonetheless, using non-linear model inversion position tracking control, Piyabongkarn et al [13] have been able to stabilise the actuator and achieve travel almost over the entire available gap between comb-fingers, i.e. travelling *4* μm over a *4.5* μm full range.

A different version of NIST's nanopositioner discussed in Section 1.3.2, having 1D motion capability has been dynamically modeled using a Lagrangian approach for interstellar beam steering applications [14, 15]. The design consists of a flexure hinge mechanism, a piezoelectric actuator and a spherical flexure hinge coupler between the actuator and the flexure hinge mechanism. Analysis and design tools for parallel mechanisms containing flexure joints (only lumped approximation is considered) in the nanopositioner based on pseudo-rigid-body model has also been presented [16, 17]. The static performance measures such as task space stiffness and manipulability, while subject to constraints such as joint stress, mechanism size, workspace volume and dynamic characteristics has been considered. The motion and compliance consideration has been balanced based on these performance measures and constraints through a multi-objective optimisation. A modified version of this nanopositioner designed as a nested structure based on serial kinematic mechanism (SKM) is used for multifinger manipulation [18]. The in-plane behaviour has been analytically modeled based on stiffness equations and the results are corroborated with FEA electrical, structural and thermal analyses. The actuator is able to achieve more than *50* μm in-plane motion with minimal coupling.

In a different design of a thermal actuator, researchers have addressed the design and optimisation of the actuator for its use in MEMS-based material testing system for measuring the mechanical properties of thin films, CNTs and nanowires [19, 20]. The actuator is capable of producing tens of millinewton force and a few microns displacement in-plane. The actuator has chevron V-shaped beams anchored at both ends, a capacitive load sensor with a

specimen in between. The analytical modeling is based on an elastic stiffness matrix approach similar to ours. The analytical and the electrothermal multiphysics FEA results are in close proximity to each other. Nonetheless unlike ours, where element stiffness matrices have been computed for all the elements in the microrobotic structure, for this work, the model has been simplified by computing element stiffness matrix for only one element.

Thus the critical finding from the review of the positioning stages in this section reveal that although different designs have been modeled using interesting mathematics, none of these models take into consideration the effect of translation, torsion, bending and shear stress on the beam components of the microrobot like our model do. Our grid stiffness matrix model treats the structure more holistically compared to other models discussed above.

3.2 Analytical modeling of the 4SA microrobot

Analysis of the electrostatic actuator requires a coupled electric and mechanical investigation. In this section, the mechanical behaviour is investigated by analytically deriving the effective stiffness of the actuator on the basis of the following assumptions: longitudinal stretching of the tethering beams is negligible, as made evident in Section 2.3 through Figures 2.9 and 2.14; small torsional rotation about the *x* and *y* axes and bending rotation about the *z* axis are considered during out-of-plane actuation; stiffness in one direction is not significantly affected by the structural deformations along other directions; and any effect of axial displacement is ignored during out-of-plane actuation.

3.2.1 In-plane elastic stiffness model of the 4SA microrobot

We will first discuss the in-plane analytical elastic stiffness model of the 4SA microrobot followed by a grid stiffness matrix model in the following section. The nodes *A*, *B*, *C* and *D* in Figure 3.4 represent the individual sides consisting of the comb actuators which are

connected to the stage, node *E*, via springs. Each of the springs in the schematic represents two pair of spring beams connected in parallel for every side.

For a driving voltage *V*, the electrostatic force, F_e generated by the comb drive actuator, shown in Figure 3.5, between the movable and fixed fingers is given by [21], where $i =$ number of actuation comb-finger pairs, $\varepsilon =$ permittivity of air $8.85\times10^{-12} C^2 N^{-1} m^{-2}$,

$$F_e = \frac{1}{2}\frac{i\varepsilon t_f}{g s_f} V^2 \tag{3.1}$$

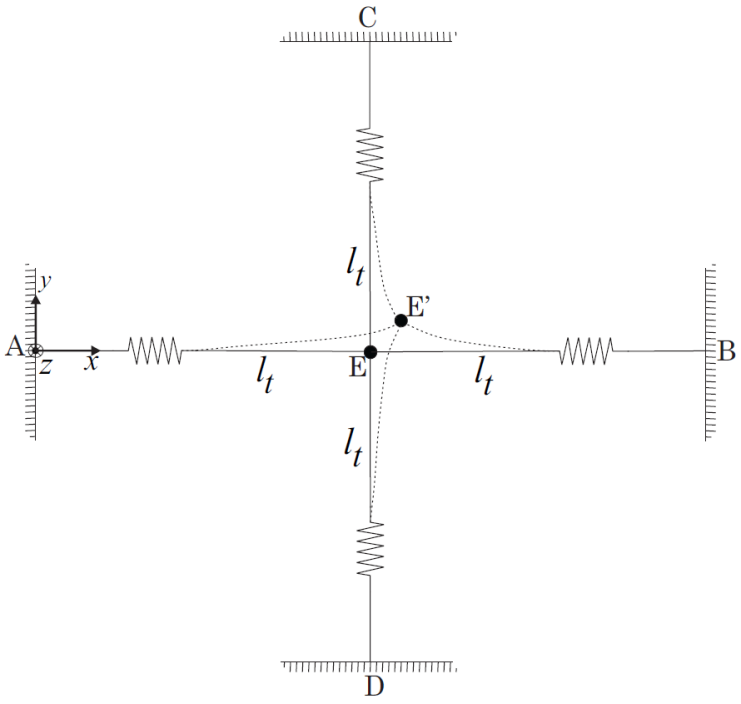

Figure 3.4 Schematic of the 4SA microrobot for analysing the in-plane actuation.

Figure 3.5 Comb-finger electrodes.

t_f =thickness of comb finger, V = actuation voltage and gs_f is the gap spacing between the adjacent comb fingers.

Nonetheless, apart from the electrostatic force in the *x*-axis, there is also perpendicular electrostatic force acting along the *y*-axis, generating a lateral pull on both the movable and fixed fingers. Assuming that the movable finger structure moves by a small displacement *y* along the *y*-axis, the net electrostatic force F_{el} in the lateral direction generated by both sides of the movable fingers [10],

$$F_{el} = \frac{1}{2}\left[\frac{i\varepsilon t_f (m_o + \delta_x)}{(gs_f - y)^2} - \frac{i\varepsilon t_f (m_o + \delta_x)}{(gs_f + y)^2}\right]V^2 \tag{3.2}$$

where δ_x is the comb finger displacement in the *x*-axis and is given by,

$$\delta_x = \pm\frac{F_e}{K_{x,y}} = \pm\frac{1}{2}\frac{i\varepsilon t_f}{gs_f K_{x,y}}V^2 \tag{3.3}$$

It is evident that the net lateral electrostatic force F_{el} generated by both sides of the movable fingers, will push them off the equilibrium position instead of pulling them back to the original position, which works like a *negative spring*. The moving electrode pairs will be unstable without the mechanical restoring force in the *y*-direction.

The equivalent *negative* spring constant k_n is [22],

$$k_n = \left.\frac{\partial F_{el}}{\partial y}\right|_{y=0} = \frac{2i\varepsilon t_f \left(m_o + \delta_x\right)}{gs_f{}^3}V^2 \tag{3.4}$$

For stability of the comb-drive actuator without the motion being compromised due to lateral deflection, the following relation needs to be satisfied,

$$k_l > k_n \tag{3.5}$$

where k_l is the lateral spring constant.

Substituting Equation (3.3) in Equation (3.4), the equivalent negative spring constant as a function of in-plane spring stiffness is,

$$k_n = \frac{2K_{x,y}(m_o + \delta_x)\delta_x}{gs_f{}^2} \tag{3.6}$$

Thus, from Equations (3.5) and (3.6), the maximum static displacement in the direction of motion without motion compromise due to lateral electrostatic deflection,

$$\delta_x^{\max} = \frac{1}{2}\sqrt{m_o{}^2 + 2\frac{k_l}{K_{x,y}}gs_f^2} - \frac{m_o}{2} \tag{3.7}$$

Equation (3.7) is critical for maintaining the stability of the actuator during in-plane motion. Since the springs on each sides are connected in parallel, the effective in-plane axial spring constant in the direction of motion as derived from the beam deflection theory [21] is,

$$K_{x,y} = 4k_s + k_t = 4\left(\frac{2Eh_s w_s^3}{l_s^3}\right) + \left(\frac{2Eh_t w_t^3}{l_t^3}\right) \tag{3.8}$$

where k_s = in-plane axial stiffness of the spring flexure beam, k_t = in-plane axial stiffness of the tethering beam, E = Young's modulus of silicon *129.5* GPa, h_s, w_s, l_s are the height, width and length of the spring flexure beams respectively, and h_t, w_t, l_t are height, width and length of the tethering beams respectively.

And the effective lateral spring constant perpendicular to the direction of motion is,

$$k_l = 4\left(\frac{2Eh_s w_s}{l_s}\right) \tag{3.9}$$

From Equations (3.8) and (3.9), the stiffness ratio between axial and lateral stiffness of the spring and tethering beam system is,

$$\frac{K_{x,y}}{k_l} = \frac{4\left(\frac{2Eh_s w_s^3}{l_s^3}\right)+\left(\frac{2Eh_t w_t^3}{l_t^3}\right)}{4\left(\frac{2Eh_s w_s}{l_s}\right)} = \frac{4\left[h_s\left(\frac{w_s}{l_s}\right)^3\right]+\left[h_t\left(\frac{w_t}{l_t}\right)^3\right]}{4\left[h_s\left(\frac{w_s}{l_s}\right)\right]} \tag{3.10}$$

Thus, the in-plane pull-pull static displacement $U_{x,y}$ is given by,

$$F_e = 8F_{act} = \pm K_{x,y}U_{x,y} \tag{3.11}$$

where F_{act} is the electrostatic force from the individual comb-finger actuators.

$$\therefore U_{x,y} = \pm\frac{F_e}{K_{x,y}} = \pm\frac{F_e}{4\left(\frac{2Eh_s w_s^3}{l_s^3}\right)+\left(\frac{2Eh_t w_t^3}{l_t^3}\right)} = \pm 2\frac{i\varepsilon t_f}{gs_f E\left[4h_s\left(\frac{w_s}{l_s}\right)^3 + h_t\left(\frac{w_t}{l_t}\right)^3\right]}V^2 \tag{3.12}$$

This in-plane displacement of the microstage caused by the pull-pull mode of the comb-drive actuators represents the maximum motion achievable at particular voltages.

3.2.2 In-plane grid-stiffness model of the 4SA microrobot

In addition to the elastic stiffness model discussed in the section above, we have also developed a grid-stiffness matrix [1] to evaluate the motion performance of the microrobot. Figure 3.6 shows the schematic of the actuator with the nodes and elements. To compute the in-plane displacement of the node *9* (from E to E') because of electrostatic force F_e, due to an electric field when voltage V is applied to the comb-drive actuators such as at node C, we

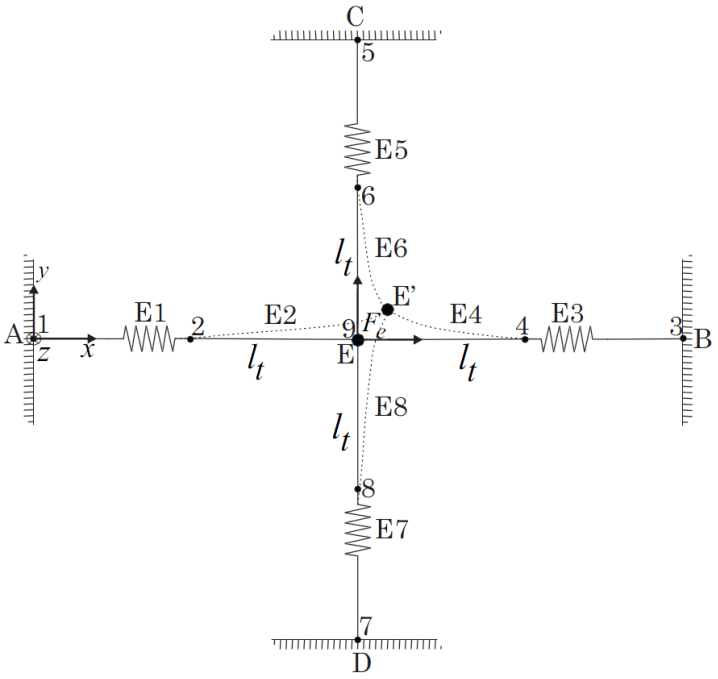

Figure 3.6 Schematic of the 4SA microrobot for analysing the in-plane actuation using grid-stiffness matrix model.

form an equivalent grid stiffness matrix of the tethering and spring flexure beams. The schematic of the microrobot is divided into nine nodes, *1* to *9* and eight elements *E1* to *E8*, each corresponding to a beam structure, as shown in Figure 3.6. Every spring represents two pairs of spring flexure beams which have been condensed into a single element. Dividing the model into larger number of nodes and elements can lead to greater precision of the results while compromising the simplicity of the current approach.

The element stiffness, $[k]_2, [k]_4, [k]_6, [k]_8$, of the tethering beam elements *E2, E4, E6* and *E8* inclined at an angle of 90^0 to each other is given by [19],

$$[k]_2, [k]_4, [k]_6, [k]_8 = \frac{12EI}{l_t^3}\begin{bmatrix} s^2 & -cs & -s^2 & cs \\ -cs & c^2 & cs & -c^2 \\ -s^2 & cs & -s^2 & -cs \\ cs & -c^2 & -cs & c^2 \end{bmatrix} \tag{3.13}$$

Similarly, the element stiffness $[k]_1, [k]_3, [k]_5, [k]_7$ of the spring flexure beam elements *E1*,

E3, *E5* and *E7* is given by,

$$[k]_1,[k]_3,[k]_5,[k]_7 = \frac{8Eh_s w^3}{l_s^3}\begin{bmatrix} c^2 & cs & -c^2 & -cs \\ cs & s^2 & -cs & -s^2 \\ -c^2 & -cs & -c^2 & cs \\ -cs & -s^2 & cs & s^2 \end{bmatrix} \tag{3.14}$$

where $c = \cos\theta_n$ and $s = \sin\theta_n$, and the subscripts indicate the corresponding element number. *I* is the second moment of inertia of the beam.

After adding the terms of the individual element stiffness matrices into their corresponding locations in the global stiffness matrix $[K]$, the total *21×21* stiffness matrix is,

$$[K]_{eq} = \underbrace{\frac{8Ehw^3}{l_s^3}\begin{bmatrix} c^2 & cs & -c^2 & -cs \\ cs & s^2 & -cs & -s^2 \\ -c^2 & -cs & -c^2 & cs \\ -cs & -s^2 & cs & s^2 \end{bmatrix} + [k]_3 + [k]_5 + [k]_7}_{Spring} + \underbrace{\frac{12EI}{l_t^3}\begin{bmatrix} s^2 & -cs & -s^2 & cs \\ -cs & c^2 & cs & -c^2 \\ -s^2 & cs & -s^2 & -cs \\ cs & -c^2 & -cs & c^2 \end{bmatrix} + [k]_2 + [k]_4 + [k]_6}_{Tethering} \tag{3.15}$$

Each *4×4* matrix of Equation (3.15) when added and assembled would generate the appropriate *21×21* stiffness matrix on the left hand side. Therefore the two sides are equivalent to each other and not equal due to the different orders of matrix of both sides before assembly.

Thus, writing the total structure stiffness equation accounting for the applied electrostatic force on nodes *9* and *5* and force and displacement boundary constraints at the other nodes,

$$\begin{bmatrix} F_{1x} \\ F_{1y} \\ F_{2x} \\ F_{2y} \\ F_{3x} \\ F_{3y} \\ F_{4x} \\ F_{4y} \\ F_{5x} = F_e \\ F_{5y} \\ F_{6x} \\ F_{6y} \\ F_{7x} \\ F_{7y} \\ F_{8x} \\ F_{8y} \\ F_{9x} \\ F_{9y} = F_e \end{bmatrix} = [K]_{21\times 21} \begin{bmatrix} U_{1x} \\ U_{1y} \\ U_{2x} \\ U_{2y} \\ U_{3x} \\ U_{3y} \\ U_{4x} \\ U_{4y} \\ U_{5x} = U_e \\ U_{5y} \\ U_{6x} \\ U_{6y} \\ U_{7x} \\ U_{7y} \\ U_{8x} \\ U_{8y} \\ U_{9x} \\ U_{9y} = U_e \end{bmatrix} \tag{3.16}$$

Thus, the final displacement can be found by solving (3.16),

$$\therefore [U_y] = [K^{-1}]_{21\times 21} [F_e] \tag{3.17}$$

where $[F_e]$ can be derived from Equation (3.1).

3.2.3 Out-of-plane grid-stiffness model of the 4SA microrobot

The out-of-plane motion of the 4SA microrobot has been analysed using a grid stiffness matrix model. A grid is a structure on which loads are applied perpendicular to the plane of the structure. The elements of the grid structure of the 4SA microrobot as shown in Figure 3.7 are assumed to be rigidly connected as also evident from Section 2.3, so that the original angles between them remain constant. This leads to torsional and bending moment continuity at the nodal points of the grid. For the 4SA microrobot design, there are nine nodes, one each for the comb-drive actuator and spring flexure beam arrangement, one each for the tethering beams and one for the microstage-microneedle structure. There are eight elements, *E1* to *E8*,

connecting these nodes and the electrostatic force acts on the ninth node that deflects it along the *z*-axis.

The degrees of freedom at each node are a vertical deflection d_{iz} (perpendicular to the grid) about the *z*-axis, a torsional rotation ϕ_{ix} about the *x*-axis, and a bending rotation ϕ_{iy} about the *y*-axis. The nodal forces include a transverse force f_{iz} about the *z*-axis, a torsional moment m_{ix} about the *x*-axis, and a bending moment m_{iy} about the *y*-axis. The effect of axial displacement is ignored, i.e. $d_{ix} = 0$. Thus the grid elements do not resist axial loading, i.e. $f_{ix} = 0$.

Thus, the local stiffness matrix equation for a grid element joining nodes *i* and *j* [1] is,

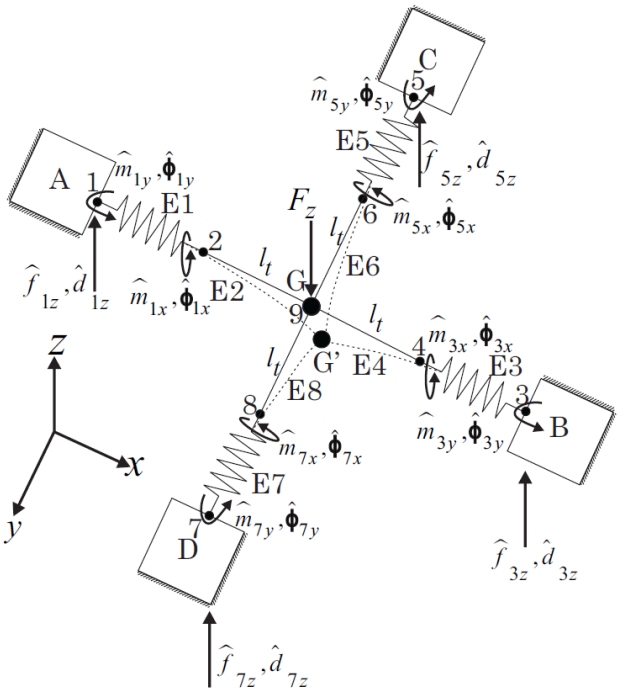

Figure 3.7 Schematic of the 4SA microrobot with forces, moments and displacements for analysing the out-of-plane motion using grid stiffness matrix model.

$$\begin{Bmatrix} f_{iz} \\ m_{ix} \\ m_{iy} \\ f_{jz} \\ m_{jx} \\ m_{jy} \end{Bmatrix} = \begin{bmatrix} \frac{12EI}{l_t^3} & 0 & \frac{6EI}{l_t^2} & -\frac{12EI}{l_t^3} & 0 & \frac{6EI}{l_t^2} \\ 0 & \frac{GJ}{l_t} & 0 & 0 & -\frac{GJ}{l_t} & 0 \\ \frac{6EI}{l_t^2} & 0 & \frac{4EI}{l_t} & -\frac{6EI}{l_t^2} & 0 & \frac{2EI}{l_t} \\ -\frac{12EI}{l_t^3} & 0 & -\frac{6EI}{l_t^2} & \frac{12EI}{l_t^3} & 0 & -\frac{6EI}{l_t^2} \\ 0 & -\frac{GJ}{l_t} & 0 & 0 & \frac{GJ}{l_t} & 0 \\ \frac{6EI}{l_t^2} & 0 & \frac{2EI}{l_t} & -\frac{6EI}{l_t^2} & 0 & \frac{4EI}{l_t} \end{bmatrix} \begin{Bmatrix} u_{iz} \\ \phi_{ix} \\ \phi_{iy} \\ u_{jz} \\ \phi_{jx} \\ \phi_{jy} \end{Bmatrix} \tag{3.20}$$

where $[k]_m$ for a grid element represents the local stiffness matrix where *m* is the number of the grid element.

The shear modulus of rigidity G is given by,

$$G = E/2(1+\rho) \tag{3.21}$$

where ρ is the poison's ratio of silicon *0.28*.

The torsional constant for the rectangular cross-section of the tethering beam is,

$$J = w_t h_t^3 \left(\frac{1}{3} - 0.21 \frac{h_t}{w_t} \left(1 - \frac{h_t^4}{12 w_t^4} \right) \right) \tag{3.22}$$

The elements which are not in local coordinates have to be transformed into global coordinates to be included into the total stiffness matrix. The transformation matrix relating local to global degrees of freedom for a grid is given by,

$$[T_G] = \begin{bmatrix} 1 & 0 & 0 & 0 & 0 & 0 \\ 0 & C & S & 0 & 0 & 0 \\ 0 & -S & C & 0 & 0 & 0 \\ 0 & 0 & 0 & 1 & 0 & 0 \\ 0 & 0 & 0 & 0 & C & S \\ 0 & 0 & 0 & 0 & -S & C \end{bmatrix} \tag{3.23}$$

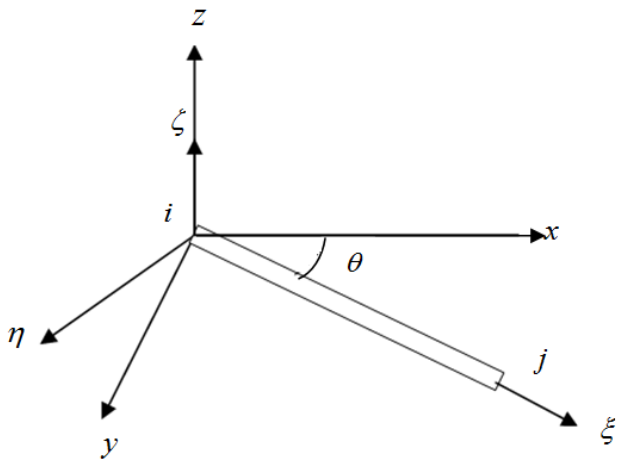

Figure 3.8 Grid element arbitrarily oriented in the *x*-*y* plane.

where θ is positive, taken anti-clockwise from ξ to x in the $x-y$ plane as shown in Figure 3.8. Thus,

$$C = \cos\theta = \frac{x_j - x_i}{L} \text{ and } S = \sin\theta = \frac{y_j - y_i}{L} \tag{3.24}$$

where L is the length of the element from node i to node j. And as evident from Equation (3.23), the vertical deflection d_z is invariant with respect to a coordinate transformation, i.e. $z = \zeta$.

Thus, the global stiffness matrix for a grid element arbitrarily oriented in the $x-y$ plane is,

$$[K_G] = \left[T_G^T\right][k]_m[T_G] \tag{3.25}$$

Equation (3.20) can be re-written for each individual grid element as,

$$
\begin{aligned}
&[f]_m \equiv [k]_m [u]_m \\
&\Rightarrow \begin{Bmatrix} f_i \\ f_j \end{Bmatrix} \equiv \begin{bmatrix} {k_{ii}}^m & {k_{ij}}^m \\ {k_{ji}}^m & {k_{jj}}^m \end{bmatrix} \begin{Bmatrix} u_i \\ u_j \end{Bmatrix} \\
&\Rightarrow \begin{Bmatrix} f_{iy} \\ m_{ix} \\ m_{iz} \\ f_{jy} \\ m_{jx} \\ m_{jz} \end{Bmatrix} \equiv \begin{bmatrix} & & \\ k_{ii}^m & & k_{ij}^m \\ & & \\ & & \\ k_{ji}^m & & k_{jj}^m \\ & & \end{bmatrix}_{6\times 6} \begin{Bmatrix} u_{iy} \\ \phi_{ix} \\ \phi_{iz} \\ u_{jy} \\ \phi_{jx} \\ \phi_{jz} \end{Bmatrix}
\end{aligned} \tag{3.26}
$$

where *i, j* denotes the nodes, *1* to *9*.

Combining all the grid element stiffness matrix equations obtained in Equation (3.26), the final connectivity matrix becomes,

$$[F_i] = \sum [k_{ii}][U_i]$$

$$
\begin{Bmatrix} F_i \\ F_{i+1} \\ F_{i+2} \\ .... \\ .... \\ .... \\ .... \\ .... \\ F_j \end{Bmatrix} = \begin{bmatrix} k_{i,i}^m & k_{i,i+1}^m & k_{i,i+2}^m & .... & .... & .... & .... & .... & k_{i,j}^m \\ k_{i+1,i}^m & k_{i+1,i+1}^m & k_{i+1,i+2}^m & .... & .... & .... & .... & .... & k_{i+1,j}^m \\ k_{i+2,i}^m & k_{i+2,i+1}^m & k_{i+2,i+1}^m & .... & .... & .... & .... & .... & k_{i+2,j}^m \\ .... & .... & .... & .... & .... & .... & .... & .... & .... \\ .... & .... & .... & .... & .... & .... & .... & .... & .... \\ .... & .... & .... & .... & .... & .... & .... & .... & .... \\ .... & .... & .... & .... & .... & .... & .... & .... & .... \\ .... & .... & .... & .... & .... & .... & .... & .... & .... \\ k_{j,i}^m & k_{j,i+1}^m & k_{j,i+2}^m & .... & .... & .... & .... & .... & k_{j,j}^m \end{bmatrix}_{27\times 27} \begin{Bmatrix} U_i \\ U_{i+1} \\ U_{i+2} \\ .... \\ .... \\ .... \\ .... \\ .... \\ U_j \end{Bmatrix} \tag{3.27}
$$

Thus, the final connectivity stiffness matrix equation is,

$$
\begin{Bmatrix} F_{iz} \\ M_{ix} \\ M_{iy} \\ .... \\ F_{jz} \\ M_{jx} \\ M_{jy} \end{Bmatrix}_{27\times 27} = [K]_{27\times 27} \begin{Bmatrix} U_{iz} \\ \phi_{ix} \\ \phi_{iy} \\ .... \\ U_{jz} \\ \phi_{jx} \\ \phi_{jy} \end{Bmatrix}_{27\times 27} \tag{3.28}
$$

Equation (3.28) can be further decomposed depending on the nodes that are fixed and have zero displacement. Since only the vertical out-of-plane displacement of the microneedle node is considered, the other nodes will have zero vertical displacement, torsional and bending moments. Thus, the vertical out-of-plane displacement is,

$$[U_z] = \left[K^{-1}\right]_{27\times 27}[F_z] \tag{3.29}$$

The results from this analytical modeling have been validated by the FEA simulation results discussed next, thus proving the accuracy of our model.

3.3 Finite element analysis of the 4SA microrobot

After analytically modeling the simplified geometry of the microrobot, we investigate the motion performance of the more complicated geometry using finite element analysis (FEA). While the analytical model is good at giving quick estimation of the motion range of the actuator for different actuation voltages, we have applied a more accurate model using FEA to validate the results from the analytical model. These results have eventually been validated against the experimental test results of the 4SA microrobot in Chapter 5, thus proving the accuracy of our models. It must be noted, however, that rather than deciding a potential candidate for modeling the system behaviour and concluding which model is superior, we use both analytical and FEA as complementary to each other. We look at both these results objectively and infer significant design insights to form a generalised understanding of the performance of the actuator under loading.

The simulations have been performed in ANSYS *v13.5*/*v14.0* to study the stiffness of the actuator design, effects of beam dimensions and shapes on the actuation performance, stress developed in the components of the actuator and natural frequency. The beam dimensions for performing the simulations have been derived from the results obtained from the generalised

design conceptualisation as discussed in Section 2.3 in Chapter 2. The simulations have been performed for different lengths and thicknesses of suspended actuator beam components and parallel-plate actuators. The 3D models generated in CAD softwares Solidworks *v2010*/*v2012* and CATIA *v5* are imported into ANSYS to perform the simulations. The simulations performed on a *32* GB RAM computer system have been divided into two phases:

a. Perform the in-plane and out-of-plane electrostatic simulation on comb-drive and parallel-plate actuators respectively to understand the behaviour of the in-plane and out-of-plane electrostatic force with voltage as shown in Figures 3.9 and 3.10.
b. Perform the in-plane and out-of-plane structural simulation on the suspended actuator grid by applying the electrostatic force values obtained from the first phase (a) as shown in Figure 3.18. These electrostatic force values are applied to solid rectangular beams of equivalent mass and density, approximated for comb-drive actuators to simplify the meshing and thus decrease the computation time. The parameters that have been studied include displacements for different values of applied DC voltage, stress developed in the structure and modal analysis to determine the natural frequencies and modal shapes.

Limitations in fabrication infrastructure of the 4SA microrobot have led to significant changes in actuator dimensions which have been discussed later in the subsequent sections. Thus the FEA results in the forthcoming sections have been presented for both designed and manufactured 4SA microrobot. Our definition of these two types of microrobots is as follows:

- Designed 4SA microrobot: It represents the original dimensions with which the microrobot has been designed. The microrobot is not fabricated using these dimensions, but this FEA study is critical for the design of the 3SA microrobot which has been dealt with in Chapter 3.

- Manufactured 4SA microrobot: It represents the dimensions with which the microrobot has been fabricated. A separate FEA study has been performed to re-design the dimensions so that they can be incorporated within the clean-room facility's specifications.

3.3.1 Electrostatics FEA of the 4SA microrobot

The in-plane electrostatic simulation of the comb-drive actuator is performed with element SOLID*123*. SOLID*123* is a 3D, *10*-node, charge-based electric element. It has one degree of freedom, voltage, at each node. This element is applicable to 3D electrostatic and time-harmonic quasistatic electric field analyses. The out-of-plane electrostatic simulation is performed with elements PLANE*121* (for the parallel plates) and SOLID*122* (for the air-gap volume). PLANE*121* is a 2D, *8*-node, charge-based electric element and has one degree of freedom, voltage, at each node [23].

This element is based on the electric scalar potential formulation, and it is applicable to 2D electrostatic and time-harmonic quasistatic electric field analyses. SOLID*122* is a 3D, *20*-node, charge-based electric element and has one degree of freedom, voltage, at each node. This element is applicable to 3D electrostatic and time-harmonic quasistatic electric field analyses. The in-plane motion due to the comb-drive actuators occurs due to the resulting electrostatic field pattern as shown in Figure 3.9c. The lateral electrostatic field lines cancel each other on the side of the moving fingers due to the fixed fingers. The field lines from the fixed fingers are converging toward the edge of the moving fingers resulting in the attractive force. For the out-of-plane actuation, the field lines are shown in Figures 3.10b and c. It is to be noted that under a DC potential difference (positive-negative/ positive-positive/ negative-positive/ negative-negative), a capacitor always experiences an attractive force between the plates or the fingers.

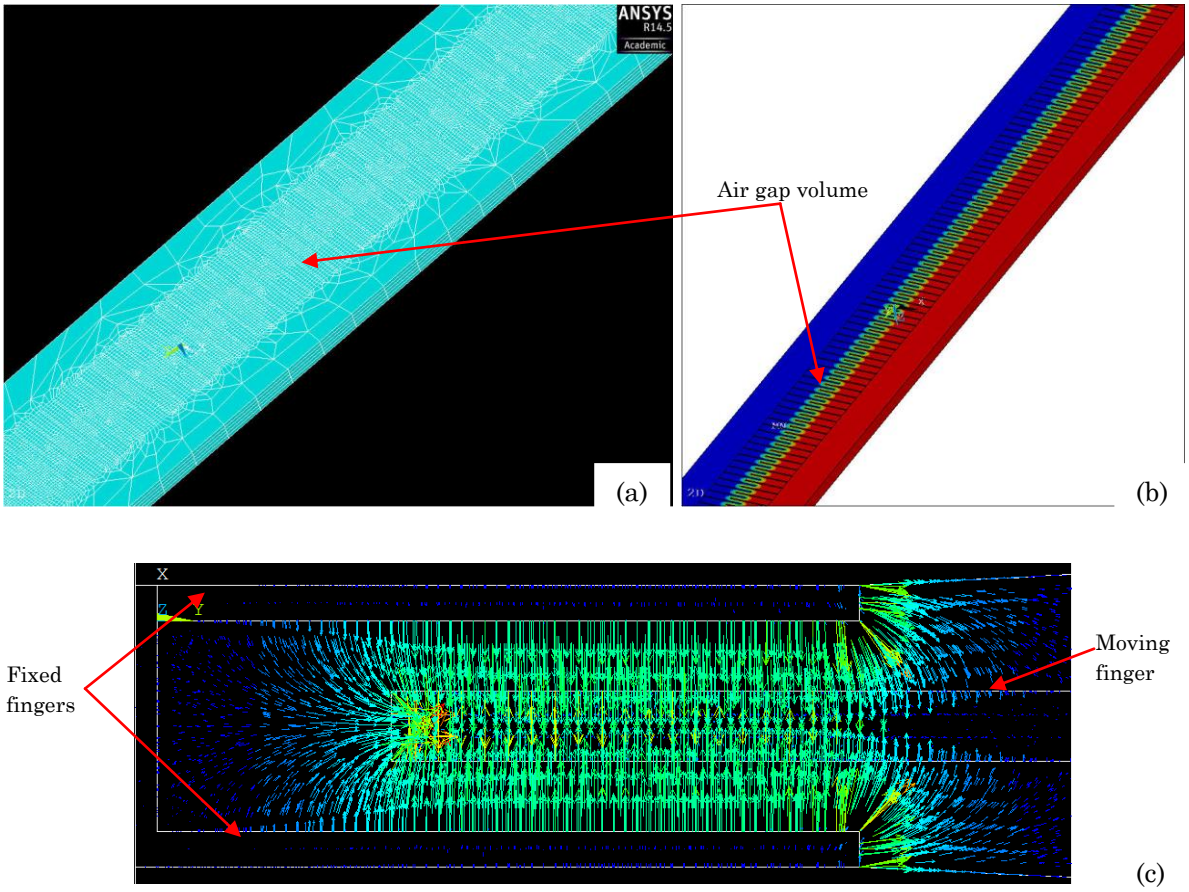

Figure 3.9 Comb-drive electrode in-plane actuation simulation (a) a meshed comb-finger electrode, meshed with element SOLID*123* (b) a solved electrode model for a potential difference of *100* V depicting the air-gap which was individually meshed as highlighted in (a) (c) Electric field lines across a pair of comb-fingers showing electric field lines cancelling each other on the sides of the finger and converging into the moving finger on the edge.

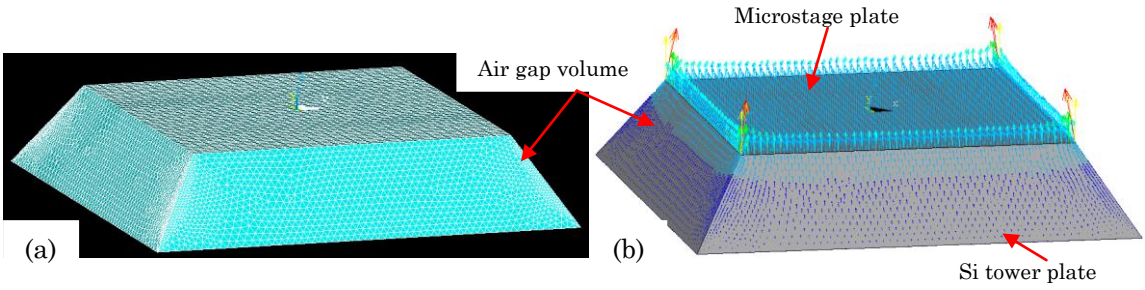

Figure 3.10 Parallel plate actuator out-of-plane FEA (a) a parallel plate volume meshed with elements PLANE*121* (for plates) and SOLID*122* (for air-gap volume) (b) Electric field lines between the parallel plates for the 4SA microrobot.

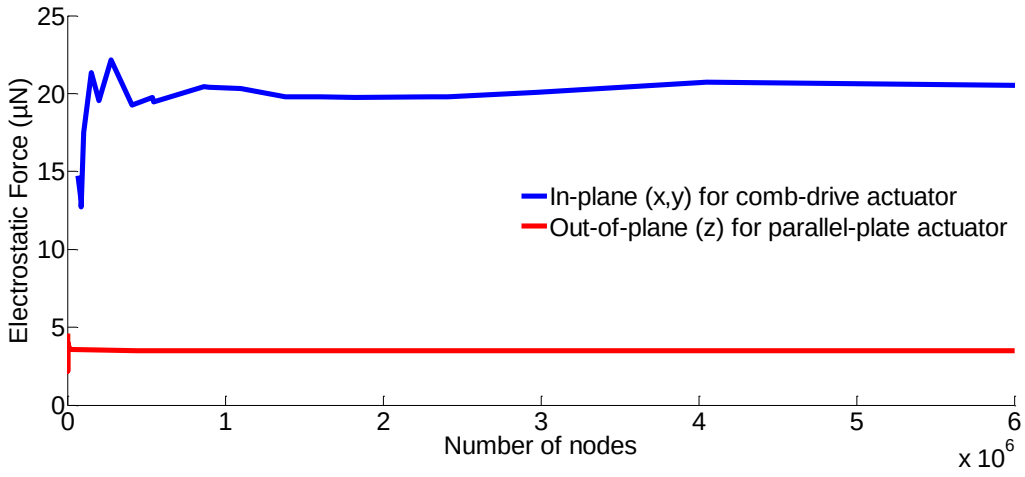

Figure 3.11 Convergence analysis of electrostatic force for finding the optimal number of nodes for simulation. For the comb-drive actuators, the convergence is performed at *75* V and for the parallel-plate actuators, the convergence is performed at *15* V.

The electrostatics simulation is performed in 3D instead of 2D due to the effect of fringing fields in the third dimension. A convergence based mesh-analysis is performed prior to the simulations to optimise the mesh size that can be used for all runs. The densities chosen vary from extremely coarse (e.g. 10,000 nodes) to extremely fine (e.g. 5 million nodes). The in-plane convergence analysis is performed for comb-drive actuators of different thicknesses. A representative of such analysis is shown in Figure 3.11. The simulations are performed for an applied DC voltage of *75* V and the electrostatic force values are noted for different number of nodes. The range of results vary up to *40%* for coarse mesh densities which becomes constant as the density becomes finer. For in-plane actuation, it can be seen that the electrostatic force becomes almost constant beyond *1.5* million nodes. For the out-of-plane actuation, beyond *500,000* nodes, the value becomes comparatively steady and the simulations are performed using *2* million nodes for better accuracy of results. Thus the electrostatic simulations are henceforth performed using these selected refined mesh sizes. The computation time increases exponentially as the number of nodes increase.

For both comb-drive and parallel plate actuators, additional air-gap volume is created

between the plates so that the electrostatic field can be created upon the application of voltage. Creating this volume is also critical for meshing to be consistent with the entire structure as shown in Figures 3.9a and 3.10a. This air-gap volumes are created in ANSYS. The voltage boundary conditions are applied across the interface of the comb fingers thus leading to a potential difference. For the parallel-plate actuator, the voltage is applied between the micro-stage and silicon tower plates. The model is solved and the electrostatic forces are computed.

Comparing the electrostatic force values for the designed and manufactured 4SA

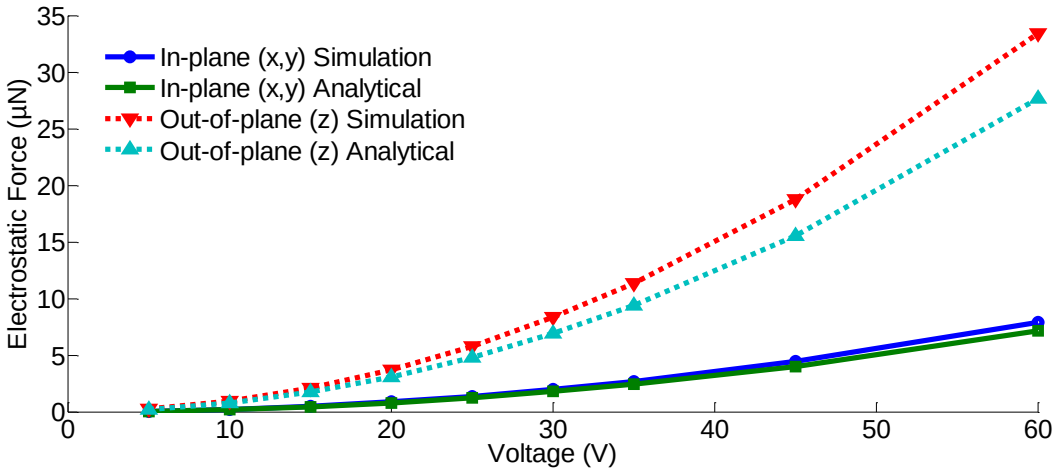

Figure 3.12 Electrostatic forces for different applied DC voltages for designed 4SA microrobot.

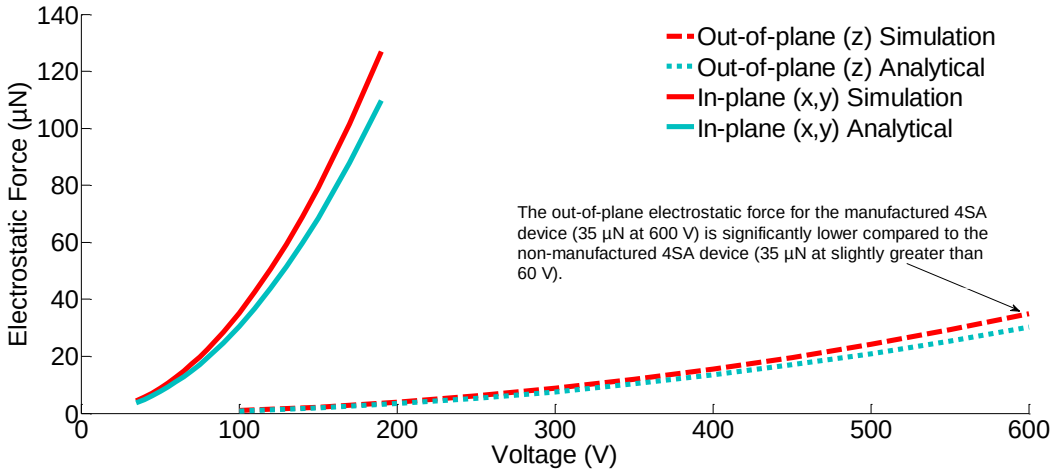

Figure 3.13 Electrostatic forces for different applied DC voltages for manufactured 4SA microrobot.

microrobots, a significant difference can be seen in the out-of-plane electrostatic forces for different applied DC voltages (Figures 3.12 and 3.13). Due to the limitations of fabrication infrastructure, there have been significant changes in the dimensions of the manufactured 4SA microrobot compared to the designed 4SA microrobot. For example, for the designed 4SA microrobot the distance between the parallel plates of the parallel-plate actuator is *12* μm. In the manufactured 4SA microrobot, this distance varies between *45* μm and *50* μm. Further the area of overlap of the top surface of the bottom silicon tower with the bottom surface of the microstage in the parallel-plate actuator has decreased from *800* μm^2 (designed 4SA microrobot) to almost *140* μm^2 (manufactured 4SA microrobot). Since the electrostatic force decreases with the square of the distance between the two plates along with the area of overlap of the plates, this significantly affects the electrostatic force values. The out-of-plane electrostatic force at a given voltage for the manufactured 4SA microrobot is *35* μN at *600* V which is significantly lower in comparison to the designed 4SA microrobot, which is *35* μN at around *62* V (Figure 3.13). Types of elements, quadratic or hexahedral, linear or quadratic used for meshing along with finer mesh density can lead to a closer conformity between the analytical and simulation results.

3.3.2 Structural FEA of the 4SA microrobot

The in-plane and out-of-plane structural simulations of the suspended structures of the 4SA microrobot are performed with element SOLID*187* as shown in Figure 3.14. It is a higher order 3D, *10*-node element and has a quadratic displacement behavior and is well suited to modeling irregular meshes. The element has three degrees of freedom at each node: translations in the nodal *x*, *y*, and *z* directions.

As in electrostatic simulation, a convergence based mesh-analysis is performed for structural analysis prior to the simulations to optimise the mesh sizes that can be used for all

runs. A representative of such analysis is shown in Figure 3.15. For the in-plane simulation, the analysis is performed for an applied DC voltage of *75* V and for the out-of-plane simulation, the applied DC voltage is *15* V. The range of results varies up to *22%* for coarse mesh densities which becomes constant as the density becomes finer. For in-plane actuation, it can be seen that the displacement becomes comparatively steady beyond a million nodes and the refined mesh value is chosen to be *2* million nodes for better accuracy of results. Similarly for out-of-plane actuation, beyond *2* million nodes, the value becomes comparatively steady and the refined mesh value is chosen to be *5* million nodes for better accuracy of results.

In order to reduce computation time, the comb-drive actuators are replaced by rectangular solid beams of equivalent mass and density. This significantly simplifies the meshing of the grid. The boundary conditions applied to the structure include the net electrostatic forces

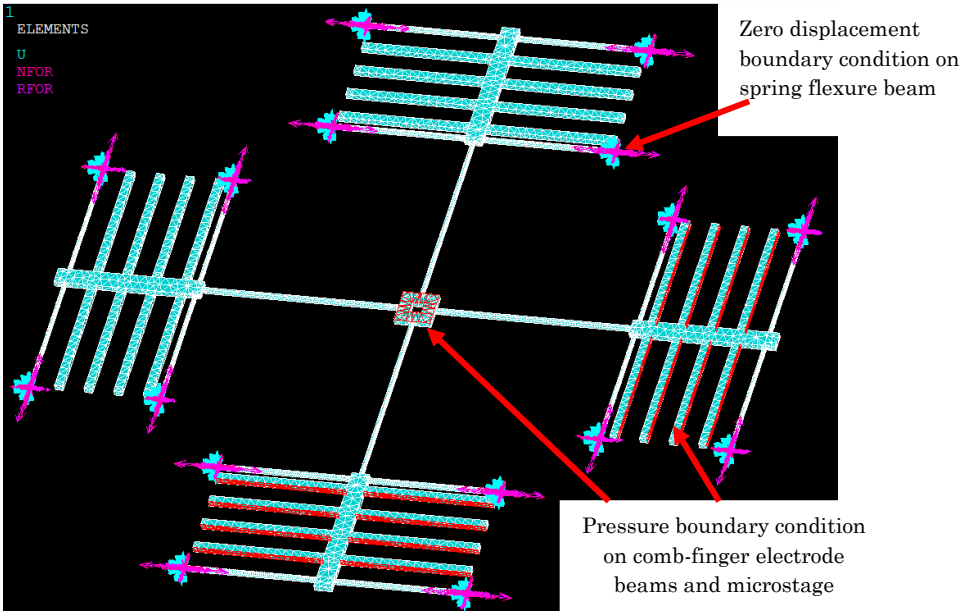

Figure 3.14 Structural simulation of the 4SA microrobot with the applied boundary conditions, zero displacement at the end of the hinge of spring flexure beams and pressure on the comb-drive fingers (electrostatic force corresponding to different voltages divided by surface area of the beam, substituted for the comb-finger electrodes) and microstage.

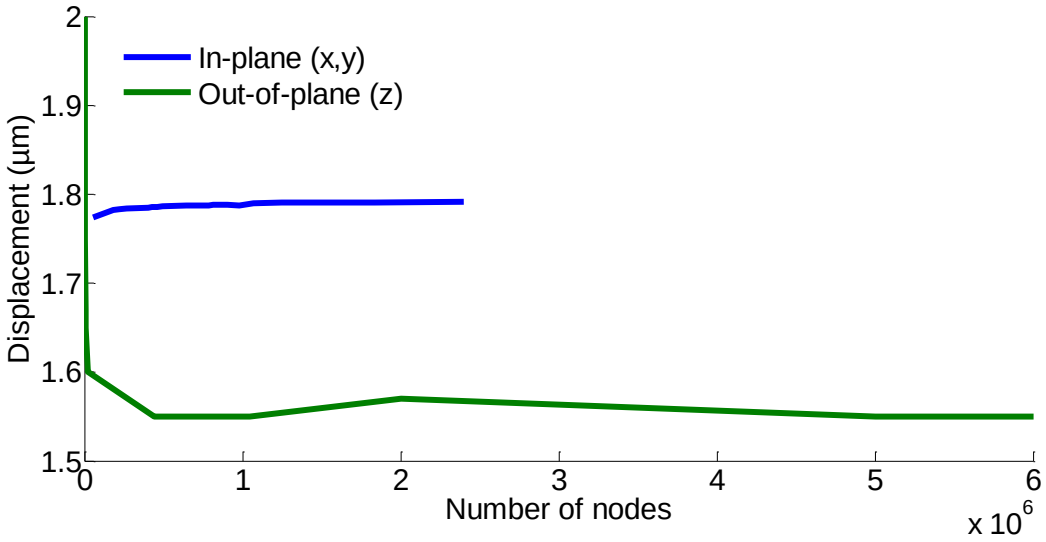

Figure 3.15 Convergence analysis of displacement for finding the optimal number of nodes for simulation. The convergence is performed at *75* V for in-plane motion and at *15* V for out-of-plane.

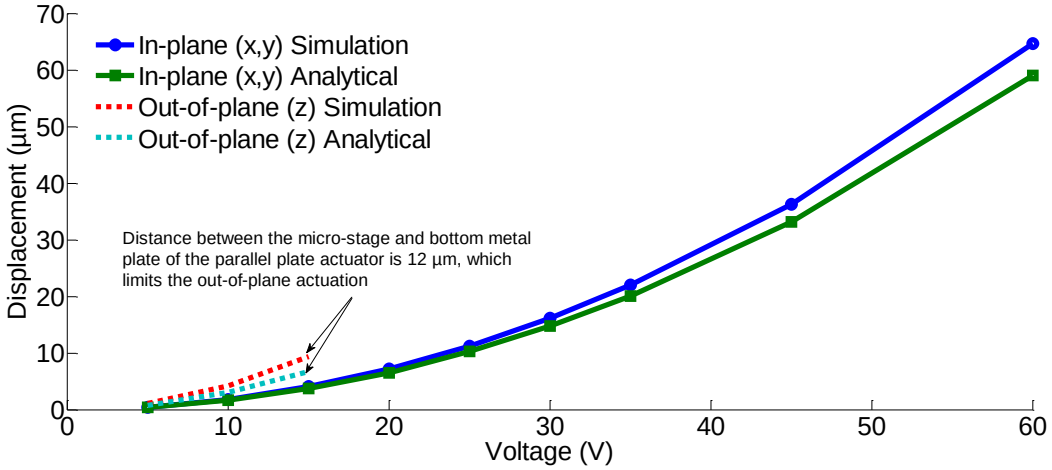

Figure 3.16 Displacements for different applied DC voltages for designed 4SA microrobot.

applied to the rectangular beams (simplified for comb-drive actuators) for in-plane actuation as shown in Figure 3.14. For out-of-plane motion, the electrostatic forces are applied to the top surface of the microstage. These forces are applied as structural pressures on to the surface area. The microneedle on top of the stage has been replaced by an equivalent amount of mass and density being added to the microstage. These electrostatic forces correspond to the different applied DC voltages obtained from phase one of the simulation. The

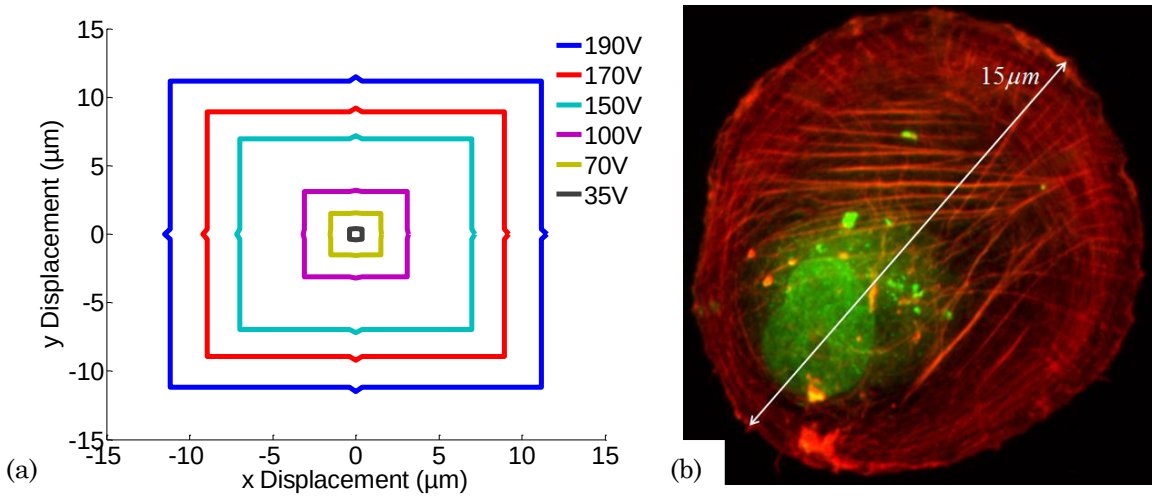

Figure 3.17 (a) 2D surface plots of the in-plane actuation of the manufactured 4SA microrobot (thickness = *25* µm). (b) Confocal microscopy images of ISHI cells growing on glass. Images are isolated from series showing 3D representation of cell slices. F-actin stained with Texas Red phalloidin (red); nucleus stained with Hoechst 33342 (green/blue). Note: nuclear stain representation colour was changed through confocal software[24].

displacement boundary conditions applied to the end cross-section of the spring flexure beams restrict these ends from experiencing any motion. The model is solved and parameters including displacement, stress and natural frequencies are computed. The corroboration of the analytical, FEA and experimental results of the manufactured 4SA microrobot have been discussed in section 5.2.

As discussed earlier limitations in fabrication of the 4SA microrobot has led to significant change in spring stiffness of the beams. The in-plane stiffness of the manufactured 4SA microrobot is *91.75* µN/µm, which is 316 times greater than that of the designed 4SA microrobot i.e. *0.29* µN/µm. Similarly, the out-of-plane stiffness of the manufactured 4SA microrobot is *124.78* µN/µm, which is 524 times greater than that of the designed 4SA microrobot i.e. *0.23* µN/µm. This affects the motion performance of the manufactured 4SA microrobot as evident from Figure 3.17a. Nonetheless in Chapter 5, we establish the successful implementation of the 4SA microrobot.

To understand the significance of such change in effective stiffness of the actuator components, an in-plane displacement of *5* μm in one side with a pull-mode can be achieved at less than *20* V with the designed 4SA microrobot. It takes *120* V for the manufactured 4SA microrobot to achieve a similar displacement. For the out-of-plane motion, a displacement of more than *0.5* μm can be achieved at less than *5* V with the designed 4SA microrobot which takes up to *600* V with the manufactured 4SA microrobot. The experimental results from the 3D motion of the actuator are discussed in Section 5.2. The 2D surface plot of the in-plane actuation of the manufactured 4SA microrobot gives an idea of the actuation performance of the microstage with respect to a mammalian cell as shown in Figure 3.17a. The microstage is capable of a total in-plane displacement of more than *10* μm (±*5* μm) at a driving DC voltage of *120* V in a pull-pull mode. The pull-in occurs beyond the *5* μm distance as the spacing between the opposite electrodes is *10* μm.

Given a human ISHI cell of diameter *15* μm as shown in Figure 3.17b, the in-plane motion of the manufactured 4SA microrobot can cover up to *67%* of the surface area of the cell at a driving voltage of *120* V. The in-plane motion of the 4SA microrobot illustrated in Figure 3.18 has been exaggerated to make the displacement more visually prominent. Also it must

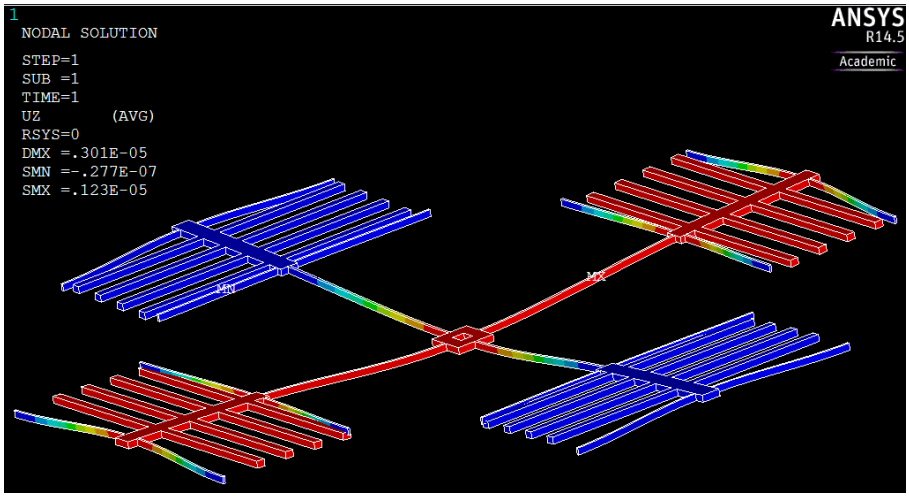

Figure 3.18 3D motion of the 4SA microrobot after the model is solved.

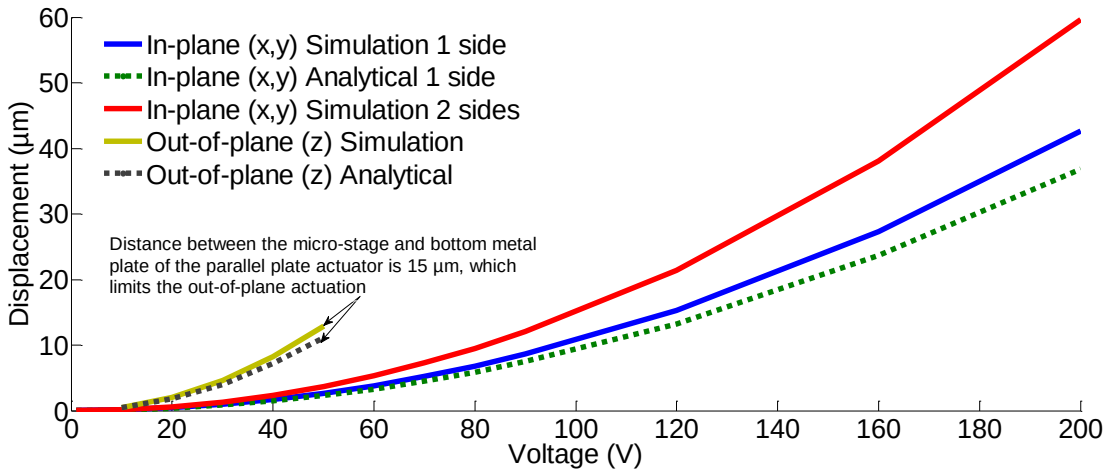

Figure 3.19 Displacements for different applied DC voltages for designed 4SA microrobot. Suspended structure thickness = *10* µm, Actuator gap = *15* µm, Length of tethering beam = *800* µm.

be noted that the simulation values are *10 - 15%* higher than the analytical values on an average as discussed in the sections above. For the in-plane motion as shown in Figure 3.19, at *160* V, 4SA microrobot can achieve an in-plane motion of around *27* µm with a single side actuating and around *38* µm with double-sided actuating. In terms of out-of-plane actuation, at *30* V, 4SA microrobot is capable of achieving a motion of around *4.5* µm.

3.3.3 Stress and Modal Analysis

The maximum stress developed in the microrobot as a result of its motion is significantly lower than the yield strength of silicon, i.e. *7000* MPa, as seen in Figure 3.20. For thicknesses of up to *25* µm and regardless of the motion being one-sided or two-sided, the maximum stress does not exceed beyond *800* MPa. Thus, the von-mises stress within the operation range is between *5-10%* of the yield strength of silicon. Sagging of the suspended structure under its own weight can cause unnecessary twisting of the spring flexure beams and disorientation of the comb fingers. The simulation of the sagging of the suspended structures in the microrobot under its own weight confirms the value to be in the picometer range. This

is done by applying surface load corresponding to the weight of the structure. Thus sagging is negligible as compared to the overall dimension of the structure.

Albeit, the current behavior of the actuator is purely static, knowing the natural frequencies of the microrobot would be useful for widening the application of the arrayed architecture in the near future. Such applications involve single molecule force spectroscopy, cell mechanical measurements, local functionalisation of polymeric layers and molecular electronics such as depositing conductive polymers onto nanoelectrodes. Some of these applications have been addressed in Chapter 1. Moreover for biomanipulation tasks where accuracy of the positioning of the microneedle is a critical factor, the design should be such that nearby oscillations, vibrations and other forms of noise do not affect its motion while operating.

A high designed natural frequency would allow the actuator to respond quickly and accurately to the rapid changes in the command signal. The eigen-frequency analysis is performed for the vertical out-of-plane motion of the microstage. As mentioned in Section 3.3.2, the microneedle on top of the stage has been replaced by an equivalent amount of mass and density being added to the stage. The first five most dominant mode shapes are shown in Figure 3.21. The details regarding the modal frequencies and their respective behaviors are summarized in Table 3.1. The first in-plane mode of vibration at *12* KHz is pure translational. The second mode of vibration at *27* KHz is out-of-plane translational plus rotation. The last three modes of vibration at *29* KHz involve parasitic rotation of the comb-finger electrodes. The last three eigen-frequencies are almost *2.5* times higher than the desired translational mode of the microstage. Since these modes are located far from the first dominant mode, it indicates a significantly high stiffness to excite these parasitic motions.

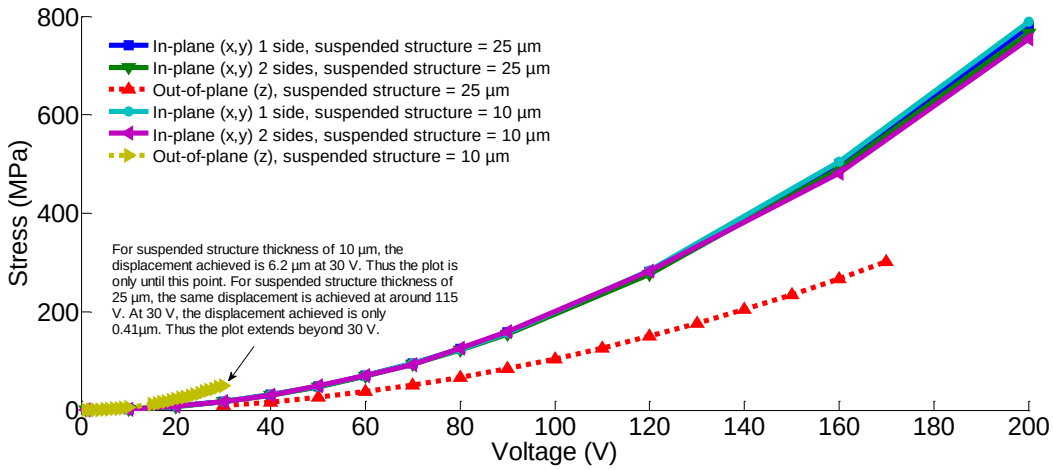

Figure 3.20 Maximum stress developed in the 4SA microrobot for tethering beam length of *800* µm and suspended structure thicknesses of *10* µm and *25* µm for different applied DC voltages. Yield stress of Si = *7000* MPa. Actuator gap = *15* µm.

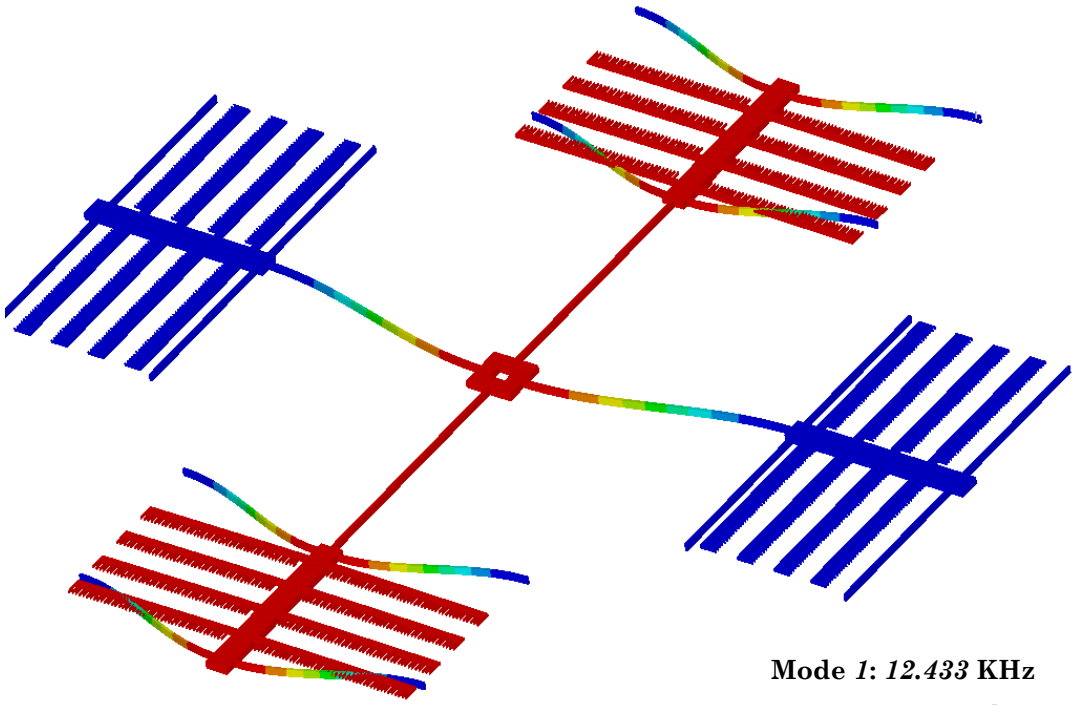

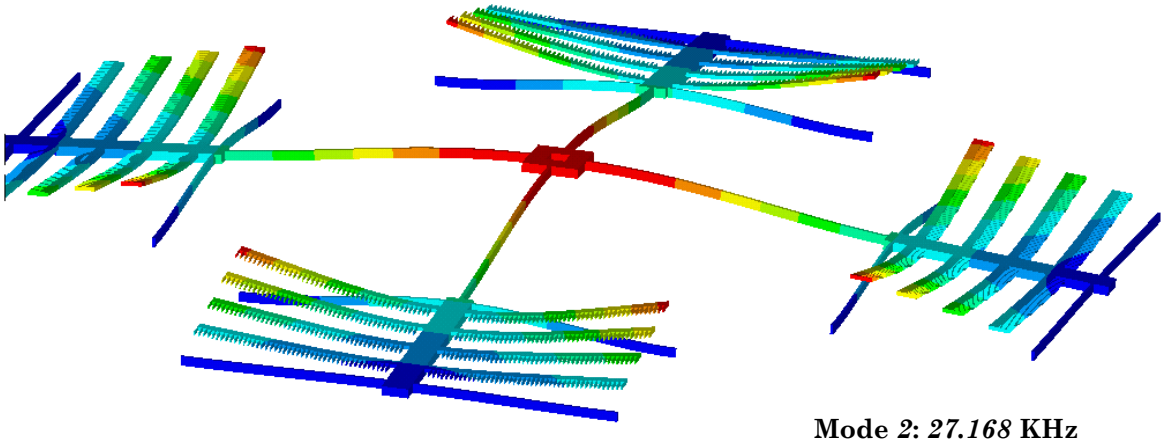

Mode *2*: *27.168* KHz

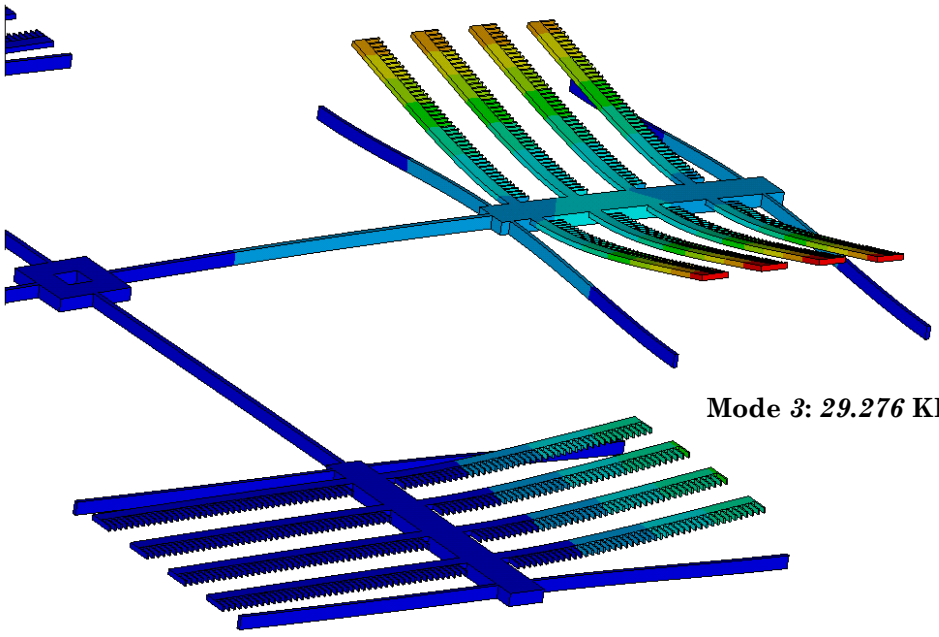

Mode *3*: *29.276* KHz

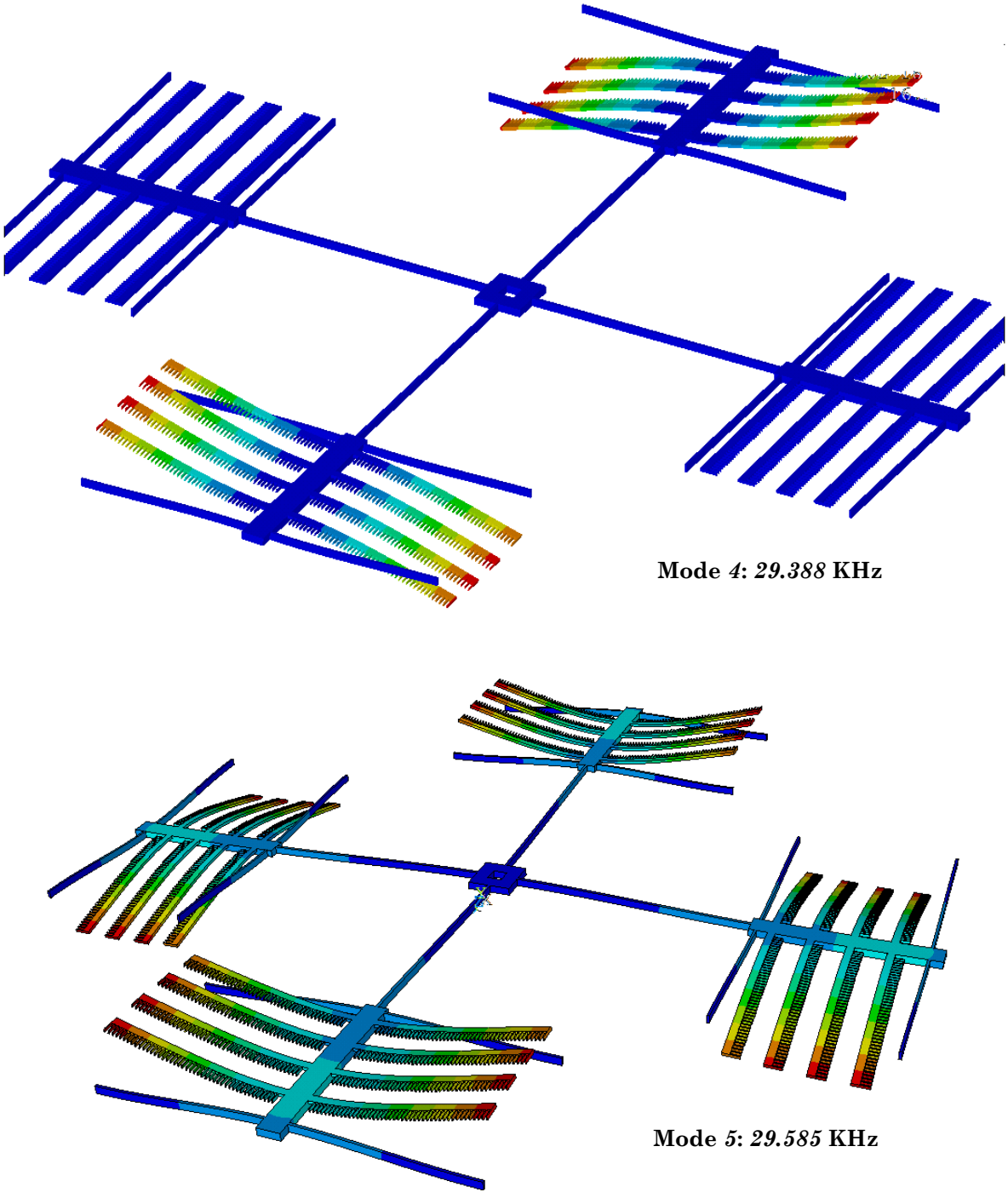

Figure 3.21 Modal shapes and their corresponding eigen-frequencies of the microstage of the manufactured 4SA microrobot.

Table 3.1 Summary of modal analysis for the manufactured 4SA microrobot design.

Mode numbers	Eigen-frequencies (KHz)	Mode behaviors
1	12.433	in-plane mode for in-plane xy motion
2	27.168	out-of-plane z mode motion including flexure of comb-finger electrodes
3	29.276	single sway mode plus minimal flexure of the comb-finger electrodes in two sides
4	29.388	single sway mode of the comb-finger electrodes in the same axis
5	29.585	dual reverse sway mode

Table 3.2 Design dimensions of the designed 4SA microrobot.

Structural parameters	
Spring flexure beams	$w_s = 2.5$ μm, $h_s = 10$ μm, $l_s = 1200$ μm
Tethering beams	$w_t = 4$ μm, $h_t = 10$ μm, $l_t = 1945$ μm
Area of microstage	*500* μm × *500* μm
Parallel plate actuator gap	*15* μm
Height of silicon tower	*385* μm – *425* μm
Microneedle	Height = *50* μm -*100* μm, Tip diameter = *30* nm – *50* nm
Comb-drive actuator	$i = 1200$, $t_f = 2$ μm, $gs_f = 3$ μm, $h = 10$ μm
Length of comb-finger	*105* μm
Opposite electrode spacing	*100* μm

3.3.4 Critical findings and final design specifications of the 4SA microrobot

The critical findings from the FEA study of the microrobotic design are as follows:

- Validation with the analytical model thus proving the accuracy of both our models. These results are further corroborated with the experimental test results of the motion performance of the 4SA microrobot in Chapter 5. These successive validation shows that our model is reliable to analyse the design of 3SA microrobot's motion performance as discussed in Chapter 6.
- The value of electrostatic forces from multiple comb-drive actuators and parallel-plate actuator and numbers of such actuators needed and their corresponding dimensions.

- Maximum stress developed is within the maximum stress limit for stability of the microrobot.

Based upon results obtained from the design conceptualisation, analytical and simulation models, the following design dimensions as summarised in Table 3.2 have been selected for fabrication.

3.4 Closure and original contributions

This chapter introduces modeling techniques, both analytical and FEA to understand the behaviour and study the motion performance of the actuator under the application of DC voltages. The behaviour has been analytically modeled using elastic stiffness equations and grid stiffness matrix model. Detailed finite element analyses are performed in ANSYS to understand the motion of the actuator, stress developed and natural frequencies. Analytical and FEA results are used to finalise the dimensions of the microrobot pre-fabrication. Limitations in fabrication infrastructure have led to change of original design dimensions, thereby changing the motion performance which has been discussed at length. The mechanical stress developed within the operational range is between to *5 -10%* of the yield strength of silicon. The microrobot also has a high natural frequency which will allow for quick response to the fast changes in the commanded position for dynamic applications.

Chapter 3 makes the following original contributions to the field of structural analysis:

- We have developed a grid stiffness matrix model to analytically study the motion performance of the microrobot that treats the structure more holistically compared to other models discussed in the review of the prior art in Section 3.1. None of these models take into consideration the effect of translation, torsion, bending and shear stress on the beam components of the microrobot like our model do.

- We have performed extensive FEA study to investigate the motion performance, stress and modal frequencies of the microrobot. We have thus validated these results with the analytical model proving a close consistency between these two models. These models will be used to design a new type of actuator, 3SA microrobot which has been analysed in Chapter 6. To the best of our knowledge as evident from the review of the prior art in Section 3.1, most of these prominent works have not performed such extensive analyses on their designs prior to fabrication.

BIBLIOGRAPHY

[1] D. L. Logan, *A First Course in the Finite Element Method*, 5 ed.: Cengage Learning, 2011.

[2] J. Dong et al., "Design, fabrication and testing of a silicon-on-insulator (SOI) MEMS parallel kinematics XY stage," *Journal of Micromechanics and Microengineering*, vol. 17, p. 1154, 2007.

[3] J. Dong and P. M. Ferreira, "Electrostatically actuated cantilever with SOI-MEMS parallel kinematic XY stage," *Journal of microelectromechanical systems*, vol. 18, p. 641, 2009.

[4] D. Mukhopadhyay, J. Dong, E. Pengwang and P. Ferreira, "A SOI-MEMS-based 3-DOF planar parallel-kinematics nanopositioning stage," *Sensors and Actuators A: Physical*, vol. 147, pp. 340-351, 2008.

[5] S. Polit and J. Dong, "Development of a high-bandwidth xy nanopositioning stage for high-rate micro-/nanomanufacturing," *IEEE/ASME Transactions on Mechatronics*, vol. 16, pp. 724-733, 2011.

[6] H. Shi, HJ. Su, N. Dagalakis and J.A. Kramer, "Kinematic modeling and calibration of a flexure based hexapod nanopositioner," *Precision Engineering*, vol. 37, pp. 117-128, 2013.

[7] M. Olfatnia, S. Sood, J.J. Gorman and S. Awtar, "Large stroke electrostatic comb-drive actuators enabled by a novel flexure mechanism," *Journal of Microelectromechanical Systems*, vol. 22, pp. 483-494, 2013.

[8] A.G. Fowler, A.N. Laskovski, A.C. Hammond and S.O.R. Moheimani, "A 2-DOF electrostatically actuated MEMS nanopositioner for on-chip AFM," *Journal of Microeletromechanical Systems*, vol. 21, pp. 771-773, 2012.

[9] J.D. Grade, H. Jerman and T.W. Kenny, "Design of large deflection electrostatic actuators," *Journal of Microelectromechanical Systems,* vol. 12, pp. 335-343, 2003.

[10] G. Zhou and P. Dowd, "Titled folded-beam suspension for extending the stable travel range of comb-drive actuators," *Journal of Micromechanics and Microengineering,* vol. 13, pp. 178-183, 2003.

[11] B.D.Jensen, S.Mutlu, S.Miller, K.Kurabayashi and J.J.Allen, "Design and simulation of shaped comb fingers for compensation of mechanical restoring force in tunable resonators," presented at the 2001 ASME IMECE, New York, 2001.

[12] I.P.F. Harouche and C.Shafai, "Simulation of shaped comb-drive as a stepped actuator for microtweezers application," *Sensors and Actuators A: Physical,* vol. 123-124, pp. 540-546, 2005.

[13] D.Piyabongkarn, Y.Sun, R. Rajamani, A. Sezen and B.J. Nelson, "Travel range extension of a MEMS electrostatic microactuator," *IEEE Transactions on Control Systems Technology,* vol. 13, pp. 138-145, 2005.

[14] J.J. Gorman and N.G. Dagalakis, "Modeling and disturbance rejection control of a nanopositioner with application to beem steering," in *ASME International Mechanical Engineering Congress*, Washington D.C., 2003, pp. 1-9.

[15] J.J. Gorman, N.G. Dagalakis and B.G. Boone, "Multi-loop control of a nanopositioning mechanism for ultra-precision beem steering," in *SPIE*, San Diego, California, 2003, pp. 1-12.

[16] B.H. Kang, J.T. Wen, N.G. Dagalakis and J.J. Gorman, "Analysis and Design of Parallel Mechanisms with Flexure Joints," in *IEEE International Conference on Robotics & Automation,* New Orleans, Louisiana, 2004, pp. 4097-4102.

[17] B.H. Kang, J.T. Wen, N.G. Dagalakis and J.J. Gorman, "Design optimization for a Parallel MEMS Mechanism with Flexure Joints," in *ASME Design Engineering Technical Conferences*, Salt Lake City, Utah, 2004, pp. 1-10.

[18] YS. Kim et al., "Design, fabrication and testing of a serial kinematic MEMS *xy* stage for multifinger manipulation," *Journal of Micromechanics and Microengineering*, vol. 22, pp. 085029-08538, 2012.

[19] Y. Zhu, A. Corigliano and H.D. Espinosa, "A thermal actuator for nanoscale *in situ* microscopy testing: design and characterization," *Journal of Micromechanics and Microengineering*, vol. 16, pp. 242-253, 2006.

[20] H.D. Espinosa, Y. Zhu and N. Moldovan, "Design and optimization of a MEMS-based material testing system for nanomechanical characterization," *Journal of Microelectromechanical Systems*, vol. 16, pp. 1219-1231, 2007.

[21] G. Fedder, "Simulation of Microelectromechanical Systems," PhD, Electrical Engineering and Computer Sciences, Massachusetts Institute of Technology, Cambridge, 1994.

[22] T Hirano, T Furuhata, KJ Gabrial and H Fujita, "Design, fabrication and operation of submicron gap comb-drive microactuators," *IEEE Journal of Micromechanical Systems*, vol. 1, pp. 52-59, 1992.

[23] ANSYS, "Mechanical APDL Documentation," ed, 2013.

[24] L. Murray, "Influence of substrate topography and materials on behaviour of biological cells," PhD, Electrical and Computer Engineering, University of Canterbury, Christchurch, 2012.

Chapter 4: Fabrication of 4SA Microrobot

4.1 Introduction[1]

Given the complicated nature of fabrication in terms of integrating microneedles and bottom tower shaped electrode, we have designed two new fabrication processes to fabricate the 4SA microrobot which have been presented in this chapter. The fabrication of the 3SA microrobot has been introduced separately in Chapter 7. This chapter deals solely with the fabrication of 4SA microrobot. The first fabrication process uses techniques borrowed from the SCREAM (Single-crystal reactive etching and metallisation) and SHARP *(*Scream for high aspect ratio proportions) process. It involves a combination of photolithography, thermal oxidation, sputter deposition of SiO_2 and aluminium, wet etching using KOH and anisotropic and isotropic reactive ion etching RIE. The process involves four masks and the entire fabrication is performed on a single silicon wafer without the need for SOI wafers and wafer bonding techniques. The second process is based on techniques borrowed from the SOIMUMPs, an SOI micromachining process. Our first 4SA microrobot (without the microneedle) has been fabricated using the second process. It involves a combination of photolithography, CMP, DRIE, oxidation, KOH wet etching and silicon fusion bonding. The process involves six masks and is performed using three different wafers, one SOI and two silicon wafers.

Sections 1.3.1 and 1.3.2 discuss exclusively the recent advances in the microneedle and positioning stage technologies along with the fabrication techniques used to develop them. This chapter will strive to shed some further light into the different fabrication processes used to develop such structures and the novelty of the fabrication processes themselves. Section

[1] Elements of the following chapter have been published/ presented in conferences C2, C3, C4 and C6 or in preparation for journal(s) J1 and J3.

4.2 briefly discusses the state-of-the-art in fabrication processes used to fabricate different forms of micro and nanoprobes and positioning stages and makes clear distinction between our designed fabrication processes and the existing ones. Section 4.3 details the two fabrication processes respectively. Section 4.4 discusses the mask design and the associated design rules that need to be followed to ensure a reliable final product. Section 4.5 presents some interesting results from our etch characterisation studies of SiO_2 where formation of nanopillared structures have been observed. The etch chemistry and our explanation behind the formation of such nano structures is presented in conjunction with some existing studies that sheds light into the creation of such structures. The SEM images of the 4SA microrobot are presented in Section 4.6 and Section 4.7 summarises the critical points in the chapter.

It must be noted that every new design would need to have customised fabrication process to enable the manufacturing of the actuator. For fabricating our 4SA microrobot, various fabrication processes like the ones to be discussed in the review of the prior art below and in Chapter 1 have been searched through to design a customised fabrication process. It must be noted that this thesis research is not about developing a new fabrication process but to utilise existing ones in a novel way to make the fabrication of the microrobot possible.

4.2 Background and prior art

The first fabrication process designed is inspired by the SCREAM [1-3] and SHARP [4] processes developed in the 1990s at Cornell University by Noel MacDonald and his research team. It is a single mask process for high aspect ratio structures in bulk silicon that involves a series of etching, oxidation and metallisation processes. Electrical isolation is achieved by post release metallisation. This process and its modified version have been used to manufacture various types and design of actuators and actuator arrays [5, 6], optoelectronic devices [7, 8], integrated STM [9, 10] among others. The process would not be described in

here. Rather the interested readers are requested to refer to the following sources listed herein. These easy to use processes have also been used to fabricate multi-level high-aspect-ratio 3D structures with arbitrary surface height profiles like our first designed fabrication process flow [11-15]. The fundamental principle of using such fabrication relies on the exploitation of RIE lag to simultaneously define all features using a single lithographic masking step. Different mask pattern openings to define the features result in variations of etch depth across the pattern, translating in surface height variation through the removal of the superstructure above the etched floors.

The second fabrication process designed is inspired by the SOI Multi-user MEMS process (SOIMUMPs), a four mask level SOI patterning and etching process. Several of the works discussed henceforth utilises similar fabrication process in novel ways. Favre et al [16] have developed a 2D cantilever array, shown in Figure 4.1, to perform topographical and mechanical investigations on cells in both air and liquid medium. Instead of using piezoresistive sensing approach for measuring the deflection of the probes, an interferometric system has been used by first expanding the diameter of the laser beam and then splitting it into a reference beam that falls on the cantilever array. As discussed in Section 1.2, this type of vertical deflection read-out can be used in our experimental setup as shown in Figure 1.4, leading to individual out-of-plane motion readout scheme of the microneedles. The fabrication, shown in Figure 4.1c is based on the processing of two wafers using standard silicon micromachining techniques. These wafers are then fusion bonded with further post-processing to etch away the sacrificial layers using a combination of RIE, KOH anisotropic etch and buffered hydrofluoric acid (BHF) to release the suspended probe structure from the wafer.

Another *128* self-sensing and self-actuated parallel piezoresistive probe architecture has been designed and developed for imaging applications and lithography using (*100*) SOI wafer

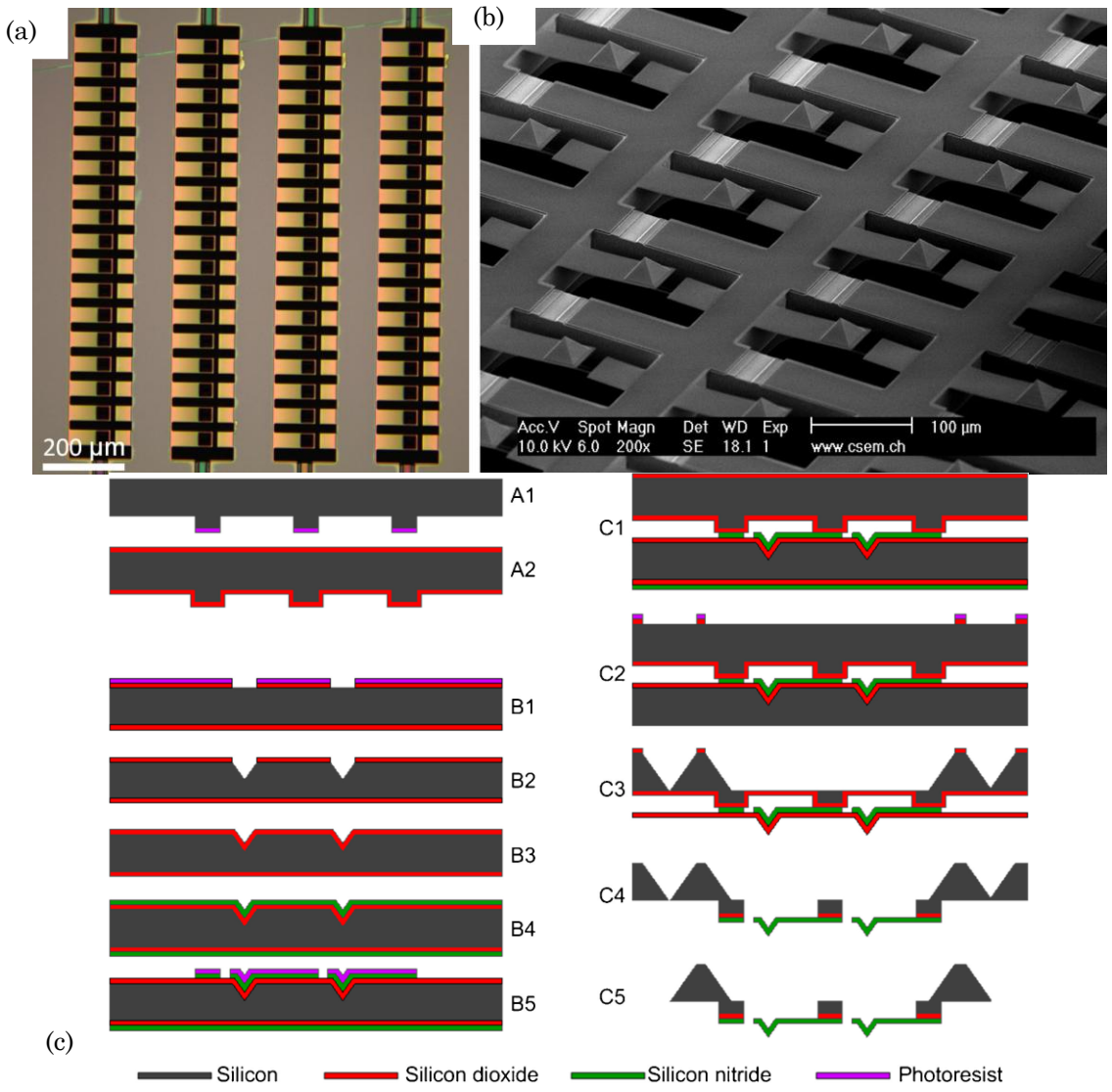

Figure 4.1 (a) Optical image of a *4×17* probe array with *100* µm long SiN cantilevers anchored on parallel-beam frame. The dark square at the end of each cantilever corresponds to the pyramidal shaped tip. (b) SEM images of a probe arrays with SiN cantilevers anchored on a grid like frame. (c) Process flow for the microfabrication of arrays of SiN AFM cantilevers. The fabrication is based on the processing of two wafers (A and B), which are then fusion bonded and further processed (C) [16].

technology [17]. The fabrication involves wet chemical etching of the tips, followed by RCA clean, thermal oxidation, boron contact implantation for piezoresistors, metal deposition of aluminium, RIE to form the cantilever beam and then pre-bent as shown in Figure 4.2 by a Si_3N_4 low pressure chemical vapour deposition. Continuing on this work, Sarov et al [18] reports a four-layer thermally driven piezoresistive cantilever array architecture with *240* µm

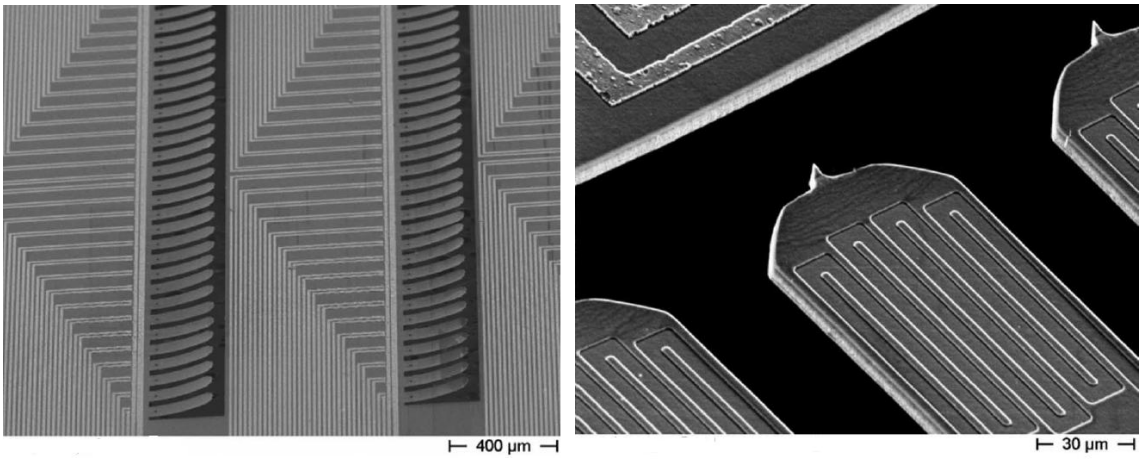

Figure 4.2 SEM images of fabricated pre-bent cantilever probes with integrated Si tips, readout electronics and bimorph thermally driven actuator [17].

long and *3* µm thick silicon cantilevers with AFM tips. Deflections of up to *5* µm could be achieved for an actuation voltage of *1* V.

IBM Zurich's millipede technology for high density computer data storage has been discussed in Section 1.3.2. Lutwyche et al [19], King et al [20] and Drechsler et al [21] report the fabrication of 2D piezoresistive cantilever array for parallel imaging having common in-plane and independent vertical motion. The common fabrication starts with an SOI wafer being patterned using CHF_3/O_2 RIE to form the mask and then isotropic SF_6/Ar RIE to form the silicon tips. The tips are sharpened by thermal oxidation and BHF and KOH etch followed by definition of piezoresistors and tip heaters and local p^+ boron implantation and thermal annealing for activating the dopants. Further Si_3N_4 insulation layer is added to the wafer by PECVD, subsequently patterned and contact holes to the silicon are made using BHF. This is followed by the metal wiring for the piezoresistors and tip heaters, DRIE to form the cantilevers and finally back-side RIE to release the cantilever-tip structures. Similar work has been done by Sache et al [22] and Ahn et al [23]. Sache et al [22] have fabricated an array of *27×27* cantilevers with a *150* µm pitch on a *5* mm^2 device. The cantilevers are *100* µm in length, *10* µm in width and *1.5* µm in thickness. The fabrication starts with an SOI

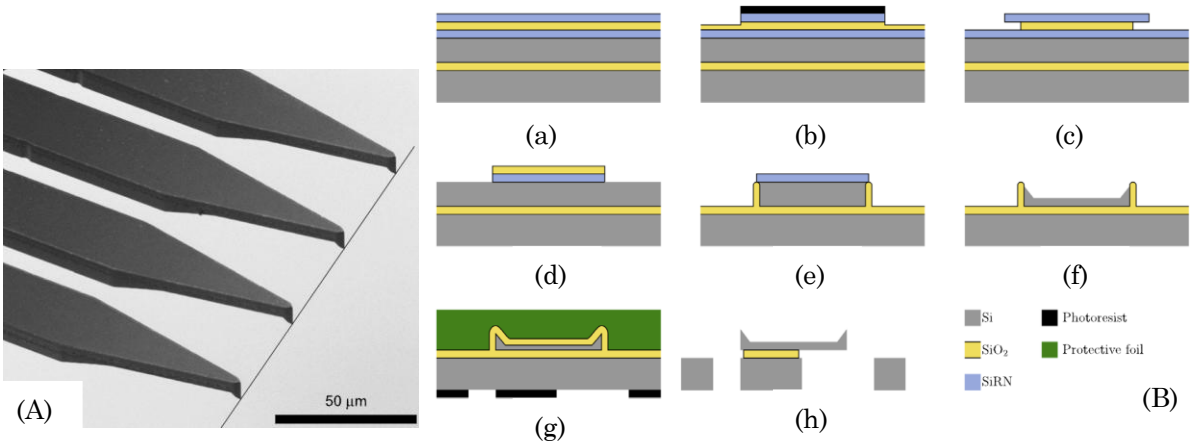

Figure 4.3 (A) An SEM image of a fabricated cantilever array. The tips are self-aligned in the convex corner at the free end of the cantilever. A line is drawn in the image to highlight that the tips are aligned on a virtual line. (B) Process flow for fabricating cantilevers with self-aligned tips. (a) SOI wafer with SiRN, SiO_2 and again SiRN deposited on top. (b) Pattern top SiRN using standard photolithography. (c) Convex-corner sharpening of sacrificial SiO_2 layer in a BHF etch. (d) Strip-exposed SiRN in hot H_3PO_4 etches. (e) Transfer pattern into Si using DRIE, strip SiO_2 and oxidize thermally. (f) Strip SiRN in hot H_3PO_4 and etch uncovered Si in KOH to create the tips. (g) Strip SiO_2, re-oxidize thermally to sharpen the tips, fit protective foil to front side and pattern back side. (h) Etch back side by DRIE, remove foil from front side and strip SiO_2 in BHF [24].

wafer with KOH anisotropic etch of the bulk wafer, followed by thermal oxidation and patterning, EDP etching to form the probes and sharpened by wet oxidation. Further, BHF etch, RIE to form the cantilever, Si_3N_4 LPCVD, aluminum and oxide sputtering, another two DRIE etch of the backside oxide layer and finally releasing the cantilever-probe structures by BHF and aluminum etching. Ahn et [25] have fabricated arrays consisting of *104* probes using similar processes as discussed above. First the SOI wafer is thermal oxidised and patterned followed by wet-etching in TMAH to form the probe-tip. It is then followed by a series of etching using BHF, ICP-RIE and SF_6 RIE to form the final structure.

Further examples of fabricated cantilever arrays include the ones incorporating tetrahedral tips fabricated by anisotropically etching a convex corner of a square post of single-crystal silicon, shown in Figure 4.3A [24]. The fabrication on (*100*) SOI wafer (device layer

thickness of *10* μm) involves two masks, one for fabricating the cantilevers and tips and second for performing a back side etch. The fabrication process flow is shown in Figure 4.3B. The tips of uniform height are formed by a cryogenic RIE which ensures their straight and smooth etch profile. The tetrahedral tip is sharpened by means of a wet chemical etch irrespective of the shape of the convex corner. The tips are placed at the end of the cantilever by self-alignment. A 1D array of *10* cantilevers has been fabricated spanning *430* μm with a

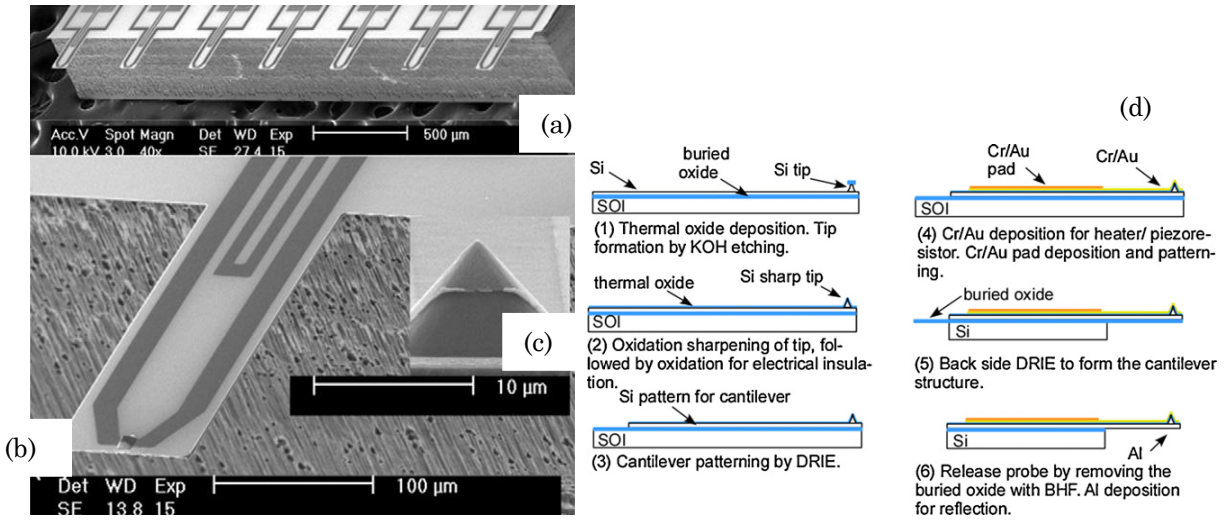

Figure 4.4 (a) SEM of the probe array. (b) Individual cantilevers include two resistors, one over the tip serving as a localised heater/thermal sensor and a second closer to the base serving as a resistor for deflection sensing. Inset (c) SEM close-up of the tip. (d) Fabrication process flow [26].

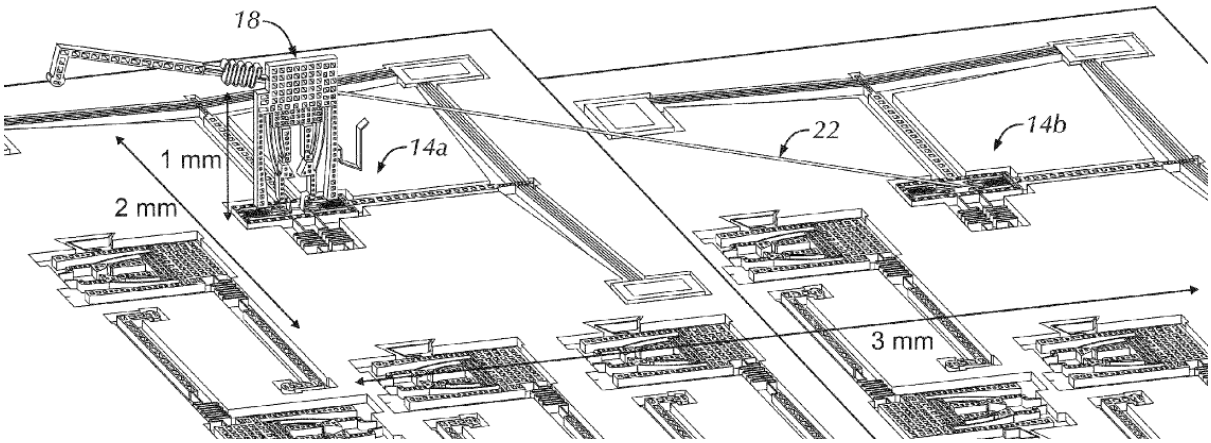

Figure 4.5 Top view of the 4D microrobot; *14a* and *14b* are the in-plane *xy* actuators that cooperate to control the robot in 4D, *18* is the arm and *22* is the cable. For the SEM image, please refer to this paper [27].

standard deviation of the tip position of *11* nm. 2D Si_3N_4 cantilever arrays with different spring constants for parallel force spectroscopy of biological samples like the one discussed above in this section has been fabricated [28]. The fabrication incorporating V-groove structures along the cantilevers to increase the area moment of inertia, involves an advanced moulding process and a thermocompression bonding of two (*100*) silicon wafers. The 2D array is composed of *3×8* cantilevers (length = *200* μm, width = *50* μm, thickness= *0.45* μm) that are distributed in a working area of *1×1* mm.

An array of piezo-thermal probes for high throughput scanning probe microscopy is developed that have *5-10* nm thick gold films to form sensing elements [26]. The fabrication as shown in Figure 4.4d uses a combination of KOH anisotropic etching, oxide masking, series of oxide growth to sharpen the tips and HF etching of the oxide, DRIE to form the cantilevers and metal evaporation. Arrays of 1D thermal biomorph actuators having such cantilever tips capable of vertical motion have been fabricated for cell force spectroscopy [29]. The fabrication involves a combination of SiO_2 sputtering, RIE of silicon, PECVD deposition of Si_3N_4, metal deposition and KOH etching. The concept of RIE lag effect is used in the fabrication to control the etch depth by varying the density and size of the openings in the hard mask. For example, trenches or square apertures of exposed Si, having smaller dimensions equal to *1–5* μm, will have a significantly lower etch rate than apertures larger than *10* μm.

An interesting four axes microrobotic actuator, shown in Figure 4.5 with capability of motion across four axes: *x*, *y*, in-plane yaw and out-of-plane pitch, has been developed that has an operating workspace of *50* μm × *50* μm × *75* μm [27, 30, 31]. It is capable of applying up to *50* mN of in-plane and *25* mN of out-of-plane force through an end-effector type cantilever arm. The microrobot joints are driven by four electrothermal actuators, which turn this in-plane motion into out-of-plane motion via a microwire cable. Although the actuator is

fabricated through standard lithographic microfabrication processes, the vertical interconnections are accomplished by 3D assembly. This can pose a serious challenge when there are parallel actuators, which would make the fabrication quite complicated. Another 3D parallel kinematic manipulator like the one discussed in Section 3.1 has been fabricated using a two-mask process using highly doped (*100*) SCS wafers for its use in transmission electron microscopy, shown in Figure 4.6a [32]. The fabrication enables high-aspect-ratio structures in conjunction with electrical trench insulation. It can drive up to ±*10* μm in-plane and $\pm 2^0$ rotation at a driving voltage of *50* V with minimal out-of-plane motion crosstalk during in-plane motion in resonance. The fabrication process is shown in Figure 4.6b. The same group has developed another MEMS-based 6D manipulator designed on the principles of exact constraint design, resulting in a high actuation compliance (flexibility) combined with a

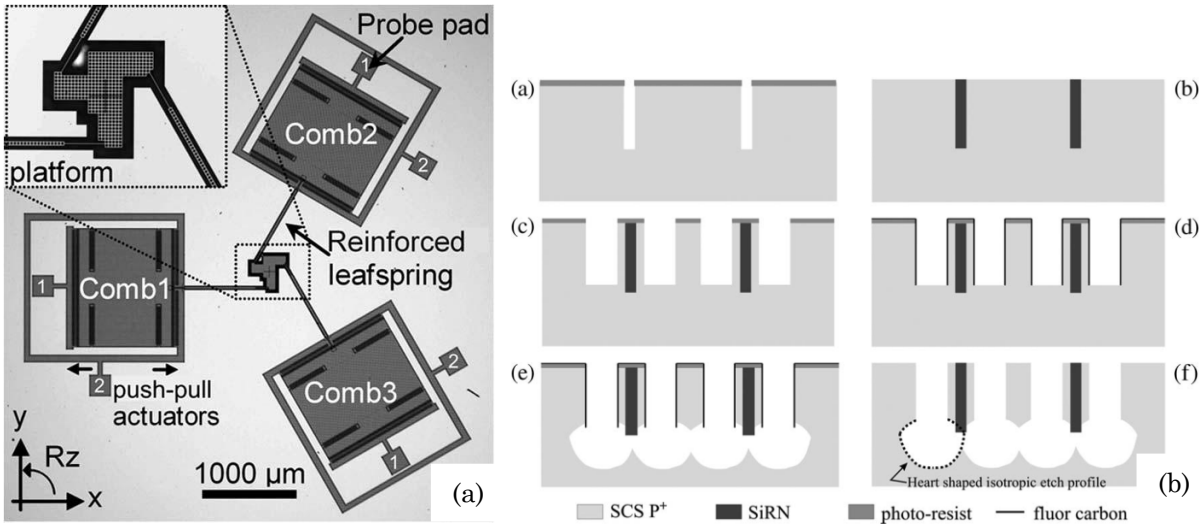

Figure 4.6 (a) Top view of the fabricated 3D manipulator. Each comb-drive actuators numbered from 1 to 3 has two probe pads for push and pull actuation (common potential is the surrounding bulk). Dark gray areas are pierced by etch holes for device release and electrical isolation from the bulk. Inset: an enlargement of the platform. **(b)** Fabrication process flow (a) Dry etching of isolation trenches, (b) filling of isolation trenches with SiRN, (c) dry etching of mechanical structure including etch holes, (d) sidewall protection with fluorocarbon, (e) dry isotropic under etching, and (f) the final result with indication of the heart shaped isotropic etch profile [32].

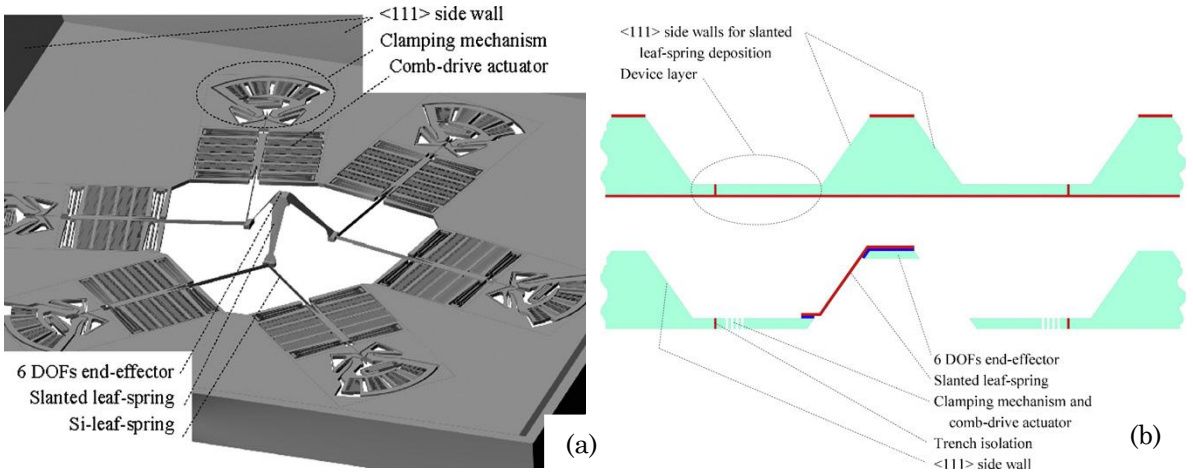

Figure 4.7 (a) The 6D precision manipulator with clamping mechanisms (b) Brief overview of the fabrication of the slanted leaf-springs [33].

relatively high suspension stiffness, shown in Figure 4.7a [33]. In addition, this group has designed slanted leaf-springs into the mechanism to convert the motion of six in-plane electrostatic comb-drives into six DOFs at the end-effector. The fabrication of these springs is based on the deposition of Si_3N_4 on a silicon pyramid, which in turn is obtained by selective crystal plane KOH etching, shown in Figure 4.7b.

Some other examples of innovative actuators include an out-of-plane micro electrostatic actuator consisting of repulsive-force rotation actuators, middle beams, converting springs and a central plate fabricated by PolyMUMPs surface micromachining technology [34]. The actuator can achieve a static out-of-plane motion of *86* μm at *200* V. The principle of actuation is based on potential difference between the aligned and unaligned fixed electrodes shown in Figure 4.8 generating an asymmetric electric field about the horizontal central line of each moving electrode. This results in upward net force acting on each moving electrode thereby pushing the moving electrodes away from the fixed electrodes. Another 2D stage driven by double-hot arm horizontal thermal microactuators integrated with a piezoresistive sensor is developed for low voltage operation and precise control [35]. Using chevron V-beams as discussed before in Section 1.3.2, the fabrication involves SOI wafer (*10* μm in

device layer, *1* μm in buried oxide layer and *325* μm in handle layer thickness) and a series of thermal oxidation, backside silicon wet etching using TMAH solution, front side silicon DRIE, metal deposition and BHF etching of oxide. The total in-plane motion of the actuator is close to *32* μm at an input power of approximately *44* mW. The long range 2D electrostatic comb-drive actuators discussed in Section 3.1 using C-DP-DP guidance flexures are also fabricated using similar process flow using SOI wafers [36].

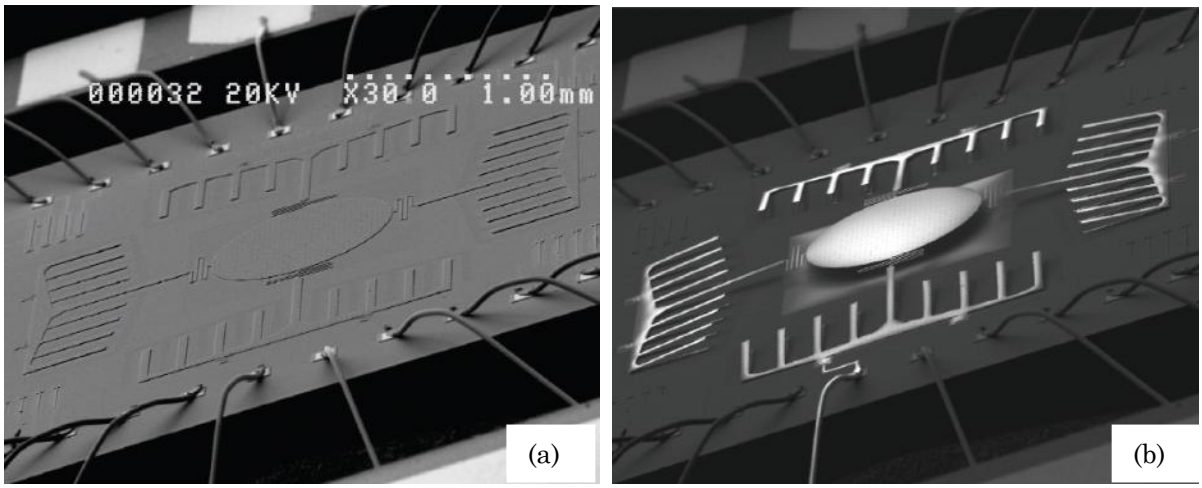

Figure 4.8 SEM images of the actuator subject to voltages (a) *0* V (b) *200* V [34].

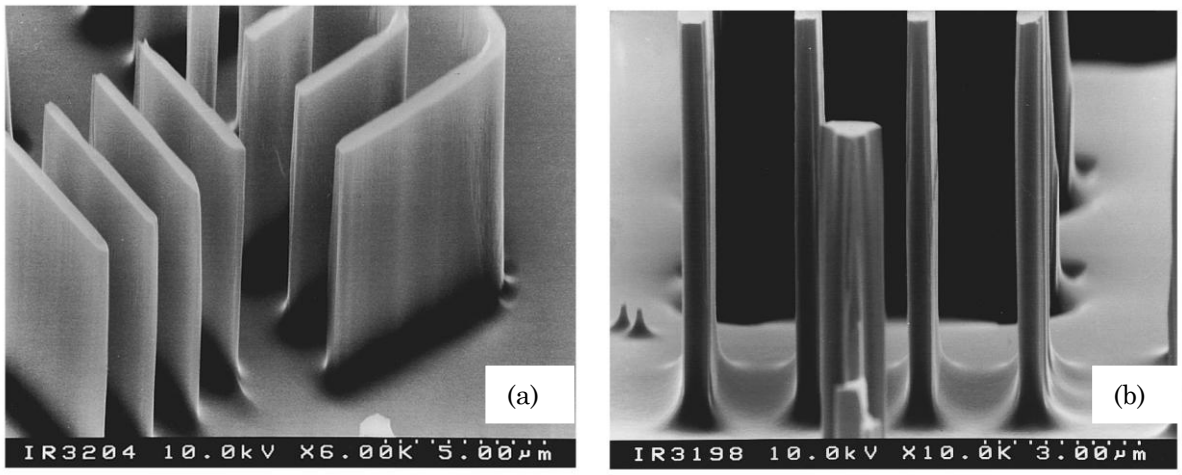

Figure 4.9 (a) High aspect ratio (*~15*) structures etched into Si with Cl_2/HBr plasma chemistry at *20* ^{0}C using a *0.3* μm thick TEOS-oxide masking layer. Etching depth is *7.2* μm. Si etch rate is *280* nm/min, selectivity *25:1*.(b) High aspect ratio (*~25*) structures etched into Si with SF_6 /O_2 /CHF_3/Ar plasma chemistry at *20* ^{0}C using a *0.1* μm thick Cr film masking layer. Etching depth is *~7.5* μm. Si etch rate is *340* nm/min [37].

One of the critical steps in the microrobotic manufacturing process is the fabrication of the bottom standing silicon tower that gives the vertical motion to the microneedle-integrated microstage. The fabrication process using DRIE is discussed in Section 4.4. A few of the related literatures which have dealt with such fabrication have been briefly discussed here.

Maintaining etch uniformity of silicon with high-aspect-ratio vertical side wall and minimal lateral undercut depends on the choice of gas phase chemistry, pressure conditions, reactant transport to the surface and product transport away from the surface. Rangelow and Loschner [37] have performed RIE with both chlorine and bromine containing plasma chemistry and fluorine containing plasma chemistry as shown in Figure 4.9. With Cl_2/BCL_3 plasma, the etch rate is between *100* to *300* nm/min with near vertical walls. The RIE lag effect has been reduced by chopping the BCL_3 gas flow in periods of *200* sec instead of permanently adding BCL_3 to Cl_2. This prevents the formation of oxidised unsaturated halogenated film onto the bottom surfaces. Comparatively, with SF_6 plasma the etch rate is *1* μm/min even at low rf power densities of *0.15* W/cm^2. This is due to the high reaction probability of fluorine with silicon compared to any other halogens (*Cl, Br, I*). Using hard masks such as Cr, Ni, Al or SiO_2 with *100* nm thickness, high-aspect-ratio (*>25*) structures can be achieved with a depth of *6* μm etched into Si with $SF_6/O_2/CHF_3$/Ar gas chemistry.

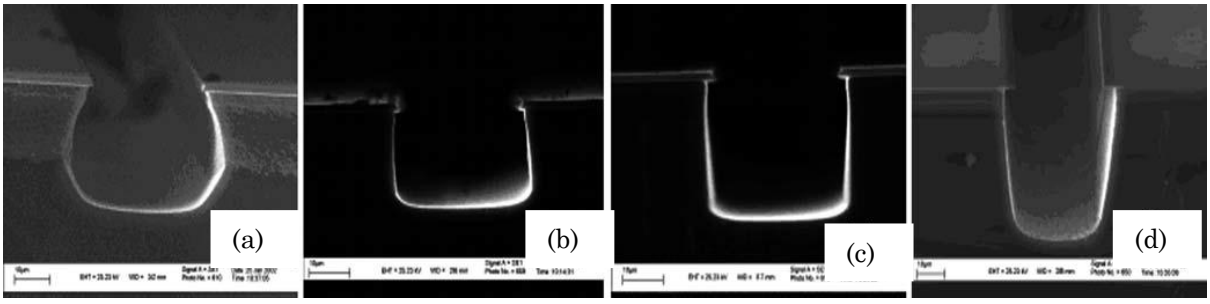

Figure 4.10 SEM cross section micrographs of *30* μm wide trenches etched at different O_2 flow rates of (a) *4* sccm, (b) *6* sccm, (c) *9* sccm, (d) *12* sccm respectively. Other conditions: SF_6: *12* sccm; system pressure: *200* mTorr, RF power: *160* W [38].

Using soft mask such as *2.5* μm thick photoresist mask (AZ*4562*), deep trenches can be achieved in SCS with $SF_6/CCl_2F_2/Ar$ or $SF_6/C_2F_8/O_2$ plasma chemistries with etch rates greater than *1* μm/min. Keeping the substrate temperature low to the range of *-50* ^{0}C to *-100* ^{0}C, can increase the etch rate to *2-5* μm/min with SF_6 plasma chemistry. Inductively coupled DRIE of silicon using SF_6/C_4F_8 gas chemistry has been characterised based on various etching variables to understand the plasma processes and the dependence of response variables on operating conditions [39]. Such variables include silicon etching rate, photoresist etching rate, uniformity, anisotropy and profile control and surface morphology. Using similar gas chemistry of $Ar/SF_6/C_4F_8$ in single-step DRIE process and holographic lithography, arrays of silicon nanopillars have been fabricated with high-aspect-ratio and controllable sidewall profiles [40].

Other works of high-aspect-ratio silicon etch studies using SF_6/O_2 chemistry have achieved anisotropic profiles with depths in excess of *100* μm [38]. It is found that etch profiles and etch rates are primarily affected by O_2 concentration and system pressure respectively, as shown in Figure 4.10. The ratio of beam depth to the mask undercut is *10:1*. Such deep features have been also fabricated using capacitively coupled RIE using $SF_6/O_2/CHF_3$ chemistry and different etch masks such as gold/chrome/aluminum film [41]. With aluminum masked silicon, the etch rate which is between *2.5 – 2.8* μm/min is *10%* faster than photoresist masked silicon. Isotropic etching properties in ICP etcher using SF_6 gas chemistry has further been investigated for fabricating arrays of microneedles [42]. Different etch variables such as pressure, vertical etching depth, lateral etching depth and ratio of vertical to lateral etching have been studied using factorial design of experiment (DOE) analysis. It is found that the vertical and lateral etching is hugely dependent on coil power and SF_6 flow rate. We will now use this information to design the fabrication process for manufacturing our sophisticated actuator structure.

Thus, the critical finding from the review of the prior art in fabrication processes of microneedles and positioning/actuation stages are:

- There are isolated reports [32, 33] of the design and fabrication of multiple axes actuators, but mostly exists as a stand-alone system rather than being a part of the parallel architecture. On the contrary, there are several reports [16, 17, 24, 28] of parallel architecture of microneedle/microprobes, but with only 1D motion capability in vertical or *z* axis. The reason for the existence of either categories of such systems but not as an integrated 3D motion based parallel architecture is the complexity of the fabrication processes designed to manufacture such devices in the first place.

4.3 Fabrication Processes

Two new fabrication process flows have been designed for manufacturing the microrobotic actuator. These two processes have been described below.

4.3.1 Fabrication process flow *1*

The fabrication starts with a (*100*) silicon wafer with low resistivity (<*0.005* Ωm) and a pre-deposited thin film of nitride (*200* nm) on top of it. SiO_2 (~*500* nm-*800* nm) is first sputtered onto this thin film of nitride. This is followed by spinning of photoresist (*PR*), baking and patterning with the ***first mask***, the microneedle. The substrate is then subjected to a CHF_3 reactive ion dry etching to transfer the pattern of the microneedles onto the dielectric stack. The PR is then stripped off using O_2 plasma etching followed by a wet anisotropic KOH etching to form the tip of the micro-needle.

A thin layer of around *100* nm – *300* nm of SiO_2 is thermally grown in a furnace, that coats the floor of the substrate along with the microneedle, acting as an etch mask for the microneedle from being etched away in the subsequent steps. Another dry RIE is performed

using CHF_3/Ar to etch the floor oxide to make way for forming the body of the microneedle in the next step. A deep vertical etch is performed using SF_6 that forms the height of the microneedle followed by thermally growing SiO_2 to sharpen the tip of the microneedle. To protect the floor oxide from being etched away during subsequent etching, a thick photoresist like SU-*8* is spun on the substrate. Chrome metal is then deposited onto this SU-*8* layer

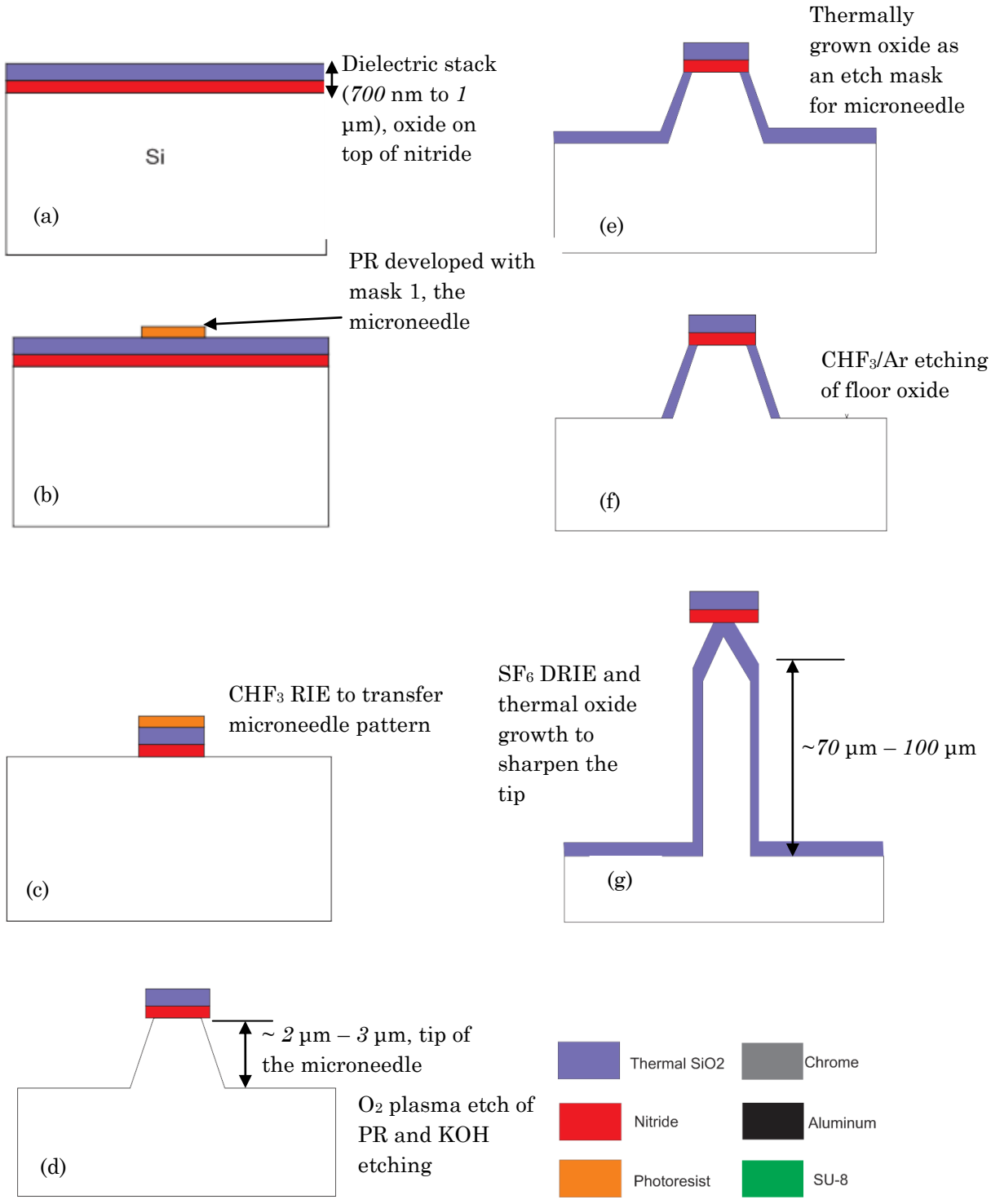

CHF_3 RIE to etch SU-*8* and floor oxide.
O_2 plasma etching of SU-*8*.

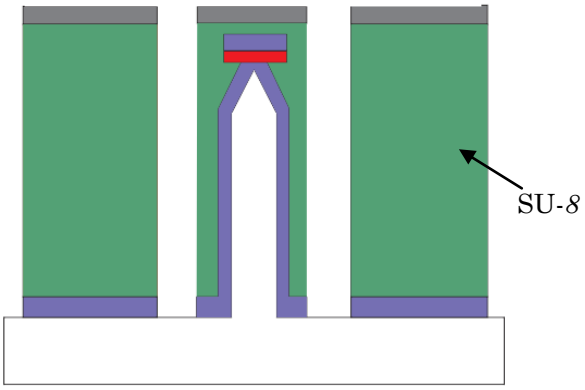

(h)

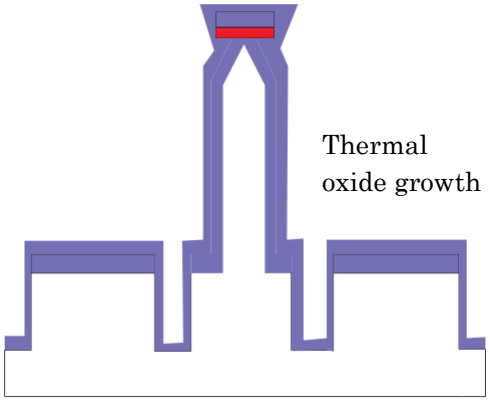

(k)

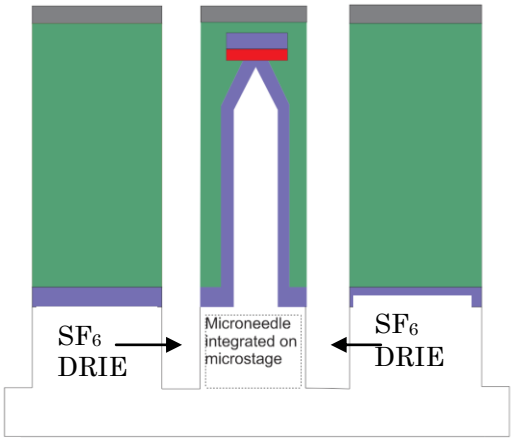

(i)

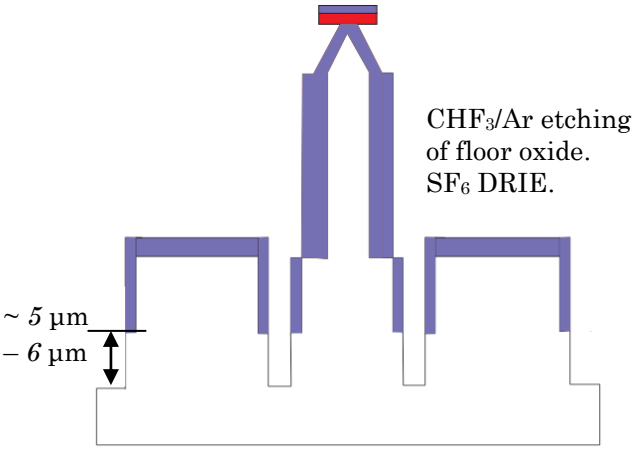

(l)

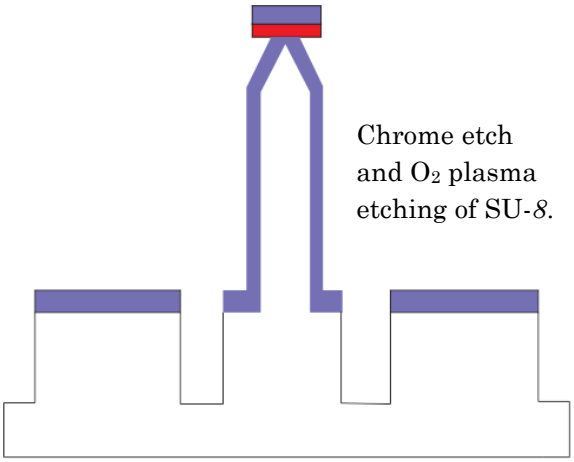

(j)

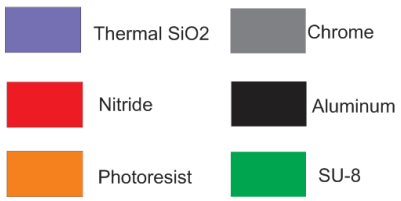

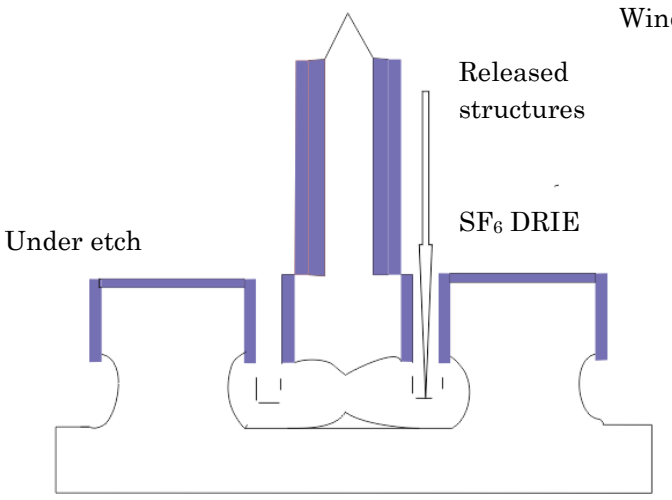

(m)

Window mask opening Substrate Si etches away

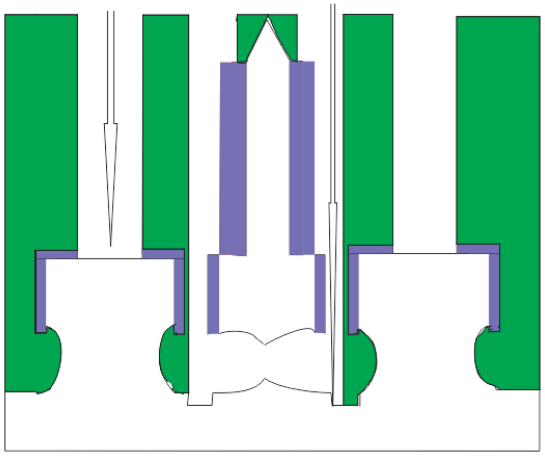

Photolithography using mask 3, metal pads. CHF_3/Ar RIE (n)

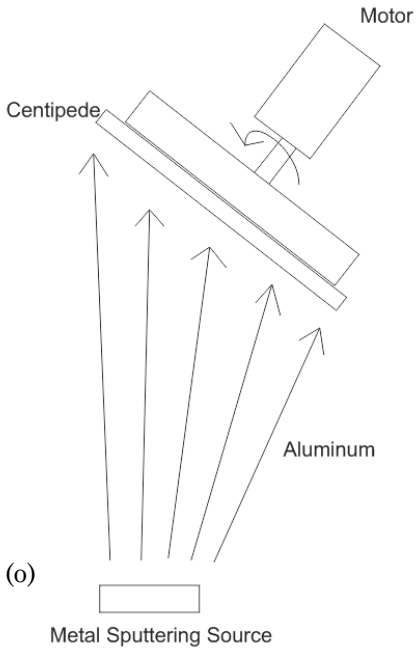

(o)

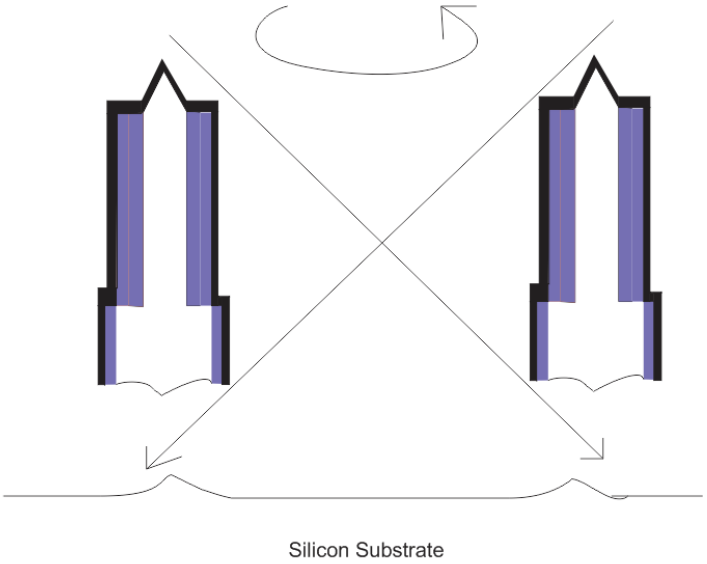

(p)

Etching of SU-*8*. Sputtering of Aluminum at an inclined angle.

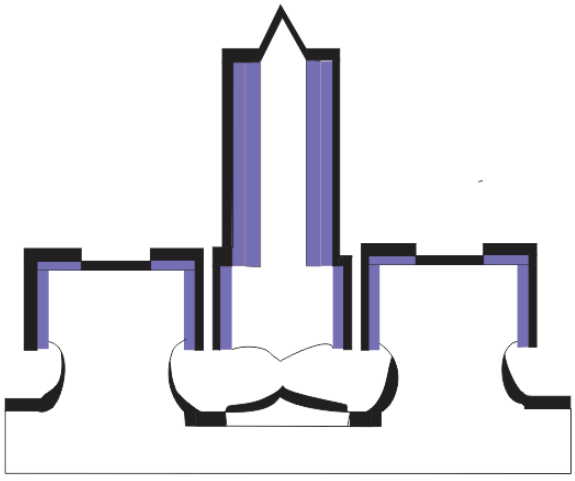

(q)

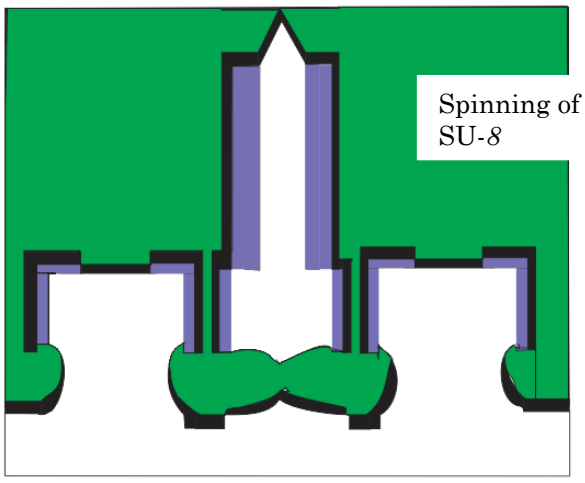

(r)

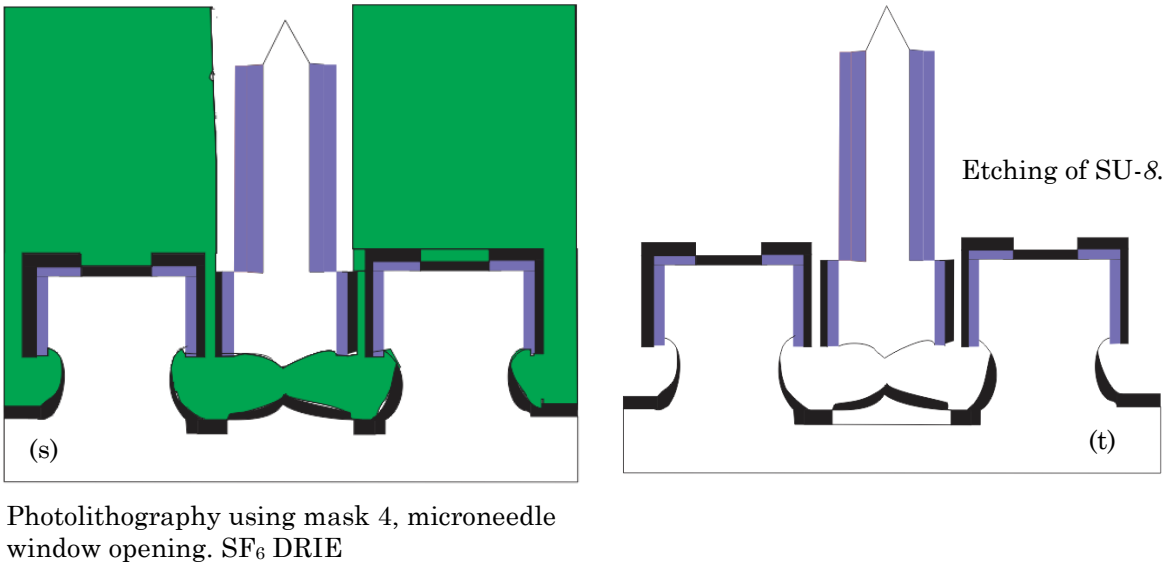

Figure 4.11 Fabrication process flow *1*. The figure is not drawn to scale.

which acts as an etch mask for forming the suspended comb-drive actuator structure.

The ***second mask***, the suspended actuator is patterned and developed using photolithography. The metal is then etched away using a chrome etch in ceric ammonium nitrate ($(NH_4)_2Ce(NO_3)_6$) and nitric acid (HNO_3) and thus the pattern is transferred from the metal to the SU-*8* layer. The SU-*8* layer and subsequently the floor oxide layer are then etched using CHF_3 RIE. The PR is stripped away using O_2 plasma etching. SF_6 deep vertical etch is next performed to form the suspended actuator structure. The chrome metal is etched away using chrome etch and SU-*8* is stripped away using O_2 plasma etching. Another layer of SiO_2 is thermally grown which acts as an etch mask for subsequent RIE. Another dry etch using CHF_3/Ar gas chemistry etches away the horizontal floor oxide which is then followed by a vertical SF_6 dry etch into silicon to make space for releasing the suspended actuator structures. An isotropic etching in SF_6 releases the suspended actuator structures. The anchored structures that are still connected to the silicon substrate are underetched by tens of microns.

Another SU-*8* layer is spun, baked, patterned using a ***third mask***, the metal pads and electrical interconnects, and developed to produce a window for laying out the connections. A dry etch is then performed in CHF_3/Ar to create the window that etches through the oxide. In this process, the substrate silicon that is not covered with PR and on which the bottom electrode will subsequently be formed, gets etched away by tens of microns as explained in Section 4.4 through Figure 4.14. SU-*8* is then etched away by a wet chemical and O_2 plasma etch. Aluminium is then sputtered for the electrical connections at an angle sufficient to provide metal coverage under the micro-stage as shown in Figure 4.11. This also provides metal connections for all interconnects. SU-*8* is additionally spun, baked, patterned using the ***fourth mask***, micro-needle window opening, and developed. This is followed a dry etch using SF_6 that etches away the metal from the microneedle. SU-*8* is then removed by a wet chemical and O_2 plasma etching step to produce the final microrobotic actuator.

4.3.2 Fabrication process flow 2

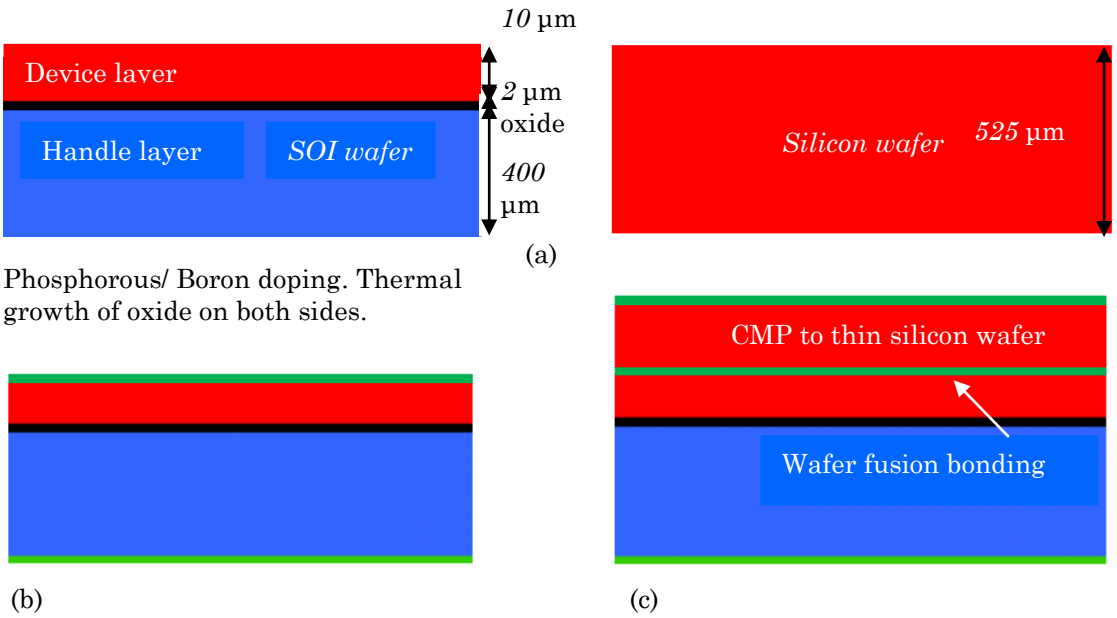

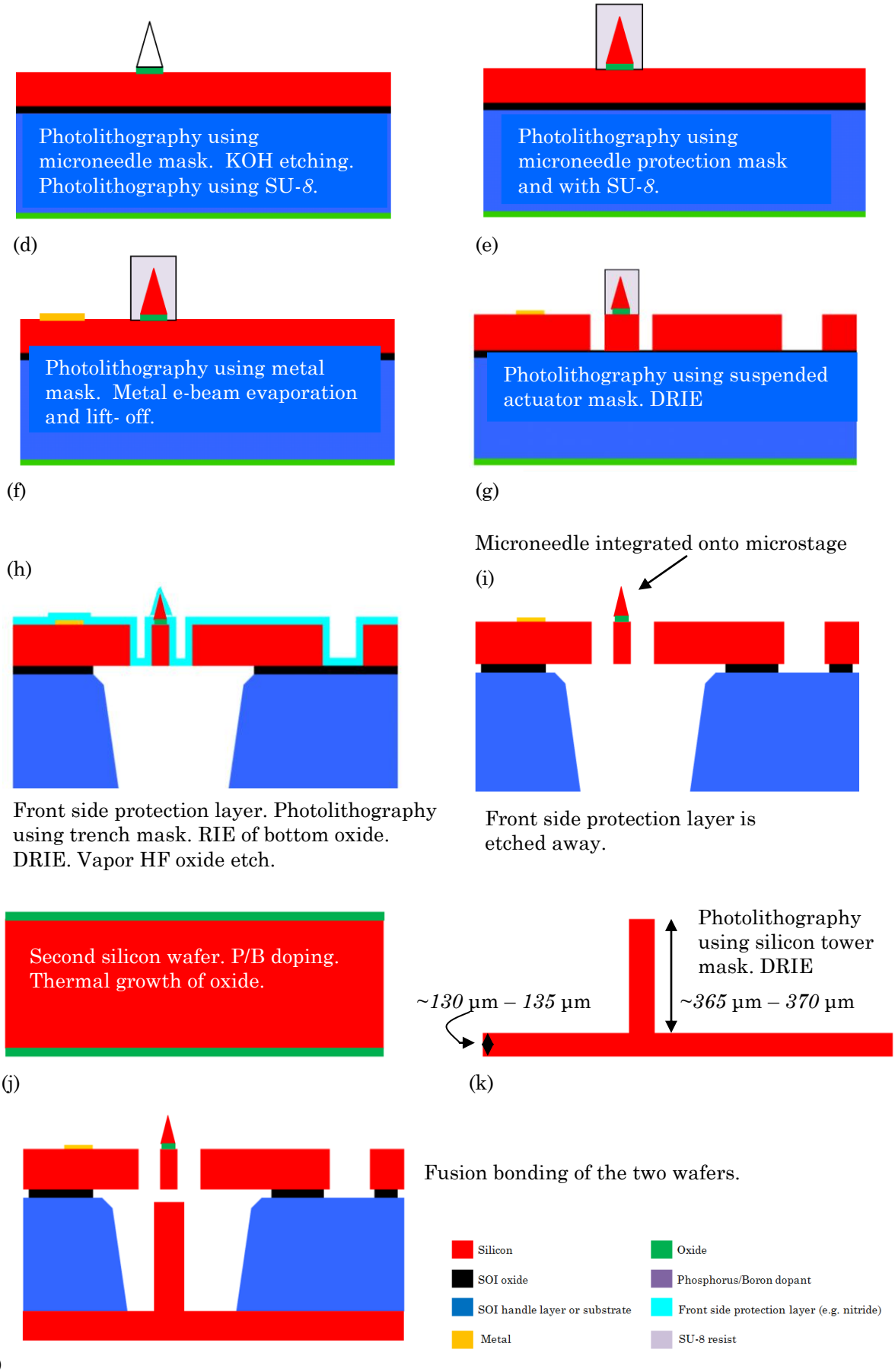

Figure 4.12 Fabrication process flow *2*. The figure is not drawn to scale.

The process starts with an SOI wafer (device layer is *10/25* μm, the oxide layer is *2* μm and the handle layer is *400* μm thick) and a silicon wafer. SOI wafer is used for the formation of the suspended structures including comb-drive actuators, spring flexure beams, suspension beams and microstage. The silicon wafer is used for the formation of the microneedle. The silicon device layer of the SOI wafer is doped with phosphorus or boron. Oxide is then thermally grown on both sides of the SOI wafer to protect the silicon from being etched away in subsequent etching. The silicon wafer is bonded with the SOI wafer using fusion bonding. The silicon wafer is thinned up to the appropriate height of the microneedle e.g. *35* μm - *50* μm using chemical mechanical polishing. Oxide is then sputtered onto the top surface of the silicon wafer that acts as an etch mask.

Using photolithography, the ***first mask***, the microneedle in patterned and the sharp tip is formed by KOH etching. The silicon is etched away outside the masked oxide region with etching stopping on the exposed buried oxide film. This oxide protects the microneedle from being electrocuted when the voltage is applied to the actuator. This helps protect the biological entities from getting electrocuted as well. SU-*8* resist is then spun and patterned with the ***second mask***, the microneedle protection, to prevent the needle from being etched away in subsequent etching steps. The wafer is then coated with a negative photoresist and lithographically patterned by exposing the photoresist with ultraviolet light through the ***third mask***, metal pads and then developing it. This is for making the electrical connections for actuating the suspended actuators. A metal stack consisting of *20* nm chrome and *500* nm gold is deposited over the photoresist pattern by e-beam evaporation. The photoresist is then dissolved to leave behind metal in the opened areas using the lift-off process.

The wafers are coated with UV-sensitive photoresist and lithographically patterned by exposing the photoresist to ultraviolet light through the ***fourth mask***, suspended actuator and then developing it. The photoresist in exposed areas is removed, leaving behind a patterned

photoresist mask for etching. DRIE is used to etch the silicon down to the oxide layer. After etching, the photoresist is chemically stripped. A front side protection material (e.g. nitride) is applied to the top surface of the patterned silicon layer. The bottom side of the wafers are coated with photoresist and is lithographically patterned using the ***fifth mask***, the trench. RIE is used to remove the bottom oxide layer. A DRIE silicon etch is subsequently performed to etch completely through the substrate layer, stopping on the oxide layer. After the etching is completed, the photoresist is removed. A wet oxide vapour HF etch process is then used to remove the oxide layer in the regions defined by the trench mask, which allows for electrical contact to the substrate and underetches the oxide layer as shown in Figure 4.14. The front side protection material is then stripped using a dry etching process. The second silicon wafer is used for fabricating the silicon tower for the vertical actuation of the microneedle. It is doped with phosphorus or boron like discussed before and then oxide is grown and photolithographically patterned using the ***sixth mask***, the silicon tower. The silicon wafer is etched away leaving behind the tower. The two wafers are then bonded using fusion bonding to produce the final actuator.

4.4 Mask design rules

The fabrication of the 4SA microrobotic actuator (excluding the microneedle) has been jointly undertaken at the Canadian Microelectronics Corporation [43] in Quebec, Canada and the Nanofabrication laboratory [44] at the University of Canterbury. The fabrication of the microstage along with the suspended actuator structure has been performed at the Canadian foundry using their SOIMUMPs multi-user MEMS process technology [45] and the fabrication of the silicon tower at the University. These two separate wafers have been further bonded in-house at the University.

The mask is designed in L-Edit *v15.2*, a 2D layout editor from Tanner EDA, as shown in Figure 4.13. The purpose of designing mask is to ensure the maximum probability of successful fabrication. The design rules are a set of requirements that are defined by the limits of the fabrication process that in turn are defined by the capabilities of the individual process steps. The minimum design rules are defined by the resolution and alignment capabilities of the lithography and resolution and uniformity of the etching systems. It is to be noted that minimum feature sizes and spaces for all the mask layers and their overlay accuracies are vital. Design rules define the minimum feature sizes and spaces for different masks and overlay accuracies between different mask layers. The mandatory boundary conditions include minimum line widths and spaces to ensure compatibility with the lithographic and etch process tolerances. Violating these rules will lead to missing, undersized, oversized or fused features.

Table 4.1 outlines the different mask layer names, thicknesses and the objective of each of these lithography steps. Table 4.2 lists the minimum and maximum feature sizes for the structures to be etched in silicon. There is no upper limit on the maximum length for features patterned in SOI layer but they need to have a minimum width of *6* μm. Otherwise the structures may be released from the substrate due to the undercutting of the oxide layer when the exposed oxide regions are being removed during the HF vapor process. For SOI patterns less than *6* μm in width, the SOIMUMPs design criteria [45] requires a maximum length of *100* μm for structures anchored at one end and *500* μm for structures anchored at two or more ends. The problem with long released silicon structures is that they can lead to out-of-plane distortions. Most commonly they tend to curl out of plane due to the intrinsic stresses in the silicon layer, and the surface stress caused by the doping process. For example, silicon beams with *2* μm in width and anchored at one end will curl out-of-plane to a greater extent compared to silicon beams of the same width but anchored at both ends.

The purpose of having a separate SOI hole mask layer is to extract holes from a digitised feature. In this case, it is used to fabricate a hole in the central microstage for post assembly of a microneedle on it. The maximum and minimum feature sizes ensure the mechanical integrity of the substrates which must be strictly followed. Another critical parameter is the amount of silicon to be etched during DRIE so that there are no non-uniformities during the etching process. For mask *2*, the SOI suspended actuator, the amount of silicon etched must be only *33%* of the chip area, i.e. *3.6* mm^2 for the actuator chip area of *3.3* mm × *3.3* mm. For mask *4*, the trench, the amount of substrate (handle layer) etched must be only *20%* of the chip area, i.e. *2.2* mm^2.

Table 4.3 tabulates the critical rules of overlay tolerances between the different mask levels. The edge-to-edge overlay tolerance between the metal mask and SOI mask layers indicate that the metal layer must be enclosed by the SOI layer on all edges by at least *3* μm to avoid masking during DRIE. Similarly the center-to-center overlay tolerance between the

Table 4.1 Mask layer names, thicknesses and lithography levels.

Mask layer	Thickness (μm)	Lithography level	Purpose
Metal	*0.52* (*20* nm chromium and *500* nm gold)	Metal	Electrical interconnections
Silicon (device layer)	*25.0*	SOI	Define structures in the device layer of SOI wafer
Oxide	*1.0*		
Substrate (handle layer)	*400*	Trench	Define through-hole structures in the handle layer of SOI wafer to suspend the structures

Table 4.2 Mask layer design rules.

Mask layer	Minimum feature size (μm)	Minimum space (μm)	Maximum feature length (μm)	Maximum patterned (*etched*) area (mm^2)
Metal	*3*	*3*	*5000*	*20*
SOI	*2*	*2*	Unlimited for width > *6* μm	*33*
SOI hole	*3*	*3*	N/A	N/A
Trench	*200*	*200*	*5000*	*20*

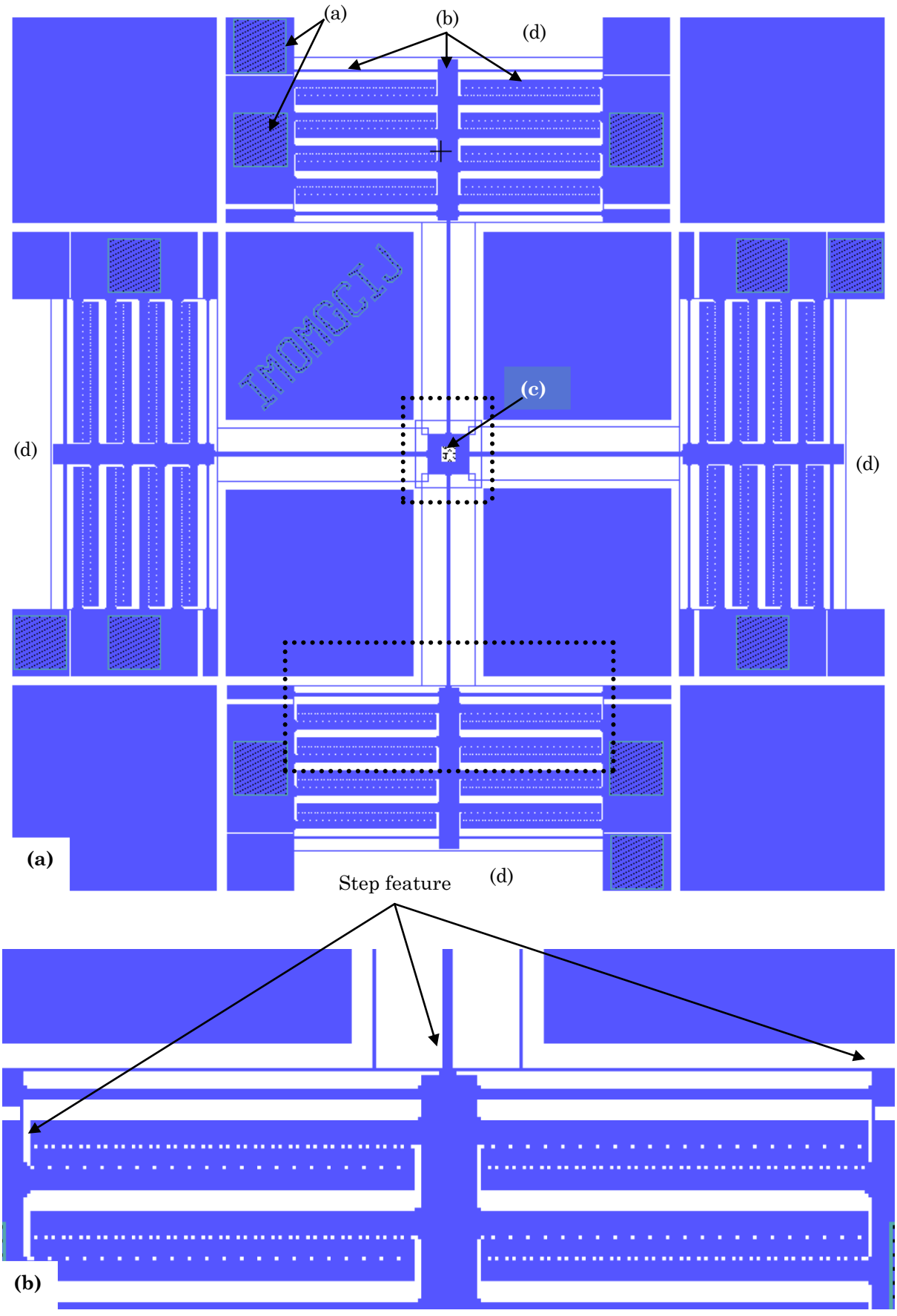
(a)
(b)
(d)
(c)
(d)
(d)
(a)
Step feature
(d)
(b)

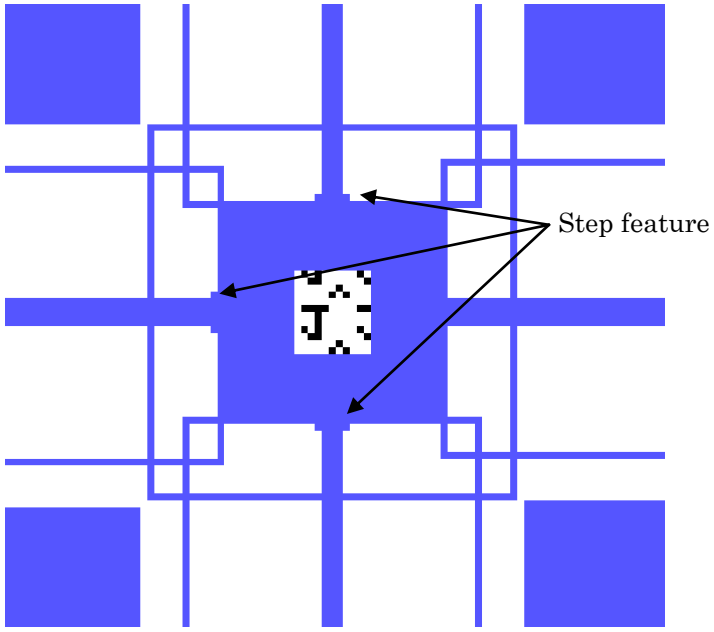

(c)

(a) Mask *1* = Metal pads; (b) Mask *2* = SOI suspended actuator; (c) Mask *3* = SOI hole; (d) Mask *4* = Trench (the white region under the blue silicon substrate)

Figure 4.13 Mask layout as imported from L-Edit *v15.2* having four masks, namely metal pads, SOI suspended structure, SOI hole and trench **(a)** Full preview of the mask **(b)** step feature at the end of the beams to avoid cracking **(c)** Zoomed in view of the step features.

trench and SOI mask layers accounts for the bottom side to the top side lithography alignment. The edge-to-edge overlay tolerance between the trench and SOI mask layers accounts for the etch profile during backside DRIE up to the oxide layer. The SOI and metal mask layers are light field (dark tracks in a light background), typical for positive resist and etching tracks. The trench and SOI hole mask layers are dark field (light areas in a dark

Table 4.3 Rules for overlaying of different masks.

Mask layers	**Overlay tolerance (µm)**	
	Centre to centre	**Edge to edge**
Metal to SOI	*±3*	*±3*
Trench to SOI	*±5*	*< 50*

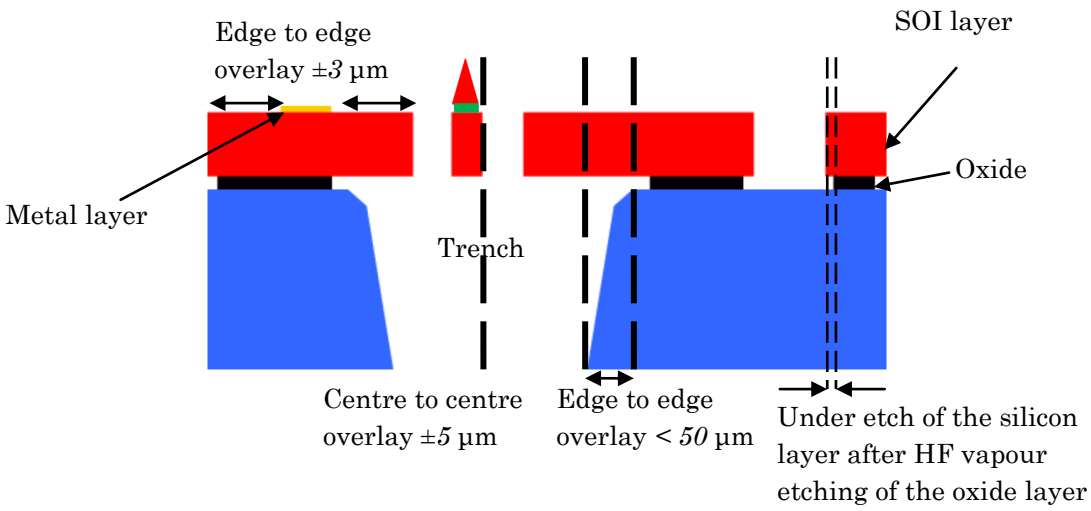

Figure 4.14 Overlay tolerances of different mask layers.

Table 4.4 Design dimensions of the manufactured 4SA microrobot.

Structural parameters	
Spring flexure beams	$w_s = 8$ µm, $h_s = 25$ µm, $l_s = 550$ µm
Tethering beams	$w_t = 10$ µm, $h_t = 25$ µm, $l_t = 813$ µm
Area of microstage	150 µm × 150 µm with a 50 µm × 50 µm hole at the center for loading microneedle
Parallel plate actuator gap	~40 µm – 45 µm
Height of silicon tower	~365 µm – 375 µm
Comb-drive actuator	$i = 360$, $t_f = 3$ µm, $gs_f = 3$ µm, $h = 25$ µm
Length of comb-finger	30 µm
Opposite electrode spacing	10 µm

background), typical for positive resist and contact holes. The thickness of the suspended actuator structure is not a design feature, but a process feature that depends on the number of masks used and the thickness of the actuators (*25* µm for manufactured 4SA microrobot). The die, as shown in Figure 4.13a takes up roughly *3.3* mm × *3.3* mm space on the wafer. When it is bonded with the bottom wafer containing the standing silicon tower, the total surface area of the chip increases to *5* mm × *5* mm as shown in Figure 2.1b. During the HF vapor etch of the remaining oxide after the DRIE silicon etch of the substrate using the trench mask, as described in Section 4.3.2, there is minor underetching of the buried oxide as shown in Figure 4.14. Thus the mask design should have the SOI feature be placed at a distance more than *50*

μm from the edge of the trench feature, if the size of the SOI feature is greater than *10* μm on a side. This ensures the silicon features to remain anchored to the substrate after the DRIE trench and oxide HF vapour etch. Further, note the step structure added at the intersections of the beams and anchored structures and microstage. This is done to mechanically strenghten the structure and avoid cracking at these intersections when the protective frontside material (e.g. nitride) is deposited prior to the back side trench etching of the silicon handle layer. The design dimensions of the manufactured 4SA microrobot are demonstrated in Table 4.4. The measured fabricated dimensions are tabulated in Table 4.6.

4.5 Formation of nanopillars during SiO_2 etch study

Different steps involved in the fabrication of the 4SA microrobot including thermal oxidation, metal deposition using sputtering and evaporation, KOH and SF_6 etching of silicon and etching of SiO_2 using CHF_3/Ar gas chemistry, have been characterised to understand the effect of etch parameters on the final geometry. Nonetheless, only the etch study of SiO_2 is presented here due to some interesting results observed.

P-type silicon wafer (*100*) with resistivity of *1-10* Ωcm is cleaned through a wet chemical etch process, using the RCA cleaning method. This desorbs the ionic and heavy metal atomic contaminants and removes the thin film of native oxide on its surface. *350* nm film of oxide is thermally grown on a silicon wafer in a tube furnace temperature of 1000^0C using wet oxygen at 95^0C for *2* hours. The thickness of the oxide is measured through the technique of *in situ* ellipsometry [46], a non-invasive measurement technique to obtain the optical properties of a sample material by means of the reflected light waves. *1.8* μm thick photoresist AZ*1518* is then spun onto the oxide, soft/hard baked, pattern transferred and developed, as shown in Figure 4.15a. Soft baking of PR involves heating the PR for almost *2* minutes at 95^0C in an oven compared to hard baking which occurs at almost 185^0C for *30*

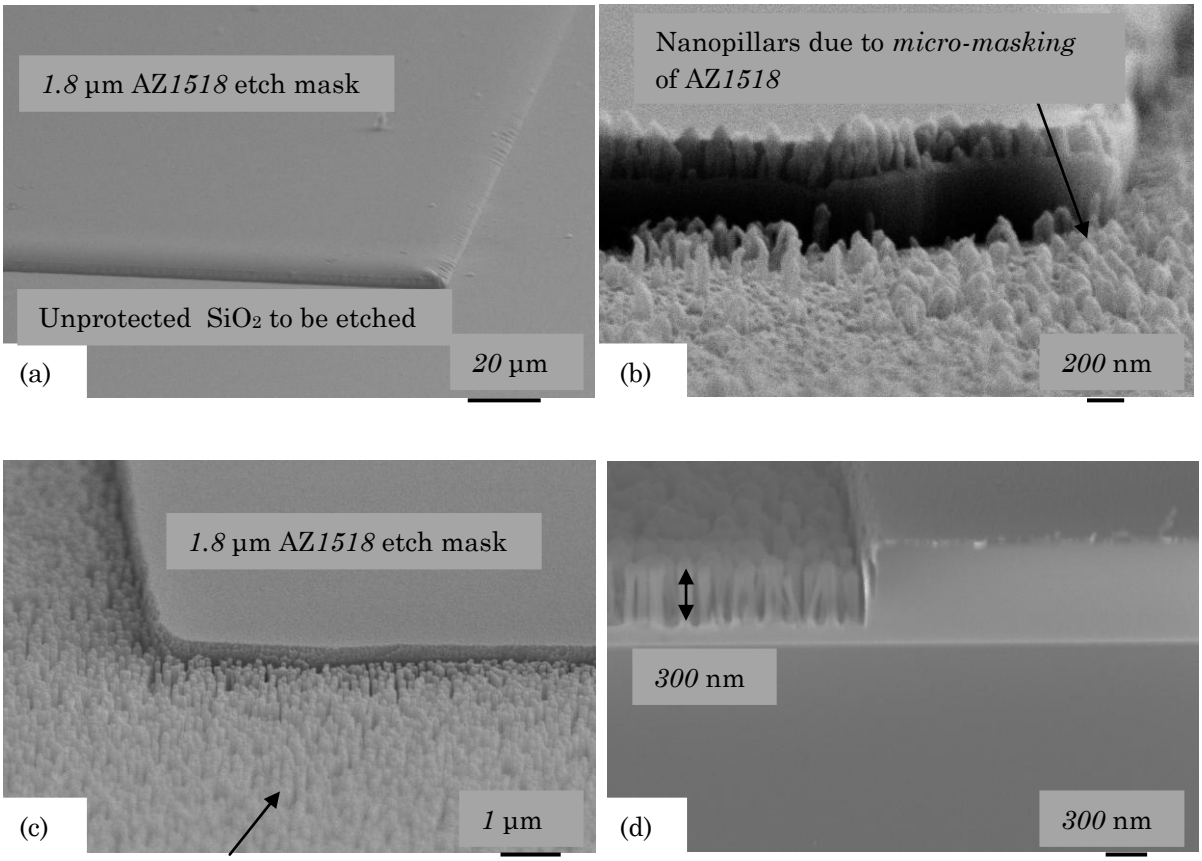

Figure 4.15 SEM images of anisotropically etched SiO_2 using CHF_3/Ar gas chemistry (a) PR AZ*1518* spun onto oxide, soft baked, pattern transferred and developed (b) Case I RIE (c) Case II RIE (d) Case III RIE. Etching has been performed for *35* minutes.

Table 4.5 RIE of SiO_2 using CHF_3/Ar gas chemistry. The common average etch rate has been observed to be around *40* nm/min. Power = *200* W, Cryogenic temperature = *253* ^{0}K (*-20* ^{0}C), Electrode = NiCr, Substrate Bias = *13.56* MHz, Wafer Bias Potential = *-430* V.

Cases	CHF_3/Ar flow rate (sccm)	Pressure (mTorr)
Case I	*40/25*	*20*
Case II	*25/25*	*30*
Case III	*40/0*	*10*

minutes. This photoresist acts as an etch mask for the subsequent etching of the oxide film. This is followed by etching of the floor oxide in an Oxford PlasmaLab*80* system using CHF_3/Ar gas chemistry and baseline parameters as tabulated in Table 4.5 using information based on the works of Rueger et al [47] and Gatzert et al [48]. The SEM images are

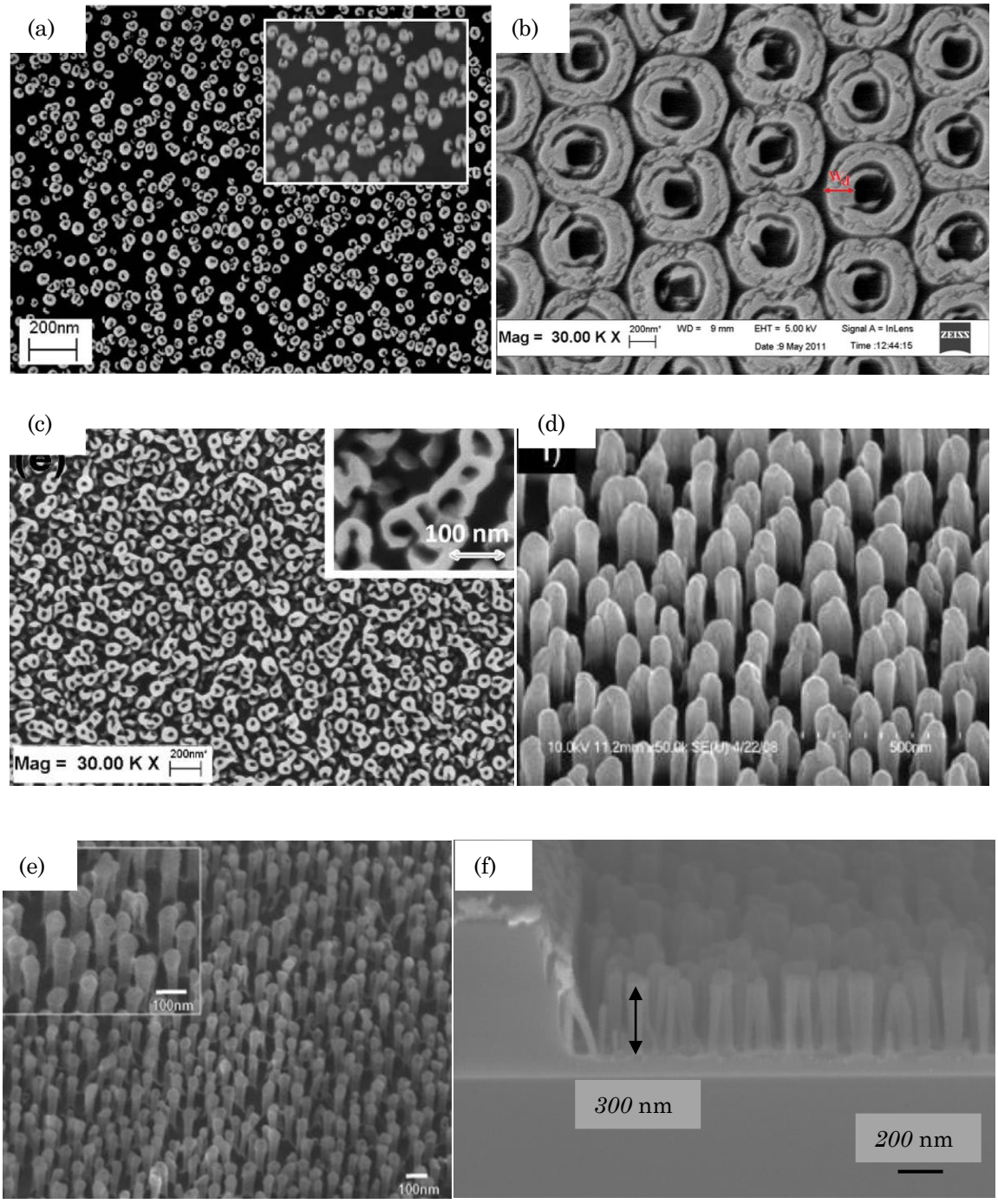

Figure 4.16 SEM image of (a) fluorocarbon nanostructure deposited on SiO_2 surface after *7* min of RIE [49]. (b) Nanoring around pits after *7* min of RIE [50]. (c) PMMA/SiO_2 sample after *6* min of RIE [51]. (d) Dot patterns formed after 1 min O2 RIE and subjected to CF4 RIE for 4 min [52]. (e) Dot patterns after *1* min O_2 RIE and *10* min CF_4 followed by immersion in ethyl acetate, subsequent heating for *1* hour at 900^0C and cleaning [52]. (f) Nanopillars formed in our experiments after *35* min of Case III RIE.

illustrated in Figure 4.15a to d. Record is made for RIE after every *2-4* minutes. These images show the duty-cycle etching of SiO_2 after *35* minutes. It has been observed that mixing Argon with CHF_3 results in more homogeneous oxide etching, rather than using just CHF_3.

Oxide etch rates are dependent on the inductive power and the etching mechanism is a reactive sputtering or direct reactive ion sputtering in which the energetic ion species are reacting with the oxide and producing volatile etch products. As the pressure increases, the oxide etch rate increases as the average ratio of fluorine/chlorine of the bombarding ion flux increases. This dependence on pressure is due to the fact that with increasing pressure inside the reactor, there is less dissociation due to the sharing of energy between a larger number of parent molecules [47]. Further the etch rate is dependent on the flow rate of CHF_3 and Ar. Using solely Ar (purely physical) or CHF_3 (purely chemical) produces the lowest etch rate. With CHF_3 plasma, polymer-forming radicals deposited on the substrate form a protective barrier layer consisting of various bonds of chlorine or fluorine. This layer prevents the fluorine radical from reaching the surface of the SiO_2 to be etched and also for volatile compounds such as SiF_4 to diffuse out [48]. Min et al [53] have studied the mechanism of re-deposition of etch products on the sidewall during RIE of step-shaped SiO_2 pattern using CF_4/Ar gas chemistry. They have found that particles sputtered from the bottom surface are re-deposited on the sidewall leading to the formation of a thick passivation layer consisting of Silicon oxide, Si_xO_y and C_xF_y on the bulk SiO_2. This decreases the etch rate of SiO_2 significantly.

PR as an etch mask should be hard baked as it's etch rate is similar to the rate of SiO_2. Referring to Figure 4.15, the growth of nanopillar like structures on SiO_2 can be clearly observed. These towers are *50* nm - *80* nm in diameter and almost *300* nm - *400* nm in height. One possible hypothesis is the formation of *micro-masks* of hard baked organic photoresist AZ*1518* which prevents the oxide from getting etched away. These *micro-masks* are almost

the same height as the oxide layer which has been protected by the photoresist. Using NiCr or chromium metal as a masking material instead of hard baked AZ*1518* photoresist can avoid micro-masking and can help getting rid of these nanopillars, since NiCr is significantly resistant to RIE [54]. Nonetheless, these ring-shaped nanopillars can have useful applications in fuel cell membranes, filters for biochemical MEMS, etc [49]. Such plasma nanotexturing in a controlled fashion can be used as a significant tool in surface chemistry, increasing protein adsorption as high-intensity protein microarays, manufacturing nanoimprint masks for organic polymers and photovoltaics among others [55].

Some other works have also discovered such nano structures. For example, while etching *300* nm thick SiO_2 with CHF_3/O_2 (*45/5* sccm, *30* mTorr) gas chemistry in a capacitive coupled plasma reactor, nano ring-shape pattern of fluorocarbon macromolecules have been observed [49]. These patterns are around *50* nm in diameter, *10* nm in wall thickness and *50* nm in height after *7* minutes of etching as shown in Figure 4.16a. They have varied the etching time, chamber pressure and types of substrates to obtain different variations of such nano structures. Other examples include similar nano-rings with different shapes observed during electron beam lithography (EBL) and RIE of *600* nm thick SiO_2 using CHF_3/O_2 (*50/5* sccm, *6.66* Pa) gas chemistry and *200* nm thick poly methyl methacrylate (PMMA) etch mask for more almost *8* minutes (Figure 4.16b) [50]. Increasing the etching times results in increasing width of the rings. The readers may refer to these papers to understand the chemistry of the formation of these rings. In another work [51], researchers have observed dot-like nanotextures containing small Al particles by a mask-less etching of PMMA on a SiO_2 surface for *60* seconds with CHF_3/Ar (*25/25* sccm, *30* mTorr) gas chemistry (Figure 4.16c). Further etching of up to *2* minutes, resulted in high-density ring-shaped nanomasks with an outer diameter of *80* nm and a wall thickness of *20* nm. Another case of such high-aspect-ratio pillar-like structures have been observed over a large area of quartz surface spin-

coated with PMMA while etching with CF_4/O_2 gas chemistry [52]. This has been combined with engineered viral particles derived from hepatitis *B* virus capsid to develop a 3D assay system for early detection of disease markers.

Comparing our nanopillar structures (Figure 4.16f) with the nano structures from the works discussed above (Figure 4.16a-e), the similarity of shape and structure can be observed, although in our case, the gas chemistry and etch mask used is different from the above discussed recent works. Further investigation into the morphology of these nano structured pillars would be important to understand its potential applications.

4.6 Fabrication of bottom silicon tower and SEM of the 4SA microrobot

The silicon tower has been separately fabricated and bonded with the suspended actuator silicon wafer at the University of Canterbury. The fabrication starts with a *p-type* (*100*) silicon wafer highly doped with phosphorus and very low resistivity (*<0.005* Ωcm), so that it is highly conductive. The wafer is given a standard RCA clean as described above in Section 4.5 along with plasma etching treatment for two minutes to remove any polymer and native oxide layer from the wafer surface. The substrate is then diced using an automatic

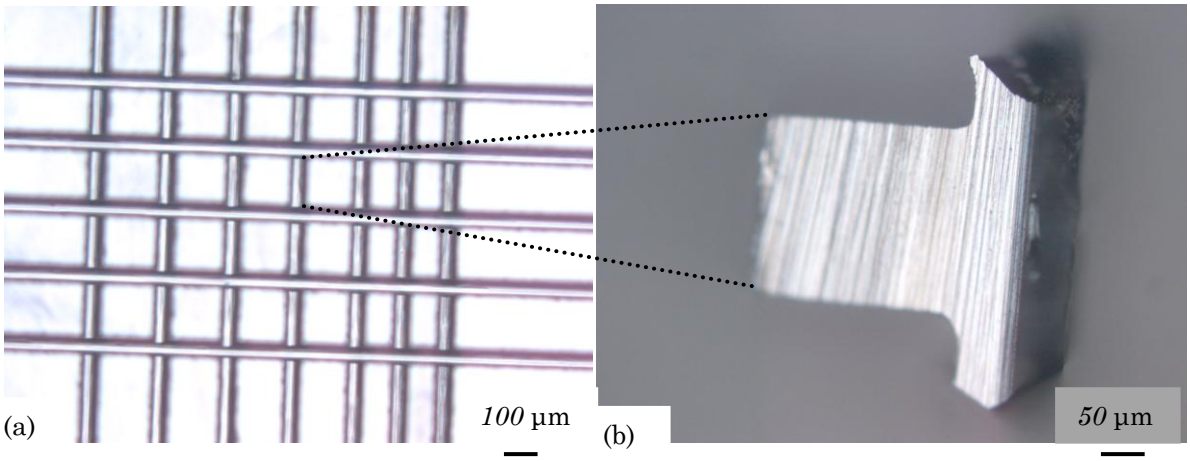

Figure 4.17 Optical microscopy images of (a) Diced silicon structure (b) Silicon tower after being diced from the substrate in (a) placed sideways having dimensions *220* µm × *220* µm × *375* µm.

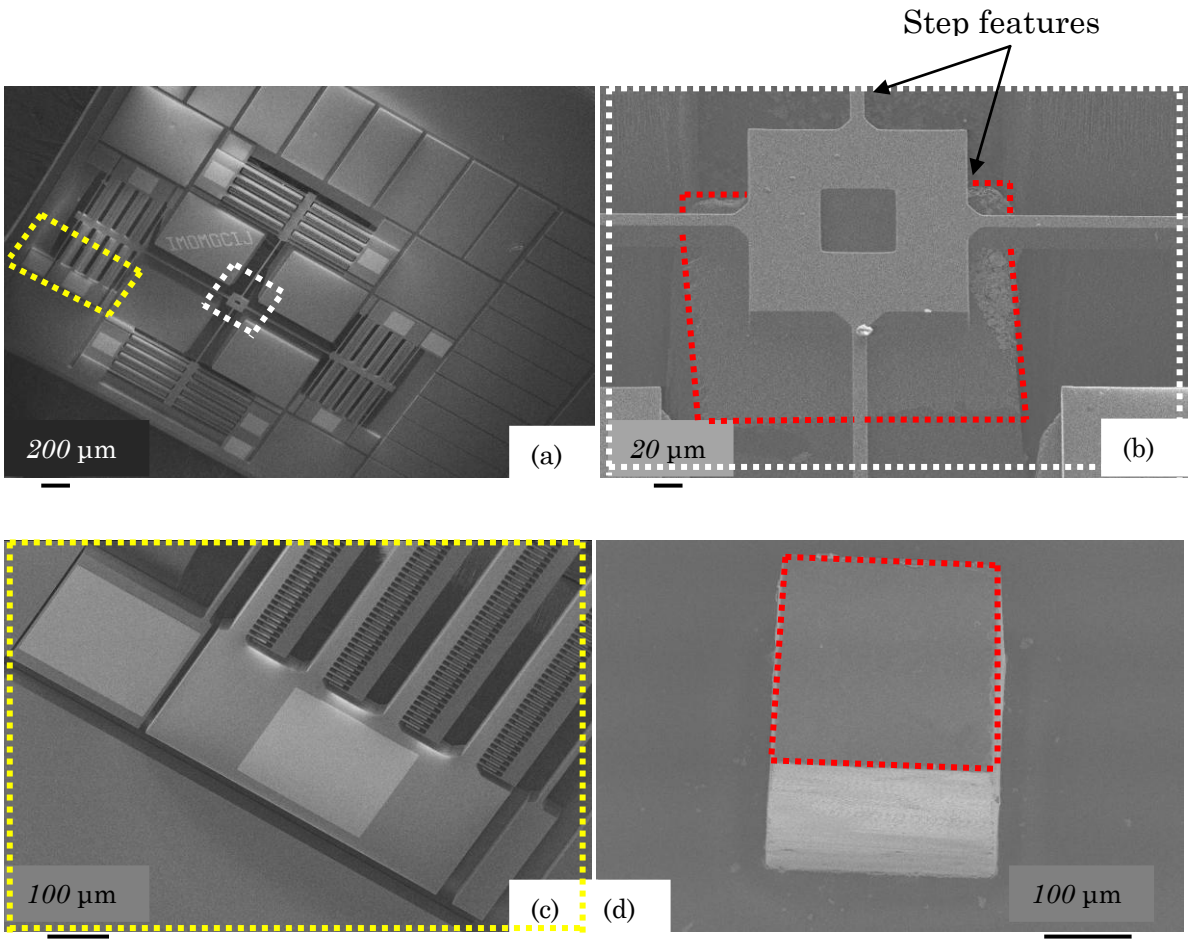

Figure 4.18 SEM images of the 4SA microrobotic actuator without the microneedle. (a) Full preview of the actuator (b) Zoomed in view of the parallel-plate actuator with microstage and silicon tower underneath (c) Zoomed in view of the actuator (d) Silicon tower (~*375* µm in height).

dicing saw (Tempress Model *602*) that uses a high speed (*25000* - *30000* rpm) diamond impregnated blade to make slicing on the substrate as shown in Figure 4.17a. The substrate is then transferred to a separate dish and carefully separated along the diced lines with tweezers. The silicon towers formed are on average *220* µm × *220* µm × *375* um in dimensions. The SEM image of the standing tower is shown in Figures 4.18b to c and the optical image of the tower placed sideways in Figure 4.17c. Another *p-type* (*100*) silicon wafer highly doped with phosphorus and with very low resistivity (*<0.005* Ωcm) is cleaned as mentioned above and then sputtered with *255* nm of aluminum using a DC voltage Magnetron sputterer (Edwards Auto*500* DC/RF Magnetron Sputtering System). After spinning *1.8* µm AZ*1518* photoresist

Table 4.6 Measured dimensions of the manufactured 4SA microrobot from ten different samples.

	Structural parameters
Spring flexure beams	$w_s = 7.81\text{-}8.23$ μm, $h_s = 25$ μm, $l_s = 548.31\text{-}551.21$ μm
Tethering beams	$w_t = 9.41\text{-}10.93$ μm, $h_t = 25$ μm, $l_t = 811.95\text{-}814.67$ μm
Area of microstage	*150* μm × *150* μm with a *50* μm × *50* μm hole at the center for loading microneedle
Parallel plate actuator gap	*~40* μm – *45* μm
Height of silicon tower	*~365* μm – *375* μm
Comb-drive actuator	$i = 360$, $t_f = 2.8\text{-}3.6$ μm, $gs_f = 2.7\text{-}3.4$ μm, $h = 25$ μm
Length of comb-finger	*29.77-31.45* μm
Opposite electrode spacing	*9.11-11.98* μm

onto the aluminum coated silicon substrate, it is baked, pattern transferred and developed with a square mask (*230* μm × *230* μm). Aluminium is then wet-etched using *40%* buffered HF solution for *3-5* minutes in the regions not covered by the square mask.

Aluminium is used as an interface between the tower and the silicon substrate to ensure better contact and conductivity between these surfaces. For the vertical motion of the microstage, the DC voltage is applied to this entire silicon substrate. This tower is then bonded onto the silicon substrate over the aluminum pattern using ESL*9913* high conductive silver paste from ESL Electroscience. Following this step, the suspended actuator silicon wafer is then bonded with this silicon tower wafer using the same conductive paste to produce the final chip as shown in Figure 4.18b. The scanning electron micrograph images have been captured using Raith*150* electron beam lithography system. The measured fabricated dimensions of the 4SA microrobot accumulated from *10* different samples are recorded in Table 4.6.

4.7 Closure and original contributions

This chapter presents two new fabrication processes for manufacturing the 4SA microrobot with an integrated microneedle and bottom silicon tower for vertical motion of the actuator. The first process involves the fabrication using four masks and a single silicon wafer. The

second process involves six masks, two silicon wafers and one SOI wafer bonded to fabricate the final structure. The 4SA microrobot fabricated using the second process has been jointly manufactured at a Canadian clean-room facility and the University. The design, fabrication process flow, types of materials to be used and dimensions have been provided to the clean-room facilities. The mask design rules followed while designing the different mask layers to maintain mechanical integrity of the actuator post-fabrication have also been discussed. Such rules take into account underetching, overlay tolerances, minimum feature sizes and spaces among others. Some interesting results from the SiO_2 etch study have also been presented which needs to be further investigated for future potential applications. Etching of the SiO_2 using CHF_3/Ar gas chemistry has resulted in nanopillar structures which have been hypothesised to be formed due to micro-masking of the photoresist particles that prevents the oxide from getting further etched away. These towers are *50* nm - *80* nm in diameter and almost *300* nm - *400* nm in height. Finally the SEM images of the fabricated 4SA microrobotic actuator (without the microneedle) have been illustrated. The following Chapter 5 will discuss the characterisation of motion performance from the electrical tests of the 4SA microrobot.

Chapter 4 makes the following original contributions to the frontier of MEMS fabrication:

- The first fabrication process designed adds several steps to the SCREAM (Single-crystal reactive etching and metallisation) process in the beginning to fabricate microneedles integrated to the 3D actuator and steps to protect this microneedle using SU-*8* from further etching in subsequent steps. This process involves just a single silicon wafer without the need for silicon-on-insulator (SOI) wafers and wafer bonding techniques.
- The second fabrication process designed adds several steps to the SOIMUMPs (Silicon-on-Insulator Multi-User MEMS processes) including steps to fabricate the microneedle

atop the microstage, protecting this microneedle from subsequent etching steps and fabricate the bottom silicon tower including wafer bonding.

- We have discovered formation of nanopillars during characterisation phase of developing high-aspect ratio structures integral to our microrobot. Etching of the SiO_2 using CHF_3/Ar gas chemistry has resulted in nanopillar structures which have been hypothesised to be formed due to micro-masking of the photoresist particles that prevents the oxide from getting further etched away. Further investigation into the morphology of these nano structured pillars would be important to understand its potential applications.

BIBLIOGRAPHY

[1] K.A. Shaw, Z.L. Zhang and N.C. MacDonald, "SCREAM I: a single mask, single-crystal silicon, reactive ion etching process for microelectromechanical structures," *Sensors and Actuators A: Physical*, vol. 40, pp. 63-70, 1994.

[2] N. C. MacDonald, "SCREAM MicroElectroMechanical Systems," *Microelectronic Engineering*, vol. 32, pp. 49-73, 1996.

[3] K.A. Shaw, Z.L. Zhang and N.C. MacDonald, "Microstructures and single mask, single-crystal process for fabrication thereof," US Patent #5,719,073, 1998.

[4] A. Jazairy and N.C. MacDonald, "Planar very high aspect ratio microstructures for large loading forces," *Microelectronic Engineering*, vol. 30, pp. 527-530, 1996.

[5] KF. Bohringer, B.R. Donald and N.C. MacDonald, "Single Crystal Silicon Actuator Arrays for Micro Manipulation Tasks," in *IEEE Workshop on MEMS*, San Diego, California, 1996, pp. 7-12.

[6] Z.L. Zhang and N.C. MacDonald, "Compound stage MEM actuator suspended for multidimensional motion," US Patent # 5,726,073, 1996.

[7] S.A. Miller, K.L. Turner and N.C. MacDonald, "Drive electrodes for microfabricated torsional cantilevers," US Patent #6,000,280, 1999.

[8] S.A. Miller, N.C. MacDonald and Y. Xu, "Microfabricated torsional cantilevers for sensitive force detection," US Patent # 6,073,484, 2000.

[9] Y. Xu, N.C. MacDonald and S.A. Miller, "Integrated micro-scanning tunneling microscope," *Applied Physics Letters*, vol. 67, pp. 2305-2307, 1995.

[10] S.A. Miller, K.L. Turner and N.C. MacDonald, "Microelectromechanical scanning probe instruments for array architectures," *Reveiw of Scientific Instruments*, vol. 68, pp. 4155-4162, 1997.

[11] M.P. Rao, M.F. Aimi and N.C. MacDonald, "Single-mask, three-dimensional microfabrication of high-aspect-ratio structures in bulk silicon using reactive ion etching lag and sacrificial oxidation," *Applied Physics Letters,* vol. 85, pp. 6281-6283, 2004.

[12] K. Subramanian, "Single mask, multiple level single crystal silicon processes: MEMS out-of-plane actuators and 3D wire arrays," PhD, Electrical Engineering, Cornell University, New York, 2003.

[13] K. Subramanian, X.T. Huang and N.C. MacDonald, "Three dimensional high aspect ratio micromachining," US Patent # US2004/0198063 A1, 2004.

[14] K. Subramanian, X.T. Huang and N.C. MacDonald, "Multi-finger Z-actuator," US Patent #US7,504,757 B2, 2009.

[15] W.M.J. Hofmann, H. Neves, N.C. MacDonald and S.G. Adams, "Multiple-level actuators and clamping devices," US Patent #US2004/0067346 A1, 2004.

[16] M. Favre, J. Polesel-Maris, T. Overstolz, P. Niedermann, S. Dasen, G. Gruener, R. Ischer, P. Vettiger, M. Liley, H. Heinzelmann and A. Meister, "Parallel AFM imaging and force spectroscopy using two-dimensional probe arrays for applications in cell biology," *Journal of Molecular Recognition,* vol. 24, pp. 446-452, 2011.

[17] Y. S. K. Ivanova, Tzv. Ivanov, A. Frank, J. Zollner, Ch. Bitterlich, U. Wenzel, B.E. Volland, S. Klett, I.W. Rangelow, P. Zaweirucha, M. Zielony, T. Gotszalk, D. Dontov, W. Schott, N. Nikolov, M. Zier, B. Schmidt, W. Engl, T. Sulzbach and I. Kostic, "Scanning proximal probes for parallel imaging and lithography," *J. Vac. Sci. Technol. B,* vol. 26, pp. 2367-2373, 2008.

[18] Y. Sarov, T. Ivanov, A. Frank and I.W. Rangelow, "Thermal driven multi-layer actuator for 2D cantilever arrays," *Appl Phys A,* vol. 102, pp. 61-68, 2011.

[19] M. Lutwyche, C. Andreoli, G. Binnig, J. Brugger, U. Drechsler, W. Haberle, H. Rohrer, H. Rothuizen, P. Vettiger, G. Yaralioglu and C. Quate, "5×5 2D AFM cantilever arrays a first step towards a terabit storage device," *Sensors and Actuators A: Physical,* vol. 73, p. 89, 1999.

[20] W.P. King, T.W. Kenny, K.E. Goodson, G.L.W. Cross, Mi. Despont, U.T. Durig, H. Rothuizen, G. Binnig and P. Vettiger, "Design of Atomic Force Microscope cantilevers for combined thermomechanical writing and thermal reading in array operation," *Journal of Microelectromechanical Systems,* vol. 11, pp. 765-774, 2002.

[21] U. Drechsler, N. Burer, M. Despont, U. Durig, B. Gotsmann, F. Robin and P. Vettiger, "Cantilevers with nano-heaters for thermomechanical storage application," *Microelectronic Engineering,* vol. 67, pp. 397-404, 2003.

[22] L. Sache, H. Kawakatsu, Y. Emery and H. Bleuler, "Massively parallel atomic force microscope with digital holographic readout," *Journal of Physics: Conference Series,* vol. 61, pp. 668-672, 2007.

[23] Y. Ahn, T. Ono and M. Esashi, "Micromachined Si cantilever arrays for parallel AFM operation," *Journal of Mechanical Science and Technology,* vol. 22, pp. 308-311, 2008.

[24] W.W. Koelmans et al., "Cantilever arrays with self-aligned nanotips of uniform height," *Nanotechnology,* vol. 23, p. 135301, 2012.

[25] H. Cho and C.H. Ahn, "A bidirectional magnetic microactuator using electroplated permanent magnet arrays," *Journal of Microelectromechanical Systems,* vol. 11, pp. 78-84, 2002.

[26] A. Gaitas and P. French, "Piezo-thermal probe array for high throughput applications," *Sensors and Actuators A: Physical,* vol. 186, pp. 125-129, 2012.

[27] D.O. Popa and R. Murthy, "Microrobot with large actuation volumes, and controllers, systems and methods," US Patent # US8,539,854 B2, 2013.

[28] F. Loizeau, "Two-dimensional cantilever array with varying spring constants and tip radii for life-science applications," *Micro & Nano Letters,* vol. 7, pp. 301-305, 2012.

[29] J. Henriksson, M.R. Gullo and J. Brugger, "Integrated long-range thermal bimorph actuators for parallelizable bio-AFM applications," *IEEE Sensors,* vol. 13, pp. 2849-2856, 2013.

[30] R. Murthy and D.O. Popa, "A Four Degree of Freedom Microrobot with Large Work Volume," in *IEEE International Conference on Robotics and Automation*, Kobe, Japan, 2009, pp. 1028-1033.

[31] R. Murthy, H. E. Stephanou and D.O. Popa, "AFAM: An articulated four axes microrobot for nanoscale applications," *IEEE Transactions on Automation Science and Engineering,* vol. 10, pp. 276-284, 2013.

[32] B.R. de Jong et al, "Design and fabrication of a planar three-DOFs MEMS-based manipulator," *Journal of Microelectromechanical Systems,* vol. 19, pp. 1116-1130, 2010.

[33] D.M. Brouwer, B.R. de Jong and H.M.J.R. Soemers, "Design and modeling of a six DOFs MEMS-based precision manipulator," *Precision Engineering,* vol. 34, pp. 307-319, 2010.

[34] S. He, R.B. Mrad and J. Chong, "Repulsive-force out-of-plane large stroke translation micro electrostatic actuator," *Journal of Micromechanics and Microengineering,* vol. 21, pp. 075002-075013, 2011.

[35] YS. Choi, Y. Zhang and DW. Lee, "A thermal-driven silicon micro xy-stage integrated with piezoresistive sensors for nano-positioning," *Journal of Micromechanics and Microengineering,* vol. 22, pp. 055002-055007, 2012.

[36] M. Olfatnia, L. Cui, P. Chopra and S. Awtar, "Large range dual-axis micro-stage driven by electrostatic comb-drive actuators," *Journal of Micromechanics and Microengineering*, vol. 23, pp. 105008-105018, 2013.

[37] I.W. Rangelow and H. Loschner, "Reactive ion etching for microelectrical mechanical system fabrication," *Journal of Vacuum Science and Technology B*, vol. 13, pp. 2394-2399, 1995.

[38] H. Zou, "Anisotropic Si deep beam etching with profile control using $SF_6/0_2$ plasma," *Microsystem Technologies*, vol. 10, pp. 603-607, 2004.

[39] A.A. Ayon et al., "Deep reactive ion etching of silicon," in *Materials research society symposium* San Francisco, California, 1999, pp. 51-61.

[40] YJ. Hung, SlL. Lee, B.J. Thibeault and L.A. Coldren, "Realization of silicon nanopillar arrays with controllable sidewall profiles by holography lithography and a novel single-step deep reactive ion etching," in *Materials Research Society Symposium*, Boston, Massachusetts, 2010, pp. 1-11.

[41] WC. Wang, J.N. Ho and P.G. Reinhall, "Double-sided micromachining process for silicon cantilever using a parallel capacitively coupled plasma," *Journal of Microlithography, Microfabrication and Microsystems*, vol. 4, pp. 013010-1 - 013010-6, 2005.

[42] J. Ji, F.E.H. Tay, J. Miao and J. Sun, "Characterization of silicon isotropic etch by inductively coupled plasma etcher for microneedle array fabrication," *Journal of Physics: Conference Series*, vol. 34, pp. 1137-1142, 2006.

[43] CMC Microsystems. *Canadian Microelectronics Corporation*. Available: http://www.cmc.ca/

[44] University of Canterbury. *Nanofabrication Laboratory, The MacDiarmid Institute for Advanced Materials and Nanotechnology*. Available: http://www.elec.canterbury.ac.nz/resources/laboratories/micro.shtml

[45] A. Cowen, G. Hames, D. Monk, S. Wilcenski and B. Hardy, "SOIMUMPs Design Handbook," ed: MEMSCAP Inc., 2011.

[46] C.M. Herzinger, B. Johs, W.A. McGahan and J.A. Woollam, "Ellipsometric determination of optical constants for silicon and thermally grown silicon dioxide via a multi-sample, multi-wavelength, multi-angle investigation," *Journal of Applied Physics*, vol. 83, pp. 3323-3336, 1998.

[47] N.R. Rueger et al., "Selective etching of SiO_2 over polycrystalline silicon using CHF_3 in an inductively coupled plasma reactor," *Journal of Vaccum Science and Technology A*, vol. 17, pp. 2492-2502, 1999.

[48] C. Gatzert et al., "Investigation of reactive ion etching of dielectrics and Si in CHF_3/O_2 or CHF_3/Ar for photovoltaic applications," *Journal of Vaccum Science and Technology A*, vol. 24, pp. 1857-1865, 2006.

[49] S.H. Lee and JQ. Lu, "Nano-ring-shape growth of fluorocarbon macromolecules during SiO2 etching.," *Nanotechnology*, vol. 21, pp. 1-5, 2010.

[50] M.A. Rad, K. Ibrahim and K. Mohamed, "Surface morphology and structural analysis of fluorocarbon nano-rings formation through EBL and SiO_2 plasma etching," *Vacuum*, vol. 86, pp. 1284-1288, 2012.

[51] M.A. Rad, K. Ibrahim and K. Mohamed, "Formation of SiO_2 surface textures via CHF_3/Ar plasma etching process of poly methyl methacrylate self-formed masks," *Vacuum*, vol. 101, pp. 67-70, 2014.

[52] JH. Lee et al., "A Three-Dimensional and Sensitive Bioassay Based on Nanostructured Quartz Combined with Viral Nanoparticles," *Advanced Functional Materials,* vol. 20, pp. 2004-2009, 2010.

[53] JH. Min, SW. Hwang, GR. Lee and SH. Moon, "Redeposition of etch products on sidewalls during SiO_2 etching in a fluorocarbon plasma. I. Effect of particle emission from the bottom surface in a CF_4 plasma," *Journal of Vaccum Science and Technology A,* vol. 20, pp. 1574-1581, 200.

[54] K.R. Williams, K. Gupta and M. Waslik, "Etch Rates for Micromachining Processing—Part II," *Journal of Microelectromechanical Systems,* vol. 12, pp. 761-778, 2003.

[55] E. Gogolides et al, "Controlling roughness: from etching to nanotexturing and plasma-directed organization on organic and inorganic materials," *Journal of Physics D: Applied Physics,* vol. 44, pp. 174021-174023, 2011.

Chapter 5: Characterisation of the 4SA Microrobot

5.1 Introduction[1]

Following our previous discussion of the design, analyses and fabrication of the 4SA microrobot, this chapter presents the test results from the electrical characterisation of the 4SA microrobot in terms of in-plane and out-of-plane motion performance, decoupling and repeatability. The analytical, simulation and experimental results are in close conformity to each other, verifying the accuracy of our design model, discussed in Chapters 2 and 3. The chapter is summarised in Section 5.5.

5.2 Characterisation of the 4SA microrobot

The motion performance of the 4SA microrobot is characterised by the steady-state relationship between applied actuation voltages and displacements of the microstage. Applying voltages across the bond pads of the comb-drive actuators cause the fingers to move which therefore moves the microstage through the arrangement of support and tethering beams. This pushes the spring flexure beams. Applying voltages across the bottom silicon tower substrate and the bond-pad of the microstage cause the stage to vertically move. Based on electrostatic force law, the output motion of the microstage is expected to be proportional to the square of the actuation voltage, $U_{x,y,z} \propto V^2$.

The motion performance of the manufactured 4SA microrobot as shown in Figure 4.17 has been experimentally characterised for maximum displacement in a 3D workspace, positioning repeatability and decoupling in motion. The experimental setup for carrying out this motion characterisation has been shown in Figure 5.1a and the corresponding block

[1] Elements of the following chapter have been published/ presented in conferences C1, C2 and C3 or in preparation for journal(s) J1 and J2.

diagram in Figure 5.1c. The actuator is glued and wire-bonded onto a ceramic package or the PCB as shown in Figure 5.1a. This ceramic package sits on a ZIF (zero insertion force) socket that uses a lever to push the package and have a firm grip. The actuator is controlled via a PC running the LabVIEW program written to automate the actuation and direct the microstage to any position within the 3D workspace that follows a square path for in-plane motion as shown in Figure 5.1b and Figure 5.3a. The out-of-plane motion is set at a single level with a particular voltage value. The PC is connected to the compact DAQ (NI*9263 ±10* V power output). It is the interface that handles the information transfer from the computer to the output modules. The DAQ has two plug-in modules which supplies a programmable voltage output via five channels (four for *x, y* and one for *z*) to the *5* high voltage MOSFET operational amplifiers (please refer to Appendix C for the circuit diagram). The isolation barrier prevents the high voltage accidently feeding back to the computer. The high voltage generator (LHV Power Series-B *0-9* V DC Input/*0-1250* V DC Output) generates the voltage necessary to set the maximum output voltage of the amplifier. This is connected to the main DC power supply (Powertech MP*3087*). This amplifier is connected either to the ZIF socket or the PCB housing the 4SA microrobot.

The ZIF socket/PCB is placed under an inverted fluorescence microscope (Leica DM IRM) or an optical microscope (Olympus BH) fitted with a digital camera (Spot insight, 2.0 megapixel resolutions) to visualise the actuation and capture the images for post-processing on MATLAB. The 3D output motion of the microrobot is measured under the optical microscope with the digital camera so that it can capture images for step-by-step incremental static changes in the movement of the microstage for different actuation voltages. For in-plane motion, both the resultant motion of the comb-drive actuators, at the edge of the fingers, microstage and at the edge of the stage is measured. Multiple images are taken from different actuator samples to measure the repeatability of the motion as shown in Figure5.4.

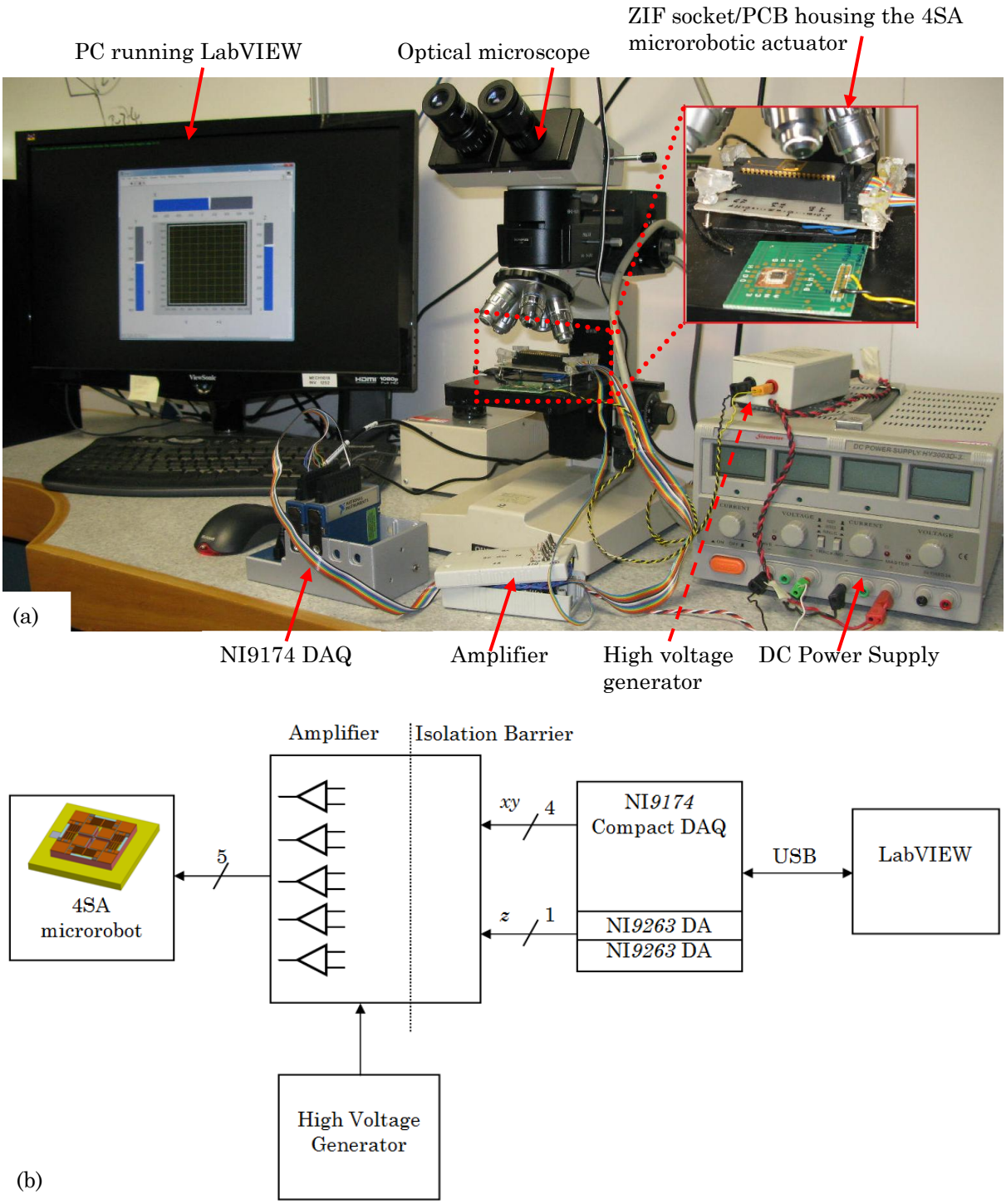

Figure 5.1 (a) Experimental setup for characterisation the motion performance of the 4SA microrobotic actuator. (b) LabVIEW interface for controlling the *x*, *y* and *z* motion of the microstage. (c) Block diagram of the experimental setup showing the electrical connections.

While image processing (please refer to Appendix D for the MATLAB code) has been applied to process the captured images to measure the in-plane displacement, a calibration technique on the microscope has been applied to measure the out-of-plane displacement of

the microstage. For the in-plane motion, a reference box has been positioned on the screen of the computer and the microstage or the comb-drives are placed within this box. When the actuation voltage is applied, the microstage or the comb-drives move and images are captured. Care must be taken to keep the placement of the reference box static to avoid erroneous post-processing of the images by the program. The image processing involves applying a thresholding algorithm to transform the gray-scale image into black and white image which highlights the edge of the microstage and comb-fingers. We then apply a search and averaging algorithm to calculate the relative displacement over a set of images and calculate the mean values for a final particular displacement value.

For the out-of-plane motion, we first derive a relationship between the scale of the fine adjustment knob on the microscope and the actual displacement of the microstage. A calibration test is conducted by measuring similar profile features such as height on commercially available AFM cantilever probes (Bruker OTR4-*10* Contact Mode AFM tip). The tip height is between *2.5-3.5* μm. By adjusting the depth of focus with the coarse and fine adjustment knob of the microscope, as shown in Figure 5.2, the adjustment resolution of the microscope is determined to be *50* nm for one division on the knob. Next the microrobot is placed under the microscope and we focus on an edge of the microstage. When the actuation voltage is applied, the microstage moves out-of-focus. By adjusting the focus, the total rotation of the fine adjustment knob is measured and the out-of-plane displacement is computed. It is to be noted that side etching and footing can cause deviations from the design dimensions which have been recorded in Table 4.6. A few microns worth of variation in dimension can be enough to cause significant changes in the experimental results compared with analytical and simulated results.

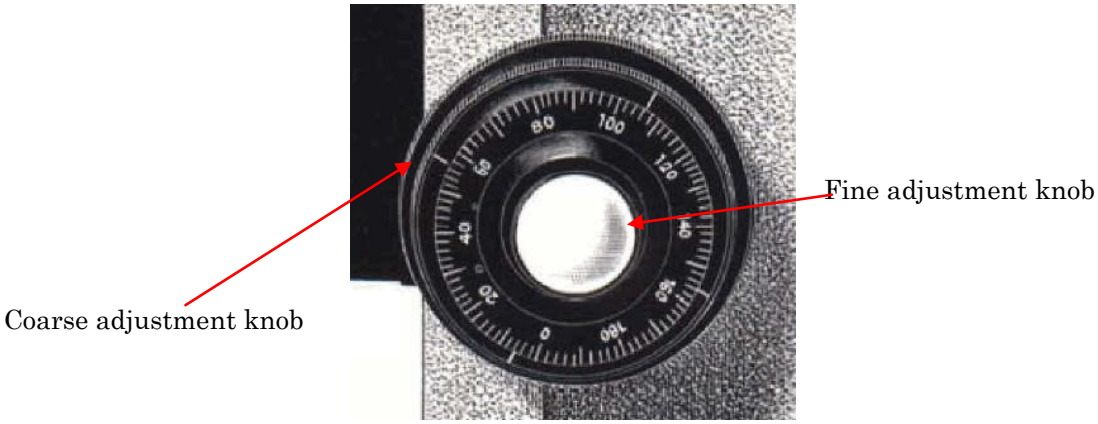

Figure 5.2 Adjustment knob calibration technique used to measure the vertical displacement [1].

5.2.1 3D motion of 4SA microrobot

In-plane actuation voltages of up to *125* V have been provided for moving the microstage in *x* and *y* axes and up to *600* V has been provided for moving the microstage in *z* axis. The resultant displacements are measured under a high-resolution microscope at *200*× magnification. Increasing the magnification beyond this point causes the objective to touch the wire-bonding on the actuator. The DC voltage is applied in increments of *5* V for in-plane motion and *50* V for out-of-plane motion. The videos of the motion have also been captured. The interested readers may email the author for these motion videos. For capturing the videos of the out-of-plane performance, vibratory motion has been provided to the parallel-plate actuator using a signal generator (Isotech GFG*2004*) at a frequency of *1* Hz since the vertical motion to be captured in the form of static displacement is quite small. The measured displacements versus the predicted displacements through our analytical and simulated models are illustrated in Figures 5.3a and c. The in-plane motion has been plotted as a 2D surface plot with respect to the zone of actuation of the microstage over a typical mammalian cell of *15* μm in diameter as also shown previously in Figure 3.21. The actuator has a total in-plane motion range of more than *9* μm (±*4.5* μm) at a driving voltage of *120* V satisfactorily covering almost *60%* surface area of the cell. For a majority of the mammalian cells, the volume occupied by nucleus to the total volume of the cell is quite high ranging between *30*-

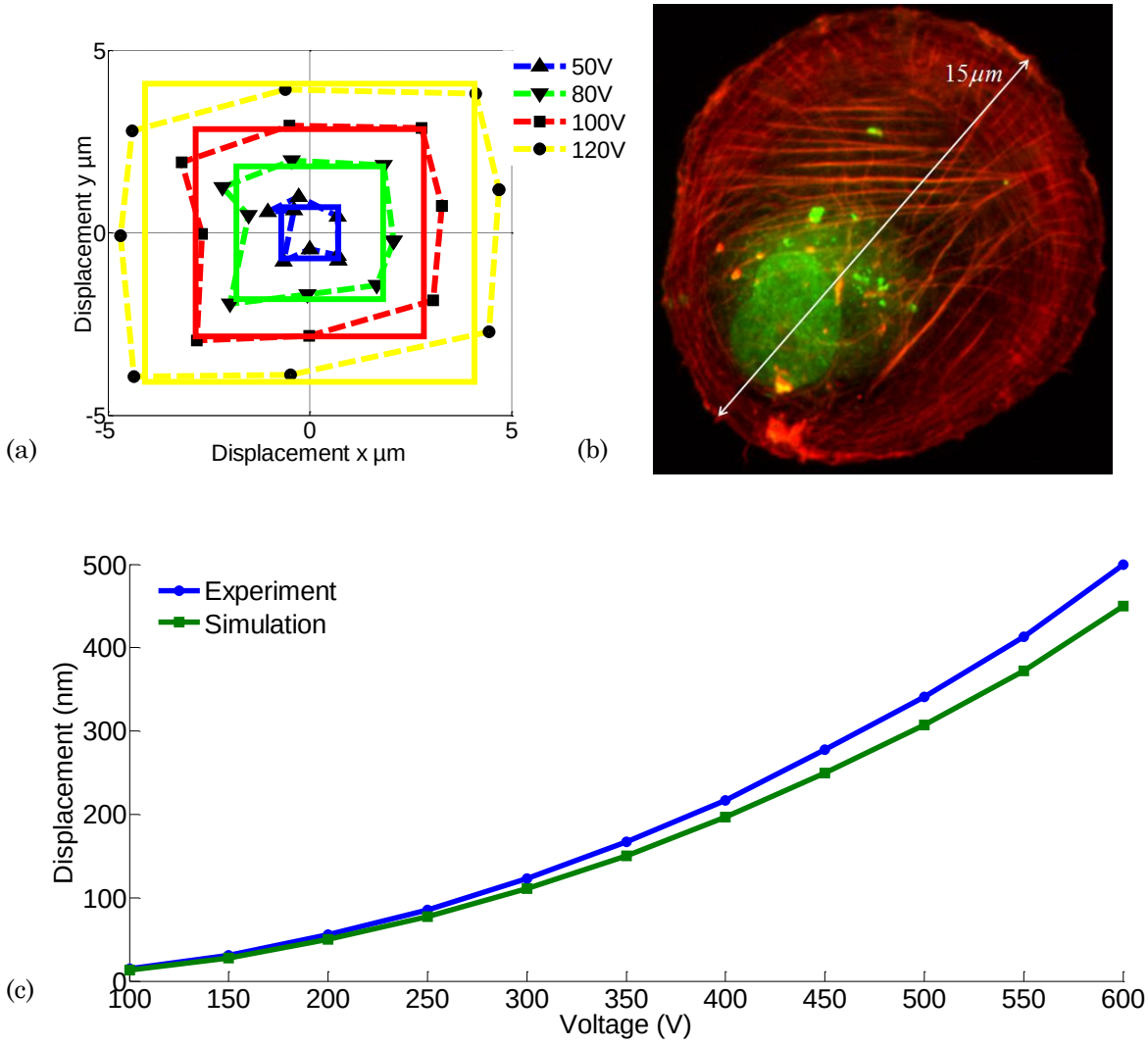

Figure 5.3 (a) 2D surface experiment plots of the in-plane (*x*, *y*) actuation testing of the manufactured 4SA microrobot (dotted lines represent the experimental values and the solid lines represent the analytical values) (b) Confocal microscopy images of ISHI cells growing on glass. Images are isolated from series showing 3D representation of cell slices. F-actin stained with Texas Red phalloidin (red); nucleus stained with Hoechst 33342 (green/blue). Note: nuclear stain representation colour was changed through confocal software (c) Line experimental plot of the out-of-plane (*z*) actuation testing.

80% [2]. Thus with the current in-plane motion performance of the 4SA microrobot, the microstage and therefore the microneedle can be easily placed over a cellular organelle such as nucleus before the vertical manipulation proceeds. The out-of-plane motion is plotted as a line graph where the microstage can move by more than *0.5* µm at around *600* V. The preliminary out-of-plane motion performance is significantly lower compared to what it has

been designed for, owing to the limitations in fabrication infrastructure. For example, the in-plane stiffness of the manufactured 4SA microrobot is *91.75* μN/μm, which is 316 times greater than that of the designed 4SA microrobot i.e. *0.29* μN/μm. Similarly, the out-of-plane stiffness of the manufactured 4SA microrobot is *124.78* μN/μm, which is 524 times greater than that of the designed 4SA microrobot i.e. *0.23* μN/μm.

We define absolute error in our measurements as the uncertainty in values between the experimental readings, analytical and finite element analyses. These occur primarily due to certain assumptions made during theoretical modeling explained below, errors in calibrating the optical microscope during vertical motion reading and more systematic errors such as fabrication limitations as explained above. For the in-plane motion, the mean absolute error between the theoretical and experimental motion values varies between *4-5%*. For the out-of-plane motion, the mean absolute error is around *13%*. For the in-plane motion, the error between the values almost remains constant throughout the different applied actuation voltages of up to *120* V. Nonetheless for the out-of-plane motion, the error is less than *7%* for applied voltage values of up to *300* V, beyond which the error increases to almost *13%* for *600* V. The proximity between the experimental results and theoretical plot for both in-plane and out-of-plane motion can be seen, except for higher applied voltages in vertical motion. We hypothesise that such variation between the out-of-plane values as the applied voltage increases is due to the error involved with the measurement resulting from the calibration technique of the optical microscope at higher applied voltages. We also attribute such variations to fabrication irregularities. For example, when the bottom silicon tower is bonded to the bottom substrate followed by its bonding to the suspended actuator substrate, the alignment error will vary from sample to sample as it is done manually. Thus in addition to the stiffness increase as discussed above, such alignment errors can reduce the interacting surface area between the microstage and the tower. This leads to a significant offset between

the two plates leading to the requirement for such high voltage values and variations with the theoretically predicted values. Normally, such high voltage is unnecessary for operating the microrobot, but due to the significant change in stiffness values resulting from fabrication, we had no other option, but to operate it until we could achieve a significant vertical motion. This has been rectified as can be seen in design analyses of the 3SA microrobot in Chapter 6 which is currently under fabrication. If the reader recalls from Chapter 3, we have also made several assumptions during structural simulations. For example, the microneedle has been replaced by adding an equivalent mass and density to the micro-stage; and the comb-finger electrodes have been replaced by rectangular beams of equivalent mass and density. Nonetheless, our hypothesis of a parallel-plate actuator using an arrangement of a long-standing silicon tower underneath a microstage is proven by this vertical motion.

5.2.2 Decoupling in motion of 4SA microrobot

As seen in Figure 5.4, the in-plane motion is linear to the square of the actuation voltage with minimal decoupling. The coupled motion of the microstage between the *x* and *y* axes has been measured by actuating only one axis side and keeping the other axis at zero applied voltage. This has been verified by testing five different microrobotic actuators to get a range of the coupled motion values and calculating the maximum coupled displacement across either axis. The results from one such microrobotic chip have been tabulated in Table 5.1. For example, when the microstage is driven at ±*4.5* μm at *120* V in either *x* or *y* axis, the maximum displacement in the *y* or *x* axis respectively does not exceed *80* nm and *470* nm. Thus at this voltage for different samples, coupled motion across *y* axis varies between *0.5-1.7%* of the original *y* motion, and across *x* axis varies between *5-9%* of the original *x* motion. Although this motion coupling is negligible, the *x*-axis coupling is higher than *y*-axis possibly due to fabrication imperfection. The displacements of the comb-drives have similar values to the micro-stage for in-plane motion verifying the predicted negligible stretching from our

Table 5.1 Coupled motion values from the testing of a 4SA microrobotic chip.

	X	Y	Z
Actual motion (µm)	4.9	4.9	0.5
Coupled motion (µm)	0.47	0.08	-

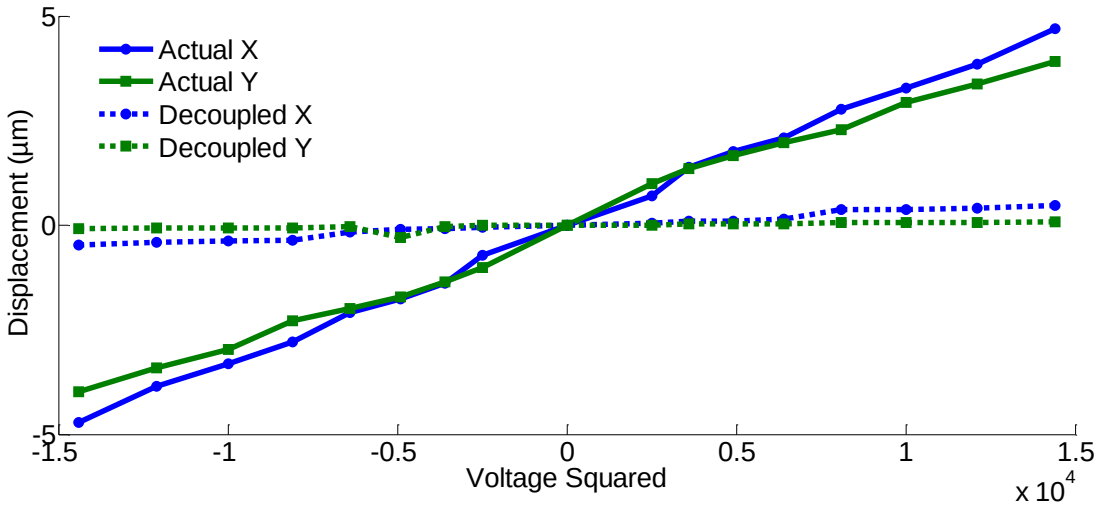

Figure 5.4 Actual and decoupled actuation experimental results for different values of DC voltage squared.

design conceptualisation in Chapter 2.

Due to the significantly low motion along the *z*-axis, we haven't measured the coupling along this direction. But given the high vertical stiffness of the tethering beams, we expect the coupling between the in-plane axes and out-of-plane *z* axis to be significantly lower in comparison to the in-plane motion coupling. Nonetheless, our 4SA microrobot proves the stability of the designed structure in achieving decoupled 3D motion.

5.2.3 Repeatability of motion of 4SA microrobot

The microstage has been repeatedly actuated and the results have been tabulated and plotted for the first *50* tests for five different microrobotic chips, as shown in Figure 5.5. We have applied an actuation voltage of *120* V for the in-plane motion and *600* V for the out-of-plane

motion. The standard deviations of the 3D motion across each of these chips have been noted in Table 5.2. The mean standard deviations of the maximum *x,y,z* motion during the repeatability tests with the five different chip samples have been found to be *384* nm, *400* nm and *15* nm well within the elastic limit of the tethering and spring flexure beams already predicted in Section 3.3.3. The 3D motion at various voltages has been found to be repeatable with a quadratic behavior to the driving voltage within the resolution of the optical microscope as shown in Figure 5.5. Repeated tests for displacement have not resulted in any permanent damage to the microrobot. The repeatability has also been measured by increasing the applied voltage and noting the average position of the microstage during this course. Maximum error is then determined when the applied voltage is reduced and the microstage comes back to a particular position.

Comparing the actuation motion performance of five different 4SA microrobots and having closely related motion values confirms the accuracy and fault tolerance of the fabrication process and the design of the microrobot. Evaluating this movement of the microstage with respect to the specifications as set forth in Section 2.2, this gives us suitable confidence that variation in the motion performance of every individual microrobot in a

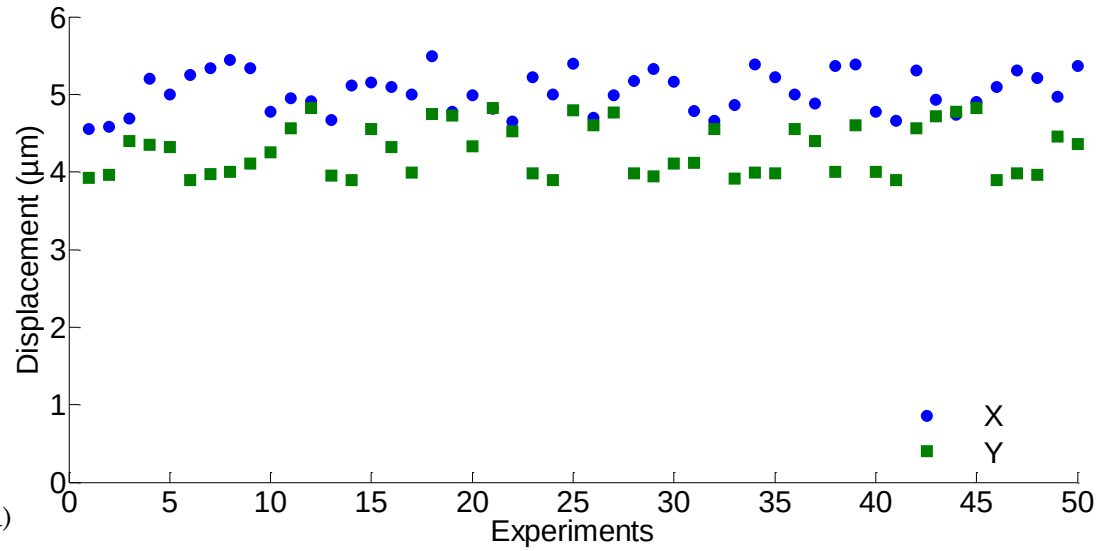

(a)

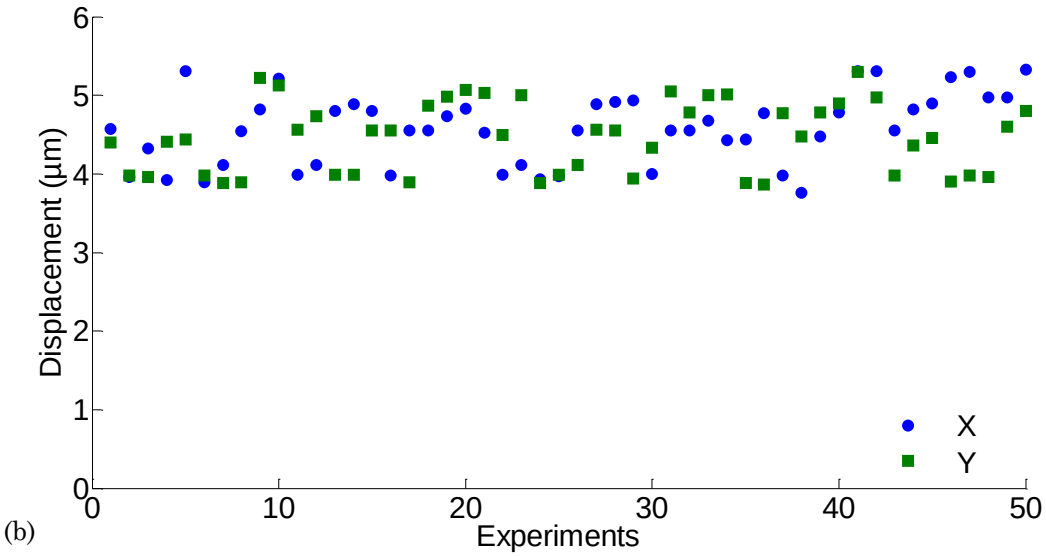
Displacement (µm)
Experiments
X
Y
0
1
2
3
4
5
6
0
10
20
30
40
50

(b)

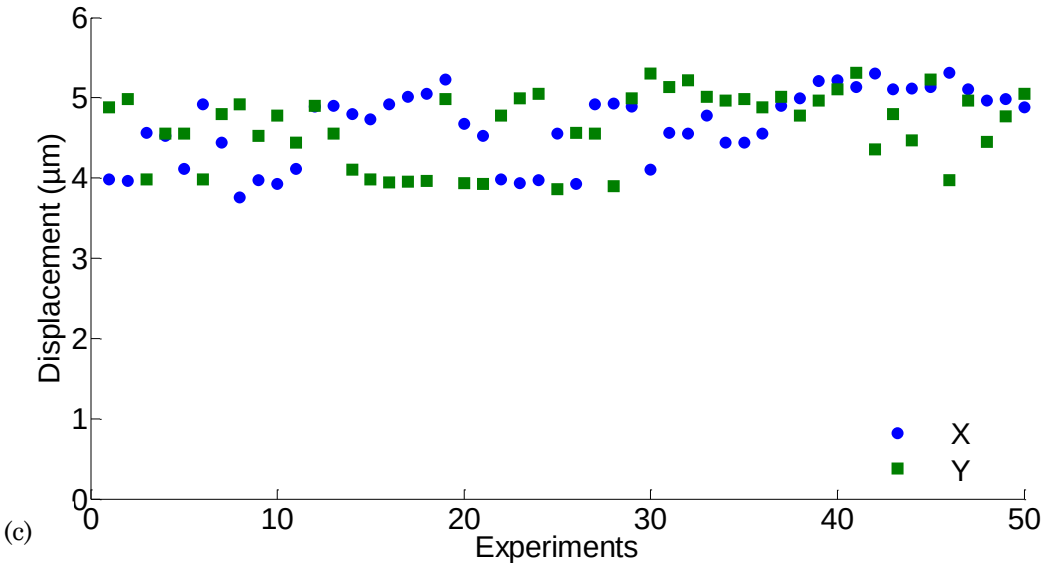
Displacement (µm)
Experiments
X
Y
0
1
2
3
4
5
6
0
10
20
30
40
50

(c)

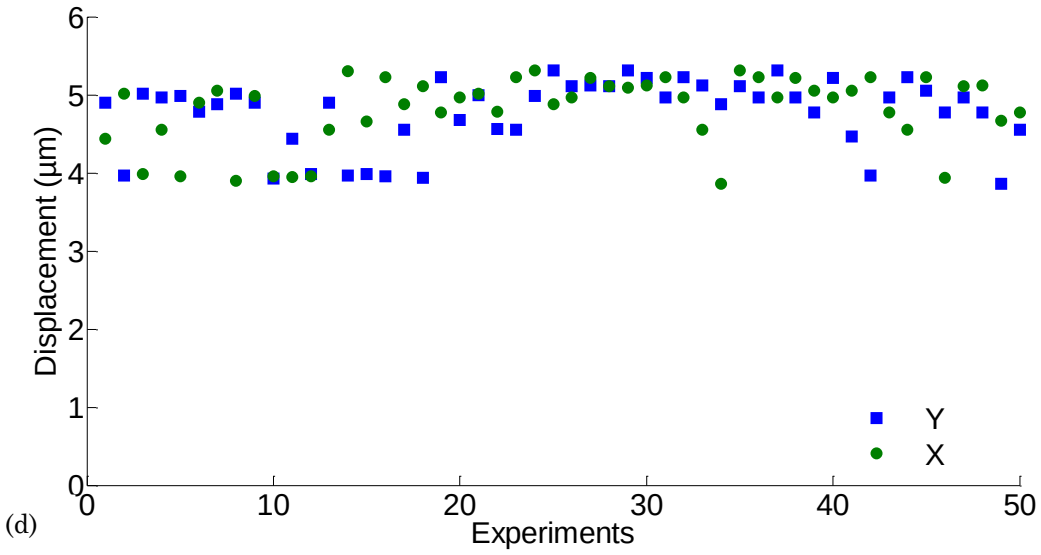
Displacement (µm)
Experiments
Y
X
0
1
2
3
4
5
6
0
10
20
30
40
50

(d)

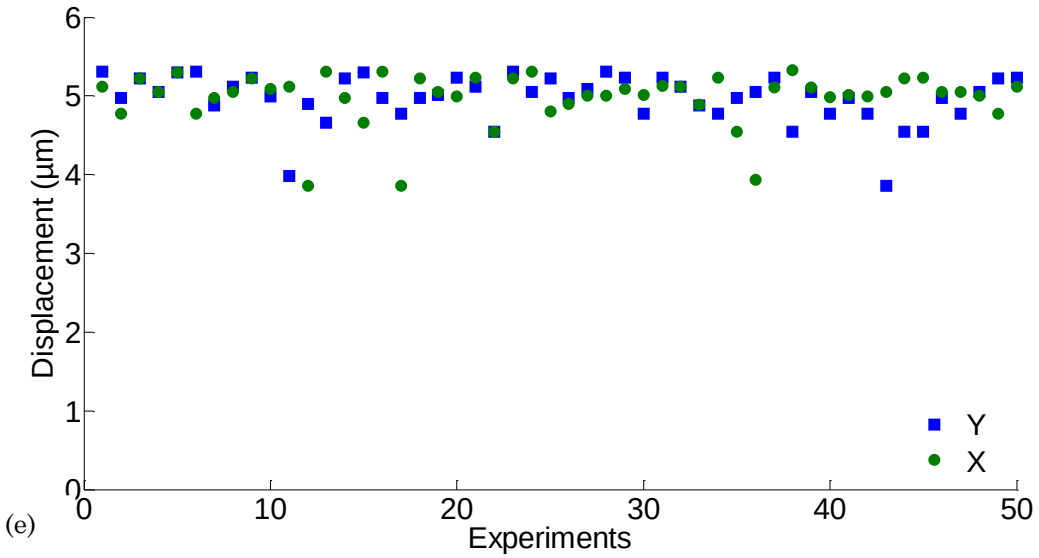

(e)

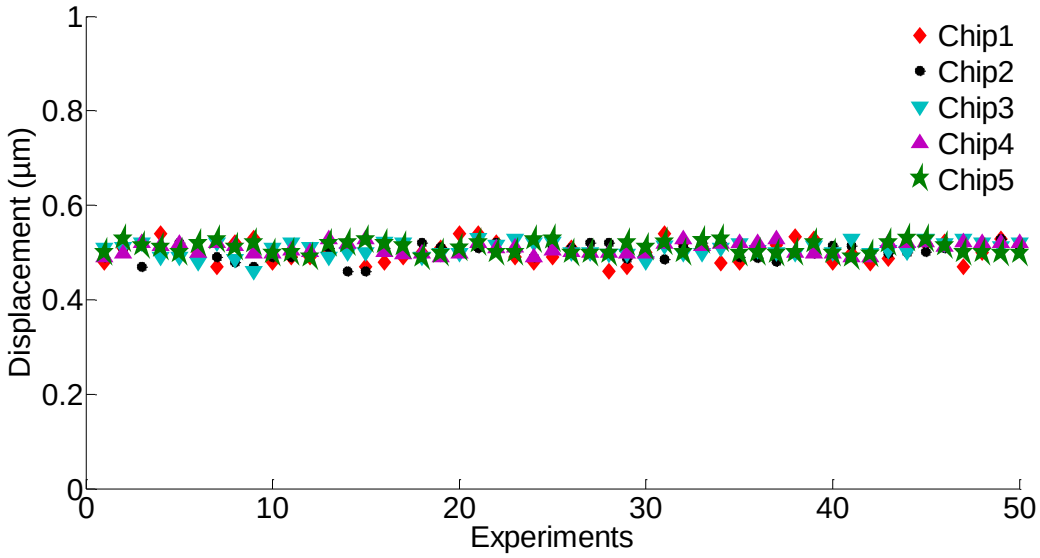

(f)

Figure 5.5 Experimental results of the positioning repeatability for 50 tests of the 4SA microrobot. In-plane tests for (a) Chip 1 (b) Chip 2 (c) Chip 3 (d) Chip 4 and (e) Chip 5. (f) Out-of-plane tests for Chips 1 to 5.

Table 5.2 Standard deviation and mean values of the *x,y,z* motion values from the repeatability tests conducted on five different 4SA microrobotic chips.

	Chip 1	Chip 2	Chip 3	Chip 4	Chip 5	Mean
Std. Dev (*x*) nm	268.821	452.12	449.72	443.31	310.4	384.87
Std. Dev (*y*) nm	329.85	450.561	447.22	444.55	334.234	401.283
Std. Dev (*z*) nm	21.63	16.13	14.87	12.03	12.54	15.44

parallel architecture system will be within a few hundred nanometres. As discussed above in Section 5.2.1 in reference to Figure 5.3, we have analysed and discussed the error in results between the proposed motion performance as predicted from our analytical models and the actual measured performance. Given the in-plane motion range of *1* μm to *30* μm and out-of-plane motion of up to *7* μm that we are targeting, this variation in the motion of the individual microrobots in a parallel architecture is insignificant. Therefore it would not affect the positioning of the microneedles over specific organelles of different types of mammalian cells. This is critical as explained later in Chapter 8 during the individual control of the microneedles. With an open-loop control, the microstage and therefore the microneedle will be capable of precise positioning over the individual cell surfaces along all there axes.

5.3 Closure and original contributions

The results presented above demonstrate a major outcome of this research. The vertical motion using a parallel-plate actuator arrangement of a long standing silicon tower and microstage has been successfully demonstrated. Albeit the out-of-plane motion is low for the 4SA microrobot owing to the fabrication limitations, but it proves our hypothesis that vertical motion is achievable by incorporating parallel-plate actuator in the design. The experimental setup for characterising the motion performance of the 4SA microrobot has been described followed by analyses of the test results from 3D motion. The microrobot is able to achieve a reasonable displacement of up to *10* μm at an applied DC voltage of *120* V in-plane which can successfully cover almost *60%* of the surface area of a typical human cell, *15* μm in diameter. The vertical displacement achieved is slightly above *0.5* μm at *600* V. The microrobot performs quite well in terms of achieving a decoupled motion and repeatability. Hitherto, in the preceding chapters, we focused on the design, analyses, fabrication and testing of the 4SA microrobot. Henceforth in the following chapters, we will focus on the design, analyses and fabrication of the new design, 3SA microrobot.

Thus, Chapter 5 makes the following contribution to the field of sensors and actuators:

- We have successfully implemented and demonstrated the 3D actuation of the 4SA microrobot through experimental tests. We have successfully tested the vertical motion achieved by the parallel-plate actuator with an arrangement of microstage with a silicon tower standing underneath. As evident from the review of the existing positioning stages and systems in Chapters 1, 3 and 4, this is the first-of-its-kind 3D actuated microrobot.

BIBLIOGRAPHY

[1] Olympus Corporation, "Olympus series BH system microscope," ed.

[2] R. Milo, P. Jorgensen and M. Springer, "The database of useful biological numbers," *Nucleic Acids Research,* vol. 38, pp. 750-753, 2010.

Chapter 6: Performance Analysis of the Behaviour of 3SA Microrobot

6.1 Introduction[1]

The previous chapters 3, 4 and 5 have been solely dedicated to the discussion of the design, analyses, fabrication and testing of the 4SA microrobot, our first generation actuator. We now shift our focus to the design, analyses and fabrication of the 3SA microrobot, our second generation actuator. In this chapter, we will discuss in detail regarding the analytical model and FEA simulations which we have borrowed from the design of the 4SA microrobot as discussed in Chapter 3. The design of the actuator has evolved from the 4SA to 3SA structure in order to design a parallel architecture with a high density of microrobots without compromising on their motion performance. In this chapter, we will detail how we have been able to achieve better motion performance with the 3SA microrobot compared to a 4SA microrobot. We will mainly focus on the results of the analyses rather than the process, as they have already been discussed in detail in Chapter 3. Nonetheless the new equations of the analytical model have been detailed.

6.2 Analytical modeling of the 3SA microrobot

The electromechanical behaviour of the 3SA microrobot has been analytically investigated by deriving the effective stiffness of the actuator beam components using grid stiffness matrix slope-deflection models.

6.2.1 In-plane grid stiffness matrix model of the 3SA microrobot

To compute the in-plane displacement of the node *7* (from D to D') because of electrostatic force F_e, due to an electric field when voltage V is applied to the comb-drive actuators such

[1] Elements of the following chapter have been published/ presented in conferences C2 and C3 or in preparation for journal(s) J1.

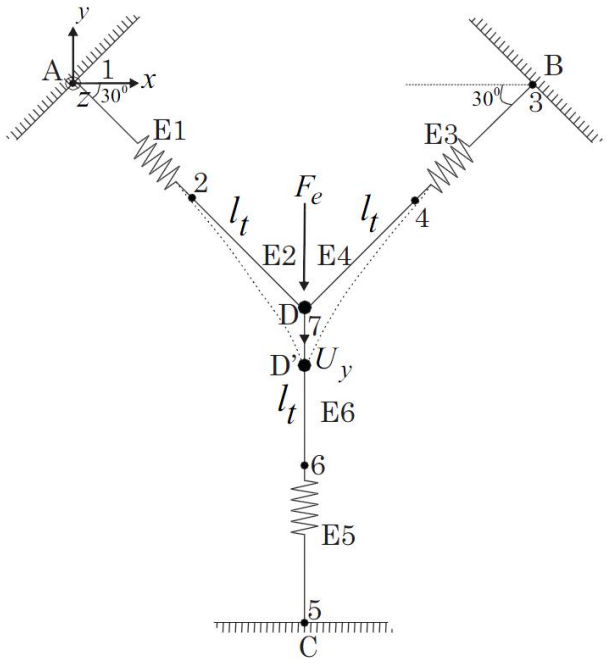

Figure 6.1 Schematic of the 3SA microrobot for analysing the in-plane actuation using elastic stiffness matrix model.

as at node C, we form an equivalent grid stiffness matrix of the tethering and spring flexure beams. The schematic of the microrobot is divided into nine nodes, *1* to *7* and eight elements *E1* to *E6*, each corresponding to a beam structure, as shown in Figure 6.1.

The element stiffness, $[k]_2, [k]_4, [k]_6$ of the tethering beams *E2*, *E4* and *E6* inclined at an angle of 120^0 to each other is given by [1],

$$[k]_2, [k]_4, [k]_6 = \frac{12EI}{l_t^3}\begin{bmatrix} s^2 & -cs & -s^2 & cs \\ -cs & c^2 & cs & -c^2 \\ -s^2 & cs & -s^2 & -cs \\ cs & -c^2 & -cs & c^2 \end{bmatrix} \tag{6.1}$$

Similarly, the element stiffness, $[k]_1, [k]_3, [k]_5$ of the spring flexure beams *E1*, *E3* and *E5* is given by,

$$[k]_1, [k]_3, [k]_5 = \frac{8Eh_s w^3}{l_s^3}\begin{bmatrix} c^2 & cs & -c^2 & -cs \\ cs & s^2 & -cs & -s^2 \\ -c^2 & -cs & -c^2 & cs \\ -cs & -s^2 & cs & s^2 \end{bmatrix} \tag{6.2}$$

where $c = \cos\theta_n$ and $s = \sin\theta_n$, $\theta_3 = \theta_4 = 60^0$, $\theta_1 = \theta_2 = 120^0$, $\theta_5 = \theta_6 = 240^0$ and the subscripts indicate the corresponding element number. *I* is the second moment of inertia of the beam.

After adding the terms of the individual element stiffness matrices into their corresponding locations in the global stiffness matrix $[K]$, the total *14×14* stiffness matrix is,

$$[K]_{eq} = \underbrace{\frac{8Ehw^3}{l_s^3}\begin{bmatrix} c^2 & cs & -c^2 & -cs \\ cs & s^2 & -cs & -s^2 \\ -c^2 & -cs & -c^2 & cs \\ -cs & -s^2 & cs & s^2 \end{bmatrix} + [k]_3 + [k]_5}_{Spring} + \underbrace{\frac{12EI}{l_t^3}\begin{bmatrix} s^2 & -cs & -s^2 & cs \\ -cs & c^2 & cs & -c^2 \\ -s^2 & cs & -s^2 & -cs \\ cs & -c^2 & -cs & c^2 \end{bmatrix} + [k]_2 + [k]_4}_{Tethering} \tag{6.3}$$

Each *4×4* matrix of Equation (6.3) when added and assembled would generate the appropriate *14×14* stiffness matrix on the left hand side. Therefore the two sides are equivalent to each other and not equal due to the different orders of matrix of both sides before assembly.

Thus, writing the total structure stiffness equation accounting for the applied electrostatic force on nodes *7* and *5* and force and displacement boundary constraints at the other nodes,

$$\begin{bmatrix} F_{1x} \\ F_{1y} \\ F_{2x} \\ F_{2y} \\ F_{3x} \\ F_{3y} \\ F_{4x} \\ F_{4y} \\ F_{5x} \\ F_{5y} = F_e \\ F_{6x} \\ F_{6y} \\ F_{7x} \\ F_{7y} = F_e \end{bmatrix} = [K]_{14\times14} \begin{bmatrix} U_{1x} \\ U_{1y} \\ U_{2x} \\ U_{2y} \\ U_{3x} \\ U_{3y} \\ U_{4x} \\ U_{4y} \\ U_{5x} \\ U_{5y} = U_y \\ U_{6x} \\ U_{6y} \\ U_{7x} \\ U_{7y} = U_y \end{bmatrix} \tag{6.4}$$

Thus, the final displacement can be found by solving Equation (6.5),

$$\therefore \left[U_y\right] = \left[K^{-1}\right]_{14\times 14}\left[F_e\right] \tag{6.5}$$

Unlike for a 4SA microrobot where the beams are placed orthogonal to each other, the analytical model of the 3SA microrobot has to include angular components in the effective mathematical treatment of the design. Thus, a transformation matrix is used to transform the local displacement components into global ones and this result in the global stiffness matrix.

6.2.2 In-plane slope-deflection model of the 3SA microrobot

The in-plane motion of the 3SA microrobotic actuator has also been analytically modeled using slope-deflection equations [2], shown in Figure 6.2, as an additional tool to investigate the design of the actuator. In this case, all the joints are considered rigid and the angle between the beams at the joints is constant under the loading. The distortion due to axial and shear stresses are considered negligible. Each side *A*, *B* and *C* consists of an arrangement of

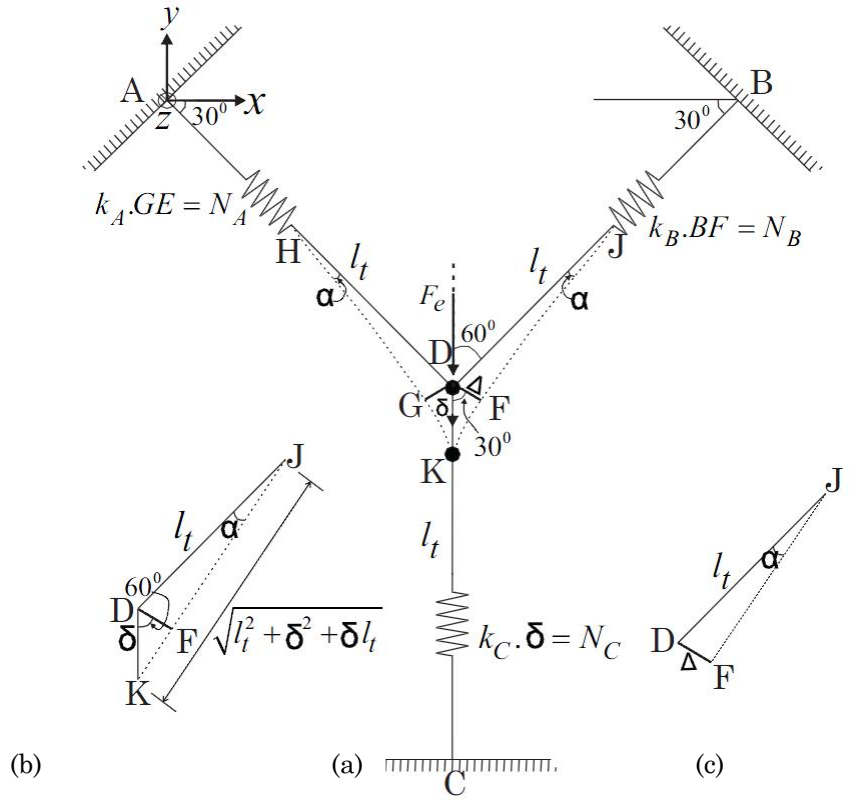

Figure 6.2 Schematic of the 3SA microrobot for analysing the in-plane actuation using slope-deflection equations (a) Main model (b) ΔDIE (c) ΔDIF.

comb-drive actuators and spring flexure beams which are connected to microstage *D*. The tethering beam length is l_t and the angle between the corresponding tethering beams is 120^0. When voltage *V* is applied to the comb actuators on side *C*, the tethering beams connected to *A* and *B* are displaced sideways by Δ, vertically by δ and by an angle α. The detailed treatment and the derivation of equations can be found in Appendix A. Thus, the electrostatic force due to the comb-drive actuators in side *C* in terms of the slopes, deflection and stiffness of the component beams is,

$$F_e = \frac{8l_t E h_s w_s^3}{l_s^3}\frac{\sin^2\alpha}{(6-8\sin^2\alpha)}\left(1\pm\sqrt{-3\left(1+\frac{1}{\sin^2\alpha}\right)}\right)+\frac{2Eh_s w_s^3}{l_s^3}\left(\sqrt{l_t^2+\delta^2+\delta l_t}-\frac{4l_t}{3\cos\alpha+\sqrt{3}\sin\alpha}\right)$$
$$-24\sqrt{3}\frac{EI}{l_t^2}\frac{\sin\alpha}{\sqrt{3}\cos\alpha+\sin\alpha} \qquad (6.6)$$

Thus, the effective in-plane stiffness of the actuator is,

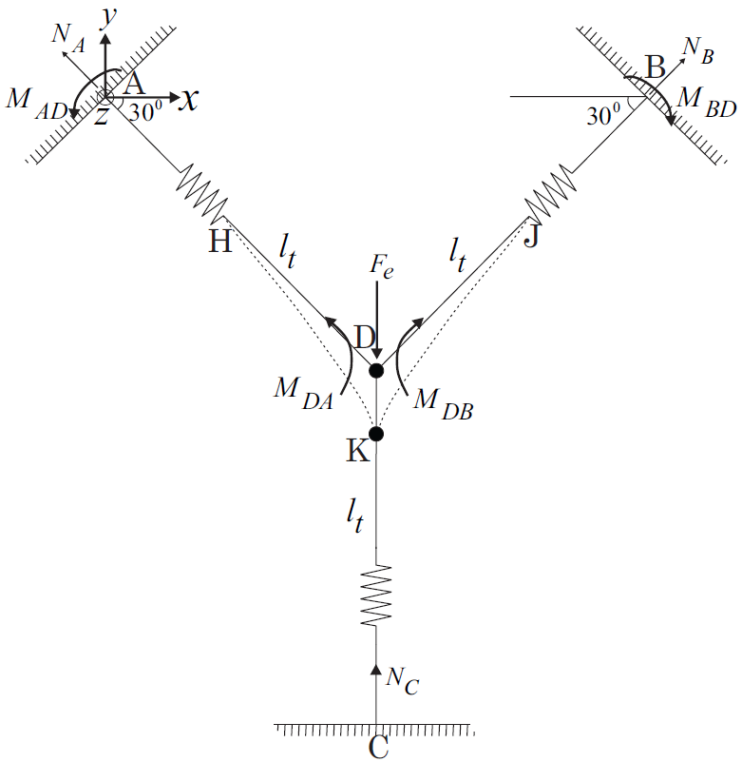

Figure 6.3 Free body diagram of the 3SA microrobot showing the shear force, moments and restoring forces across the structure.

$$K_{x,y} = \left[\frac{4Eh_s w_s^3 \sin\alpha\left(1 \pm \sqrt{-3\left(1+\frac{1}{\sin^2\alpha}\right)}\right)(\sqrt{3}\cos\alpha + \sin\alpha)}{l_s^3(6-8\sin^2\alpha)} \right. \tag{6.7}$$

$$\left. + \frac{Eh_s w_s^3}{l_s^3 l_t \sin\alpha}\left(\sqrt{3}\cos\alpha + \sin\alpha\right)\left(\sqrt{l_t^2+\delta^2+\delta l_t} - \frac{4l_t}{3\cos\alpha+\sqrt{3}\sin\alpha}\right) - \frac{12\sqrt{3}EI}{l_t^3} \right]$$

This analytical derivation gives a different perspective on calculating the effective in-plane stiffness compared with the stiffness matrix approach discussed before. To compute the stiffness value, it is assumed that the microstage *D* has a unit displacement due to the motion of the comb-drive actuators on side *C*.

6.2.3 Out-of-plane grid-stiffness model of the 3SA microrobot

For the 4SA microrobot design, there are seven nodes, one each for the comb-drive actuator and spring flexure beam arrangement, one each for the tethering beams and one for the microstage-microneedle structure. There are seven elements, *E1* to *E7*, connecting these nodes and the electrostatic force acts on the ninth node that deflects it along the *z*-axis.

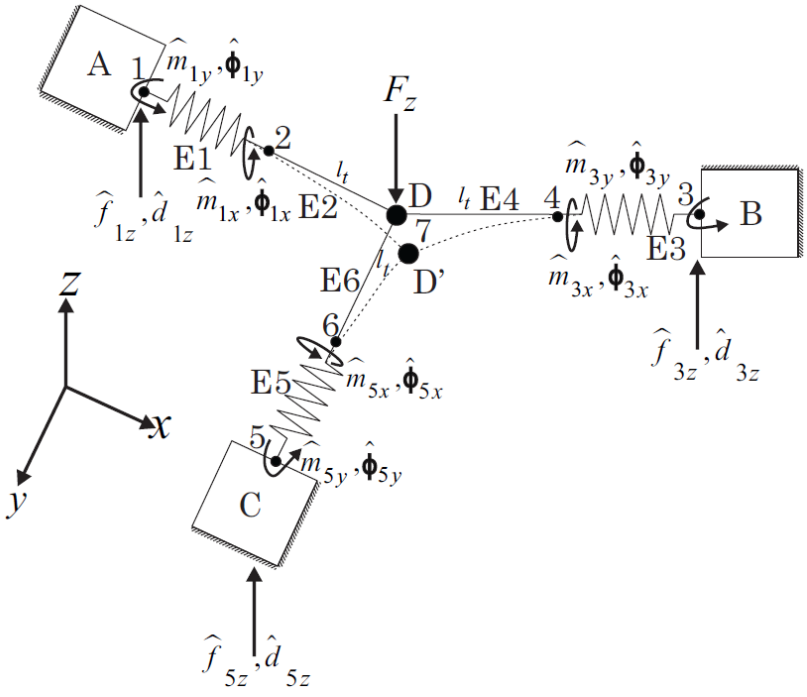

Figure 6.4 Schematic of the 3SA microrobot for analysing the out-of-plane actuation.

For detailed treatment on the grid stiffness model, the readers may refer to Section 3.2.3. In order to avoid repetition, we will straight go to the final set of equations. Thus the final connectivity matrix becomes,

$$\begin{Bmatrix} F_i \\ F_{i+1} \\ F_{i+2} \\ .... \\ .... \\ .... \\ .... \\ .... \\ F_j \end{Bmatrix} = \begin{bmatrix} k^m_{i,i} & k^m_{i,i+1} & k^m_{i,i+2} & .... & .... & .... & .... & .... & k^m_{i,j} \\ k^m_{i+1,i} & k^m_{i+1,i+1} & k^m_{i+1,i+2} & .... & .... & .... & .... & .... & k^m_{i+1,j} \\ k^m_{i+2,i} & k^m_{i+2,i+1} & k^m_{i+2,i+1} & .... & .... & .... & .... & .... & k^m_{i+2,j} \\ .... & .... & .... & .... & .... & .... & .... & .... & .... \\ .... & .... & .... & .... & .... & .... & .... & .... & .... \\ .... & .... & .... & .... & .... & .... & .... & .... & .... \\ .... & .... & .... & .... & .... & .... & .... & .... & .... \\ .... & .... & .... & .... & .... & .... & .... & .... & .... \\ k^m_{j,i} & k^m_{j,i+1} & k^m_{j,i+2} & .... & .... & .... & .... & .... & k^m_{j,j} \end{bmatrix}_{21\times21} \begin{Bmatrix} U_i \\ U_{i+1} \\ U_{i+2} \\ .... \\ .... \\ .... \\ .... \\ .... \\ U_j \end{Bmatrix} \quad (6.8)$$

Thus, the final connectivity stiffness matrix equation is,

$$\begin{Bmatrix} F_{iz} \\ M_{ix} \\ M_{iy} \\ .... \\ F_{jz} \\ M_{jx} \\ M_{jy} \end{Bmatrix}_{21\times21} = [K]_{21\times21} \begin{Bmatrix} U_{iz} \\ \phi_{ix} \\ \phi_{iy} \\ .... \\ U_{jz} \\ \phi_{jx} \\ \phi_{jy} \end{Bmatrix}_{21\times21} \quad (6.9)$$

Thus, the vertical out-of-plane displacement is,

$$\left[U_z\right] = \left[K^{-1}\right]_{21\times21}\left[F_z\right] \quad (6.10)$$

6.3 Finite element analysis of the 3SA microrobot

Detailed FEA treatment has been discussed in Chapter 3. Thus, rather than explaining the process of how the simulations have been performed again, we solely focus on the results here. The validation of the analytical, FEA and experimental results in Chapters 3 and 5, gives us the confidence to rely on the accuracy of our models and thereby design the 3SA microrobot for fabricating the first parallel architecture as detailed in Chapter 7.

6.3.1 Electrostatics FEA of the 3SA microrobot

After performing convergence tests for electrostatics simulations in order to optimise the number of nodes and elements for meshing, we have used the following parameters for meshing. The comb-drive actuators are meshed with approximately *1.5* million SOLID*123* (3D 10-node) elements. The parallel-plate actuator as shown in Figure 6.5 are meshed with approximately *2* million PLANE*121* (2D 8-node) elements for the plates (silicon tower and microstage) and SOLID*122* (3D 20-node) elements for the air-gap volume.

For the comb-drive actuators, the in-plane electrostatic force values increase as thickness increases as is evident from Equation (3.1). This however does not affect the out-of-plane electrostatic force in the parallel plate actuators, which primarily depends on the overlapping area of the plates and the distance between them (Figure 6.6). In this case, the distance between the two plates is *15* μm and the overlapping area is *300* μm up from *140* μm in the case of manufactured 4SA microrobot. The out-of-plane electrostatics FEA have been performed by considering the microstage and the bottom silicon tower as individual plates of unit thickness. The effect of the thickness of the microstage is taken into consideration during subsequent structural FEA. The electrostatic force effect in the parallel plate actuator always leads the two plates to attract.

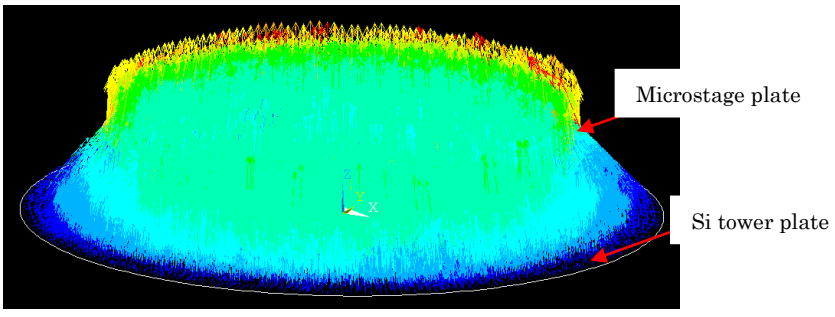

Figure 6.5 Parallel plate actuator out-of-plane electrostatics FEA with electric field lines between the parallel plates for the 3SA microrobot.

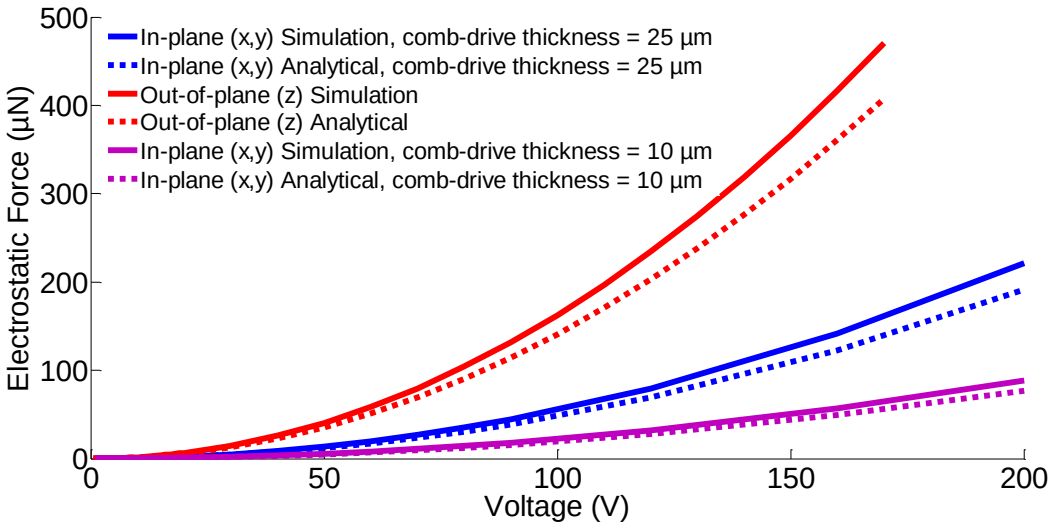

Figure 6.6 Electrostatic forces for different applied DC voltages for 3SA microrobot for comb-drive actuator thicknesses of *10* µm and *25* µm and parallel-plate distance at *15* µm.

6.3.2 Structural FEA of the 3SA microrobot

The suspended actuator grid structure is meshed with approximately *5* million SOLID*187* (3D 10-node) elements. For the 3SA microrobot, an in-plane displacement of more than *36* µm can be achieved at *160* V in one direction in a pull-mode. Thus it can achieve a total in-plane displacement of more than *72* µm (±*36* µm) at *160* V in a pull-pull mode. Neither the tethering beam length nor the thickness of the suspended grid structure affects the in-plane motion significantly. This is also true if instead of actuating one side, two sides are simultaneously actuated for better targeted control of the microneedle. The stretching in the beams is also negligible in the order of sub nanometres, as is evident from the design conceptualisation discussed in Section 2.3. Nonetheless in case of the out-of-plane motion, the actuation performance is affected more significantly by these parameters. The out-of-plane displacement increases as the length of the tethering beams increase or the thickness of the suspended structure decreases as shown in Figure 6.10. For example an out-of-plane displacement of more than *6* µm can be achieved at *30* V with a tethering beam length of *800* µm. Since the out-of-plane stiffness of the actuator reduces significantly by such change in

dimensions, the same displacement can be achieved at *22* V with a tethering beam length of *1000* μm and at *17* V with a tethering beam length of *1200* μm. Nonetheless, it is to be noted that there has to be a trade off between the overall surface area of the actuator and its performance. In this case, albeit increasing the length of the tethering beams from *800* μm to

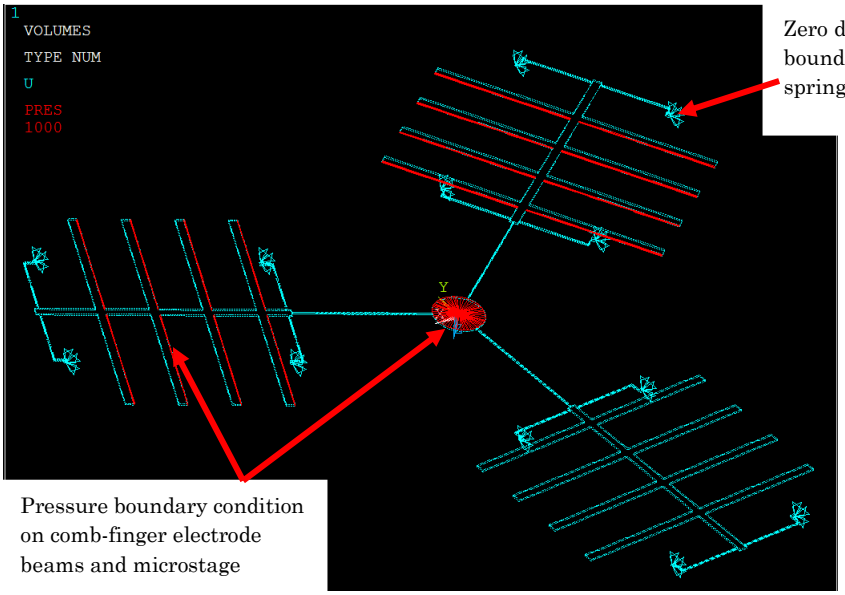

Figure 6.7 Structural simulation of the 3SA microrobot with the applied boundary conditions, zero displacement at the end of the hinge of spring flexure beams and pressure on the comb-drive fingers (electrostatic force corresponding to different voltages divided by surface area of the beam, substituted for the comb-finger electrodes) and microstage.

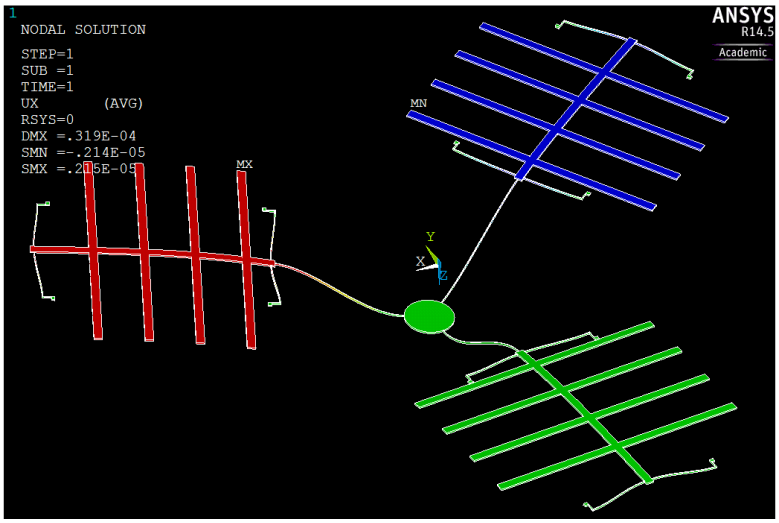

Figure 6.8 3D motion of the 3SA microrobot after the model is solved.

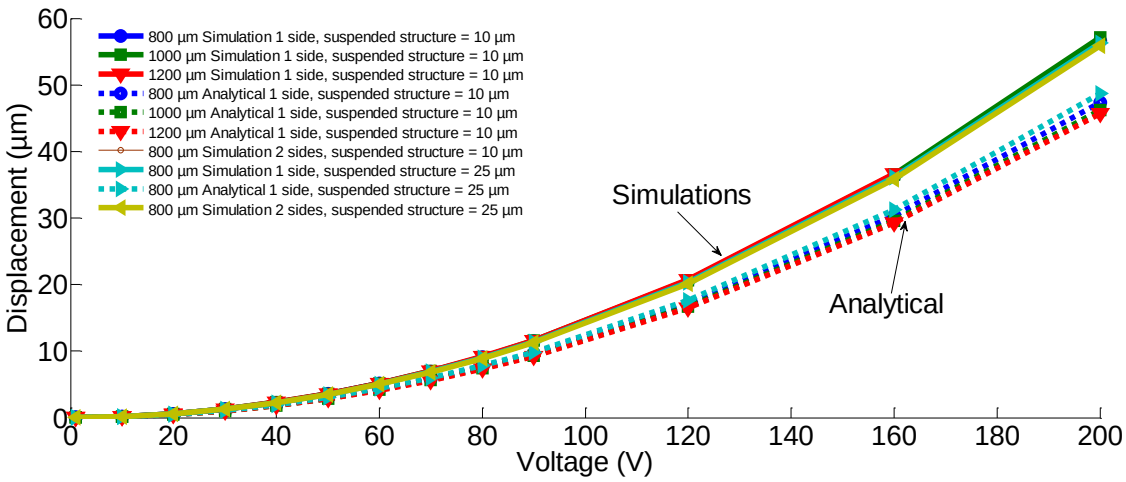

Figure 6.9 In-plane displacements for different applied DC voltages for 3SA microrobot for different tethering beam lengths and for suspended structure thickness of *10* µm and *25* µm.

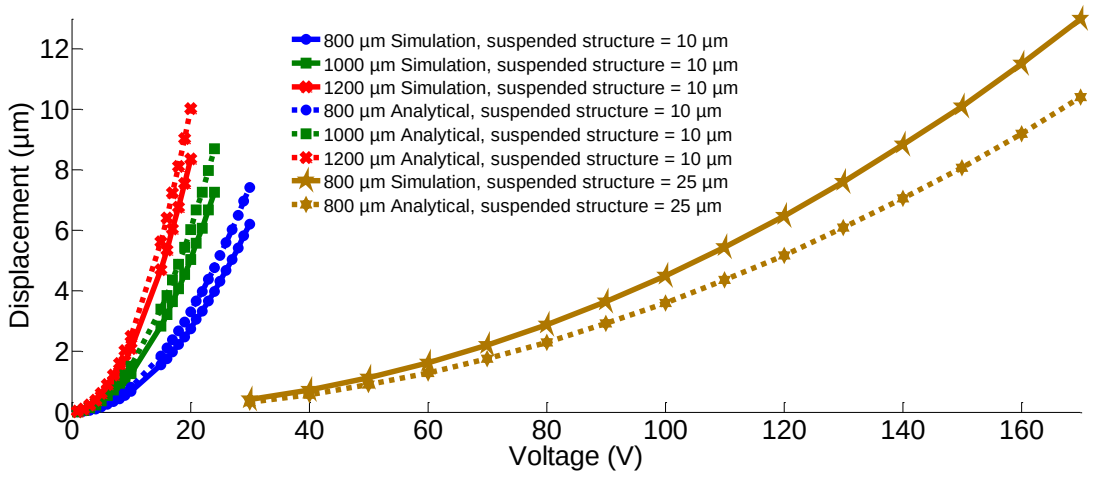

Figure 6.10 Out-of-plane displacements for different applied DC voltages for 3SA microrobot for different tethering beam lengths and suspended structure thicknesses of *10* µm and *25* µm. Actuator gap = *15* µm.

1200 µm does increase the out-of-plane motion, however it also increases the surface area of the arrayed actuator by at least *40%*. Moreover, increasing the thickness of the suspended structure from *10* µm to *25* µm significantly increases the DC voltage required to attain similar out-of-plane motion. In this case, it takes approximately *115* V to get a displacement of more than *6* µm. The out-of-plane simulations have been performed for parallel-plate actuator gap of *15* µm.

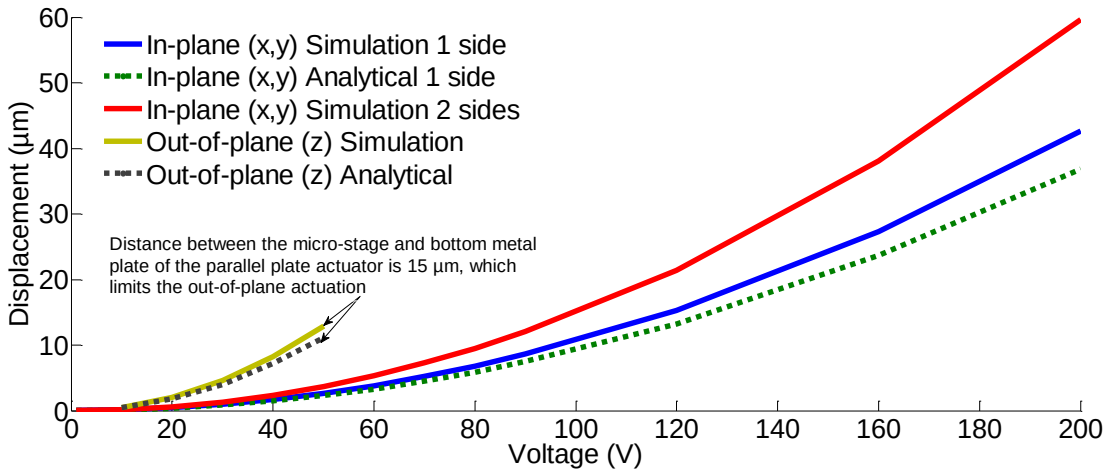

Figure 6.11 Displacements for different applied DC voltages for 4SA microrobot with same dimensions as the 3SA microrobot. Suspended structure thickness = *10* µm, Actuator gap = *15* µm, Length of tethering beam = *800* µm.

Comparing the results from the 3SA microrobot with the 4SA microrobot design, given all the dimensions is same, several interesting points can be observed as seen in Figure 6.12. For the in-plane actuation, the displacement achieved with single side actuating in a 4SA microrobot is lesser than that achieved with a 3SA microrobot. For example, at *160* V, 4SA microrobot can achieve an in-plane motion of around *27* µm with a single side actuated in comparison to slightly above *36* µm with the 3SA microrobot. Nonetheless, the displacement achieved with 4SA microrobot with double sided actuation is slightly greater than that with a 3SA microrobot design. For example, at *160* V, 4SA microrobot can achieve an in-plane motion of around *38* µm with double-sided actuation compared to slightly above *36* µm with the 3SA microrobot. Adding an extra side does add to the total stiffness of the structure. In terms of out-of-plane actuation, at *30* V, 4SA microrobot achieves a motion of around *4.5* µm compared to more than *6* µm with a 3SA microrobot. It becomes evident the performance enhancement in actuation by reducing an extra side while increasing the number of single-unit actuators that can be integrated in the parallel architecture surface area up by *40%*. The zone of actuation is shown through a 3D volume plot with respect to a human cell type in

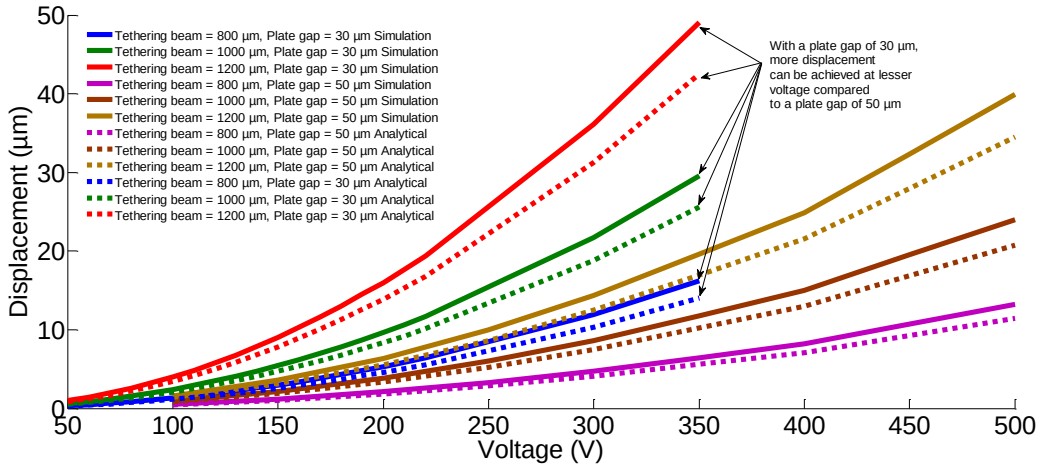

Figure 6.12 Out-of-plane displacements for different applied DC voltages for 3SA microrobot for different tethering beam lengths and for actuator plate gaps of *30* µm and *50* µm. Suspended structure thickness = *10* µm.

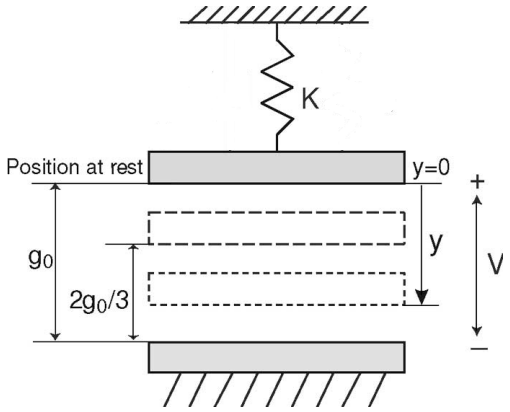

Figure 6.13 Schematic of an electromechanical system with parallel-plate actuation. The static pull-in occurs when the distance between plates is *2/3* of the initial gap. Reproduced from [3].

Figure 6.14. This actuator has a tethering beam length of *800* µm, a suspended structure thickness of *10* µm and an actuator gap of *15* µm. Given the cell size is about *25* µm in diameter, the actuator can easily move the microneedle over the size of the cell both in-plane and to a reasonable extent in out-of-plane.

Increasing the parallel-plate actuator gap from *15* µm to *30* µm and *50* µm affects the out-of-plane motion significantly. The results in Figure 6.12 demonstrate this effect. The suspended structure thickness of the 3SA microrobot is *10* µm and all the other dimensions

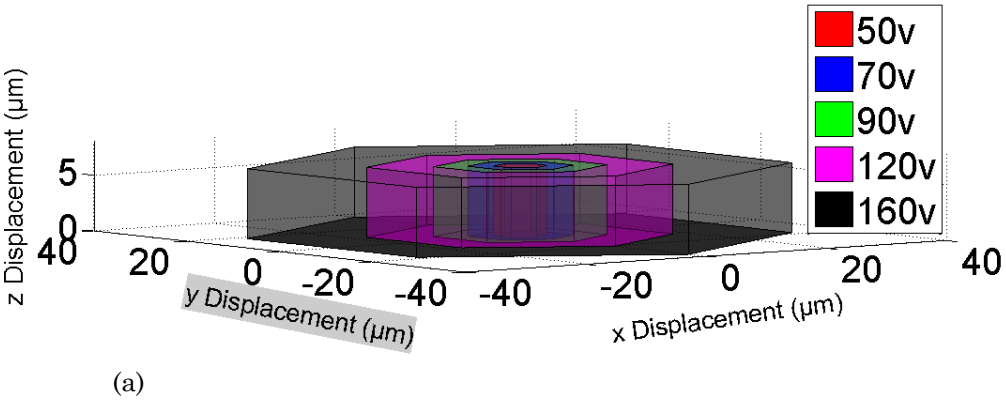

(a)

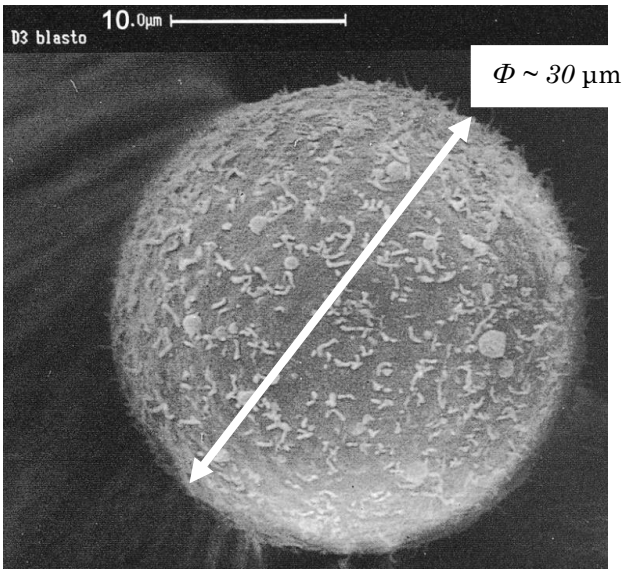

(b)

Figure 6.14 (a) Simulation 3D volume plot of the actuation of the 3SA microrobot. Suspended structure thickness = *10* µm. Actuator gap = *15* µm. (b) SEM image of a single blastomere from a stage *2*, *7*-cell embryo in vitro on post-insemination day *3* [4].

are kept constant, except increasing the parallel-plate actuator gap. Comparing the results for tethering beam length of *800* µm, it takes more than *200* V to achieve an out-of-plane motion of more than *6* µm with a gap of *30* µm and around *320* V with a gap of *50* µm. Increasing the length of the tethering beam does ease up the requirement of voltage, but it compromises the surface area of the arrayed architecture. Albeit decreasing the actuator gap does result in greater out-of-plane motion at a low voltage, but it limits the total motion range of the

actuator due to the pull-in effect. As seen in Figure 6.13, the static pull-in occurs when the distance between plates is two-third of the initial gap. Thus, increasing the parallel-plate gap increases the motion range, but consequently decreases the displacement available at a particular voltage. In the future design of the microrobot, it would be critical to find a trade-off where greater out-of-plane motion can be achieved at a reasonable voltage. This would be important in vertical bio-manipulation tasks where the cell sizes are reasonably large, such as between *30* μm - *50* μm in diameter.

6.4 Stress and Modal Analysis

For detailed discussion on these analyses, the reader may refer to Section 3.3.3. Herein we briefly mention the results from the stress and modal analysis of the design of the 3SA microrobot. The maximum von Mises stress developed in the structure is around *800* MPa at *160* V which is between *5-10%* of the yield strength of silicon, *7000* MPa. We have also simulated the downward sagging of the device under its own weight of the suspended structures, to be less than *0.005* nm, which is insignificant compared to the overall dimensions of the actuator.

Albeit, the current behaviour of the actuator is purely static, knowing the natural frequencies of the microrobot would be useful for widening the application of the arrayed architecture in the near future. Such applications involve single molecule force spectroscopy, cell mechanical measurements, local functionalisation of polymeric layers and molecular electronics such as depositing conductive polymers onto nanoelectrodes. A high designed natural frequency would allow the actuator to respond quickly and accurately to the rapid changes in the command signal. For the vertical out-of-plane motion of the microstage the first in-plane mode of vibration at *12* KHz is pure translational. The second mode of vibration at *27* KHz is out-of-plane translational plus rotation. The last three modes of vibration at *29*

KHz involve parasitic rotation of the comb-finger electrodes. The last three eigen-frequencies are almost *2.5* times higher than the desired translational mode of the microstage. Since these modes are located far from the first dominant mode, it indicates a significantly high stiffness to excite these parasitic motions.

6.5 Final design specifications of the 3SA microrobot

Based upon results obtained from the design conceptualisation, analytical and simulation models, the following design dimensions as summarised in Table 6.1 have been selected for fabrication.

6.7 Closure and original contributions

This chapter introduces for the first time in this dissertation the detailed treatment of the design of the 3SA microrobot. After discussing the design, analysis, fabrication and testing of motion performance of the 4SA microrobot, we now shift our focus to the design of the 3SA microrobot. This transition in design from 4SA to 3SA is strategic in that not only do we

Table 6.1 Design dimensions of the 3SA microrobot.

Mechanical properties of silicon	
Young's modulus	*129.5* GPa
Poisson's ratio	*0.28*
Desired actuation parameters	
In-plane actuation	At least *35* μm
Out-of-plane actuation	At least *5* μm
Resonant frequency	At least *10* KHz
Structural parameters	
Spring flexure beams	$w_s = 5$ μm, $h_s = 10$ μm, $l_s = 425\text{-}450$ μm
Tethering beams	$w_t = 4$ μm, $h_t = 10$ μm, $l_t = 800$ μm
Diameter of microstage	*300* μm
Parallel plate actuator gap	*15* μm
Height of silicon tower	*385* μm – *425* μm
Microneedle	Height = *50* μm -*100* μm, Tip diameter = *30* nm – *50* nm
Comb-drive actuator	$i = 800$, $t_f = 2$ μm, $gs_f = 2$ μm, $h = 10$ μm
Length of comb-finger	*105* μm
Opposite electrode spacing	*100* μm

achieve a better motion performance, but it leads to a higher density of packing in the parallel architecture as discussed earlier in Chapter 2. FEA and analytical studies show that a 3SA microrobot is better than a 4SA microrobot in terms of better actuation performance and easier integration of multiple actuators in a parallel architecture. The 3SA microrobot design can achieve an in-plane actuation (x, y) of *72* μm (±*36* μm) at 160 V and an out-of-plane actuation (z) of *7* μm at *35* V. Compared to this, a 4SA microrobot can achieve similar in-plane actuation and an out-of-plane actuation of *5.8* μm at *35* V.

Therefore, chapter 6 makes the following original contributions to the field of structural analysis:

- We have designed a new set of slope-deflection equations to study the behaviour of the actuator theoretically in addition to the grid-stiffness matrix model developed to analytically study the motion performance of the microrobot. From the review of the prior-art as discussed earlier in Section 3.1, none of the works have introduced a slope-deflection model which is capable of treating structures with angular components.
- Our 3-sided angular arrangement of the actuator sides in the microrobot is the first of its kind structure with 3D motion capability with the integration of the parallel actuator. From our review as evident in Sections 1.3.2 and 3.1, no such systems exist with a design like ours having 3D motion without being bulky in size.

BIBLIOGRAPHY

[1] Y. Zhu, A. Corigliano and H.D. Espinosa, "A thermal actuator for nanoscale *in situ* microscopy testing: design and characterization," *Journal of Micromechanics and Microengineering*, vol. 16, pp. 242-253, 2006.

[2] R. C. Hibbeler, *Structural Analysis*, 8th ed.: Prentice-Hall, 2012.

[3] A. Fargas-Marques, J. Casals-Terré and A.M. Shkel, "Resonant pull-in condition in parallel-plate electrostatic actuators," *Journal of Microelectromechanical Systems*, vol. 16, pp. 1044-1053, 2007.

[4] G.Nikas, A. Ao, R.M.L. Winston and A.H. Handyside, "Compaction and surface polarity in the human embryo in vitro," *Biology of Reproduction*, vol. 55, pp. 32-37, 1996.

Chapter 7: Fabrication of 3SA Microrobot and Parallel Architecture

7.1 Introduction[1]

Having analysed the design of the 3SA microrobot in Chapter 6, this chapter presents the fabrication process of the 3SA microrobot and the first parallel architecture incorporating *2×1* such microrobots. This is currently undergoing fabrication at the Canadian Microelectronics Corporation (CMC) in Canada. This process, called MicraGEM-Si technology uses two SOI wafers with the bottom electrode being etched on the base wafer and the suspended actuator structures on the top device wafer. The two wafers are electrically connected through the bond interface, resulting in 3D routing of electrical signals. The microneedle is separately fabricated and assembled onto the microstage using Focused Ion Beam (FIB) tool fitted with an Omniprobe micro-manipulator. Since, we have already reviewed the prior art in fabrication in detail in Chapter 4, we will directly shift our focus to discussing the fabrication process flow and the mask design rules that need to be followed to ensure a reliable final product.

7.2 MicraGEM-Si fabrication process

We have fabricated the 3SA microrobot using MicraGEM-Si™ technology which is a process platform for MEMS prototyping developed by Micralyne Inc. in Canada [1]. The advantage of this process is that using two thick SOI structure layers, different thicknesses of silicon can be fabricated on the base device layer. The top device layer undergoes silicon etch in the back side and a release etch from the top side to form the suspended actuator structures. Two SOI wafers are used to fabricate the bottom Si tower based electrode and for making

[1] Elements of the following chapter have been published/ presented in conference C2 or in preparation for journal J1.

trenches to insulate the different electrical components on the actuator. The top device SOI wafer is used to fabricate the suspended actuator structures. These two wafers are then mechanically bonded followed by further etching to create the final device. The mask designed in L-Edit shown in Figure 7.2, shows five different masks involved in the fabrication (mask Y is hidden to make the comb-drive actuators visible).

The process starts with a base SOI wafer with a device layer thickness of *50* ± *0.5* μm. The wafer properties are noted in Table 7.1. The wafer coated with photoresist is lithographically patterned by exposing the photoresist with light through the Trench *1* mask and then developing it followed by a DRIE. This etches the structure through the entire *50* μm device layer down to the buried oxide of *1* μm. This insulates the bottom electrode Si tower with the suspended actuator structures. This process is repeated with Trench *3* mask which etches up to only *10* ± *1* μm to form the electrical interconnect from the metal pad to the bottom electrode. The top device SOI wafer is patterned with mask Y (suspended actuator structures, mask Y encloses mask Z except under the microstage) for a single timed backside DRIE to a depth of *20* ± *1* μm. The device layer of this second wafer is *30* ± *0.5* μm, thus leaving a thickness of the suspended structures to *10* μm. The base SOI wafer is mechanically bonded to the top device SOI wafer with an alignment tolerance of ±*10* μm. After fusion bonding, the handle of the top wafer is removed with a grind and polish process. The buried oxide of the top wafer is also removed leaving a pristine optically flat silicon surface. This also provides electrical connection between the two silicon device layers. The top SOI handle and buried oxide layers are subjected to DRIE, finishing with wet etching to preserve silicon surface quality. This is followed by blanket physical deposition of metal film (*100* Å thickness of Ti-W and a *750* Å thickness of Au), photolithographic patterning and wet chemical etching. The substrate is then photolithographically patterned with mask Z (enclosed by mask Y as mentioned in (b)) to define the suspended actuator structures. DRIE is performed thus

Table 7.1 Wafer properties for manufacturing 3SA microrobot.

Layer property	Value
Base SOI device layer thickness	*50 ± 0.5* μm
Base SOI handle layer thickness	*500* μm
Top SOI device layer thickness	*30 ± 0.5* μm
Buried oxide thickness	*1* μm
Base SOI device layer resistivity	*0.01-0.02* Ω-cm
Base wafer handle layer resistivity	*1-100* Ω-cm
Top SOI device layer resistivity	*0.01-0.02* Ω-cm
Metal layer residual stress	*40-140* MPa

releasing the structures to form the final device as shown in Figure 7.1g. During this process, features in the lower layers are exposed to over-etching even before all suspended features have been completely etched. Very wide features open first, while high aspect ratio features open last. This is followed by a singulation process with a laser. The assembly of the micro needle on top of the microstage will be performed using similar technique as reported by Jung et al [2]. The needle is fabricated separately and then welded to the microstage by Pt deposition using a combination of ion-beam and e-beam to cover the top and sides of the needle.

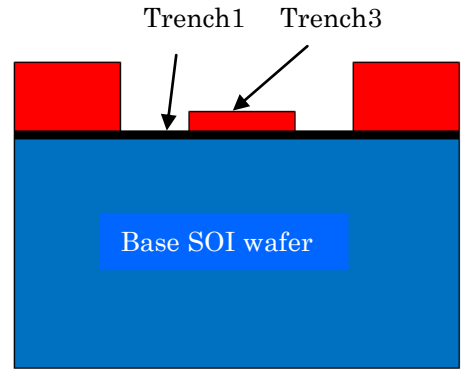
Trench1
Trench3
Base SOI wafer

(a)

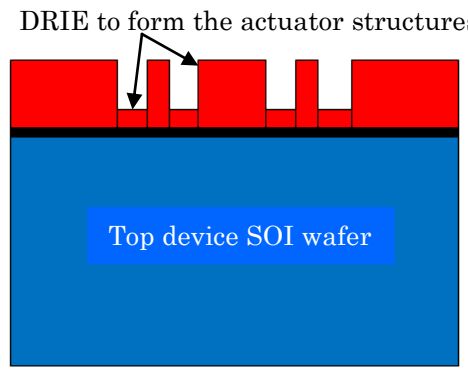
DRIE to form the actuator structures
Top device SOI wafer

(b)

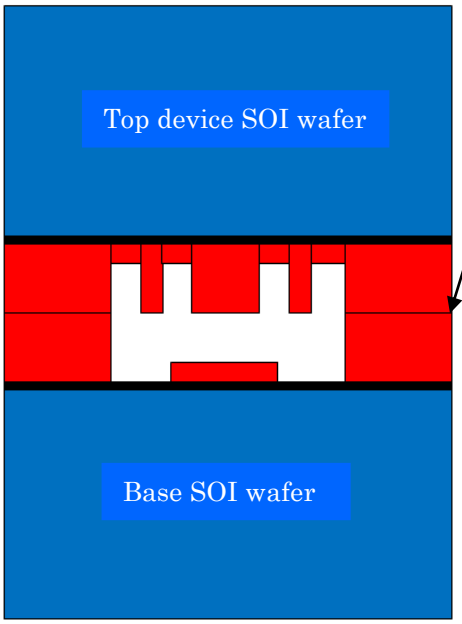
Top device SOI wafer
Mechanical bonding
Base SOI wafer

(c)

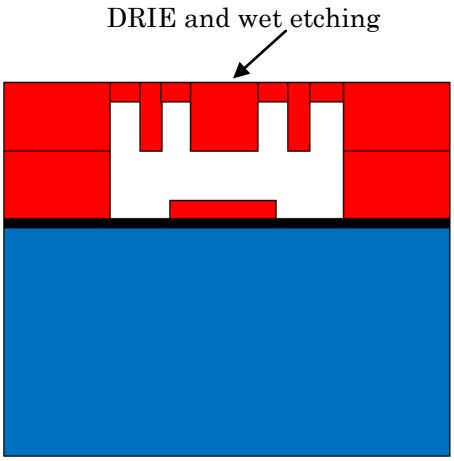
DRIE and wet etching

(d)

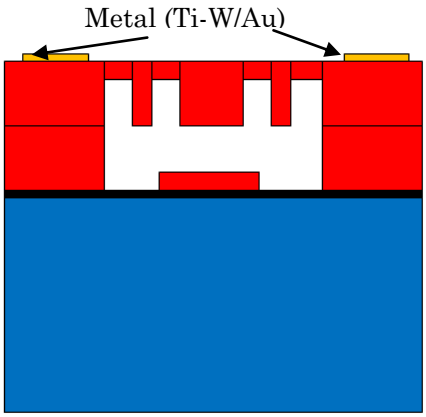
Metal (Ti-W/Au)

(e)

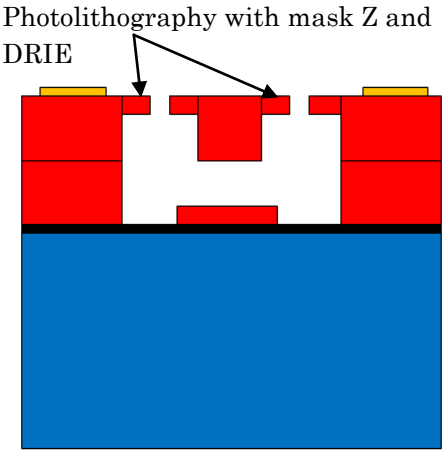
Photolithography with mask Z and DRIE

(f)

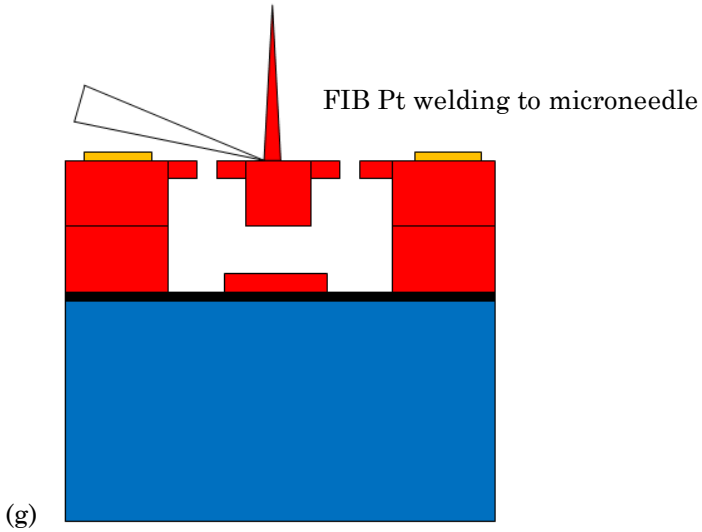

Figure 7.1 Fabrication process flow for *2×1* 3SA microrobotic parallel architecture.

7.3 Mask design rules

The mask is designed in L-Edit *v15.2*, a 2D layout editor from Tanner EDA, as shown in Figure 7.2 [1]. The mask is designed on a design area of *8×8* mm^2. Table 7.2 summarises the characteristics of the six mask layers used in the fabrication and Table 7.3 highlights the general design guidelines. The substrate mask must enclose Trench *1*, Trench *3*, metal, Y and Z by at least *112* μm. Any overlap between Trench *1* and Trench *3* will be etched as Trench 1. The maximum width of Trench *1* and Trench *3* must not exceed *1500* μm. Ideally Z should enclose all Y features. If a Y etch area is not enclosed by a Z area, not only the device layer of the top SOI wafer such as the microstage will be etched open sooner than where Y etch does not exist, but also there will be over-etching of lower features. But in our case, since we want the suspended structures to be *10* μm thick, the entire suspended structure with Z features have a Y etch underneath. Since the alignment tolerance of Y to the features on Z is *10* μm, therefore Y encloses the Z features by at least *10* μm. This helps avoid over-etching of the base layer features under the Y features region. Z must enclose all metal features; otherwise any metal feature outside of Z will be etched away before the Z mask etch. The metal mask etch all introduces undercut of the metal layer. All Z features will have metal

etched at an approximate distance of *1* μm from their edges. Thus, a *2* μm Z feature will have almost little to no Metal left atop it due to the undercut.

The bond pads are on the metal layer and therefore are placed on top of the top SOI wafer. The minimum pad size is *100* μm × *100* μm and there should be more pads on one side than bonding fingers. The wire bonding pad to the bottom silicon tower sits on top of the top device SOI wafer and is routed through a metal electrical interconnect that sits on top of Trench *1* of the base SOI wafer. In order to minimise the curvature of the microstage caused by the metal stress, the Y etch is absent from the back of the microstage (Top SOI backside) and therefore will be etched up to the full thickness of *30* μm. All concave corners of the beam intersections have been filleted to avoid the stress concentration on these corners and reduce the risk of failure.

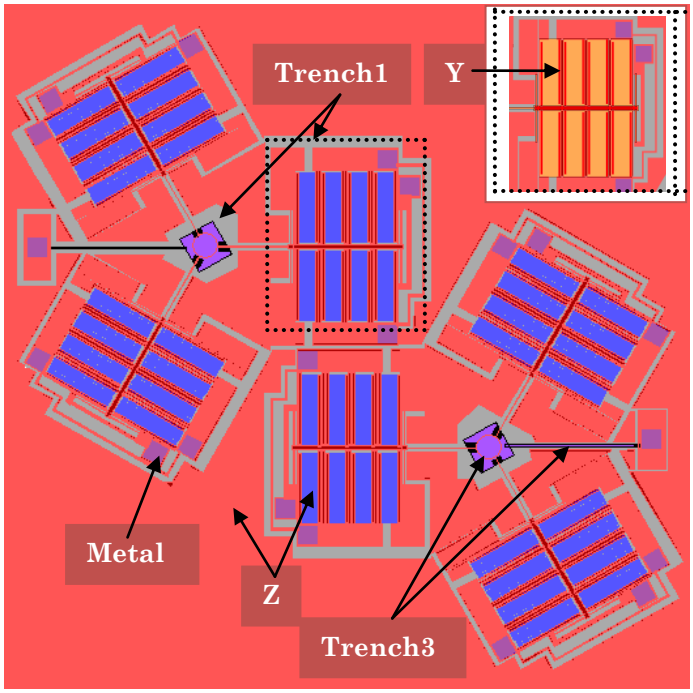

Figure 7.2 L-Edit mask design of the *2* × *1* 3SA microrobotic parallel architecture (*8* mm × *8* mm) being manufactured at CMC, Canada showing five different masks used in the fabrication. Mask Y (yellow) is kept hidden to highlight the comb-drive actuators. The upper-right corner window shows a part of the mask with mask Y visible.

Table 7.2 Design guidelines for drawing masks.

Mask------→	Trench 1	Trench 3	Z	Y	Metal
Design Rule					
Feature size	4	1	2	1.5	4
Spacing	4	1	2	1.5	3

Table 7.3 Characteristics of the mask layers.

Mask layer	Description	Digitised Features	Alignment tolerance
Substrate	Define substrate outline		
Trench 1	Define regions etched through entire *50* μm device layer down to the buried oxide to isolate regions of silicon from one another	Material to be etched	±*0.1* μm to substrate
Trench 3	Define regions etched to depth of *10*±*1* μm	Material to be etched	±*0.1* μm to substrate
Z	Define structure in Top SOI device layer	Material to be kept	±*0.4* μm to substrate
Y	Timed DRIE etch to a depth of *20* μm for partial height released features	Material to be etched	±*10* μm w.r.t features on substrate and Z layer
Metal	Metal deposition on top of the Top SOI device layer. This is defined as a positive layer i.e. the metal feature is left after etch	Material to be kept	±*0.4* μm to substrate

7.4 Closure and original contributions

We discuss the fabrication process of the first-of-its-kind parallel architecture incorporating *2×1* 3SA microrobots with independent 3D motion capability being manufactured using MicraGEM-Si process. This fabrication involves five masks, two SOI wafers and mechanical bonding and is capable of overcoming the limitations experienced during the fabrication of the 4SA microrobot. The microneedle will be assembled atop the microstage using a combination of focused ion beam and e-beam techniques.

Chapter 7 makes the following original contribution to the frontier of MEMS fabrication:

- We are fabricating the first parallel architecture incorporating multiple independently moving 3D microrobots. As reviewed in the prior art in Section 4.2, there are no such parallel architectures present that have such independent multiple-axes motion.

BIBLIOGRAPHY

[1] P. Yang and K. Sandaluk, "MicraGEM-Si Platform design handbook," CMC Microsystems, Montreal, Canada2014.

[2] I.W. Jung, B. Park, J. Provine, R.T. Howe and O. Solgaard, "Highly sensitive monolithic silicon photonic crystal fiber tip sensor for simultaneous measurement of refractive index and temperature," *Journal of Lightwave Technology*, vol. 29, pp. 1367-1374, 2011.

Chapter 8: Feedback Mechanism for Biomanipulation

8.1 Introduction[1]

Hitherto, this dissertation has primarily focused on the microrobotic platform, its design and its evolution from 4SA to 3SA microrobot, analyses, fabrication and experimental tests. This chapter will now focus on the process of biomanipulation, more specifically, cell manipulation using a feedback mechanism that we have developed to enable such tasks to occur in a 3D workspace. The feedback uses a combination of visual feedback for in-plane detection of the target site inside a cell and a blind non-visual feedback that uses the parallel-plate actuator as a sensor for vertical manipulation. We give an overview of the visual feedback process and verify the blind feedback mechanism through a macro membrane-manipulation experimental model. Section 8.2 briefly discusses the state-of-the-art in force feedback mechanisms and systems for biomanipulation and clearly discerns our feedback mechanism from the existing ones. Section 8.3 discusses the feedback mechanism, first the visual feedback developed to detect a particular target organelle inside a cell to guide the in-plane motion of the microneedle. Further it investigates the blind feedback through a macro experimental setup, and discusses the physics behind the experimental concept, the analytical model of membrane penetration and validation of the simulation and experimental results of penetration detected by a signature feedback curve. We also discuss a control scheme for the 3D motion of the microrobot incorporating our feedback mechanism. The chapter is summarised in Section 8.4.

[1] Elements of the following chapter are in preparation for submission to journal J2 and are a part of US and NZ provisional patent application pending P1.

8.2 Prior art

A major concern while manipulating multiple cells or molecules in a multi-dimensional workspace (in our case, it is 3D) is the inability to use visual feedback during vertical motion of the actuator. Referring to Figure 8.1a for the proposed experimental setup, for tracking the targeted sites inside the cell in *xy* coordinate frame, visual feedback becomes critical. Nonetheless, for vertical motion of the microneedles in the *z* coordinate frame, the camera placed sideways (Figure 8.1b) can only visualise the cells on the periphery of the cell trapping platform as shown in Figure 8.1b. The cells trapped inside the interior of the cell trapper cannot be visualised by this camera, thus leading to an uncertainty of location. The solution we propose is to use a manipulation feedback mechanism involving two variable

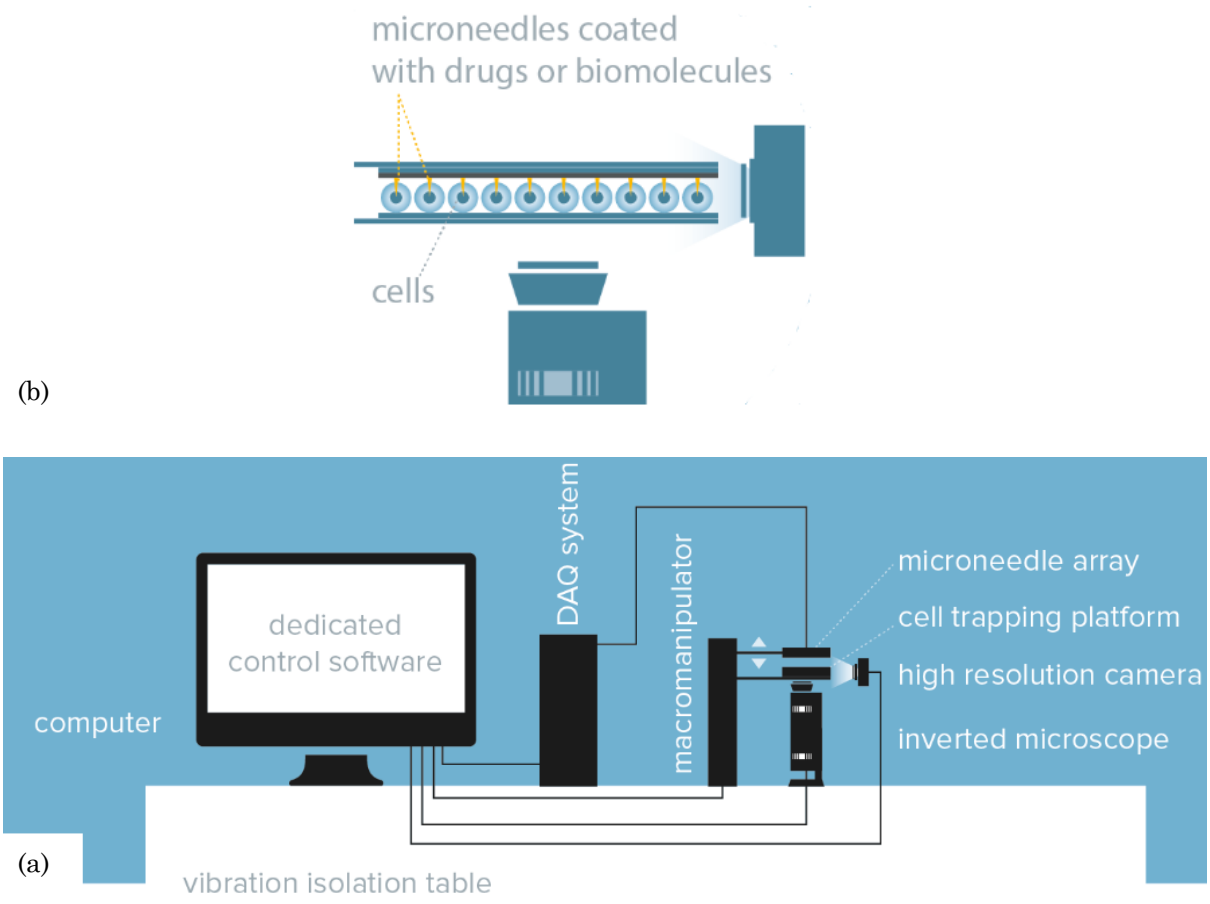

Figure 8.1 (a) Our proposed cell manipulation experimental setup. (b) High resolution camera placed sideways visualising the cells in the periphery of the cell trapper.

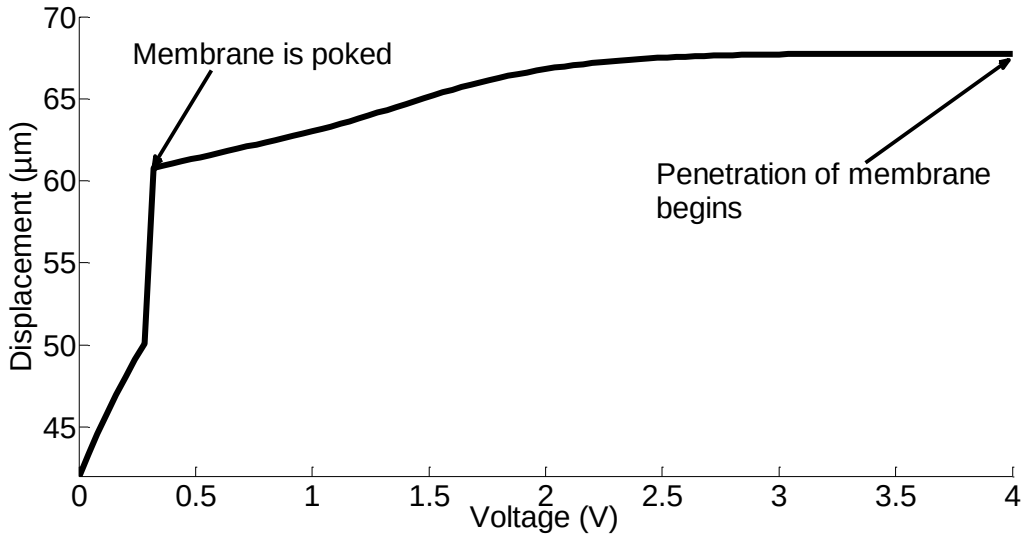

Figure 8.2 A blind feedback voltage-displacement signature curve for vertical manipulation.

parameters, namely change of potential in the parallel-plate actuator in relation to the change of position of the microstage relative to the silicon tower as shown in Figure 8.10. The sudden significant drop in the plot between the two parameters, namely voltage and displacement during vertical motion is used as a signature for feedback to the controller to enable the biomanipulation. Referring to Figure 8.2, this change in the plot can be attributed to the change in stiffness of the cell membrane that is sensed by the microneedle which is reflected in the voltage-deflection curve. This has been treated in detail in Section 8.3.2.

A majority of the work in the past decade for micro and nano manipulation has been dedicated to either vision feedback based system or force related measurements. Some examples of vision guided cell injection system developed consist of feature tracking, micropipette positioning, cell membrane penetration and biological material injection processes for cells of size around *20* µm [1]. 2D to 2D feature tracking of the micropipette tip is used for position control using sum of square difference (SSD) algorithm. The micropipette tip controlled using a modified proportional position controller is used to successfully penetrate and deposit fluorescent materials into adherent orchid petal and Chinese hamster ovary (CHO) cells. Another example is a 2D autonomous manipulation system developed for

manipulating polystyrene and silica microspheres based on an optical microscope for visual feedback and a nanoprobe [2]. These microspheres are detected using the generalised Hough transform image processing algorithm. This transform is used to produce binary image of the spheres through the Sobel edge detector, a noise-resistant algorithm, and thresholding. This binary image leads to the final processed image. This combined with the wavefront expansion motion planner is used to arrange the microspheres into user-defined patterns in the workspace. Another similar example includes a microassembly workstation developed for automated 3D assembly of microobjects such as micro polystyrene balls using a hybrid control scheme incorporating both vision and force feedback [3].

Work done at the University of Toronto has dealt quite exclusively with using both visual and force feedback during cell manipulation. An automated cell contour visual measurement technique has been developed along with a data synchronisation mechanism for real-time, high-accuracy mechanical characterization of individual cells with micropipette aspiration [4]. Human neutrophils and porcine aortic valve interstitial cell (PAVIC, *10-20* μm in diameter) deformation parameters have been accurately measured in real time at *30* Hz using a sub-pixel visual tracking algorithm with a resolution down to *0.21* pixel. An identification algorithm locates the micropipette tip. This algorithm locates the micropipette tip by establishing an initial contact between the cell and the side wall of the tip. The vision-based algorithm applies gradient subtraction, adaptive thresholding and morphological operation to identify the tip which is then used as a reference position for tracking cell deformations. Applying such a vision-based algorithm in our parallel architecture will require multiple high resolution cameras to identify the tip of arrays of microneedles. This will make the setup not only cumbersome but also impossible to track the position of the tips in the interior of the architecture. Therefore, a non-visual feedback while handling the vertical motion of the microneedles in our system is significantly better.

Using similar algorithm they have tracked cell structures such as zona pellucida, cytoplasm and polar body of a mouse embryo in real time [5]. This tracking occurs with a translation-rotation-scaling motion model, providing image position feedback to an image-based visual servo controller that is responsible for online calibration of coordinate transformation during visually servoed orientation of the first embryo. High-speed, automatic cell orientation is then conducted on other embryos in the same batch of immobilised embryos through coordinate transformation and 3D closed-loop position control. The group's automated injection system utilises the same vision-based contact detection algorithms [6] between the micropipette tip and the embryo and further deposition into the cytoplasm center inside the embryo. It is shown in Figure 8.3 [7]. This range of events takes place sequentially for every embryo until all the embryos in the batch are injected. The motion sequences of the two microrobotic stages driving both the embryo holding device and the micropipette are based on their position feedback, following the PID control law. A sequence of the microrobotic mouse embryo injection is demonstrated in Figure 8.4 [8]. Visual feedback is used through the automatic embryo injection process. The system is divided into five different coordinate frames, namely of the end-effector that drives the micropipette, *xy* translational stage and rotation stage that houses the device to immobilise the mouse embryos, camera and image plane. The cellular structures such as cytoplasm and polar body are identified using visual feedback. Three closed-loop PID position controllers using visual feedback are used to guide the micropipette, *xy* stage and rotational stage. A virtual switch, *K* controls the transition from separate control of the *xy* stage and the rotational stage (state 1) to simultaneous, cooperative control of the *xy* and rotational stages (state 2, activated during automatic embryo injection). The micropipette used here has an angular setup with respect to the microrobot driving it, thereby leading to difficulties during orientation control of the embryos (Figure 8.4b). The embryo needs to be brought into the field of view of the camera

so that the manipulation is successful. This can be achieved when dealing with one embryo or cell at the time, but in a parallel manipulation system like ours, achieving such control becomes enormously complicated. Comparatively, the microneedles in our system are all placed orthogonal to the plane of the cells and therefore avoid the complication of orientation control by using a non-visual feedback.

In terms of force-feedback systems, achieving autonomous biomanipulation requires the micro or nano end-effector to have force sensing capabilities that can detect microscopic forces when the penetration through the cell membrane occurs. In one such work [9], end-effector with injection pipette and microforce sensor made of piezoelectric polymer,

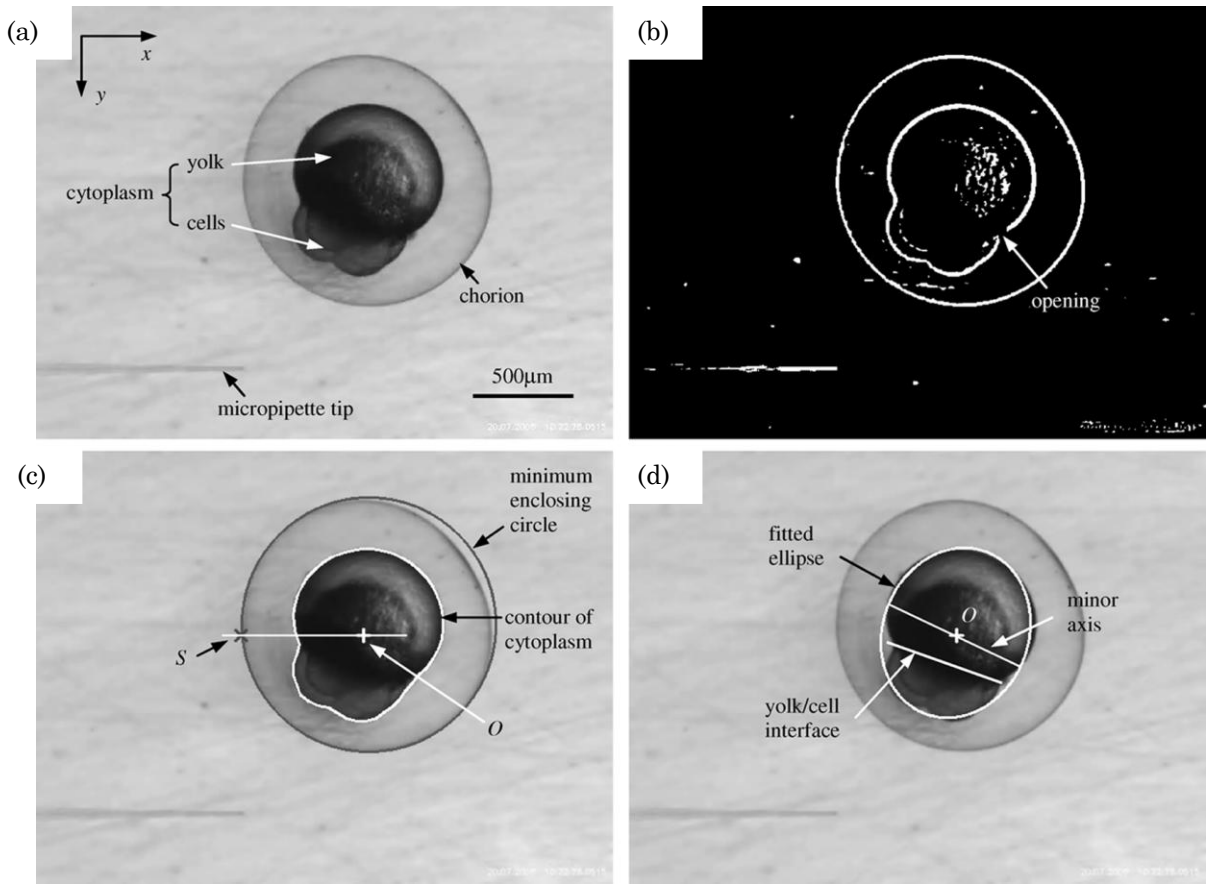

Figure 8.3 Recognition of zebrafish embryo structures. Image under *2.5*×. (a) Zebrafish embryo. (b) After pre-processing. (c) Recognized chorion, cytoplasm center, and switching point. (d) Distinguished yolk and cell portion [7].

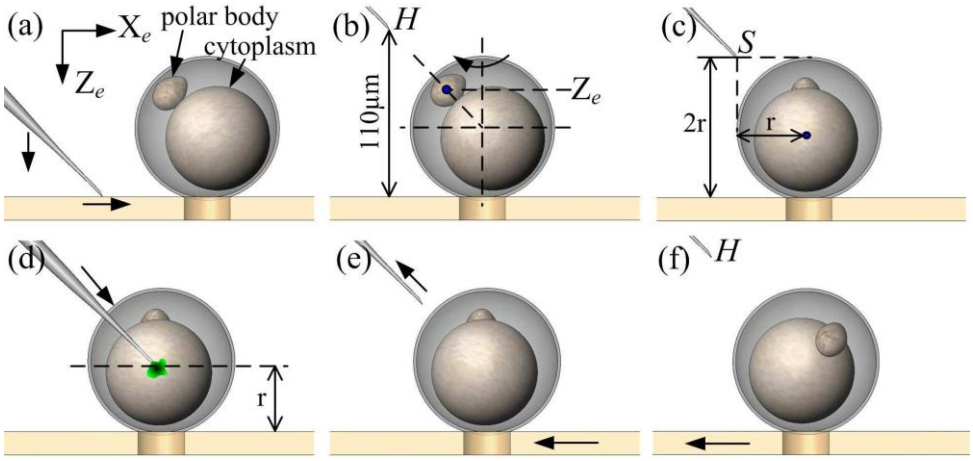

Figure 8.4 Overall control flow of microrobotic mouse embryo injection. (a) Contact between micropipette tip and cell holding cavity is detected using a vision-based algorithm. (b) The micropipette tip is elevated to a home position H, and the first embryo is brought into the field of view, recognized and centered. If the polar body faces the penetration site, the embryo is properly rotated through orientation control. (c) Micropipette is moved to a switch point, S. (d) The micropipette penetrates the embryo and deposits materials to the target destination. (e) The micropipette is retracted out of the embryo. (f) Micropipette is moved to the home position. Simultaneously, the next embryo is brought into the field of view [8].

PVDF (poly vinylidene fluoride) has been developed. This is integrated with the micro-telemanipulation system along with a haptic interface which reflects live injection force signal to the operator with minimal noise. Cellular force profile for zebrafish egg cell (*700* μm in diameter) indicates the injection force to be a few millinewtons and the peak force goes down as the injection velocity increases. The outer membranes such as the chorion envelopes are deformed as much as *120* μm before being punctured at a force level of *1.62* mN. A similar force sensor-integrated superelastic alloy-based microgripper is used for fine alignment tasks of micro opto-electrical components [10]. The microgripper which is fabricated using electro discharge machining technology can sense the gripping force at several tens of μN level. Another PVDF-based force feedback interface, shown in Figure 8.5 with the capability of measuring forces in the range of μN-mN also uses a haptic mechanism

to measure the cell injection forces in real time [11]. They have used a combination of vision and force feedback to perform the manipulations on zebrafish egg cell preparation. The puncturing force for a zebrafish egg cell membrane is *700* µN [11] compared to a salmon fish egg cell membrane which is *2.38* mN [12]. Penetration force of living cells has also been studied using AFM probes [13]. Range of penetration forces for cells L*929* is *3-6* nN and *18-22* nN, for HeLa is *2-13* nN, for *4*T*1* is *2-17* nN and for TA*3* HA II is *3-9* nN. For every indentation however, it is found that penetration is not guaranteed.

Piezoelectric actuators have also been used for intracytoplasmic sperm injection into

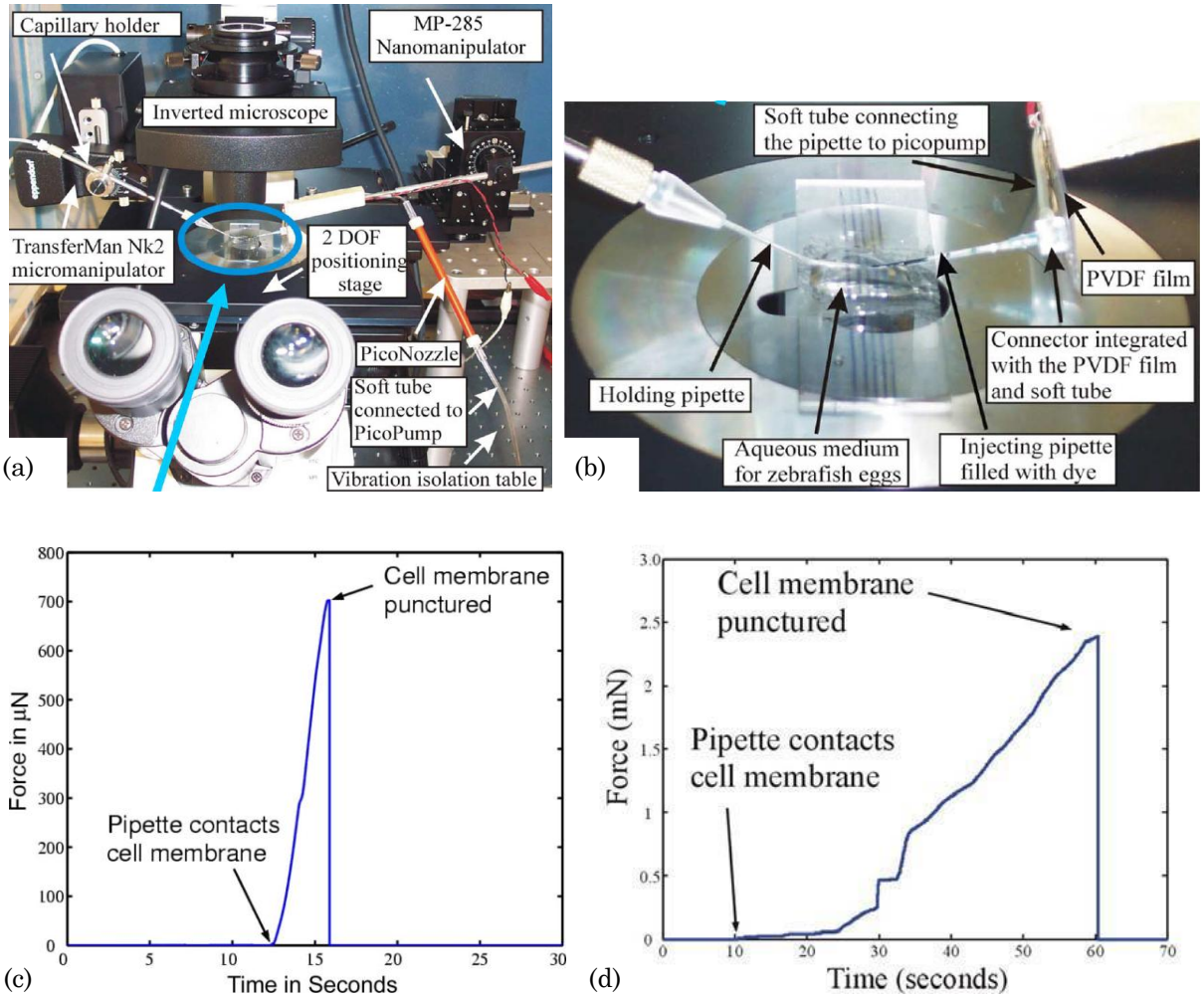

Figure 8.5 (a) Experimental system for evaluating the role of force feedback in cell injection task. (b) Magnified view of the cell injection system. Variation of force with time during membrane puncture of a (c) zebrafish egg cell (*700* µN) [11] (d) salmon fish egg cell (*2.38* mN) [12].

female oocyte using linear reciprocating motion and repetitive angular motion [14]. In linear reciprocating motion, this type of motion of the needle along the injector axis is used to assist cell penetration, generating a compressive shear force on the oocyte through repeated targeting of the same spot of the zona pellucida. In partial rotating motion, the needle is given a repetitive angular motion thus generating vertical shear force to penetrate through the membrane. Repetitive puncturing on a cell membrane may however cause significant damage to the cell. In another work [15], the researchers propose an adaptive force tracking algorithm within the impedance control framework to control the injection force applied on the cell through vibration to compensate for the cell membrane's unknown stiffness.

A millimeter sized MEMS based nanomanipulator is developed that uses a capacitive displacement sensor for detecting input displacements which are converted into output displacements allowing closed-loop controlled nanomanipulation [16]. The device is used for characterising and manipulation of nanomaterials and construction of nanodevices. It has a positioning resolution of *0.15* nm, an output motion range of *±2.55* μm and a high force output capability. Similar concept has been used to develop electrothermally actuated monolithic microgrippers integrated with 2D force feedback to enable manipulation and

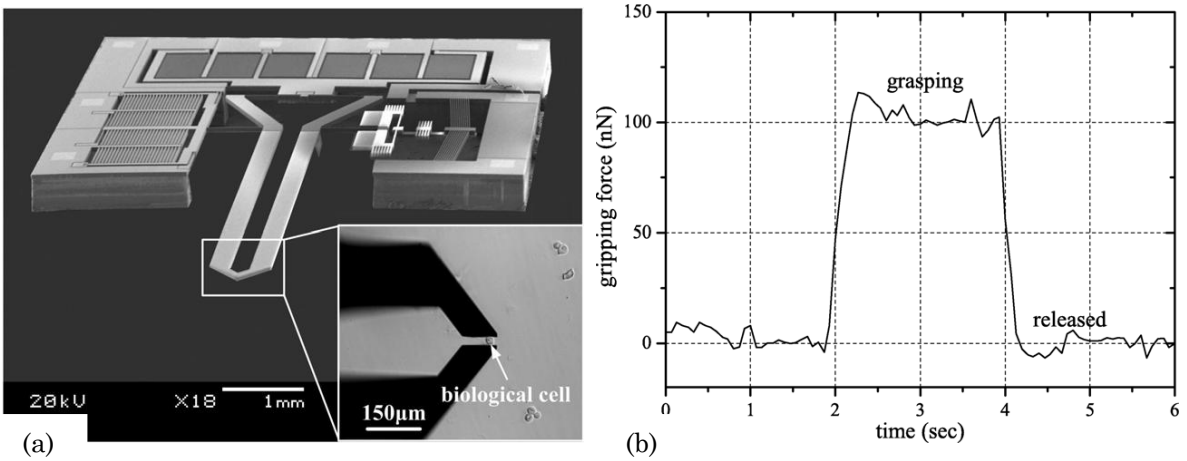

Figure 8.6 (a) MEMS-based microgripper with integrated 2D force sensor. Inset picture shows nanonewton force-controlled grasping of a biological cell. (b) Gripping force profile during micrograsping and releasing of a PAVIC [17].

positioning of porcine aortic valve interstitial cells in cell culture medium at the nanonewton force level (*20* nN) [17]. PID force controller is used to regulate gripping forces for micrograsping as shown in Figure 8.6. The temperature rise at the gripping arm tips caused by Joule heating of the electrothermal actuator is found to have caused no damage to the cells. In conjunction with a sub-pixel visual tracking algorithm with a *0.5* pixel resolution, the microgripper has also been used for microrobotic mouse embryo injection [18] and microscale compression testing of soft hydrogel microcapsules (*15-25* μm in diameter) at wet state [19]. Although such force feedback mechanisms do allow manipulating at the micro and nano scale, nonetheless, none of these designs and models can fit in the form of a 3D microrobotic actuator like ours. The very simple reason being that all of these actuators are designed to handle single manipulation tasks at a time. Scaling it up to handle parallel manipulation tasks in a 3D workspace requires more sophisticated feedback mechanism.

Gorman and Dagalakis [20] have developed a micromanipulation system that uses a sharp tungsten probe with high precision positioning system to manipulate microspheres into targeted locations and configurations within a 2D workspace. Tungsten probes are tough, cheap and have a high Young's modulus. Such manipulation using piezoelectric actuators include pushing with the side and tip of the probe in addition to picking and placing microspheres. This probe is attached to a micro force sensor to measure contact force during manipulation and also to control vertical force. The probe can be used to roll a microsphere by placing the tip on the top of the microsphere and then moving the probe parallel to the substrate. The probe is also used to vertically manipulate microspheres. In another related work shown in [21], force control of linear motor stages with force regulation on the order of micronewtons is developed with application to the microassembly of MEMS. The linear motor stage is used to move a microgripper holding a micropart into contact with an assembly surface. The force control uses an outer force control loop which feeds a position

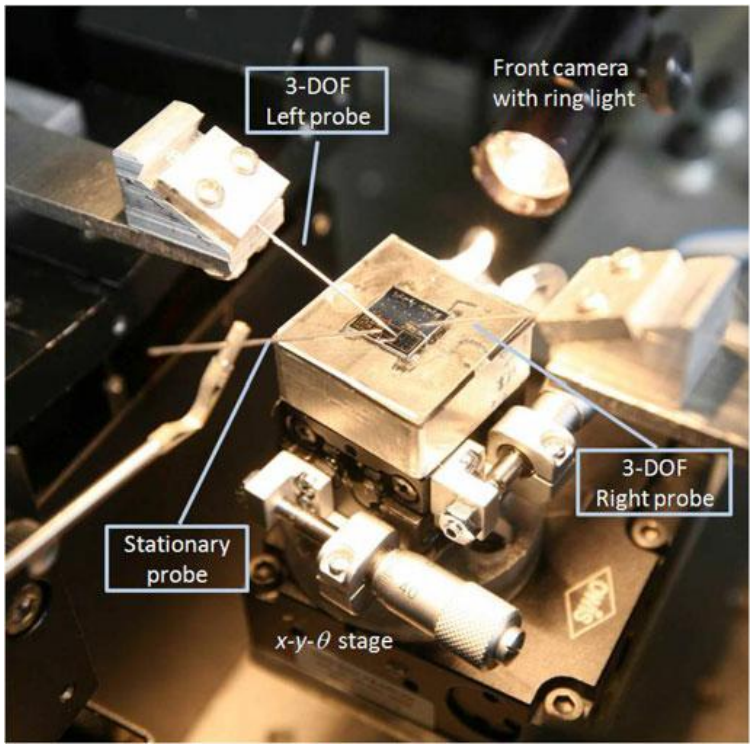

Figure 8.7 Closeup view of the microassembly experimental test bed [22].

command into an inner motion loop. The closed loop system is fed a desired force signal which is compared to the measured force at the robot end-effector. The error between the desired and actual force is then used to generate a position command based on the force control law. In addition, a high-gain trajectory estimator is included so that the inner motion control receives complete trajectory information. The proposed control design can effectively control the contact force, even when there is uncertainty in the friction and force ripple parameters on the order of ±5%.

Multiple sharp-tipped tungsten probes are coordinated to manipulate and handle parts of widely varying sizes and geometry by using vision feedback as shown in Figure 8.7 [22]. Such manipulation includes grasping, rotation and picking and placing. Some important parameters while manipulating micro and nano scale objects include proper coordination of the finger tips to apply sufficient squeeze without dropping the part or causing it to buckle and break. In another interesting and slightly different approach of using force feedback, a

versatile method for measuring in-plane and out-of-plane stiffness of microelements such as a nanopositioner has been achieved using AFM probe [23]. After calibrating the probe for vertical bending and torsional stiffness, it is pushed vertically and later laterally against the nanopositioner stage. This leads to the stage's deformation and thus the stiffness can be calculated using the force stiffness equation.

Thus, the critical finding from the review of the prior art in feedback systems for biomanipulation are:

- Almost all the systems reviewed above have exclusively used either a vision feedback or force-feedback system. In some hybrid models [17, 22], both vision and force-feedback mechanisms have been employed, but they are not only stand-alone systems but hard to scale up as in a parallel-scale operation. This is due to the difficulty faced with using multiple cameras in our system, lack of orientation control of the cells associated with the existing systems and use of multiple probes in achieving manipulation which is challenging if incorporated into a parallel architecture system like ours.

8.3 Feedback mechanism for biomanipulation

Referring to the proposed biomanipulation experimental setup, shown above in Figure 8.1, the in-plane motion of the microneedles is driven by a visual feedback mechanism and the out-of-plane motion is driven by a blind-feedback mechanism. The force feedback systems reviewed in the previous section primarily measure the force during manipulation, plotting force against time, and using it as a signature to detect penetration and poking. In comparison, our blind feedback mechanism plots voltage against displacement and use it as a characteristic signature during manipulation. Rather than measuring the force, we measure the deflection in voltage and predict the points of penetration and poking into the cell. The following two sections will discuss these two mechanisms.

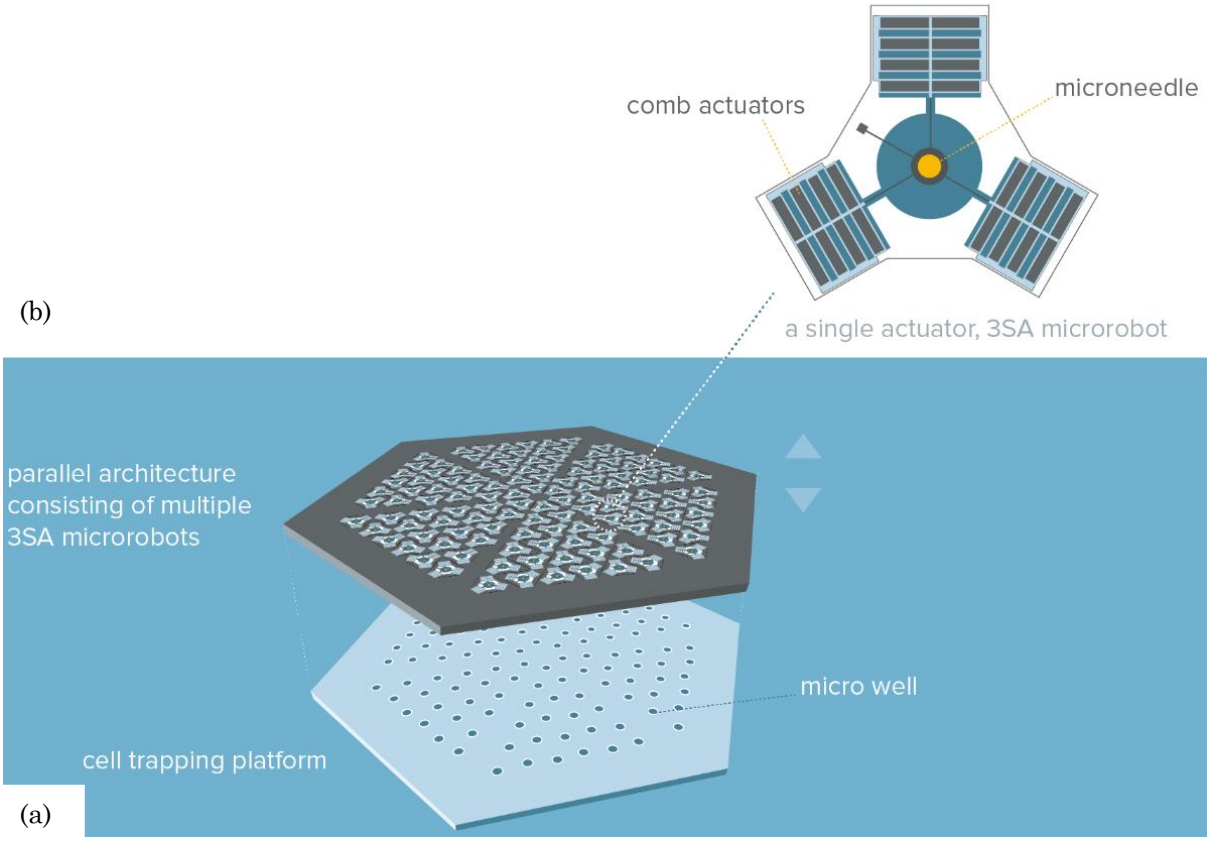

Figure 8.8 Cell trapping platform for immobilising individual cells in individual microchambers. (a) Parallel architecture chip and (b) its individual component, 3SA microrobot placed directly on top of the platform matching its geometry.

8.3.1 Visual feedback

A camera attached to the inverted microscope first scans the entire area of the cell trapping platform (Figure 8.8) as shown in Figure 8.1b, detects cells and sends these images to a computer with the vision software (an example is provided in Figure 8.9). These images are then processed accordingly with a simple image processing algorithm, as shown in Figure 8.9 to extract the coordinates of the nuclei from the cells. The image processing starts with a coloured image as shown in Figure 8.9a. In this case, we proceed with rabbit liver cells stained with methylene blue. Here we consider population of cells rather than single cells. Recent advances in single-cell analysis has created tremendous opportunities for understanding diseases by studying single cells instead of using population of cells and

concluding from the average values [24]. Understanding genetic behaviours at the single cellular level, yet having a high throughput system to manipulate multiple single cells simultaneously will provide a significant leverage to drug discovery and research [25].

We take a colour image instead of a grayscale because of the amount of information contained in its 3D matrix which improves the quality of the contrast enhancement [4, 7]. This is followed by separating each plane in the RGB image and improving the contrast of each individual plane. Every coloured image is represented as a 3D matrix where each matrix represents the level of red, green and blue for each pixel. The position of the pixel is given by the coordinates in the matrix and the level of colour is given by the value. The three RGB planes are then concatenated to enhance the contrast of the original image. Before edge detection algorithm and other features can be applied to the image, the image is grayscaled. This converts the coloured image into a 1D matrix form, containing only gray level. This is followed by another level of contrast enhancement and structural closing to enhance the image for future edge detection. The grayscale image is now binarised into a black-white image by suppressing the background noise for higher quality edge detection. This is followed by a gradient approach, the Canny edge detector to enhance and detect the edge of the cells [23]. The Canny detector is chosen because of its good signal to noise ratio and detection accuracy [26]. The next step is to compute the centroids of the individual cells. Two initialisation parameters, D_{min} and D_{max} are described which define the range of the selected centroids. Only those disk centroids are selected and plotted in the original image whose diameters are within this specified range, as shown in Figure 8.9h. The coordinates of each nucleus from every single cell are then computed and this feedback is given to the controller, discussed in Section 8.3.3 which then aligns each individual microneedle accordingly to the nuclei coordinates.

For our biomanipulation experiment, it is critical to process single cells for manipulation instead of manipulating them in a population. An illustration of a glass based cell trapping platform to trap and align single cells in shown in Figure 8.8 whose geometry is defined by the geometry of the 3SA microrobot based parallel architecture. The microchambers whose diameter is smaller than the diameter of the individual cells to be trapped can use a variety of different techniques to trap the single cells. Vacuum or suction based technique is chosen as a potential candidate due to the ease of integration with our setup and the ease of fabrication using glass and PDMS. Nonetheless, its validity or performance is not further investigated at this stage. Some recent related works include a microwell array platform fabricated from silicon and glass which has been developed for various high-resolution cell-imaging assays [27]. The wells are arranged in *400* (*20* × *20*) section of *9* × *9* wells over the chip. Another cell holding device is capable of transferring zebrafish embryos in parallel into standard *96*-well microplates, so that each well traps only one zebrafish with a *94.3%* success rate [28]. Similar microfabricated device having through-holes of around *40* μm in diameter has been used for immobilising mouse zygotes (*~100* μm) for microinjection [29]. This device is made out of PDMS and glass and use a vacuum-based technique for trapping the cells. Fabricating this cell trapping platform is a future work that needs to be undertaken for successful biomanipulation. Parameters such as microchamber diameter, inter-chamber distance, height of the chamber etc. needs to be investigated for different cells and biomanipulation tasks. In our case for biomanipulation, the preferred approach for delivering macromolecules with the microneedle is using surface functionalisation. The proposed microneedle in our microrobotic actuator can be modified to attach CNTs or other molecules such as DNA, RNA, siRNA, quantum dots among others like discussed in the works [30-32] using a variety of surface chemistry techniques.

Once the visual feedback extracts the coordinates of every nucleus and the microneedles

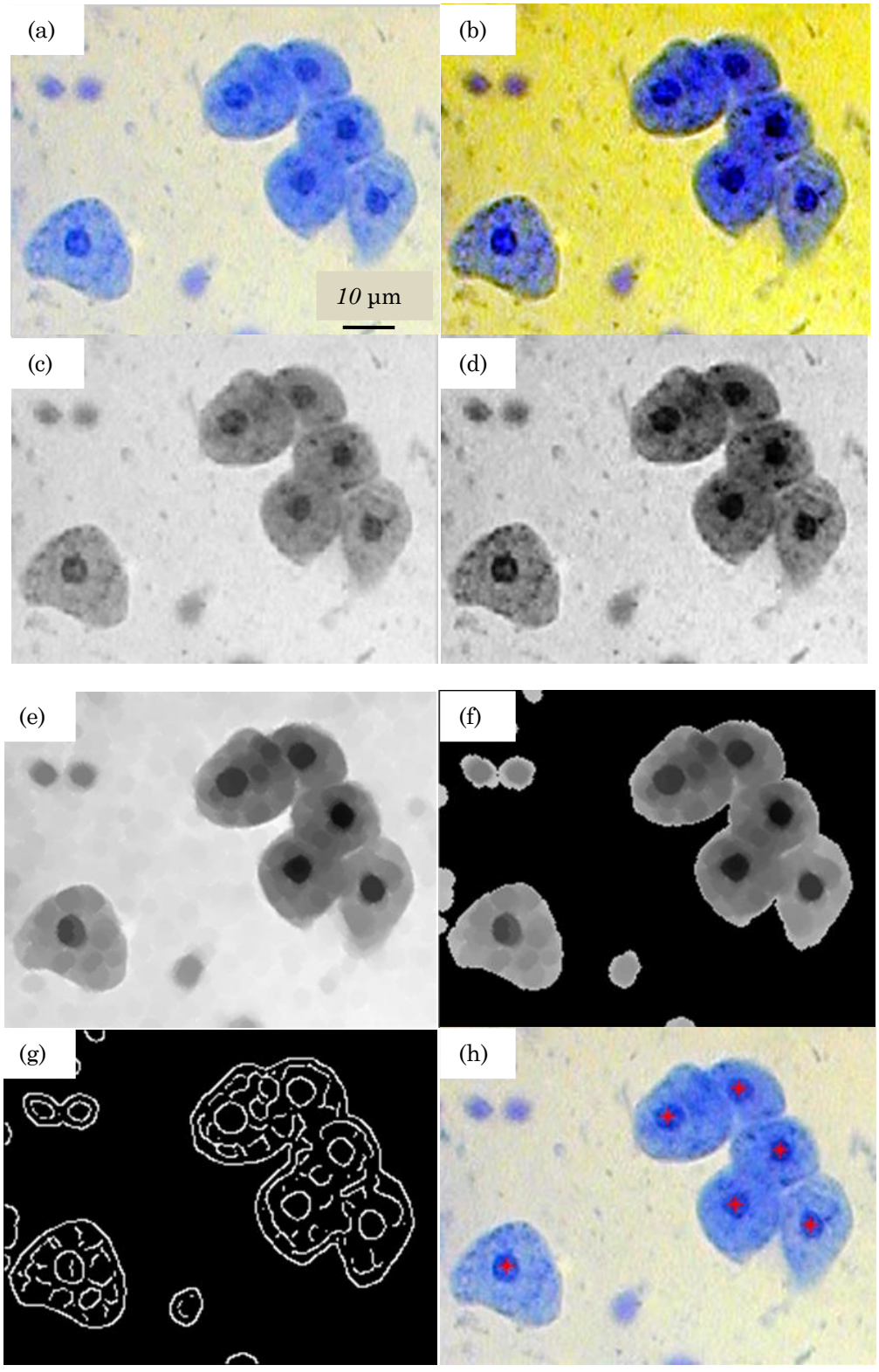

Figure 8.9 Optical microscopy image of rabbit liver cells stained with methylene blue. (a) Original image [33] (b) Contrast enhancement (c) Gray scale image (d) Contract enhancement of the gray scale image (e) Transformation to enhance edge detection (f) noise reduction (g) Filtered edge detection (h) Locating the nucleus within each individual cell.

are all aligned in-plane, the out-of-plane motion of these needles are now activated for biomanipulation. The next section describes this biomanipulation mechanism in the vertical direction and introduces a new blind feedback algorithm to detect the cell membrane and manipulate the targeted site inside the cell.

8.3.2 Blind feedback

The parallel architecture actuator uses a non-visual blind feedback mechanism using two parameters: change of voltage and displacement between the plates in the parallel-plate actuator, to manipulate multiple biological entities such as cells on a parallel scale. Due to the impossibility of having a visual feedback for multiple cells along the *z* axis by having an array of cameras dedicated to an array of cells, the vertical motion and manipulation becomes complicated. Thus, we use a non-visual feedback mechanism that can detect the manipulation through some physical change. In our case it is the change in the plot of the voltage-displacement tracking curve that identifies penetration and subsequent poking through the cell membrane. This change is the alteration of the cell membrane stiffness sensed by the microneedle during vertical manipulation and is reflected in the force-deflection curve as shown earlier in Figure 8.2. This is primarily a model-based feedback employing a blind control scheme and therefore the precision of the position of the microneedle in a *z* coordinate frame depends on the accuracy of this blind model. Based on electrostatic force law, the output motion of the microstage relative to the bottom tower is expected to be proportional to the square of the actuation voltage, $U_{x,y,z} \propto V^2$. Due to this electrostatic nature, our blind feedback scheme is a linear system with purely deterministic behaviour. Nonetheless, immediately following the poking into the cell, the behaviour becomes non-linear due to the vibration induced into the system with the rupture of the cell membrane. This depends on the types of cell and their stiffness values as illustrated in Table 8.1. A DC

voltage is applied to the parallel-plate actuators between the silicon towers and the microstages in each individual microrobot. This pulls the microstages back as shown in Figure 8.10b. The vertical macropositioning stage gripping the actuator in its retracted state then gradually brings it down to the close proximity of the cell, guided by a high-resolution camera placed sideways. This camera confirms the proximity information. The voltage is now gradually reduced (V to V*1* to V*2* to V*3*) which decreases the electrostatic force (E to E*1* to E*2* to E*3*) between the plates gradually as shown in Figures 8.10c to e. As a result, the

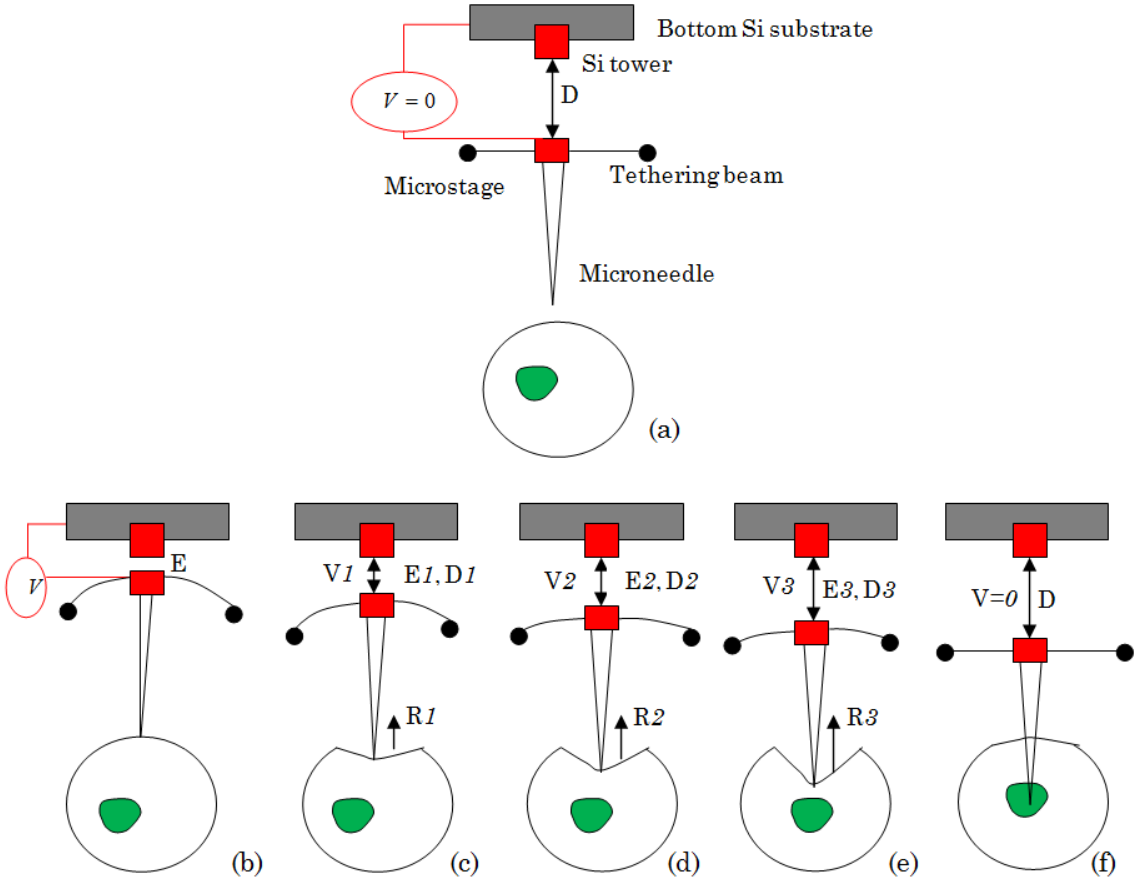

Figure 8.10 Injection of a single microneedle into a cell for manipulation. The cell has been assumed spherical for the sake of clarity. The green part denotes the nucleus. (a) Before the injection. (b) Voltage, *V* is applied to the parallel-plate actuator which pulls the microstage back toward the silicon tower. (c) - (e) Penetration occurs into the cell and the cell membrane resists with a restoring force (R*3*>R*2*>R*1*). (f) Poking occurs and the microneedle targeted inside the cell for further manipulation. V>V*1*>V*2*>V*3* and E>E*1*>E*2*>E*3*.

microstages gradually come back to their original state and the microneedles come into contact with the cell surfaces. During this operation, the microneedles gradually penetrate through the cell membranes because of the vertical stiffness of the actuator and the decreasing parallel-plate electrostatic force, until it pokes through these membranes completely and are in the target site inside the cells. Once the manipulation is complete, the microneedles are pulled back from the cell by the vertical macropositioning stage and the next set of biomanipulation task occurs. During this entire operation, the two parameters, voltage and displacement between the two plates are plotted and sudden drop occurring during the penetration to poking phase gives a feedback to the controller discussed in Section 8.3.3 to adjust the microneedle for biomanipulation tasks. Once the microneedle is inside the cell, depending on the cell organelle to be manipulated such as nucleus, the needle might undergo another motion, resulting in a subsequent drop in the plot, confirming the poking through the nucleus. The macromolecule or drug compound attached to the needle tip is released and then the microneedles are pulled back from inside the cell. It is to be noted, however, that different types of cells will have different characteristic plots. This will primarily depend on the elastic stiffness of different cell types [34], some of which have been tabulated in Table 8.1.

Manipulating at the micro and nanoscale has to overcome three primary adhesion forces that have significant effect on the process: van der Waals, capillary attraction and electrostatic. In order to simulate the biomanipulation behaviour of the actuator at the micro and nanoscale, a scaled up model has been developed. The electrostatic force acting in the parallel-plate actuator has been replaced with magnetic force acting between two magnets at the macroscale, because at this scale, electrostatic force is negligible and both forces follow a quadratic behaviour. Nonetheless, the needle has to overcome significant forces such as friction, gravity and inertia.

Table 8.1 Young's modulus of mammalian cells [34].

Cell type	E(kPa)
Endothelial cells	
HUVEC	10-11
BPAEC	0.2-2.0
Leukocytes	
Leukemia myeloid cells (HL60)	0.2-1.4
Leukemia lymphoid (Jurkat) cells	0.02-0.08
Neutrophils	0.2-0.07
Osteoblasts	0.3-20.0
Astrocytes	2-20
Fibroblasts	4-5
Migrating 3T3 cells	3-12
L 929	4-5
Epidermal keratocytes	10-55
Platelets	1-50
Skeletal muscle cells	
Murine C_2C_{12} myoblasts	11-45
Myofibrils	40-45
Erythrocytes	14-18

8.3.3 Macroscale experiment

We have performed the macroscale experiment in order to validate our blind feedback model. Due to the difficulty in having parallel readout of the vertical motion of the microneedle array, we use a non-visual blind feedback. Because of the absence of the 3SA microrobot with the microneedle (in fabrication at CMC, Canada while the thesis is written), we have designed an equivalent scaled-up macroscopic experiment. Such a design that would give us information on how the microrobot would perform under vertical manipulation is challenging. The electrostatic force generated capacitance in microscale is replaced by magnetic actuator in macroscale as they both follow quadratic behaviour. The existence of adhesion forces such as Van der Waals and capillary forces quite prominent at microscale are negligible at macro scale. In fact, gravitational and inertial forces are prominent in a macroscale whose effect is negligible in micro and nano scale [35].

Considering the manipulation of single cells, the cell membranes have been replaced by three thin elastic membranes M*1*, M*2* and M*3* of different materials representing three different cell membranes as shown in Figure 8.14a. The physical properties of these membranes are noted in Table 8.2. These properties have been experimentally measured using tensile tester (*MTS858*) at the materials laboratory of the department and the plots are

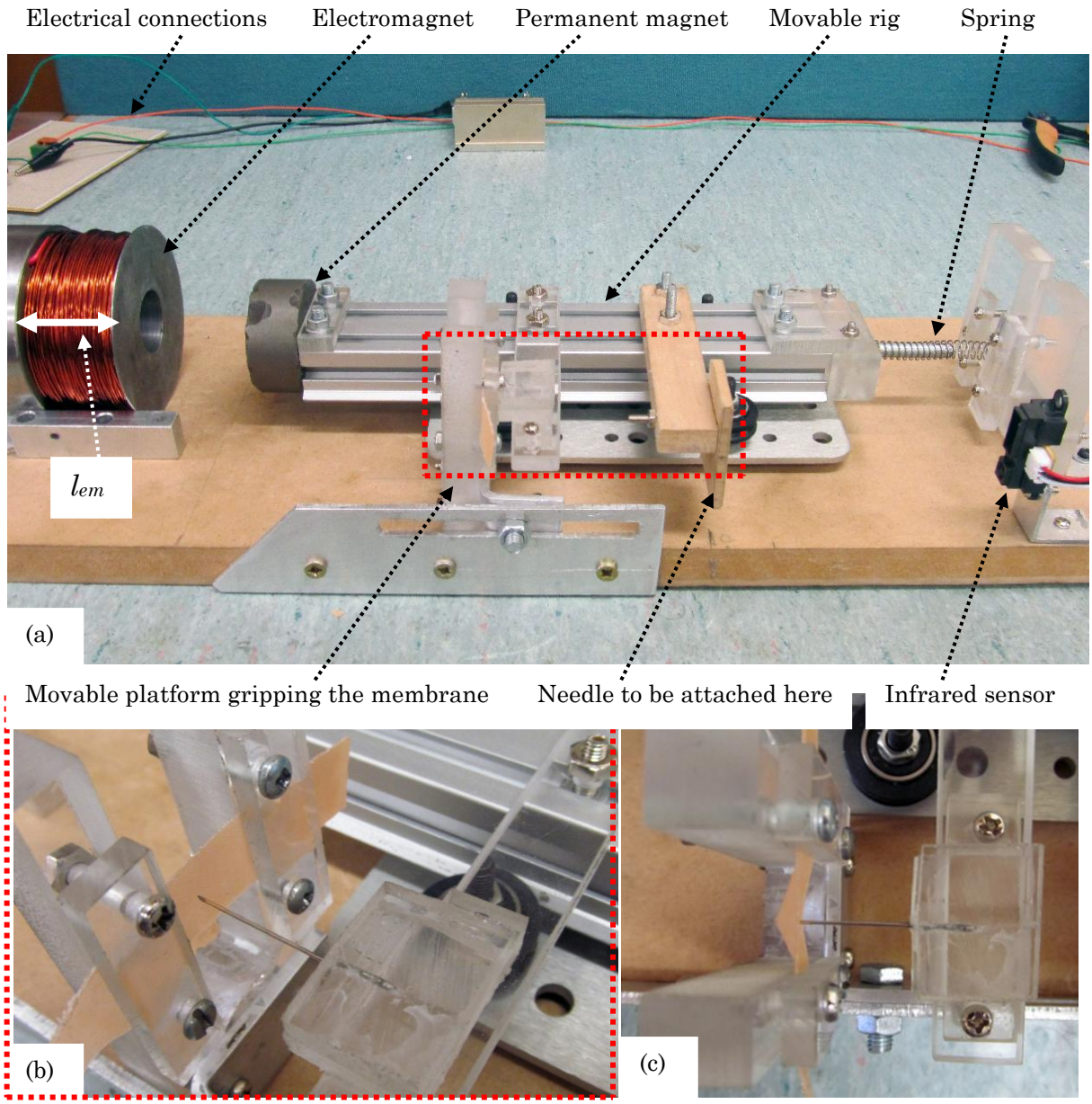

Figure 8.11 Experimental setup simulating the micromanipulation behavior (a) Full preview (b) Zoomed in view of the needle in the proximity of the membrane (c) Top view of the needle penetrating the membrane.

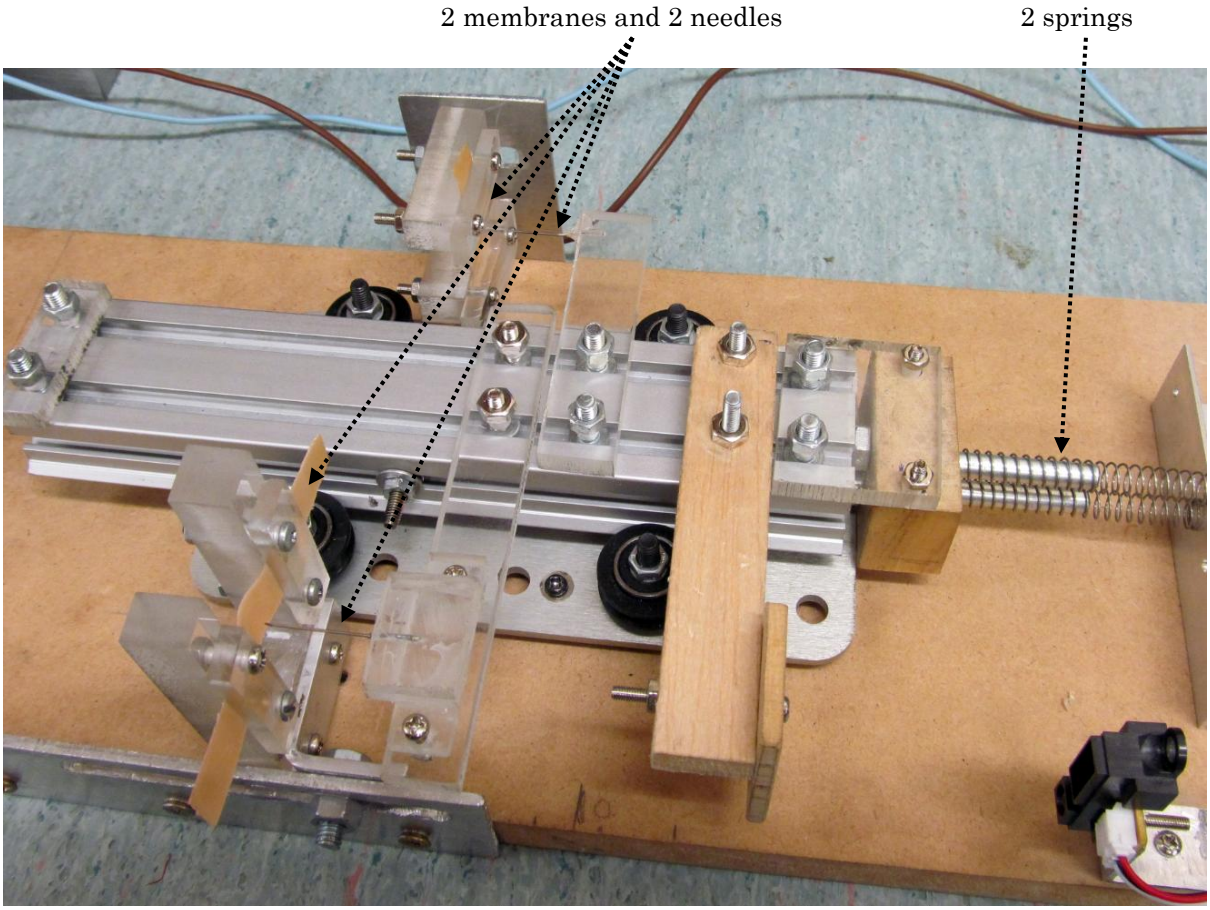

Figure 8.12 Experimental setup simulating the micromanipulation behavior with two membranes (*M2*) placed at different distances from the needles.

shown in Figure 8.14b. The experimental setup for simulating the cell manipulation behaviour is shown in Figures 8.11 and 8.12 and the corresponding circuit diagram in Figure 8.13. The setup consists of a *12* VDC electromagnet custom built for this experiment; a rare earth metal permanent magnet whose specifications are noted in Table 8.3 and attached to a movable rig being driven by an arrangement of four pulleys that provides very little friction; two platforms that mount the membranes and the needle; spring(s) (Table 8.4) attached to the end of the rig that provides the restoring force and infrared sensor that measures the displacement. This sensor (Sharp GP2YOA21YK) has got a linear CCD and focuses infrared light onto a flat surface and measures the reflection by giving analog voltage as an output. This is then converted into displacement based on its datasheet [36]. The setup is placed horizontal instead of vertical to avoid the gravitational force to a significant extent. The basic

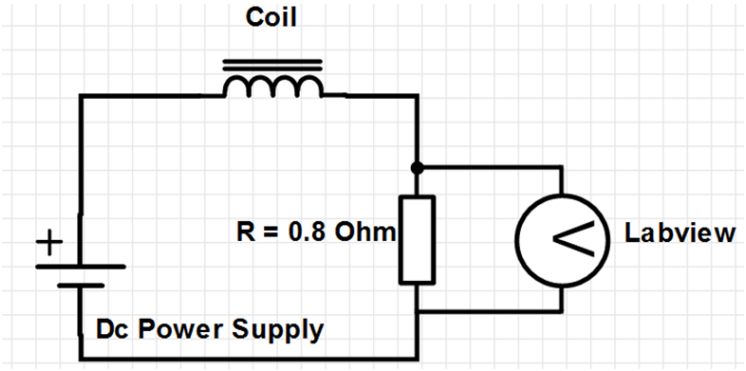

Figure 8.13 Circuit diagram for the electrical connections to run the experiment.

mechanism for the operation here is the generation of magnetic force when DC current is applied to the electromagnet that repels the permanent magnet compressing the spring at the end of the rig. As applied current is increased, the compression increases. The movable platform gripping the membrane is then brought to the proximity of the needle. When the current is now decreased continuously, the springs decompress and the needle starts penetrating through the membrane and eventually poking through it. This generates a *current-displacement signature curve* that measures the exact points of penetration and poking as a form of feedback to the controller for vertical manipulation. The setup is controlled using a LabVIEW program loaded onto a computer as shown in Figures 8.11 and 8.12.

The magnetic behavior between the electromagnet and permanent magnet is of paramount importance to the success of this experiment. The magnetic force experienced by the permanent magnet due to the electromagnet depends on the distance between them. As the current is increased, the magnetic force between these magnets can be expressed [37] as,

$$\vec{F} = \frac{1}{4\pi\mu_0}\frac{\psi_{em}\psi_{pm}}{x^2}\vec{e}_r \tag{8.1}$$

where $\vec{e}_r$ is the direction vector of the magnetic field, μ_0 is the vacuum permeability which is

(a)

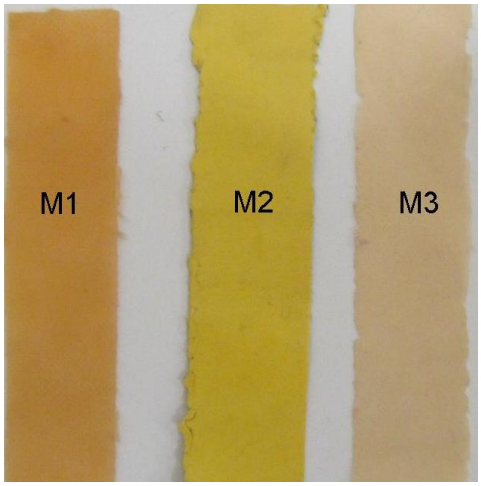

(b)

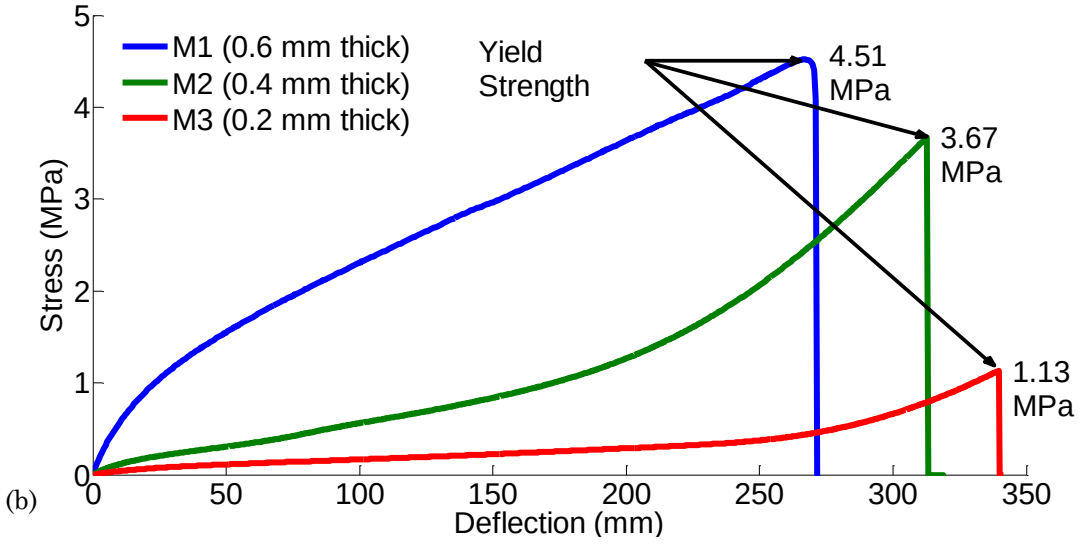

Figure 8.14 (a) Three different membranes M*1*, M*2* and M*3* used in the experiment. (b) Stress testing of three membranes for computing Young's modulus and yield strength.

Table 8.2 Measured physical properties of the three membranes for testing.

Membranes	Thickness (mm)	Young's modulus (E) (MPa)	Yield strength (σ) (MPa)
M1	0.6	13.79	4.51
M2	0.4	5.09	3.67
M3	0.2	1.27	1.13

Table 8.3 Measured physical properties of the permanent magnet.

Diameter (mm)	Length (mm)	Weight (mg)	Max. magnetic field (B_{max}) (mT)	Magnetic flux (ψ) (Tm^2)
45±0.001	*20±0.001*	*239±0.01*	*400±0.1*	$6.36\times10^{-4}\pm0.15\times10^{-4}$

Table 8.4 Measured physical properties of the spring attached at the end of the movable rig.

Diameter (mm)	Length (mm)	Weight (mg)	Max. magnetic field (B_{max}) (mT)	Magnetic flux (ψ) (Tm^2)
45±0.001	*20±0.001*	*239±0.01*	*400±0.1*	$6.36\times10^{-4}\pm0.15\times10^{-4}$

$4\pi\times10^{-7}$ V.s/A.m, x is the distance between the magnets and ψ is the magnetic flux of the electromagnet or permanent magnet.

As both the magnets are anchored, the permanent magnet has only 1D mobility according to the motion of the rig structure. For every *0.5* A applied current, the rig moves by *1* mm. Since the magnetic field from both these fixed magnets is parallel to each other, the magnetic moment effect is not considered in our experiment. The magnetic flux associated with the permanent magnet is constant but varies for electromagnet. The magnetic flux is usually solved as an integral over the surface area through which the field lines are passing. Nonetheless, to simplify our model, the magnetic flux has been assumed to be constant in the average area of interaction between the two magnets. The magnetic flux through the electromagnet [38] is,

$$\psi_{em}(I) = BA = \frac{IN\mu_0\mu_r}{2l_{em}}\left[\frac{\frac{l_{em}}{2}}{\sqrt{\left(\frac{l_{em}}{2}\right)^2 + r^2}} + \frac{\frac{l_{em}}{2}}{\sqrt{\left(\frac{l_{em}}{2}\right)^2 + r^2}}\right]\pi r^2 \tag{8.2}$$

The magnetic field between the two magnets as a function of distance, x between them can be expressed as,

$$B(x) = \frac{IN\mu_0\mu_r}{2l_{em}}\left[\frac{\frac{l_{em}}{2} - x}{\sqrt{\left(\frac{l_{em}}{2} - x\right)^2 + r^2}} + \frac{\frac{l_{em}}{2} + x}{\sqrt{\left(\frac{l_{em}}{2} + x\right)^2 + r^2}}\right] \tag{8.3}$$

where I is the current (A), l_{em} is the length of the electromagnet i.e. *0.034* m as shown in Figure 8.11a, r is the average winding radius of the copper coil over the iron core i.e. *0.026* m, and $N \times \mu_r$ is *690*.

The only variable in the Equations (8.2) and (8.3) is the applied current to the electromagnet. Thus, a change in current changes the magnetic force between the two magnets. The magnetic field of the electromagnet changes with distance and current as shown in Figures 8.15 and 8.16 and has been measured using a fluxmeter (Model 2130 from Magnetic Instrumentation Inc.) and Helmholtz coils (Model HC-12). The magnetic field decreases at a rapid rate up to a distance of around *40* mm between the two magnets. Beyond this point the rate of decrease of the field is significantly low due to the lack of attractive force between the magnets. Therefore while the analytical plot follows a quadratic behaviour, the measured plot follows first-order behaviour until about *40* mm distance, beyond which the two plots are in good agreement with each other. Thus, the experiments are conducted with the permanent magnet being placed at a distance of *42* mm from the electromagnet. The initial difference between the measured values and the analytical model is due to the lack of precise positioning of the Helmholtz coils in the proximity of the electromagnet which can lead to variations of measured results. Increasing the current increases the magnetic field and thus the magnetic force as evident from Equations (8.1) and (8.2). The electromagnet has an iron ferromagnetic core which gets magnetised under an external magnetic field. Nonetheless when the current is switched off, the electromagnet retains a significant amount of magnetisation without returning back to its original zero magnetisation state. It is driven back to zero by a field in the opposite direction, called the coercive force. Thus, while increasing the current, the magnetic force increases in a non-linear fashion from a zero-field value as shown in Figure 8.17. But while the current is gradually reduced, the new path lags behind the initial path and this non-retraceability which is called the *hysteresis effect* has been

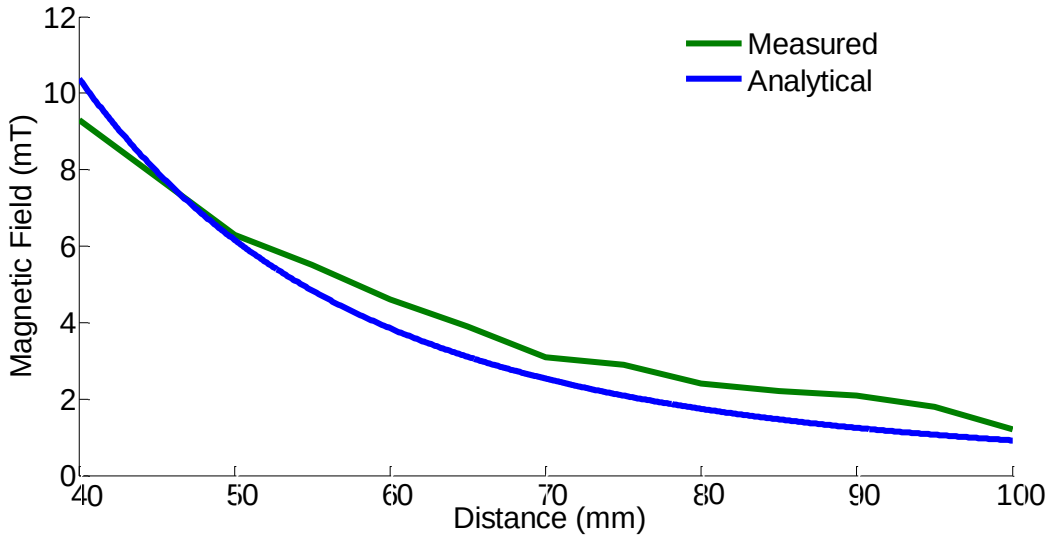

Figure 8.15 Change of magnetic field of the electromagnet with distance.

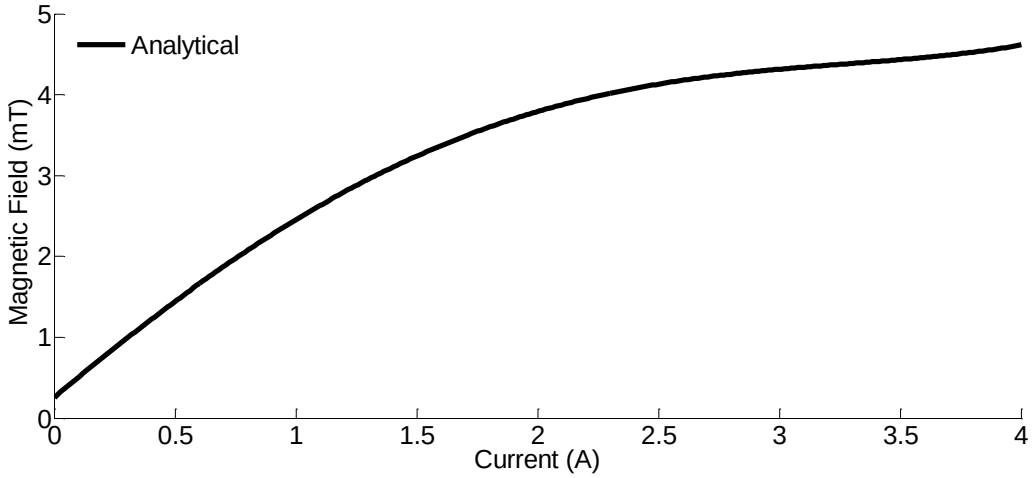

Figure 8.16 Change of magnetic field of the electromagnet with current.

modelled analytically using a bang-bang control scheme. Detailed explanations on hysteresis effect can be found in [39]. The bang-bang controller is usually used to model such hysteresis and accepts a binary input. It is used where the switching speed is much faster than what the system can respond to. In our case, we switch the coil on/off to produce magnetic field. The voltage needs to be varied to keep the current constant, which uses a bang-bang solution to switch it on/off. The Laplace transform of the bang-bang control is expressed as a Heaviside step function [40] which is,

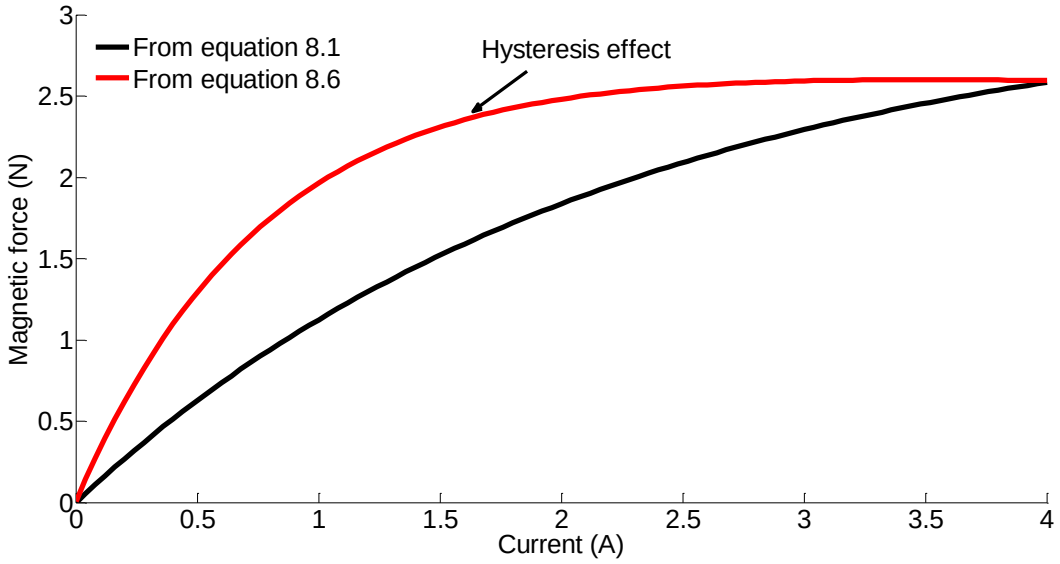

Figure 8.17 Change of magnetic force with current and the hysteresis effect with the decrease in current.

$$H(s) = K\left(\frac{1}{T1.s+1} - \frac{1}{T2.s+1}\right) \tag{8.4}$$

where *H(s)* is the Heaviside step function, *K*, *T1* and *T2* are constants and *s* is the Laplace transform from time.

Therefore, the retransformation in time area is,

$$h(t) = K\left(\frac{1}{T1}e^{-\frac{t}{T1}} - \frac{1}{T2}e^{-\frac{t}{T2}}\right) \tag{8.5}$$

Thus, rearranging the above equation as a function of current, we get,

$$F_h(I) = K\left(\frac{1}{I1}e^{-\frac{\Delta I}{I1}} - \frac{1}{I2}e^{-\frac{\Delta I}{I2}}\right) \tag{8.6}$$

where is the magnetic force due to hysteresis, $K = 2$ A.N and the currents $I1 = 4.4$ A^{-1} and $I2 = 0.7$ A^{-1} are the constants which have been optimised to fit the graph into the experimental plot.

The magnetic force is equal to the spring restoring force. The analytical model takes into account only a single axial behavior across the *x* axis to describe the displacement. The hysteresis effect can be observed in Figure 8.18 which illustrates the current-displacement feedback behavior modelled analytically. The membrane M*3* is the thinnest membrane with the lowest yield strength as seen in Table 8.2 which results in a minor step as the membrane is poked. For the other two membranes, the steps are quite significant. Nonetheless the analytical model does not take into consideration the initial magnetic effect between the two magnets which has been shown in Figure 8.19 through the experimental plot. Also the analytical model also does not take into account the restoring force from the spring. Thus, the penetration through the membrane is not easily discernable from the final poking. Nonetheless the results from the analytical model are in close proximity to the experimental results in terms of position of the needle during penetration and its final position after poking through the membrane as illustrated in Tables 8.5 and 8.6. The experimental model discussed next does take into account all of these effects in its signature plot.

Following the analytical model as developed above, we run the blind feedback experiment to determine the position of the needles during penetration and after poking. We then validate the experimental position values of the needle with the analytical values with respect to different membranes. For the experimental plot in Figure 8.19, the initial distance between the two magnets is *42* mm as explained earlier in this section. The attractive force between the magnets is absent at this point. The plot is initially constant with the increase in current until the current rises to a value between *1.75* A - *2* A depending upon the membrane property. Before the current is switched on, the only magnetic effect that the system experiences is the magnetic force on the electromagnet due to the permanent magnet. Switching on the current, the magnetic force due to the electromagnet comes into effect which takes up to *1.75* A - *2* A current to have a repulsive force on the permanent magnet. At

this point, the electromagnetic iron core becomes permanently magnetised and a sudden jump in the displacement can be seen initially as the rig structure starts moving, thereby compressing the spring. This magnetisation of the electromagnet eventually leads to the hysteresis effect, explained earlier, as the current is reduced and when the needles penetrates the membrane and eventually poking through it. Beyond this point, the displacement increases almost linearly with current until the spring is compressed to a reasonable extent. The movable platform mounting the membrane is then brought to the proximity of the needle and the current is gradually reduced. The return path lags behind the initial path due to the hysteresis effect until the current drops down to a range between *1.75* A – *2* A and then the displacement decreases linearly with current. As the needle penetrates through the membrane as shown in Figure 8.14c, eventually reaches the yield strength when the membrane is poked and the displacement drops down dramatically. This signature plot with step changes during penetration and poking gives a feedback to the controller for manipulation. Referring to Figure 8.21, plotting contact force of the needle with the membranes against the displacement, we can see a similar trend in step changes with the signature plot. The force of poking for the three membranes is in close proximity with each other. Given the membranes are made of different materials, for the thinnest membrane, M3 (*0.2* mm thick, E = *1.34* MPa), the poking force is *0.67* N, compared with M2 (*0.4* mm thick, E = *1.94* MPa) and M1 (*0.6* mm thick, E = *1.39* MPa) with forces of *0.42* N and *0.27* N respectively.

In another experiment, the two membranes (for example, M2) are placed apart in parallel by a distance of *3* mm. The setup is modified by adding an additional spring at the end of the rig structure, an extra needle and membrane as shown in Figure 8.12. The system now needs more current of up to *6* A to compress an additional spring as seen in Figure 8.21. The signature curve is similar in its behavior to the signature curve with only one membrane being injected. When the two membranes are placed in parallel without any distance between

them, only one step can be observed in the plot. When the distance between them is *3* mm, two sharp steps are clearly visible. Because of the lack of consideration of the initial magnetic effects in the analytical model, there are minor differences between the analytical and experimental values in the position of the needle during the penetration and poking of the membranes depending on their stiffness values. Therefore during penetration, there is a difference of around *6-8* mm in the position of the needle which is relatively insignificant.

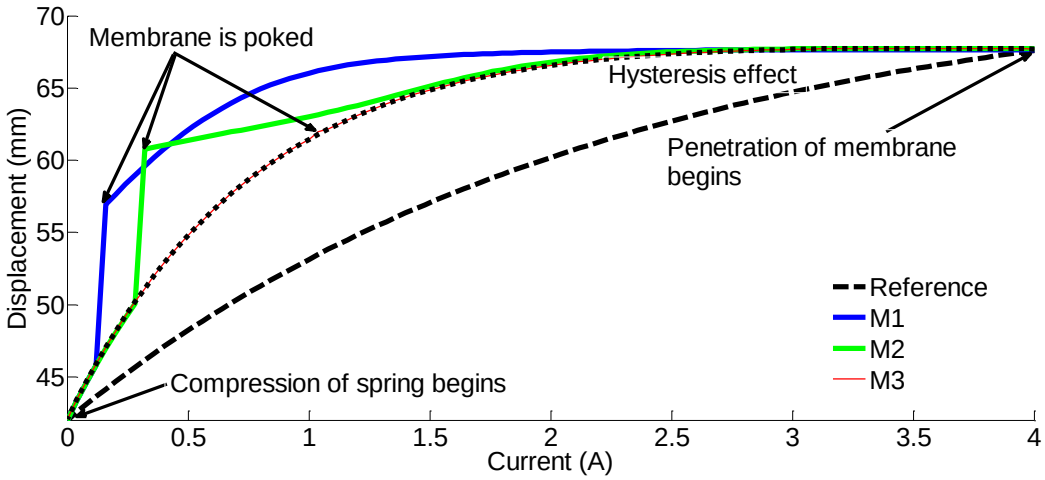

Figure 8.18 Current-displacement analytical signature curves for penetrating and poking through membranes. The reference line is when no membranes are present in the path of the needle.

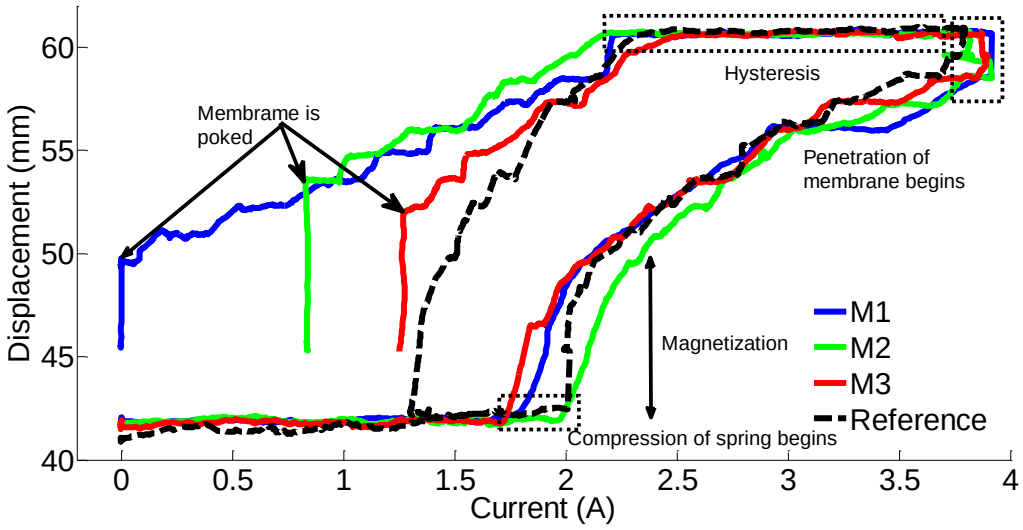

Figure 8.19 Current-displacement experimental signature curves for penetrating and poking through membranes.

After poking, the final position values of the needle are in close agreement between the theoretical and experimental models with a difference of up to *5* mm, also quite insignificant. This model which is pre-fed into the controller is discussed in Section 8.3.4.

The difference between the microscale manipulation feedback and this macroscale experimental feedback are the parameters, voltage and current. Since the macroscale

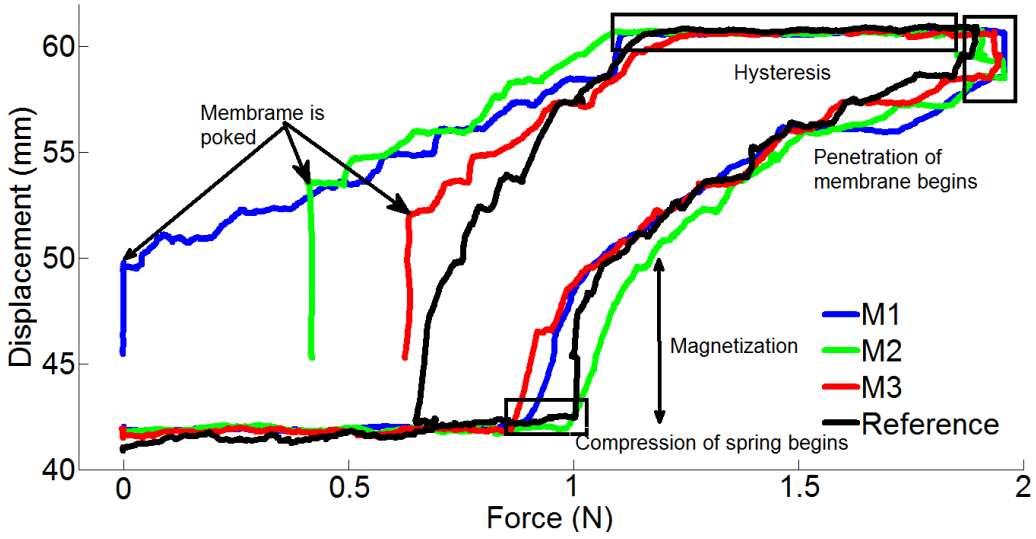

Figure 8.20 Force-displacement experimental signature curves for penetrating and poking through membranes.

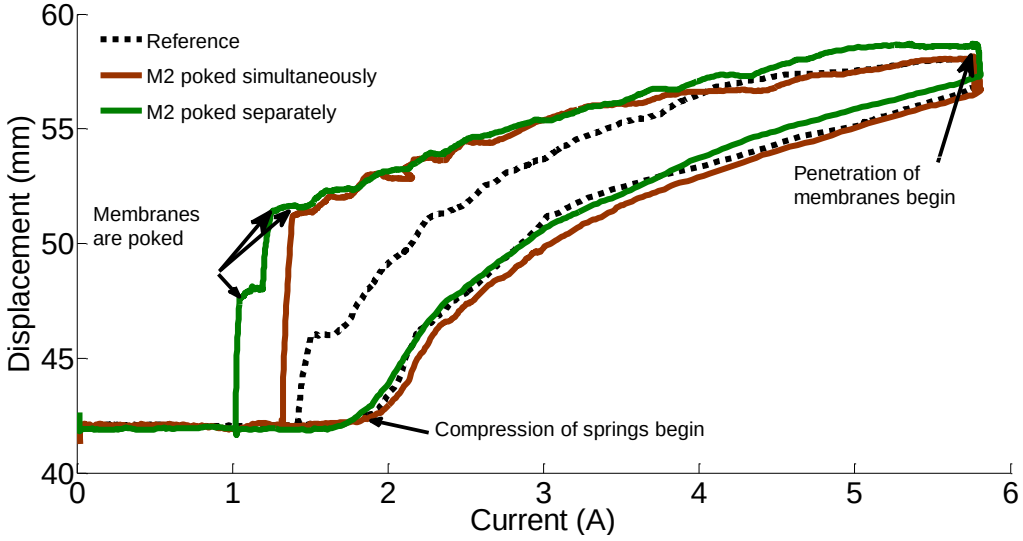

Figure 8.21 Current-displacement experimental signature curves for penetrating and poking through two M*2* membranes placed at different distance from the needles.

Table 8.5 Position of the needle when penetration occurs.

Membranes	Theoretical (mm)	Experimental (mm)
M1	56	50
M2	60	54
M3	61	52

Table 8.6 Final position of the needle after poking.

Membranes	Theoretical (mm)	Experimental (mm)
M1	46	45
M2	50	45
M3	50	45

experiment uses magnetic force to actuate the rig structure, DC current is critical.

Nonetheless, at the microscale, this current parameter is replaced by voltage as it uses electrostatic force in the parallel-plate actuator. It must be noted however, as discussed in Chapters 1 and 2, if electromagnetic force is used to achieve vertical motion, then current will become the measuring parameter instead of voltage. Thus, this blind feedback mechanism in conjunction with the visual feedback forms the backbone of the controller of our parallel architecture for successful biomanipulation tasks.

8.3.4 Controller mechanisms

Having dealt with the feedback mechanisms, both visual and blind, we now focus on the control scheme incorporating these feedback processes that would operate the microrobot. We present our proposed controller for ten cells in an array and focus on aspects including control constraints, precision of microneedles during operation and specifications such as power electronics. An overview of the components of the automated manipulation setup is illustrated in Figure 8.1. The parallel architecture incorporating ten microrobots and therefore ten microneedles is directly above the cell trapping platform with ten cells in array.

The aim of the proposed experiment, once the parallel architecture incorporating 3SA microrobot is fabricated by CMC, Canada will be to establish the viability of the cells and the efficiency of manipulation. We consider delivering, for example, green fluorescent protein (GFP) DNA adsorbed onto the microneedles directly into the nucleus of ten single primary cultured mesenchymal stem cells (MSCs) and human embryonic kidney (HEK*293*) cells in a parallel form. The single cells are to be trapped onto the cell trapper. The GFP fluorescence after *24*, *48* and *72* hours in each single cell would establish the efficiency of the chip technology and whether the cells remain viable after delivery.

There are several steps that need to be accomplished during the entire manipulation procedure. These include scanning for nucleus, system macro-alignment, fine *xy* alignment of the microneedles using visual feedback, macro *z* positioning of the microneedles to proximity of the cells and fine *z* movement of the microneedles employing blind feedback for cell manipulation. The macro-alignment of the system and nuclear scanning are achieved using a high resolution CMOS camera connected to an inverted microscope (Nikon Eclipse Ti-S). There is another high resolution CMOS camera on the side of the cell trapper for giving proximity information to the controller, so that when the chip comes to the proximity of the cell, it stops. The cameras are connected to the personal computer through an NI *1409* frame grabber from National Instruments, as it will allow higher control and frame rates with feedback. The chip is mounted onto a PCB with custom made electronics for signal transfer and processing. The PCB, in turn, is connected via a high density connector to the drive electronics consisting of a compact DAQ (NI*9263 ±10* V power output) and a high voltage generator (LHV Power Series-B *0-9* V DC Input/*0-1250* V DC Output). It is the interface that handles the information transfer from the computer to the output modules. The DAQ has two plug-in modules which supplies a programmable voltage output via five channels (four for *x*, *y* and one for *z*) to the five high voltage MOSFET operational amplifiers (please refer to

Appendix C for a simplified circuit diagram). Therefore to drive ten microneedles, there will be *50* output channels. The isolation barrier prevents the high voltage accidently feeding back to the computer. The high voltage generator generates the voltage necessary to set the maximum output voltage of the amplifier. This is connected to the main DC power supply (Powertech MP*3087*). The entire experimental setup sits on a vibration isolation table (Kinetic Systems Vibraplane). The visual and control interface supports the following five major steps of the manipulation procedure in a 3D workspace:

Scanning for nuclei: After the cells have been trapped onto the cell trapper, the computer controlled system consisting of the camera atop the inverted microscope scans a *30* mm × *30* mm area of the cell trapper and detects nuclei using the visual algorithm discussed in Section 8.3.1. Statistical data such as nuclear *xy* coordinates for all the ten cells, total area scanned etc. are displayed onto the LabVIEW user interface.

System Macro-alignment: This alignment is primarily done to first use the camera to detect the alignment marks on the chip and the cell trapper and then remove it out of the workspace and bring in the parallel architecture chip in focus and position it directly above the cell trapper. The etched alignment marks on both the cell trapper and the parallel architecture chip are used as reference objects to each other. After this macro-alignment is achieved, the microneedles will be within the range of the cell diameter trapped into the microwells on the cell trapper. Ideally the microneedles will be precise within a ±*10* μm distance in reference to the locations of every individually trapped cell. The cells in application here have a diameter of around *15-17* μm.

Fine *xy* alignment of the microneedles: Once the system macro-alignment is achieved, the nuclear *xy* coordinates computed in step *1* (scanning for nucleus) is fed into the controller running on the computer. Due to the varying *xy* position of the nucleus in each of the ten

cells, independent tracking of the microneedles is necessary. For this in-plane positioning, we use a closed-loop PID (proportional integral derivative) control scheme. For example, the microneedles will be able to track desired positions of the nucleus according to their coordinates based upon the position to be reached and desired voltage corresponding to that position. This will result in higher signal-to-noise ratio of the positioning resolution which otherwise can deteriorate due to sensor noise. Figure 8.22 shows the schematic of a closed loop control system that accepts x_d, position desired as the reference input. PID control is used to generate voltage, V which is then input into the system. The error in xy positioning precision, x_{diff} for each of the ten microneedles should be less than *5%* of the cell diameter, i.e. less than *1* μm for a *15* μm cell diameter. The closed-loop controller calculates the desired voltage to drive the system, the ten microneedles in the parallel architecture to the desired position. The gain is achieved by the high voltage generator that amplifies the analog signal from the DAQ. The desired position of the microneedle and therefore the displacement of the microstage is directly proportional to the square of the applied actuation voltage. This requires the relationship between voltage and displacement to be calibrated and data fitting be applied to this calibration data to solve the equation in terms of the voltage. As the measured microneedle position x_m is continually changing to reach x_d, the voltage V is continually changing to reach V_d. Once all the ten microneedles have aligned themselves according to the corresponding ten nuclear xy co-ordinates, they are all held in their position until the vertical

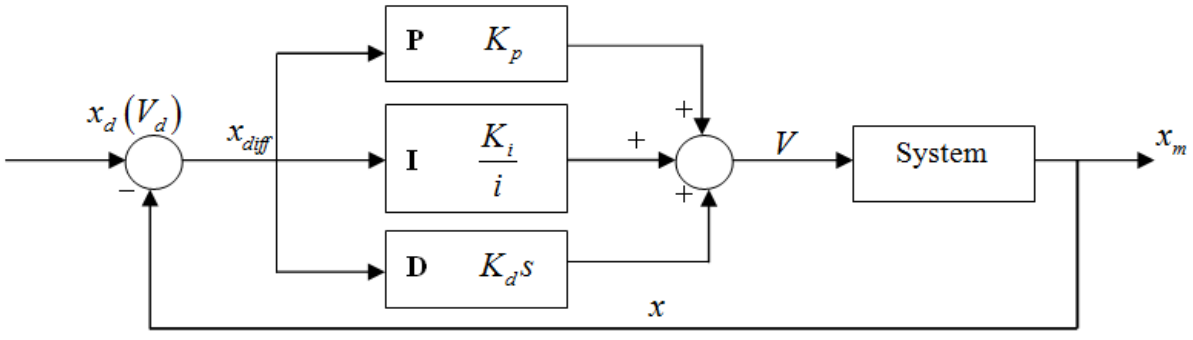

Figure 8.22 Schematic of the *xy* controller.

manipulation is achieved.

Macro *z* positioning of the microneedles: A macromanipulator (MP-285 Sutter Instrument Co.) with a coarse submicron resolution of *0.2* μm and almost *40* nm fine resolution is used to connect the parallel architecture chip using a fixture to hold it firmly in place. This provides the macro-movement to the chip and brings it down vertically so the microneedles are in close proximity of the cells. Before the vertical movement of the entire chip occurs, an actuation voltage is applied to each of the parallel-plate actuator in the ten microrobots using the *z* controller discussed in the next step. This applied voltage exerts an attractive electrostatic force on each of the microstages and pulls them back toward the standing silicon tower. The chip is then incrementally lowered by the macromanipulator to the proximity of the cell in this retracted state of the ten microneedles. The gap between the needle tip and the upper cell membrane should be within sub-micron range. This proximity information is verified by the high-resolution CMOS camera placed sideways.

Fine *z* movement of the microneedles: The blind feedback mechanism is employed during this step when the cell manipulation actually occurs. Figure 8.23 shows the schematic of the *z* controller, whose primary purpose is to enable manipulation using the blind feedback and prevent overshooting of the microneedle during the injection process. Similar to the *xy* controller, for *z* tracking, we use closed-loop control by using error in position signals as feedback to form a closed-loop. The controller accepts a desired position, x_d as the reference input and employs PID control for achieving the desired voltage, V_d and therefore avoids overshooting of the microneedle. The system is calibrated and the relationship between the voltage and displacement is fed into the controller, *a priori*. Thus, for a particular cell type, such as leukemia myeloid cells (HL60) with Young's modulus of the membrane between 0.2-1.4 kPa (Table 8.1), the system is calibrated and x_d and V_d are used as parameters to drive the microneedle to a desired position inside the cells, such as nucleus. The calibrated values of x_d

and V_d are pre-programmed into the controller for different types of cells. Referring to Figure 8.10, as the controller starts reducing the actuation voltage for each of the ten microneedles, the needles start gradually coming back to their original position due to the decrease in electrostatic force between the two plates of the parallel-plate actuator. As needles start coming out of their retracted state, they gradually penetrate through the cell membranes. There is a continuous change in the applied voltage between the two plates and therefore the change in distance between these plates. Therefore, x_d and V_d are continually changing to guide the ten microneedles to the specific target position inside these ten cells. The error, x_{diff} in z positioning precision is calculated from the estimator that uses the blind feedback model by comparing the measured position, x_m with the desired position, x_d. The PID controller calculates the desired voltage to drive the system, the ten microneedles in the parallel architecture to the desired vertical position in z axis.

The model for the z motion at the macro-scale as derived earlier in Equations (8.1) to (8.6) and the analytical model plotted in Figure 8.18 and verified against the experimental results

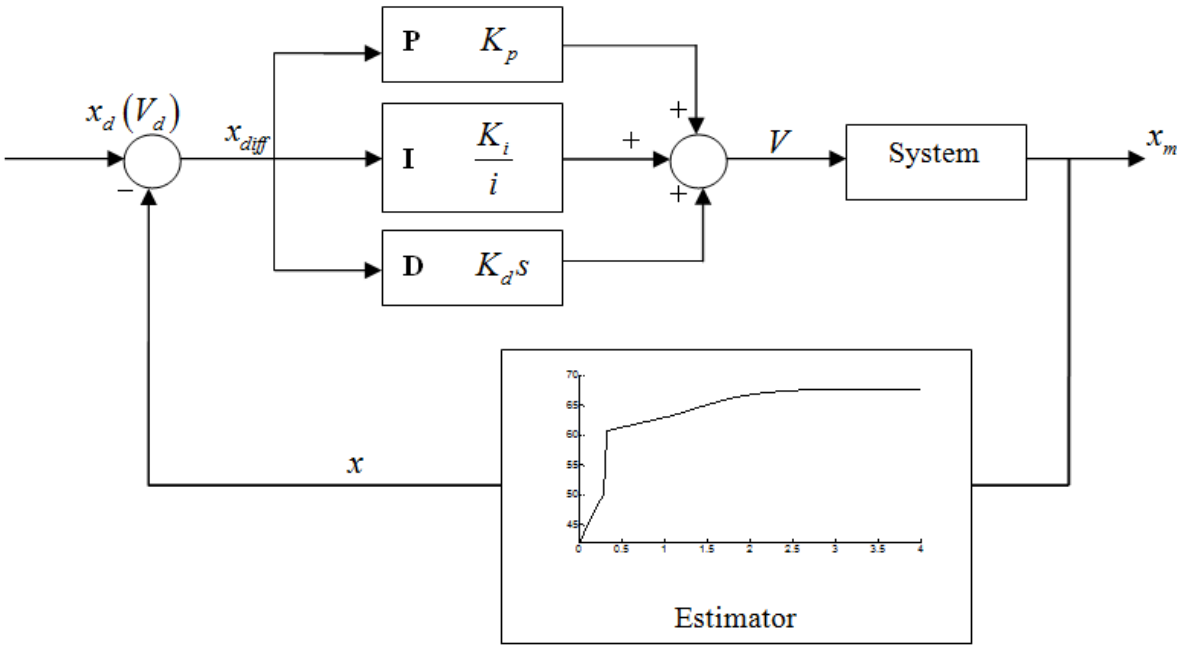

Figure 8.22 Schematic of the z controller.

in Figures 8.19 to 8.21, is replaced by a spring-mass-damper system for the microrobot. With just two parameters, the choice of gain and pole, it is possible to control and parameterise our system. In order to prevent overshooting and perform a stable manipulation without any oscillation, the new poles of the system must be negative and real.

Denoting the transfer function of the PID controller as *K* in the Laplace domain, we have,

$$K(s) = \frac{V}{X_{diff}} = \frac{1}{K_d s^2 + K_p s + \frac{K_i}{s}} \tag{8.7}$$

where, K_d = derivative gain, K_p = proportional gain and K_i = integral gain are tuning parameters; *s* is the Laplace parameter.

Denoting the transfer function of the system as *G* in the Laplace domain, we have [41],

$$G(s) = \frac{X_m}{V} = \frac{1}{ms^2 + cs + k} \tag{8.8}$$

where, *m* is the mass, *c* is the damping constant and *k* is the spring constant of the actuator; *s* is the Laplace parameter.

Therefore, the transfer function equation of the closed loop is [41],

$$H(s) = \frac{X_m}{X_d} = \frac{GK}{1 + GKE} = \frac{\frac{1}{ms^2 + cs + k} \bullet \frac{1}{K_d s^2 + K_p s + \frac{K_i}{s}}}{1 + \frac{1}{ms^2 + cs + k} \bullet \frac{1}{K_d s^2 + K_p s + \frac{K_i}{s}} \bullet E} \tag{8.9}$$

where, *E* is the transfer function of the estimator in the Laplace domain.

Therefore, the final transfer function *H* is,

$$H(s) = \frac{\left(K_d s^2 + K_p s + \frac{K_i}{s}\right)^2}{\left(ms^2 + cs + k\right)\left(K_d s^2 + K_p s + \frac{K_i}{s}\right) + E} \tag{8.10}$$

To ensure the stability of the system and therefore prevent overshooting, the real parts of the roots of the denominator must be negative and real. Therefore,

$$R_e\left\{roots\left[\left(ms^2 + cs + k\right)\left(K_d s^2 + K_p s + \frac{K_i}{s}\right) + E\right]\right\} < 0 \tag{8.11}$$

Thus, we can choose our gain and pole based on Equation (8.11) and desired performance specifications.

The velocity of injection will be around *0.5 - 2.5* mm sec^{-1}. Therefore the frequency associated with this movement is significantly less compared to the resonant frequencies of the actuator. The first resonant frequency of the actuator as predicted from FEA is *12* kHz (in-plane mode for *xy*) and second resonant frequency is 27 kHz (*z* mode motion including flexure of comb-finger electrodes). Unless the cell manipulation occurs at a very high rate, closer to the resonant frequencies when dynamic response analysis becomes critical, otherwise the movement of the microneedles are static. Once the target site, i.e. the nucleus in each of the ten cells has been reached, the microneedles deliver the GFP DNA and pulled out of the cells at a velocity again ranging between *0.5 - 2.5* mm sec^{-1}. Biological membranes stretch elastically only by *2%-4%* before they rupture [42]. Cells have an ability to resist fast changes in the membrane tension brought upon by external forces such as microneedle manipulation in our case [43]. This may be due to a small bilayer reservoir that can buffer minor increases in the membrane tension. There are other tension-sensitive surface area regulation mechanisms that help the cells to resist more dramatic and slower changes in the cellular environment [44].

8.4 Closure and original contributions

This chapter has successfully demonstrated the blind feedback mechanism using a macroscale manipulation experiment simulating the microscale biomanipulation. We show that a voltage/current-displacement signature curve can overcome the hurdle of visual feedback while dealing with multiple cells in the cell trapping platform during vertical manipulation. Blind feedback in conjunction with visual feedback for in-plane alignment of microneedles will successfully allow biomanipulation in a 3D workspace. The coordinates of multiple cells are successfully identified and this helps achieve the in-plane alignment of the microneedles. Thereafter, the current-displacement signature curve can successfully identify the points of penetration and poking through membranes. The hysteresis effect due to the magnetisation of the iron core in the electromagnet that plays a critical role in this model has also been addressed and modeled analytically. The simulations from the analytical model and the experiments are in close conformity to each other, thereby proving the accuracy of our model. We have experimentally proven our hypothesis and have given the blueprint of the corresponding control system. The in-plane motion of the microneedles will be achieved via an open-loop control and the out-of-plane motion via a closed-loop control.

Thus, Chapter 8 makes the following contributions to the field of sensors, actuators and control systems:

- We have successfully implemented a blind feedback mechanism for parallel vertical manipulation using a macro scale experiment. This is based on the fact that the parallel-plate actuator in the microrobot is used as a sensor for achieving vertical manipulation. The electrostatic force in the microrobot has been replaced with magnetic force in our experiment as both follow a quadratic behaviour. The step change in the plot of the

current-displacement provides a signature for the penetration and subsequent poking through the membrane.

- Further, we propose a new type of control mechanism for our parallel architecture system that individually controls the fine movement of the microneedles by using a visual feedback for in-plane movement and a blind feedback for the out-of-plane movement. The independent vertical control of multiple microneedles is particularly challenging given the lack of information regarding the vertical position of the target site inside the cells. This controller uses a combination of open-loop and closed-loop control to achieve such manipulation in a 3D workspace. There are existing systems reviewed in Section 8.1 that have achieved manipulation in 3D workspace using either visual feedback [1, 2, 6-8] or force feedback [16, 17, 20, 23] or a combination of both [3-5, 18, 22]. But none of these works have achieved such manipulation on parallel scale using a blind feedback scheme such as ours.

BIBLIOGRAPHY

[1] Y. Zhang et al, "Automatic vision guided small cell injection: feature detection, positioning, penetration and injection," in *IEEE International Conference on Mechatronics and Automation*, Harbin, China, 2007, pp. 2518-2523.

[2] C. Pawashe and M. Sitti, "Two-dimensional vision based autonomous microparticle manipulation using a nanoprobe," *Journal of Micromechatronics,* vol. 3, pp. 285-306, 2006.

[3] H. Bilen and M. Unel, "Micromanipulation using a microassembly workstation with vision and force sensing," *Advanced Intelligent Computing Theories and Applications. With Aspects of Theoretical and Methodological Issues. Lecture Notes in Computer Science,* vol. 5226, pp. 1164-1172, 2008.

[4] X. Liu, Y. Wang and Y. Sun, "Cell contour tracking and data synchronization for real-time, high-accuracy micropipette aspiration," *IEEE Transactions on Automation Science and Engineering,* vol. 6, pp. 536-543, 2009.

[5] X. Liu, Z. Lu and Y. Sun, "Orientation control of biological cells under inverted microscopy," *IEEE/ASME Transactions on Mechatronics,* vol. 16, pp. 918-924, 2011.

[6] W.H. Wang, X.Y. Liu and Y. Sun, "Contact detection in microrobotic manipulation," *International Journal of Robotics Research,* vol. 26, pp. 821-828, 2007.

[7] W.H. Wang, X.Y. Liu and Y. Sun, "High-throughput automated injection of individual biological cells," *IEEE Transactions on Automation Science and Engineering*, vol. 6, pp. 209-219, 2009.

[8] X. Liu and Y. Sun, "Automated mouse embryo injection moves toward practical use," in *IEEE International Conference on Robotics and Automation*, Kobe, Jaoan, 2009, pp. 526-531.

[9] DH. Kim, B. Kim, S. Yun and S. Kwon, "Cellular force measurement for force reflected biomanipulation," in *IEEE International Conference on Robotics & Automation*, New Orleans, Louisiana, 2004, pp. 2412-2417.

[10] DH. Kim, B. Kim and H. Kang, "Development of a piezoelectric polymer-based sensorized microgripper for micro assembly and micromanipulation," *Microsystem Technologies*, vol. 10, pp. 275-280, 2004.

[11] A. Pillarisetti, M. Pekarev, A.D. Brooks and J.P. Desai, "Evaluating the effect of force feedback in cell injection," *IEEE Transactions on Automation Science and Engineering*, vol. 4, pp. 322-331, 2007.

[12] A. Pillarisetti, W. Anjum, J.P. Desai, G. Friedman and A.D. Brooks, "Force feedback interface for cell injection," in *1st Joint Eurohaptics Conference and Symposium on Haptic Interfaces for Virtual Environment and Teleoperator Systems*, Pisa, Italy, 2005, pp. 391-400.

[13] EY. Kwon, YT. Kim and DE. Kim, "Investigation of penetration force of living cell using an atomic force microscope," *Journal of Mechanical Science and Technology*, vol. 23, pp. 1932-1938, 2009.

[14] A.S. Putra et al., "Design, modeling and control of piezoelectric actuators for intracytoplasmic sperm injection," *IEEE Transactions on Control Systems Technology*, vol. 15, pp. 879-890, 2007.

[15] Y. Xie, D. Sun, C. Liu and S.H. Cheng, "An adaptive impedance force control approach for robotic cell manipulation," in *IEEE/RSJ International Conference on Intelligent Robots and Systems*, Nice, France, 2008, pp. 907-912.

[16] X.Liu, J. Tong and Y. Sun, "A millimeter-sized nanomanipulator with sub-nanometer positioning resolution and large force output," *Smart Materials and Structures*, vol. 16, pp. 1742-1750, 2007.

[17] K. Kim, X. Liu, Y. Zhang and Y. Sun, "Nanonewton force-controlled manipulation of biological cells using a monolithic MEMS microgripper with two-axis force feedback," *Journal of Micromechanics and Microengineering*, vol. 18, pp. 055013-055020, 2008.

[18] X.Liu, K. Kim, Y. Zhang and Y. Sun, "Nanonewton force sensing and control in microrobotic cell manipulation," *International Journal of Robotics Research*, vol. 28, pp. 1065-1076, 2009.

[19] K. Kim et al., "Elastic and viscoelastic characterization of microcapsules for drug delivery using a force-feedback MEMS microgripper," *Biomedical Microdevices*, vol. 11, pp. 421-427, 2009.

[20] J.J. Gorman and N.G. Dagalakis, "Probe-Based Micro-Scale Manipulation and Assembly Using Force Feedback," in *International Conference on Robotics and Remote Systems for Hazardous Environments*, Salt Lake City, Utah, 2006, pp. 621-628.

[21] J.J. Gorman and N.G. Dagalakis, "Force control of linear motor stages for microassembly" in *ASME International Mechanical Engineering Congress*, Washington D.C., 2003, pp. 1-9.

[22] J.D. Wason, J.T. Wen, J.J. Gorman and N.G. Dagalakis, "Automated Multiprobe Microassembly Using Vision Feedback," *IEEE Transactions on Robotics*, vol. 28, pp. 1090-1103, 2012.

[23] J. Chalfoun et al., "A human inspired local ratio-based algorithm for edge detection in fluorescent cell images," *Advances in Visual Computing: Lecture Notes in Computer Science* vol. 6453, pp. 23-34, 2010.

[24] National Institutes of Health (USA). (2013, February 08, 2014). Single Cell Analysis. [Funding]. Available: https://commonfund.nih.gov/Singlecell/index

[25] M. Gerlinger et al., "Intratumor heterogeneity and branched evolution revealed by multiregion sequencing," *The New England Journal of Medicine,* vol. 366, pp. 883-892, 2012.

[26] J. Canny, "A Computational Approach to Edge Detection," *IEEE Transactions on Pattern Analysis and Machine Intelligence,* vol. PAMI-8, pp. 679-698, 1986.

[27] T.W. Frisk et al., "A silicon-glass microwell platform for high-resolution imaging and high-content screening with single cell resolution," *Biomedical Microdevices,* vol. 13, pp. 683-693, 2011.

[28] X. Zhang et al., "Batch Transfer of Zebrafish Embryos Into Multiwell Plates," *IEEE Transactions on Automation Science and Engineering,* vol. 8, pp. 625-631, 2011.

[29] X. Liu and Y. Sun, "Microfabricated glass devices for rapid single cell immobilization in mouse zygote microinjection," *Biomedical Microdevices,* vol. 11, pp. 1169-1174, 2009.

[30] C. M. Cuerrier et al., "Single cell transfection using plasmid decorated AFM probes," *Biochemical and Biophysical Research Communications,* vol. 355, pp. 632-636, 2007.

[31] X. Chen et al., "A cell nanoinjector based on carbon nanotubes," *Proceedings of the National Academy of Sciences,* vol. 104, pp. 8218-8222, 2007.

[32] I. Vakarelski et al., "Penetration of living cell membranes with fortified carbon nanotube tips," *Langmuir,* vol. 23, pp. 10893-10896, 2007.

[33] La main à la pâte Foundation. Available: http://www.fondation-lamap.org/node/17992

[34] T.G. Kuznetsova, M.N. Starodubtseva, N.I. Yegorenkov, S.A. Chiznik and R.I. Zhdanov, "Atomic force microscopy probing of cell elasticity," *Micron,* vol. 38, pp. 824-833, 2007.

[35] Z. Lu, P.C.Y. Chen and W. Lin, "Force sensing and control in micromanipulation," *IEEE Transactions on Systems, Man, and Cybernetics,* vol. 36, pp. 713-724, 2006.

[36] Sharp, "GP2Y0A21YK Optoelectronic device."

[37] A. Aharoni, *Introduction to the theory of ferromagnetism*, 2nd ed.: Oxford University Press, 2001.

[38] D. J. Griffiths, *Introduction to Electrodynamics*, 4th ed.: Addison-Wesley, 2012.

[39] R. M. White, *Quantum theory of magnetism*, 3rd ed.: Springer, 2006.

[40] H. Hermes and J.P. LaSalle, Ed., *Functional analysis and time optimal control*, Mathematics in Science and Engineering. Academic Press, New York - London, vol. 56, 1969,

[41] W. S. Levine, *Control system applications*, 2nd ed.: CRC Press, 2010.

[42] R. Waugh, "Effects of abnormal cytoskeletal structure on erythrocyte membrane mechanical properties," *Cell Motil.*, vol. 3, pp. 609-622, 1983.

[43] I.Titushkin and M. Cho, "Distinct membrane mechanical properties of human mesenchymal stem cells determined using laser optical tweezers," *Biophysical Journal*, vol. 90, pp. 2582-2591, 2006.

[44] C.E. Morris and U. Homann, "Cell surface area regulation and membrane tension," *The Journal of Membrane Biology*, vol. 179, pp. 79-102, 2001.

Chapter 9: Conclusions and Future Research

This dissertation demonstrates the feasibility of incorporating multiple microrobots in a parallel architecture for biomanipulation tasks through the design and evaluation of a single-unit microrobotic actuator. The results from such design, analyses, fabrication and experiments demonstrate that:

A 3SA microrobot is more efficient than a 4SA microrobot in terms of performance and integration into parallel architecture which can lead to parallel targeted manipulation.

In summary, the unique contributions from this research and dissertation to the field of microrobotics, sensors and actuators are as follows:

1. Two new types of microrobotic designs, namely 4SA and 3SA microrobots, as outlined in Chapter 2. While the 4SA microrobot has orthogonal arrangement of the sides, the 3SA microrobot has a 120^0 arrangement of the actuator sides. We also introduce a new type of parallel architecture consisting of arrays of microrobots that can be individually controlled and capable of 3D motion of the microneedles integrated into the microrobots. We prove that in terms of dense packing of the microrobots in a parallel architecture, the 3SA microrobot is more efficient than its counterpart, the 4SA microrobot. We conceptualise the design to have an estimate of a range of dimensions for further analytical and finite element analyses. Although there are different designs to achieve manipulation on a micro and nano scale, none of these designs are on a parallel scale with multi-axes motion. Few parallel architectures do exist; however, all of them are limited to just 1D motion.
2. Design and development of two fabrication processes that can be used to manufacture microrobots with integrated microneedles and bottom tower electrodes, as outlined in

Chapter 4. There are numerous fabrication processes to develop arrays of static microneedles, parallel arrays of 1D microprobes and stand-alone actuation systems. Nonetheless, none of these processes can be used to fabricate a parallel array of microrobots with integrated microneedles that can achieve independent 3D motion and control of these needles. Both the fabrication processes which are distinctively different from each other add steps to the existing SCREAM and SOIMUMPs sequences respectively. This addition serves to fabricate microneedles integrated to the 3D microrobot, to protect the microneedle from further etching, and to fabricate the bottom silicon tower. The first process involves four masks and the entire fabrication is performed on a single silicon wafer without the need for SOI wafers and wafer bonding techniques. The second process involves six masks and is performed using three different wafers, one SOI and two silicon wafers. We have also discovered growth of nanopillared structures on silicon samples during etching of SiO_2 using CHF_3/Ar gas chemistry. Therefore, we have been successful in answering one of the critical research questions set forth in Section 1.5. We have designed fabrication processes to develop a built-in-system with *x,y,z* motion capability.

3. Successful implementation and demonstration of the 3D motion of the 4SA microrobot and a parallel-plate actuator for vertical motion, as illustrated in Chapter 5. There are different designs of actuators that have been developed, but none of them have the vertical motion capability of our microrobot thus making our design the first of its kind.
4. Analytical and FEA models similar to the models described in Chapter 3 to analyse the motion performance of the 3SA microrobot, as discussed in Chapter 6. We show that the motion performance of the 3SA microrobot is better than that of its corresponding 4SA microrobot design. None of the works discussed in existing literatures to study systems with angular components, have developed a model that can accurately predict the motion

performance of an angular design as in our 3SA microrobot. Therefore, we have developed a new set of slope-deflection equations to study the behaviour of the actuator theoretically in addition to the grid-stiffness matrix model, explained in Chapter 3. Unlike the orthogonality of the design in the 4SA microrobot, the 3SA microrobotic design has angular structures, which requires advanced analytical treatment that can predict the motion performance with significant accuracy. In previous chapters, our theoretical models are validated against each other and also with the experimental results thus proving their accuracy and therefore, the predictability of the design of the 3SA microrobot.

5. In our pursuit of answering one of our critical research questions as proposed in Section 1.5, we have successfully implemented a new blind feedback mechanism for parallel vertical manipulation using a macro scale experiment, as discussed in Chapter 8. We propose using the parallel-plate actuator in the microrobot as a sensor during manipulation. Therefore, the step change in the plot of the voltage-displacement provides a signature for the penetration and subsequent poking through the cell membrane. The novelty of our system is in the implementation of blind feedback for out-of-plane alignment of the microneedles, in conjunction with visual feedback for in-plane alignment of microneedles. This will successfully allow biomanipulation in a 3D workspace. Further, the novelty extends to our newly proposed control mechanism for our parallel architecture system that individually controls the fine movement of these microneedles through a combination of open-loop and closed-loop PID control. The originality of this research lies in the application of blind feedback in conjunction with the control mechanism to the field of single cell parallel manipulation is. None of the works in the literature reviewed have achieved such 3D manipulation on parallel scale using a blind feedback and controller such as ours.

9.1 Discussion and evaluation of new findings

This dissertation has produced a number of conclusions and insights regarding the challenges of manipulation using a parallel architecture system. Some of them have been discussed in the individual chapters. Nonetheless, this section summarises these points that are the direct consequences of this research, and makes a case for immediate and future research.

There are three major challenges that need to be addressed for successful manipulation at the micro scale in a parallel form:

- First, the individual control of the microneedles during manipulation. This issue has been addressed in Chapter 8 through the discussion of the development of a blind feedback system for recognising the points of penetration and poking through a membrane. The system is limited to manipulation tasks such as injection, delivery, pushing, grabbing and so forth of micro- objects such as biological cells. This dissertation specifically considers the case of biomanipulation and the system is developed accordingly. Nonetheless, this sort of *blind* feedback needs to be calibrated for different cell types and the model uploaded into the control system as *a priori* information. This can limit the types of micro-objects to be manipulated. For example, the blind feedback model of heart cells would be different from that of a liver cell or a neuron cell due to the variations in cell membrane elastic stiffness. Therefore, this would require characterising the model for different types of cells used in medical research. The real-time *z* positioning feedback of the position of the microneedles with respect to the cell membranes is absent. In comparison, having individual feedback from microneedles gives a real-time *a posterior* understanding of the manipulation task. Section 1.2 has briefly discussed this aspect and the use of techniques such as phase sensitive diffraction grating or the use of strobed interferometric microscopy.

- Second, the microrobot coming into contact with a chemical/polar medium during biomanipulation tasks. Since the microrobot has electrical components, under the application of voltage or current, the problems of electrolysis, anodisation and polarisation of the actuators can come into play if they are in contact with the chemical medium that houses these biological entities. However, the electrostatic actuation also gains a few orders of magnitude leading to an increase in motion performance at the same potential compared to a normal air medium. Section 1.2 briefly addresses this situation by recommending the use of frequency dependent electrostatic actuation, the temporary removal of the chemical medium when the manipulation is active, or the fabrication of long microneedles that keep the actuator isolated from the medium.
- Third, using electromagnetic actuation as a possible alternative to the present form of electrostatic actuation. The electrostatic actuation is markedly efficient: it consumes significantly less power; the actuator size is much smaller with fine resolution; and, it achieves repeatability in electromechanical positioning, faster switching speed and easier integration with control electronics. Nonetheless, the vertical motion has considerable limitations. The total distance that can be traversed out-of-plane is lower than what can be achieved with electromagnetic actuators. However, amalgamating electrostatic actuators for in-plane motion and electromagnetic actuators for out-of-plane motion can be equally challenging; this needs to be addressed in future work.

In Section 1.6 of Chapter 1, we discussed the system constraints placed on our system by either design of the actuator or fabrication or design of the experiment. We address each of the system constraints in the subsequent chapters. Evaluating this research in relation to these system constraints leads to the following conclusions:

- The vertical stiffness of the microrobot designed (at least *0.2* μN/μm) is significantly greater than the elastic stiffness of cell membranes (*0.001-0.1* mN/m), thereby resulting in a design that is strong and stable enough to manipulate most of the mammalian cells.
- We have incorporated a parallel-plate actuator in the microrobot and have overcome the challenges posed by positioning, alignment and bonding of the tower underneath the microstage. Although for our fabricated 4SA microrobot, such tasks have been achieved manually, for the 3SA microrobot, these tasks have been automatically achieved through the fabrication process.
- Although we haven't integrated microneedle atop the microstage, but we have designed fabrication processes that will be able to achieve such integration.
- We have successfully demonstrated the feasibility of our blind feedback mechanism by designing a macroscale experiment with magnetic actuators to replace electrostatic force with magnetic force.

Evaluating the feasibility and motion performance of our microrobot in comparison to the specifications set forth in Section 2.2 for the primary application of micro and nano manipulation, especially single cell manipulation, we make the following conclusions:

- The 3SA microrobot design can achieve an in-plane motion (x, y) of *72* μm *(±36* μm) at *160* V and an out-of-plane motion (z) of *7* μm at *35* V. Referring to Table 2.1, we satisfy the specification ranges with our designed actuator, both in terms of motion ranges and actuation voltages. In terms of the manufactured 4SA microrobot, we achieve a reasonable displacement of up to *10* μm at an applied DC voltage of *120* V in-plane which can successfully cover almost *60%* of the surface area of a typical human cell, *15* μm in diameter, as has been illustrated in Table 2.2. The vertical displacement achieved is slightly above *0.5* μm at *600* V. As discussed in Chapter 5, because of the limitations in

fabrication infrastructure, the out-of-plane motion is limited, which has been overcome with the design of the 3SA microrobot (currently under fabrication at CMC Canada at the time this thesis is written).

- The space limit of both the single-unit actuator and the parallel architecture is primarily based on the concept of increasing the density of microrobots that can be packed into the arrayed structure. During dense packing of these microrobots into a single architecture, the effect of electrical coupling needs to be considered. The minimum distance between these electrical interconnects before electrical coupling prevails is around *30* nm. Therefore our manufactured 4SA microrobot has a size of *5* mm × *5* mm, tiny enough to densely pack a few hundreds of these into a single arrayed structure, of the size of around *100* mm^2. Nonetheless with the design of 3SA microrobots, they occupy at least *43%* less surface area compared to the 4SA microrobots and also reduces the number of electrical interconnects on every side by two. The distance between two adjacent microneedles is *3* mm and their corresponding cells on the platform are also placed at *3* mm from each other, thus ensuring that the microneedles target specific cell organelles as their motion range is in tens of microns. Therefore, the parallel architecture incorporating 3SA microrobots have a size of around *70* mm^2, thereby satisfying the specification requirement.
- The blind feedback mechanism allows parallel vertical manipulation without the intervention of visual feedback as has been shown and implemented through the macro-scale experiment. Using the parallel-plate actuator in the microrobot as a sensor, we use step-changes in the plot of the voltage displacement as signatures for manipulation through the cell membrane. Our newly proposed control mechanism would employ a combination of open-loop and closed-loop PID control to individually control the fine movement of the microneedles by using a visual feedback for in-plane movement and the

blind feedback for the out-of-plane movement. The power electronics and the corresponding controller hardware the drives the chip consists of: high resolution CMOS cameras; PCB with custom made electronics for signal transfer and processing; PCB connected to the drive electronics consisting of a compact DAQ (NI*9263* *±10* V power output with multiple output channels corresponding to the number of microrobots in the parallel architecture) and a high voltage generator (LHV Power Series-B *0-9* V DC Input/*0-1250* V DC Output) via a high density connector; DC power supply; cell trapping platform; macromanipulator (MP-*285* Sutter Instrument Co.) and vibration isolation table.

9.2 Future work

This dissertation takes a new leap toward parallel scale targeted manipulation. Such parallel form is still at a preliminary stage and there are different opportunities that need to be explored. Moreover this type of new microrobotic actuators can be exploited to find new applications outside biology and medicine such as creation of new more efficient forms of 2D and 3D micro and nano devices and systems, surface characterisation in chemistry, 3D printing of micro and nanoscale entities among others. We anticipate the use of this actuator to transcend different academic and industrial research fields such as biology, chemistry, materials science, physics etc. as an alternative or complementary tool to atomic force microscopy. The advantage of this system is its capability of high-throughput parallel manipulation that uses mechanical means.

In terms of mechanical design, there are several immediate opportunities available. At the time of writing this dissertation, the parallel architecture incorporating 3SA microrobot has been under fabrication at the clean-room facility at Canadian Microelectronics Corporation. This will be followed by integration of the microneedle atop the microstage using a combination of focused ion beam and e-beam techniques. The future work would also involve fabricating a higher level parallel architecture system integrating hundreds of

independently moving microneedles. Another focus of future work is to design and fabricate the cell trapping platform governed by the geometry of the actuator that can efficiently trap single cells. As discussed above and in Chapters 1 and 2, the integration of an electromagnetic actuator instead of an electrostatic one can lead to higher motion performance during vertical actuation. This would require new simulation studies to understand the electromagnetic behavior and its influence in motion decoupling. Further, it would also require designing new fabrication processes.

A major area of research would involve realising the control system proposed in Chapter 8.3.3. The major challenge would be controlling the individual microneedles in *z* axis. Albeit we have developed a blind feedback mechanism and have successfully implemented at the macroscale, realising it at a microscale would not be trivial. Without a position feedback, the change in voltage of each individual parallel-actuator in the array of microrobots have to be tracked and controlled to avoid overshooting of the microneedles and targeted positioning for molecule delivery. The controller has to be designed such that the scanning of the cells, in-plane and out-of-plane movement of the microneedles happen in a short window time frame. This will avoid damaging the cells being kept outside the culture medium in the cell trapper for a prolong period of time.

The biological experiments need to be performed in terms of delivery of foreign biological substances, such as DNA into human cells to test the feasibility of this new kind of actuator system. Our first proposed experiment would involve delivering, for example, green fluorescent protein (GFP) DNA adsorbed onto the microneedles directly into the nucleus of ten single primary cultured mesenchymal stem cells (MSCs) and human embryonic kidney (HEK*293*) cells in a parallel form. The single cells are to be trapped onto the cell trapper. The GFP fluorescence after *24*, *48* and *72* hours in each single cell would establish the efficiency of the chip technology and whether the cells remain viable after delivery. The current design

can have several limitations in biological delivery with the current form of solid microneedles. This type of microneedle would require surface functionalisation to attach such macromolecules and drug compounds to its tip and depending on surface chemistry to deliver the cargo inside the cells. A major area of future research would involve integrating a hollow microneedle to perform such delivery. This will dramatically increase the application of the actuator. However, the design also needs to be modified to integrate microfluidic channels through the body of the actuator to enable fluid flow through the hollow microneedles. This would involve studying the fluid dynamics behavior inside the micro-channels of the actuator and designing a new fabrication process as such.

9.3 Final summary

We have designed, analysed, fabricated and tested the 4SA microrobot. These analyses and testing results and their validation resulted in the design, analyses and the current fabrication of the 3SA microrobot. We have successfully tested the parallel-plate actuator for achieving vertical motion and propose to use it as a sensor for blind feedback during parallel scale vertical manipulation. This feasibility of this blind feedback has been demonstrated using a macro-scale manipulation experiment. We have also developed several fabrication processes to manufacture such microrobot and to integrate microneedle and tower electrode onto the actuator. Taken as a whole, this dissertation demonstrates the thesis:

Design of an integrated system with 3D motion capability for manipulation on a parallel scale is possible.

Appendix A: Slope Deflection Method for Investigating the In-plane Motion Performance of 3SA Microrobot

To solve the model using slope deflection method, we assume a unit displacement in the microstage D, due to the motion of the comb-drive actuators on side C. Since this relative displacement and the slopes at the ends are known, the end moments can be found using slopes, stiffness, deflection and length of the tethering beams. We use basic trigonometry to find the slopes at the ends.

Using law of cosines in Figure 3.7(b),

$$\overline{KJ}^2 = l_t^2 + \delta^2 - 2\delta l_t \cos 120^o$$

$$\Rightarrow \overline{KJ} = \sqrt{l_t^2 + \delta^2 + \delta l_t} \tag{A1}$$

Using law of sines in Figure 3.7(b),

$$\frac{\delta}{\sin\alpha} = \frac{\sqrt{l_t^2 + \delta^2 + \delta l_t}}{\sin 120^o}$$

$$\alpha = \sin^{-1}\left(\frac{\sqrt{3}}{2}\frac{\delta}{\sqrt{l_t^2 + \delta^2 + \delta l_t}}\right) \tag{A2}$$

$$\frac{l_t}{\sin\beta} = \frac{\sqrt{l_t^2 + \delta^2 + \delta l_t}}{\sin 120^o}$$

$$\beta = \sin^{-1}\left(\frac{\sqrt{3}}{2}\frac{l_t}{\sqrt{l_t^2 + \delta^2 + \delta l_t}}\right) \tag{A3}$$

Using law of sines in Figure 3.7(c),

$$\frac{\Delta}{\sin\alpha} = \frac{l_t}{\sin(120^o - \alpha)}$$

$$\Delta = \frac{l_t \sin\alpha}{\sin 120^o \cos\alpha - \cos 120^o \sin\alpha} \Rightarrow \Delta = \frac{2l_t \sin\alpha}{\sqrt{3}\cos\alpha + \sin\alpha} \tag{A4}$$

where α has been derived from Equation (A2).

Using law of sines again in Figure 3.7(c),

$$\frac{FJ}{\sin 60^o} = \frac{\Delta}{\sin\alpha} \tag{A5}$$

where Δ has been derived from Equation (A4).

$$FJ = \frac{4l_t}{3\cos\alpha + \sqrt{3}\sin\alpha} \tag{A6}$$

$$\therefore KF = KJ - FJ = \sqrt{l_t^2 + \delta^2 + \delta l_t} - \frac{4l_t}{3\cos\alpha + \sqrt{3}\sin\alpha} \tag{A7}$$

Using law of sines again in Figure 3.7(b),

$$\frac{\delta}{\sin\alpha} = \frac{KJ}{\sin 120^o}$$

$$\delta = \frac{2\sin\alpha\sqrt{l_t^2 + \delta^2 + \delta l_t}}{\sqrt{3}} \Rightarrow \frac{\delta}{\sqrt{l_t^2 + \delta^2 + \delta l_t}} = \frac{2}{\sqrt{3}}\sin\alpha \tag{A8}$$

Squaring both sides and rearranging the terms, a quadratic equation in terms of δ is formed. Thus,

$$\delta^2\left(1 - \frac{4}{3}\sin^2\alpha\right) - \delta\frac{4}{3}l_t\sin^2\alpha - \frac{4}{3}l_t^2\sin^2\alpha = 0 \tag{A9}$$

The root of the above equation is,

$$\delta = \frac{\frac{4}{3}l_t\sin^2\alpha \pm \sqrt{\frac{16}{9}l_t^2\sin^4\alpha - 4\left(\frac{4}{3}l_t^2\sin^2\alpha\right)\left(1 - \frac{4}{3}\sin^2\alpha\right)}}{2\left(1 - \frac{4}{3}\sin^2\alpha\right)}$$

$$= \frac{4l_t \sin^2\alpha \left(1 \pm \sqrt{-3\left(1+\frac{1}{\sin^2\alpha}\right)}\right)}{6-8\sin^2\alpha} \tag{A10}$$

Now, writing the slope-deflection equations for the six beam end moments,

$$M_{DA} = \frac{2EI}{l_t}\left(2\theta_D + \theta_A - 3\frac{\Delta}{l_t}\right) \tag{A11}$$

$$M_{AD} = \frac{2EI}{l_t}\left(2\theta_A + \theta_D - 3\frac{\Delta}{l_t}\right) \tag{A12}$$

$$M_{DB} = \frac{2EI}{l_t}\left(2\theta_D + \theta_B + 3\frac{\Delta}{l_t}\right) \tag{A13}$$

$$M_{BD} = \frac{2EI}{l_t}\left(2\theta_B + \theta_D + 3\frac{\Delta}{l_t}\right) \tag{A14}$$

$$M_{DC} = \frac{2EI}{l_t}\left(2\theta_D + \theta_C\right) \tag{A15}$$

$$M_{CD} = \frac{2EI}{l_t}\left(2\theta_C + \theta_D\right) \tag{A16}$$

Taking moments about D,

$$\sum M_D = 0 \Rightarrow M_{DA} + M_{DB} + M_{DC} = 0 \tag{A17}$$

Since A, B and C are fixed; their in-plane rotation is zero,

$$\therefore \theta_A = \theta_B = \theta_C = 0 \tag{A18}$$

$$\therefore \frac{2EI}{l_t}\left(2\theta_D - 3\frac{\Delta}{l_t}\right) + \frac{2EI}{l_t}\left(2\theta_D + 3\frac{\Delta}{l_t}\right) + \frac{2EI}{l_t}\theta_D = 0 \Rightarrow \theta_D = 0 \tag{A19}$$

Substituting Equation (A19) in Equations (A11) to (A16),

$$M_{DC} = M_{CD} = 0 \tag{A20}$$

$$M_{DA} = M_{AD} = -\frac{6EI}{l_t^2}\Delta = -\frac{12EI}{l_t}\frac{\sin\alpha}{\left(\sqrt{3}\cos\alpha + \sin\alpha\right)} \tag{A21}$$

$$M_{DB} = M_{BD} = \frac{6EI}{l_t^2}\Delta = \frac{12EI}{l_t}\frac{\sin\alpha}{\left(\sqrt{3}\cos\alpha + \sin\alpha\right)} \tag{A22}$$

The shear force acting on parts AD and BD,

$$V_{AD} = \frac{M_{AD} + M_{DA}}{l_t} \Rightarrow V_{AD} = -\frac{24EI}{l_t^2}\frac{\sin\alpha}{\sqrt{3}\cos\alpha + \sin\alpha} \tag{A23}$$

$$V_{BD} = \frac{M_{BD} + M_{DB}}{l_t} \Rightarrow V_{AD} = \frac{24EI}{l_t^2}\frac{\sin\alpha}{\sqrt{3}\cos\alpha + \sin\alpha} \tag{A24}$$

When the electrostatic force, F_e, due to the comb actuators at side C pulls the entire structure, the restoring forces due to the spring and tethering beams at sides A, B and C are N_A, N_B and N_C respectively. These restoring forces act opposite to the direction of the electrostatic force as shown in Figure 3.8.

Using conservation of force,

$$\overset{\rightarrow +}{\sum} F_x = 0 \Rightarrow N_B = N_A \text{ and } V_{AD} = V_{BD} \tag{A25}$$

$$\overset{+}{\uparrow}\sum F_y = 0 \Rightarrow N_C + 2N_B\sin 30^o + 2V_{AD}\cos 30^o - F_e = 0$$

$$\therefore F_e = N_C + N_B + \sqrt{3}V_{AD} \tag{A26}$$

Calculating the restoring forces N_B and N_C,

$$N_B = k_B.EF = \frac{2Eh_s w_s^3}{l_s^3}\left(\sqrt{l_t^2 + \delta^2 + \delta l_t} - \frac{4l_t}{3\cos\alpha + \sqrt{3}\sin\alpha}\right) \tag{A27}$$

where δ has been derived from Equation (A10). And,

$$N_C = K_C.\delta = \frac{2Eh_s w_s^3}{l_s^3}\left(= \frac{4l_t\sin^2\alpha\left(1 \pm \sqrt{-3\left(1 + \frac{1}{\sin^2\alpha}\right)}\right)}{6 - 8\sin^2\alpha}\right) \tag{A28}$$

Substituting Equations (A23), (A27) and (A28) in Equation (A26),

$$F_e = \frac{8l_t E h_s w_s^3}{l_s^3}\frac{\sin^2\alpha}{(6-8\sin^2\alpha)}\left(1\pm\sqrt{-3\left(1+\frac{1}{\sin^2\alpha}\right)}\right)+\frac{2Eh_s w_s^3}{l_s^3}\left(\sqrt{l_t^2+\delta^2+\delta l_t}-\frac{4l_t}{3\cos\alpha+\sqrt{3}\sin\alpha}\right)$$
$$-24\sqrt{3}\frac{EI}{l_t^2}\frac{\sin\alpha}{\sqrt{3}\cos\alpha+\sin\alpha} \qquad \text{(A29)}$$

Dividing both sides by $\Delta = \frac{2l_t\sin\alpha}{\sqrt{3}\cos\alpha+\sin\alpha}$ derived from Equation (A4) to find the

spring constant $K_{x,y}$, of the system,

$$K_{x,y} = \frac{F_e}{\Delta} = \left[\frac{4Eh_s w_s^3\sin\alpha(1\pm\sqrt{-3\left(1+\frac{1}{\sin^2\alpha}\right)}(\sqrt{3}\cos\alpha+\sin\alpha)}{l_s^3(6-8\sin^2\alpha)}\right. \qquad \text{(A30)}$$

$$\left.+\frac{Eh_s w_s^3}{l_s^3 l_t\sin\alpha}\left(\sqrt{3}\cos\alpha+\sin\alpha\right)\left(\sqrt{l_t^2+\delta^2+\delta l_t}-\frac{4l_t}{3\cos\alpha+\sqrt{3\sin\alpha}}\right)-\frac{12\sqrt{3}EI}{l_t^3}\right]$$

Appendix B: ANSYS Automated Program

/com *PROGRAMME FOR IN-PLANE ELECTROSTATIC SIMULATION OF ELECTROSTATIC FORCE BY APPLYING VOLTAGES ON COMB-DRIVES.*

/prep7

allsel

/com *COMMANDS TO APPLY ELEMENT LENGTH SIZE, SOLVE THE MODEL AND COMPUTE ELECTROSTATIC FORCES (EMFT) FOR THE NODES SELECTED FROM COMB-DRIVE ACTUATORS*

allsel

vclear,all

smrtsize,1 !smartize activated at level1

esize,1e-6

mat,2 ! material selected for meshing in the next step

vmesh,3 ! meshing of the volume 3

mat,1

vmesh,1,2

!EREFINE,ALL,,,1,,CLEAN,ON !

/prep7

allsel

lsclear,all

FLST,2,176,5,ORDE,2 !Input voltage values on the inner surface of the first

comb-drive electrode, 176 areas selected

```
FITEM,2,182
FITEM,2,-357
/GO
DA,P51X,VOLT,0        !Apply 0 volt
FLST,2,176,5,ORDE,2 !Input voltage on the other comb-drive electrode
FITEM,2,2
FITEM,2,-177
/GO
DA,P51X,VOLT,75 !apply 75 volts
/solu                    ! solve LS
solve

/post1
vsel,s,volu,,2   ! selection of volume number 2
nslv,s,1          ! selection of the nodes for the current volume
emft
/stat

!END of program

da,1,volt,35     ! apply the voltage on area #1
da,2,volt,0
allsel
/solu
```

```
solve

/post1
asel,s,area,,1    ! select a subset of areas
nsla,s,1                  ! selects nodes associated with the selected areas
emft

allsel
asel,s,area,,2
nsla,s,1
emft

/com PROGRAMME FOR STRUCTURAL SIMULATION OF DISPLACEMENTS BY
APPLYING PRESSURES ON NODES

!-INPUT PARAMETERS
!-BEGIN
!-PART1  :  READ FILE
!-PART2  :  DEFINE DEGREES OF FREEDOM
!-PART3  :  SURFACE LOADS
!-PART4  :  SOLVE, NODE SELECTION, COPY DISPLACEMENTS IN
            PARAMETER
!-PART5  :  WRITE FILE
!PART3 AND PART4 ARE REPEATED FOR EACH SIMULATION
!-END
```

```
!-NEXT COMMIT
!
!THE CURRENT PROGRAM ONLY WORKS WITH STRUCTURES WHICH HAVE
ALREADY BEEN MESHED
/com INPUT PARAMETERS
!
!FINISH
!/CLEAR,,1
!*ABBR,Reload,/input,Main program_normal,txt
/prep7                          !ENTER IN THE PRE-PROCESSER PLUGIN
allsel
lsclear,all                     !CLEAR LOADS AND LOAD STEP OPTIONS
*set,Numbnode,0                 !RESET SCALAR PARAMETER
*set,Numvalue,0                 !RESET SCALAR PARAMETER
!NUMVALUE IS A SCALAR PARAMETER WHICH IS SPECIFIES THE NUMBER OF
RESULTS REQUIRED
*ask,Numvalue,How many voltage values?,0
!
!NUMBNODE IS THE NODE NUMBER TO SPECIFY
!*if,Numbnode,eq,0,then ! SCRIPT SUPPOSED TO ALLOWS A PICK-IT-UP
                          FROM THE USER DIRECTLY ON THE GEOMETRY
                          WITH THE PROGRAM ALREADY LUNCHED,IF 0
                          IS INPUT
!ksel,s,p,keypoint_nr    ! DISABLED, SELECTION OF KEYPOINTS ON THE
                         GRAPHIC DISPLAY
```

```
!*endif              ! DISABLED
!nslk,s              ! DISABLED, SELECTION OF THE NEAREST
                         ASSOCIATED NODE TO THE KEYPOINT SELECTED
!Numbnode=ndnext(0) ! DISABLED, ASSOCIATE THE NODE NUMBER IN
                         THE NUMBNODE PARAMETER
! END DISABLED
! LISTING THE VOLTAGES
*dim,voltagelist,,20,1   !DIMENSIONING A VECTOR ON 20 LINES, 1 ROW
voltagelist(1)=35
voltagelist(2)=40
voltagelist(3)=45
voltagelist(4)=50
voltagelist(5)=55
voltagelist(6)=60
voltagelist(7)=65
voltagelist(8)=70
voltagelist(9)=75
voltagelist(10)=80
voltagelist(11)=85
voltagelist(12)=90
voltagelist(13)=100
voltagelist(14)=110
voltagelist(15)=120
voltagelist(16)=130
voltagelist(17)=140
```

```
voltagelist(18)=150
voltagelist(19)=170
voltagelist(20)=190
! LISTING THE AREAS NUMBERS (DAi) AND SURFACE DENSITY (DSE)
*dim,dse,,16,1   !DIMENSIONING OF THE VECTOR FOR FORCES
*dim,da3,,16,1   !DIMENSIONING OF THE AREA
*set,dse_z,0          ! SET THE SCALAR PARAMETER TO 0
*ask,thick,what is the thickness of the model?,10
!DISPLACEMENT AND PRESSURE BOUNDARY CONDITIONS ON AREAS
*if,thick,eq,10,then      ! FOR 10 μm  MODEL
!ksel,s,kp,,205
!nslk,s              !FOR EXAMPLE, Numbnode=189110
!Numbnode=ndnext(0)
dse(1)=1
dse(2)=79
dse_z=119
da3(1)=4                !DA3(i)=AREA ON WHICH THE 3 DEGREES OF
                         FREEDOM ARE CONSTRAINED
da3(2)=8
da3(3)=19
da3(4)=23
da3(5)=30
da3(6)=34
da3(7)=45
da3(8)=49
```

```
da3(9)=56
da3(10)=60
da3(11)=71
da3(12)=75
da3(13)=82
da3(14)=86
da3(15)=97
da3(16)=101
*endif
!
*if,thick,eq,25,then                ! FOR 10 μm  MODEL
!ksel,s,kp,,116
!nslk,s
!Numbnode=ndnext(0)                 ! FOR EXAMPLE, Numbnode=778060
dse(1)=27
dse(2)=33
dse(3)=39
dse(4)=45
dse(5)=51
dse(6)=57
dse(7)=63
dse(8)=69
dse(9)=233
dse(10)=239
dse(11)=245
```

dse(12)=251

dse(13)=257

dse(14)=263

dse(15)=269

dse(16)=275

dse_z=295

da3(1)=4

da3(2)=8

da3(3)=20

da3(4)=24

da3(5)=300

da3(6)=304

da3(7)=284

da3(8)=288

da3(9)=104

da3(10)=108

da3(11)=88

da3(12)=92

da3(13)=226

da3(14)=230

da3(15)=210

da3(16)=214

*endif

! *END OF INPUT PARAMETERS*

```
! PART 1 ----------READ FILE (.TXT)
*SET,ITE,1
*dim,resu,,20,3
*dim,ps,,20,3
*CREATE,ansuitmp   !CREATE A MACRO NEEDED TO EXECUTE A
                                READ OR WRITE STEP
*VREAD,ps(1,1),'read','txt',,JIK,3,20,1        !PS(1,1) IS THE INITIATION
(es14.7,es14.7,es14.7)                    !THESE FORMAT PARAMETERS
                                                COMES FROM FORTRAN LANGUAGE
*END
/INPUT,ansuitmp
! PART 2----------DEFINE DOF CONSTRAINTS ON AREAS  (DA, AREA, Lab,
Value1 (ALL=3AXES)
*dim,programtype,char,1,1,1,,,
allsel
da,da3(1),all
da,da3(2),all
da,da3(3),all
da,da3(4),all
da,da3(5),all
da,da3(6),all
da,da3(7),all
da,da3(8),all
da,da3(9),all
da,da3(10),all
```

da,da3(11),all

da,da3(12),all

da,da3(13),all

da,da3(14),all

da,da3(15),all

da,da3(16),all

! *PART 3----------SPECIFIES SURFACE LOADS ON THE SELECTED AREAS*

(SFA, AREA, LKEY, Lab, Value1 (ALL=3AXES)

*set,kpdist,0

Kdist,194,195 ! *DISTANCE BETWEEN TWO RANDOM KEYPOINTS*

kpdist=_RETURN

*ask,programtype(1),type of simulation: *x* or *xy* or *xyz* or *z*,'*x*'

! *THIS PROMPT ALLOWS USER TO CHOOSE BETWEEN SINGLE AXIS MOTION (x/y),*

2D IN-PLANE MOTION (xy), 3D MOTION (XYZ), OR ONLY z MOTION.

!----------*SINGLE MOTION SIMULATION*----------

*if,programtype(1),eq,'x',then!*THERE ARE iF CONDITIONS FOR 4*

DIFFERENTS CASES

*if,thick,ne,10,then

!*IF KPDIST FOR 10 μm MODEL IS DIFFERENT THEN 25 μm MODEL*

!*KPDSIT SETS THE DISTANCE BETWEEN TWO KEYPOINTS (CHOOSEN AT THE*

BEGINNING OF THIS PROGRAM)

*do,ite,1,Numvalue,1

!*LOOP TO MAKE SIMULATIONS USING NUMVALUE INDICATED IN THE BEGINNING*

! *1 IS THE INITIAL VALUE WITH INCREMENTS OF 1*

allsel

```
/prep7
sfa,dse(1),1,pres,-ps(ite,1)      !PRESSURE BOUNDARY CONDITIONS ON 8
                                  ACTUATOR BEAMS
sfa,dse(2),1,pres,-ps(ite,1)
sfa,dse(3),1,pres,-ps(ite,1)
sfa,dse(4),1,pres,-ps(ite,1)
sfa,dse(5),1,pres,-ps(ite,1)
sfa,dse(6),1,pres,-ps(ite,1)
sfa,dse(7),1,pres,-ps(ite,1)
sfa,dse(8),1,pres,-ps(ite,1)
finish
! PART 4----------SOLVE, SELECTION OF NODES & COPY THE
DISPLACEMENTS IN AN ARRAY PARAMETER
/solve                            !ENTER THE SOLVE PLUGIN
solve
finish
nsel,s,node,,Numbnode                !NODE SELECTION
*get,U1,node,Numbnode,u,x  !GET THE VALUES OF DISPLACEMENT FOR
                                  THE SELECTED NODES IN x (LOCAL SYST
                                  COORDINATE) AND FILL IN U1 SCALAR
                                  PARAMETER


*vabs,1, ! APPLY ABSOLUTE VALUES TO THE DISPLACEMENT RESULTS
*vfill,resu(ite,1),data,U1        !FILL THE ARRAY PARAMATER RESU
```

```
*enddo
*else    IF THE MODEL IS NOT 25 μm THICK THEN CARRY ON FOR 10 μm
*do,ite,1,Numvalue,1
allsel
/prep7
sfa,dse(1),1,pres,-ps(ite,1)      !
finish
/solve
solve
finish
nsel,s,node,,Numbnode                          !NODE SELECTION
*get,U1,node,Numbnode,u,x             !DISPLACEMENT IN x
*vabs,1,
*vfill,resu(ite,1),data,U1
*enddo
*endif
*endif
! 2D IN-PLANE SIMULATION (xy)
*if,programtype(1),eq,'xy',then
*if,thick,ne,10,then
*do,ite,1,Numvalue,1
allsel
/prep7
sfa,dse(1),1,pres,-ps(ite,1)
sfa,dse(2),1,pres,-ps(ite,1)
```

```
sfa,dse(3),1,pres,-ps(ite,1)

sfa,dse(4),1,pres,-ps(ite,1)

sfa,dse(5),1,pres,-ps(ite,1)

sfa,dse(6),1,pres,-ps(ite,1)

sfa,dse(7),1,pres,-ps(ite,1)

sfa,dse(8),1,pres,-ps(ite,1)

sfa,dse(9),1,pres,-ps(ite,2)

sfa,dse(10),1,pres,-ps(ite,2)

sfa,dse(11),1,pres,-ps(ite,2)

sfa,dse(12),1,pres,-ps(ite,2)

sfa,dse(13),1,pres,-ps(ite,2)

sfa,dse(14),1,pres,-ps(ite,2)

sfa,dse(15),1,pres,-ps(ite,2)

sfa,dse(16),1,pres,-ps(ite,2)

finish

/solve

solve

finish

nsel,s,node,,Numbnode                    ! NODE SELECTION

*get,U1,node,Numbnode,u,x  ! DISPLACEMENT  IN x

*get,U2,node,Numbnode,u,z  ! DISPLACEMENT  IN y (CALLED z IN THE
                                          ANSYS MODEL, DUE TO THE IMPORT
                                          PARAMETRIC)

*vabs,1,1,

*vfill,resu(ite,1),data,U1
```

```
*vfill,resu(ite,2),data,U2
*enddo
!
*else
*do,ite,1,Numvalue,1
allsel
/prep7
sfa,dse(1),1,pres,-ps(ite,1)
sfa,dse(2),1,pres,-ps(ite,2)
finish
/solve
solve
finish
nsel,s,node,,Numbnode                          ! NODE SELECTION
*get,U1,node,Numbnode,u,x                      ! DISPLACEMENT  IN x
 DIRECTION*get,U2,node,Numbnode,u,z    ! DISPLACEMENT  IN y (CALLED
                                                z IN THE ANSYS MODEL)
*vabs,1,1,
*vfill,resu(ite,1),data,U1
*vfill,resu(ite,2),data,U2
*enddo
*endif
*endif
! z MOTION SIMULATION
*if,programtype(1),eq,'z',then
```

```
*do,ite,1,Numvalue,1
allsel
/prep7
sfa,dse_z,1,pres,-ps(ite,1)
finish
/solve
solve
finish
nsel,s,node,,Numbnode                    ! NODE SELECTION *get,U1,node,Numbnode,u,y  !
DISPLACEMENT  IN y
*vabs,1,
*vfill,resu(ite,1),data,U1
*enddo
*endif
! 3D MOTION SIMULATION (xyz)
*if,programtype(1),eq,'xyz',then
*if,thick,ne,10,then
*do,ite,1,Numvalue,1
allsel
/prep7
sfa,dse_z,1,pres,-ps(ite,3)
sfa,dse(1),1,pres,-ps(ite,1)
sfa,dse(2),1,pres,-ps(ite,1)
sfa,dse(3),1,pres,-ps(ite,1)
sfa,dse(4),1,pres,-ps(ite,1)
```

```
sfa,dse(5),1,pres,-ps(ite,1)
sfa,dse(6),1,pres,-ps(ite,1)
sfa,dse(7),1,pres,-ps(ite,1)
sfa,dse(8),1,pres,-ps(ite,1)
sfa,dse(9),1,pres,-ps(ite,2)
sfa,dse(10),1,pres,-ps(ite,2)
sfa,dse(11),1,pres,-ps(ite,2)
sfa,dse(12),1,pres,-ps(ite,2)
sfa,dse(13),1,pres,-ps(ite,2)
sfa,dse(14),1,pres,-ps(ite,2)
sfa,dse(15),1,pres,-ps(ite,2)
sfa,dse(16),1,pres,-ps(ite,2)
finish
/solve
solve
finish
nsel,s,node,,Numbnode                    ! NODE SELECTION
*get,U1,node,Numbnode,u,x  ! DISPLACEMENT  IN x
 *get,U2,node,Numbnode,u,z ! DISPLACEMENT  IN y
*get,U3,node,Numbnode,u,y
*vabs,1,1,
*vfill,resu(ite,1),data,U1
*vfill,resu(ite,2),data,U2
*vfill,resu(ite,3),data,U3
*enddo
```

```
!
*else
*do,ite,1,Numvalue,1
allsel
/prep7
sfa,dse_z,1,pres,-ps(ite,3)
sfa,dse(1),1,pres,-ps(ite,1)
sfa,dse(2),1,pres,-ps(ite,1)
finish
/solve
solve
finish
nsel,s,node,,Numbnode                    ! NODE SELECTION
*get,U1,node,Numbnode,u,x  ! DISPLACEMENT  IN x
 *get,U2,node,Numbnode,u,z ! DISPLACEMENT  IN y
*get,U3,node,Numbnode,u,y  ! DISPLACEMENT  IN z (CALLED y IN THE
                                          ANSYS MODEL)
*vabs,1,1
*vfill,resu(ite,1),data,U1
*vfill,resu(ite,2),data,U2
*vfill,resu(ite,3),data,U3
*enddo
*endif
*endif
! PART 5------------------------WRITE FILE (.TXT)
```

```
*CREATE,ansuitmp
*CFOPEN,'write','txt',' '
*vwrite,' ','Volt','Dsplac X',' ','Dsplac Y',' ','Dsplac Z'
(A1,A9,A8,A10,A9,A10,A8/)
*VWRITE,' ',voltagelist(1),' ',resu(1,1),adiv,resu(1,2),adiv,resu(1,3) , , , , , ,
(A1,f4.0,A2,es14.7,A5,es14.7,A5,es14.7)
*CFCLOS
*END
/INPUT,ansuitmp
! END OF PROGRAM
!tirer
!‘/’ adds a newline, and ‘$’ suppresses it.
!symbol & at the end of a line signifies that the message continues to next row
!*CREATE,ansuitmp
!*msg,ui
!/INPUT,ansuitmp
```

Appendix C: Amplifier Circuit Diagram

The Signal In contains *5* analogue voltage inputs coming from two National Instruments NI*9263* DAC modules. This is fed to the ISO124 which provides a level of safety isolation between the HV electronics and the low voltage computer data acquisition equipment. DC to DC converters provide the isolated power supply to drive the entry and exit side of the voltage isolators. The voltage signal is then fed into a PA*340* which is a high voltage op-amp. The op-amp's gain is set to *32* to scale the *0-10* V DAC output to the *0-320* V range the op-amp is capable of driving. The current coming out of the op-amp is limited by two *1* M ohm resistor to ensure that it is electrically safe for operator. High voltage is supplied via the LHV power module whose maximum output voltage is set via the LM*317* adjustable voltage regulator.

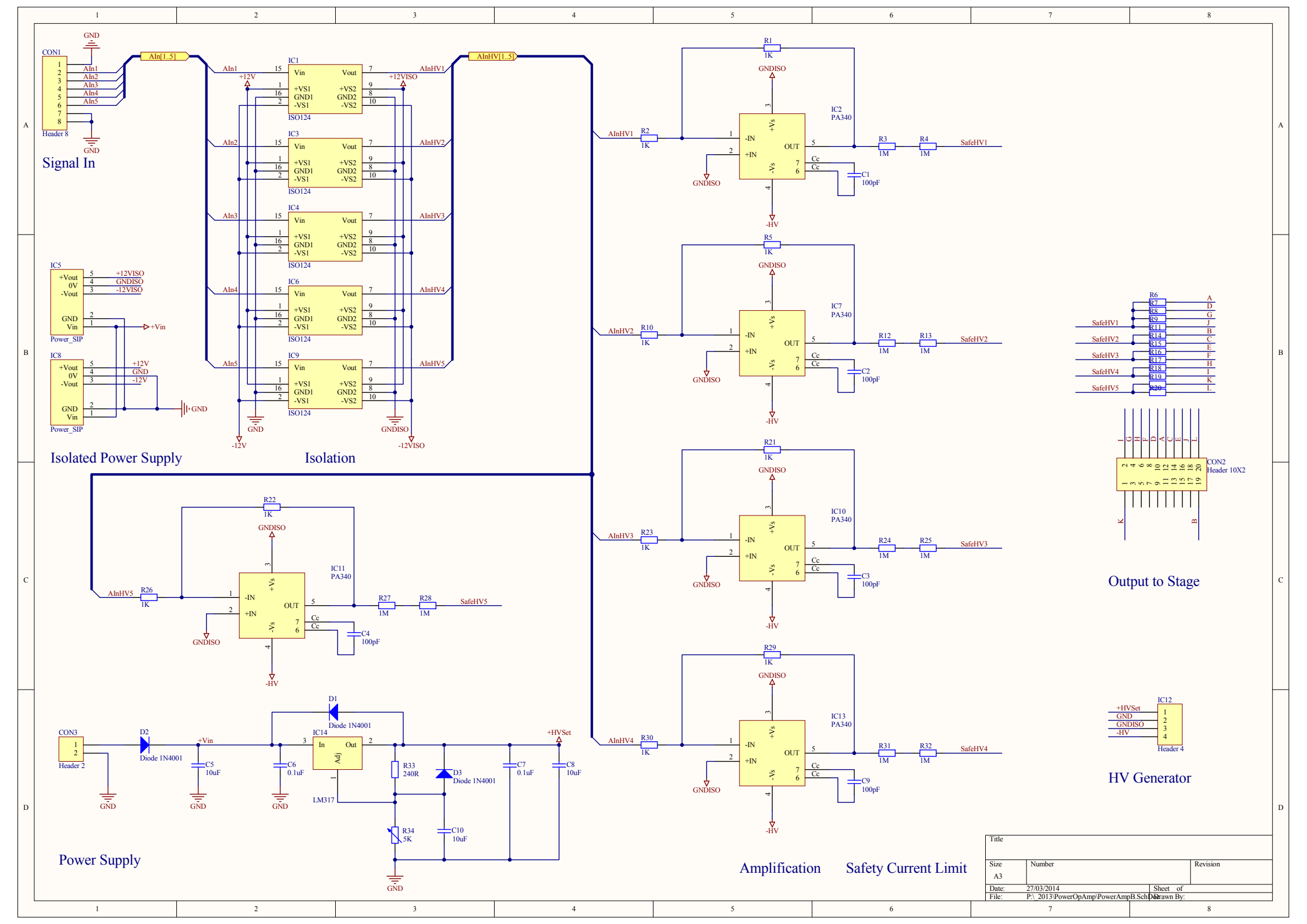
Signal In
Isolated Power Supply
Isolation
Amplification
Safety Current Limit
Output to Stage
HV Generator
Power Supply
CON1
Header 8
AIn[1..5]
AInHV[1..5]
IC1
IC2
IC3
IC4
IC5
IC6
IC7
IC8
IC9
IC10
IC11
IC12
IC13
IC14
ISO124
PA340
Power_SIP
CON2
Header 10X2
CON3
Header 2
Header 4
LM317
Diode 1N4001
+12V
-12V
+12VISO
-12VISO
GND
GNDISO
-HV
+Vin
+HVSet
SafeHV1
SafeHV2
SafeHV3
SafeHV4
SafeHV5
Title
Size
A3
Number
Revision
Date: 27/03/2014
Sheet of
File: P:_2013\PowerOpAmp\PowerAmpB.SchDoc
Drawn By:

Appendix D: MATLAB Program for Computing In-plane Motion of the 4SA Microrobot

%%This program is used to measure the displacement of the microstage from the images taken by a high-resolution camera attached to an inverted fluorescence microscope (Leica DM IRM) under a 200X magnification.

%%Please refer to Section 5.2 for details on measurement.

```
clear all;
close all;
%initialization of parameters
%Global parameters
col=1;
but=1;
n=0;
displacement=[];
scale=150/1081;
volt=[];
volt_displacement=[];
volt(1)=0;
nbImage=3;
%m=0;

%Image access
```

```
nameImageFolder={'+Xaxis' '-Xaxis' '+Yaxis' '-Yaxis' '-X-Yaxis' '+X+Yaxis' '-X+Yaxis' '+X-
Yaxis'};
%nameImage='+Xaxis';
%nameImage='-Xaxis';
%nameImage='+Yaxis';
%nameImage='-Yaxis';
%nameImage='-X-Yaxis';
%nameImage='+X+Yaxis';
%nameImage='-X+Yaxis';
%nameImage='+X-Yaxis';
folder= 'D:\Steven Banerjee';

%Parameters for the cut image
CutRow=540:620;       %width of the selection box
CutColumn=450:960; %length of the selection box
ratio=2.5;                  %scaling up by this value to magnify the image

%Parameters for the different loops
leftside=150:10:490;     %range of measurement for y displacement on the left side
                                of the stage
rightside=840:10:1200; %range of measurement for y displacement on the right
                                side of the stage
longsize=1:1:60; %range for the x measurement from the top of the picture until the bottom
of the stage
```

```
%Parameters to draw the target on each image
xy1=[];
xy2=[];
X=[];
Y=[];

%Parameters to compute the displacement of the microstage
a=0;
LY=[];
LX=[];
lengthY=[];
lengthX=[];
columnY=0;
columnX=0;

% %opening of the excel file
Excel = actxserver('Excel.Application');
Excel.Visible = true;
Workbook = Excel.Workbooks.Add;

for m=1:length(nameImageFolder)
        nameImage=char(nameImageFolder(m));
        %Original image at 0V
        folder1=fullfile(folder,nameImage);
        fileName='_20x_0V.jpg';
```

```
        baseFileName=[nameImage fileName];
        fullFileName = fullfile(folder1, baseFileName);
        Im=imread(fullFileName,'jpg');
        binary=im2bw(Im);
        %figure(1),imshow(binary),title(baseFileName);
        cutimg=binary(CutRow,CutColumn);
        cutimg=imresize(cutimg,ratio);
        [r p]=size(cutimg);
        Y1=[0 r];
        X2=[0 p];
    but=1;
    volt=[];
    col=1;
    columnsY=0;
        columnsX=0;
        LY=[];
        LX=[];
    distanceX=[];
    distanceY=[];
%This part of the program is run only if the images are needed to be suppressed instead of
displaying them

        figure(2),imshow(cutimg),title(baseFileName);
        hold on
    but=1;
```

```
while but == 1   %while loop to draw the target on each image
        [xi,yi,but] = ginput(1);
        n=n+1;
        xy1(n,:)=[xi yi];
        but=2;
end
%   X1=[xi xi];
%   Y2=[yi yi];
%   line(X1,Y1,'linewidth',1);
%   line(X2,Y2,'linewidth',1);
%   hold off
%   X(1)=xi;
%   Y(1)=yi;

for k=leftside %for loop for computing length of the left side of the
                microstage
        a=0;
        columnsY=columnsY+1;
        for l=1:r
                if cutimg(l,k)==1
                        a=a+1;
                        end
                LY(columnsY)=a;
        end
end
```

```
        for k=rightside % for loop for computing length of the left side
                        of the microstage
        a=0;
        columnsY=columnsY+1;
        for l=1:r
                if cutimg(l,k)==1
                        a=a+1;
                end
LY(columnsY)=a;
        end
end
LengthY(col)=mean(LY); %computing the average length of all the
                        measurements taken for the y
                        displacement
for K=longsize %for loop to compute the length of the side
        a=0;
        columnsX=columnsX+1;
        for l=1:250
                if cutimg(K,l)==0
        a=a+1;
                end
LX(columnsX)=a;
        end
end
LengthX(col)=mean(LX); %computing the average length of all the
```

```
                                        measurements taken for the x
                                        displacement
        %%
%       %Images 35V to 90V
%       for i=35:5:90; %reading images from 35V to 90V
%               col=col+1;
%               volt(col)=i;
%               columnsY=0;
%               columnsX=0;
%               LY=[];
%               LX=[];
%               fileName=sprintf('_20x_%dV.jpg',i);
%               folder1=fullfile(folder,nameImage);
%               baseFileName=[nameImage fileName];
%               fullFileName = fullfile(folder1, baseFileName);
%               Im=imread(fullFileName,'jpg');
%               binary=im2bw(Im);
%               cutimg=binary(CutRow,CutColumn);
%               cutimg=imresize(cutimg,ratio);
%               [r p]=size(cutimg);
%               Y1=[0 r];
%               X2=[0 p];
% % This part of the program is run only if the images are needed to be suppressed instead
of displaying them
%
```

```
%               figure(col),imshow(cutimg),title(baseFileName);
%               hold on
%               line(X1,Y1,'linewidth',1);
%               line(X2,Y2,'linewidth',1);
%               hold off
%
%               for k=leftside % for loop for computing length of the left side of the
                                    microstage
%                       a=0;
%                       columnsY=columnsY+1;
%                       for l=1:r
%                               if cutimg(l,k)==1
%                                       a=a+1;
%                               end
%                               LY(columnsY)=a;
%                       end
%               end
%               for k=rightside % for loop for computing length of the right side
                                    of the microstage
%                       a=0;
%                       columnsY=columnsY+1;
%                       for l=1:r
%                               if cutimg(l,k)==1
%                                       a=a+1;
%                               end
```

```
%                               LY(columnsY)=a;
%                       end
%               end
%               LengthY(col)=mean(LY);
%               for K=longsize %for loop for computing the length of side
%                       a=0;
%                       columnsX=columnsX+1;
%                       for l=1:250
%                               if cutimg(K,l)==0
%                                       a=a+1;
%                               end
%                               LX(columnsX)=a;
%                       end
%               end
%               LengthX(col)=mean(LX);
%       end


        %%
        %Images 100V to 120V
        for k=100:10:120 %reading images from 100V to 120V
                col=col+1;
                volt(col)=k;
                LengthYImage=[];
                LengthXImage=[];
                %for nbImageVoltage=1:1:nbImage
```

```
columnsY=0;
columnsX=0;
LY=[];
LX=[];
fileName=sprintf('_20x_%dV.jpg',k);
folder1=fullfile(folder,nameImage);
baseFileName=[nameImage fileName];
fullFileName = fullfile(folder1, baseFileName);
Im=imread(fullFileName,'jpg');
binary=im2bw(Im);
cutimg=binary(CutRow,CutColumn);
cutimg=imresize(cutimg,ratio);
[r p]=size(cutimg);
Y1=[0 r];
X2=[0 p];
```

% *This part of the program is run only if the images are needed to be suppressed instead of displaying them*

```
%                                   figure(col),imshow(cutimg),title(baseFileName);
%               but=1;
%                                   hold on
%                                   line(X1,Y1,'linewidth',1);
%                                   line(X2,Y2,'linewidth',1);
%               while but == 1   %while loop to draw the target on each image
%               [xi,yi,but] = ginput(1);
%               n=n+1;
```

```
%               xy1(n,:)=[xi yi];
%               but=2;
%       end
                                hold off


                for K=leftside % for loop for computing length of the left side
                                of the microstage
                        a=0;
                        columnsY=columnsY+1;
                        for l=1:r
                                if cutimg(l,K)==1
                                        a=a+1;
                                end
                                LY(columnsY)=a;
                        end
                end
                for K=rightside % for loop for computing length of the right
                                side of the microstage
                        a=0;
                        columnsY=columnsY+1;
                        for l=1:r
                                if cutimg(l,K)==1
                                        a=a+1;
                                end
                                LY(columnsY)=a;
```

```
                end
            end
            LengthY(col)=mean(LY);
            for K=longsize % for loop for computing length of the side
                a=0;
                columnsX=columnsX+1;
                for l=1:250
                    if cutimg(K,l)==0
                        a=a+1;
                    end
                    LX(columnsX)=a;
                end
            end
            LengthX(col)=mean(LX); % average length of the side
        end
%       LengthY(col)=mean(LengthYImage);
%       LengthX(col)=mean(LengthXImage);
%   end
    %%
    %Results
    for i=1:length(LengthY)
        distanceY(i)=(LengthY(i)-LengthY(1))*scale;
        distanceX(i)=(LengthX(i)-LengthX(1))*scale;
    end
    distanceY_volt=cat(1,distanceY,volt);
```

```
distanceX_volt=cat(1,distanceX,volt);
transpose(distanceY_volt);
transpose(distanceX_volt);
distanceX=transpose(distanceX)
distanceY=transpose(distanceY)
volt=transpose(volt)
values=[volt,distanceX,distanceY];
headers={'Volt','X in µm','Y in µm'};

%xlswrite('results',headers,1,'A1'); %replace the sheet number by m
%xlswrite('results',values,1,'A2'); %replace the sheet number by m

% Write data
% Recovery of the first worksheet in the variable
% ActiveSheet to simplify code later
ActiveSheet = Excel.Worksheets.Item(m); % replace 1 by m when it is in loop
% Change the name of the first worksheet
ActiveSheet.Name = nameImage;
ActiveSheet.Range('A1:C1').value=headers;
ActiveSheet.Range('A2:C10').value=values;
% Formatting data here
```

```
end
% nbimage=n/length(nameImageFolder);
% X1axis_results=xy1(1:nbimage,:);
% X2axis_results=xy1((nbimage+1):(2*nbimage),:);
% Y1axis_results=xy1((2*nbimage+1):(3*nbimage),:);
% Y2axis_results=xy1((3*nbimage+1):(4*nbimage),:);
% X2Y2axis_results=xy1((4*nbimage+1):(5*nbimage),:);
% X1Y1axis_results=xy1((5*nbimage+1):(6*nbimage),:);
% X2Y1axis_results=xy1((6*nbimage+1):(7*nbimage),:);
% X1Y2axis_results=xy1((7*nbimage+1):(8*nbimage),:);
%
final_results=cat(8,X1axis_results,X2axis_results,Y1axis_results,Y2axis_results,X2Y2axis_r
esults,X1Y1axis_results,X2Y1axis_results,X1Y2axis_results);
% Workbook.SaveAs(fullfile(xlspath,xlsfile));
% Workbook.Close;
% Quit(Excel);


%-------------------------------------For plotting the graph-----------------------------------
clear all
close all
% Open excel workbook
xlspath ='D:\Steven Banerjee' ;
%xlsfile = input('enter the excel file name','s');
xlsfile='results_modify.xlsx';
```

```
numberIsolines=input('How many isolines (with all the associated points) do you want to display? :');
fprintf('enter values between [0 50 60 70 80 90 100 110 120]','%s\n');
voltChosen=zeros(numberIsolines,1);
for j=1:length(voltChosen)
        voltChosen(j)=input(sprintf('The %d volt value:',j));
end
Xvalues=[];
Yvalues=[];

%initialization of variables
%variable to enter for electrostatic force

Na=44; %number of comb fingers pairs
e=8.85*10^(-12); %the permittivity of the air
ha=25; %finger thickness
ga=3; %gap between two adjacent fingers

%Electrostatic force
F=(8*Na*e*ha)/(2*ga);

%defines variables for system stiffness

E=129*10^9; %Young's modulus
h=10*10^(-6); %height of spring flexure beam
```

```
w=8*10^(-6); %width of spring flexure beam
l=551*10^(-6); %length of spring flexure beam

H=10*10^(-6); %height of tethering beam
W=4*10^(-6); %width of tethering beam
L=1000*10^(-6); %length of tethering beam

%Stiffness
K=91.67;

nameImageFolder={'+Xaxis' '-Xaxis' '+Yaxis' '-Yaxis' '-X-Yaxis' '+X+Yaxis' '-X+Yaxis' '+X-
Yaxis'};
colorstr=[0 0 1;0 1 0;1 0 0;1 1 0;0 1 1;1 0 1;0.75 0 0.75;1 1 1];
%Opening of excel file
%Opening of workbook
Excel = actxserver('Excel.Application');
Excel.Visible = false;
Workbook = Excel.Workbooks.Open(fullfile(xlspath,xlsfile));

for j=1:length(voltChosen)

for m=1:length(nameImageFolder)
% Recovery of the first worksheet in the variable
% ActiveSheet to simplify code later
        ActiveSheet = Excel.Worksheets.Item(m);
```

```
% Retrieving values of displacement in x and y from the worksheet
                range = ActiveSheet.Range('A1:A10');


                address = range.Find(voltChosen(j)).Address;


                r(1) = ActiveSheet.Range(address).get('Cells', 1, 2);
                r(2) = r(1).End('xlToRight');
                data =  ActiveSheet.get('Range', r(1), r(2)).Value;
                data = cell2mat(data);
                Xvalues(m) = data(1);
                Yvalues(m) = data(2);
        end
        Xvalues(m+1)=Xvalues(1);
        Yvalues(m+1)=Yvalues(1);
        figure(1),xlabel('displacement x µm'),ylabel('displacement y µm'),title('Comparaison
between measures and theory')
        hold on
        Xplot=plot(Xvalues,Yvalues,'--mo',...
           'LineWidth',0.2,...
           'MarkerEdgeColor','k',...
           'MarkerFaceColor',colorstr(j,:),...
           'MarkerSize',10);


end
```

```
%%
%Plot values as 2D surface plots with isolines

%hleg1=legend(nameImageFolder(1),nameImageFolder(2),nameImageFolder(3),nameImage
Folder(4),nameImageFolder(5),nameImageFolder(6));
R=F/K*voltChosen.^2;
        R=2*R.*10^6;
        for i=1:1:length(R)
                VThetaDeg = 0:1:360;
                VTheta = VThetaDeg *pi / 180;
                XCercle = R(i) * cos(VTheta);
                YCercle = R(i) * sin(VTheta);
                isolines(i)=rectangle('Position',[-R(i),-
R(i),2*R(i),2*R(i)],'LineWidth',1,'LineStyle','-');
      set(isolines(i),'edgecolor',colorstr(i,:))
   end
   grid on
hold off

% Closing workbook
Workbook.Close(false);

% Closing the excel application
Quit(Excel);
```